Tesi di Dottorato di **VIJITH KUMAR**
Matricola **821698**

HYDROGEN AND HALOGEN BONDING TOWARDS MOLECULAR RECOGNITION AND SEPARATION

**DIPARTIMENTO
DI
CHIMICA, MATERIALI
E INGEGNERIA CHIMICA
"Giulio Natta"**

Dottorato di Ricerca in Chimica Industriale e Ingegneria Chimica (CII)

PhD in Industrial Chemistry and Chemical Engineering

XXIX ciclo
2013 - 2016

Coordinatore: Prof. Alessio Frassoldati
Tutore: Prof. Pio Forzatti
Relatore: Prof. Giuseppe Resnati

Declaration

I hereby declare that the matter embodied in this thesis entitled "**Hydrogen and Halogen Bonding towards Molecular Recognition and Separation**" is the result of investigations carried out by me and it has not been submitted elsewhere for the award of any degree or diploma, membership etc. The major amount of the work reported in this thesis has been carried out in the Laboratory of Nanostructured Fluorinated Materials (NFM Lab), Department of Chemistry, Materials, and Chemical Engineering "Giulio Natta", Politecnico di Milano, Italy, under the guidance of Prof. Giuseppe Resnati and Prof. Pierangelo Metrangolo. The metal coordinated self-assembly project is carried out by myself in the Department of Applied Chemistry , School of Engineering, The University of Tokyo, Japan under the guidance of Prof. Makoto Fujita and Dr. Daishi Fujita. The solid state NMR analysis and Quantum chemical calculations described in this thesis are performed in collaboration with Prof. Roberto Gobetto and Prof. Carlo Nervi, University of Turin, Italy. Special NMR techniques like ^{19}F, ^{1}H HOESY, ^{1}H NOESY and PGSE analysis reported in this thesis are performed in collaboration with Prof. Alceo Macchioni, Department of Chemistry, Biology and Biotechnology, University of Perugia, Italy. The liquid crystal research work is carried out in collaboration with Prof. Albertus P. H. J. Schenning, Department of Functional Organic Materials and Devices, Chemical Engineering and Chemistry, Eindhoven University of Technology, Eindhoven.

In keeping with the general practice of reporting scientific observations, due acknowledgements have been made whenever the work described is based on the findings of other investigators. Any omission that might have occurred due to oversight or error in judgment is deeply regretted. A complete bibliography of the books and journals referred in this thesis is given at the end of each chapter and section.

(Vijith Kumar)

Certificate

I hereby certify that the entire work embodied in this thesis entitled "**Hydrogen and Halogen Bonding towards Molecular Recognition and Separation**" has been carried out by Mr. Vijith Kumar at the Laboratory of Nanostructured Fluorinated Materials (NFM Lab), Department of Chemistry, Materials, and Chemical Engineering "Giulio Natta", Politecnico di Milano, Italy, under my supervision and it has not been submitted elsewhere for any degree or diploma.

Giuseppe Resnati

Acknowledgements

"If the only prayer you ever say in your entire life is thank you, it will be enough."

-Meister Eckhart

I take this opportunity to thank people who have helped me directly or indirectly in the completion of this thesis and express my sincere gratitude to all of them.

I express my deepest gratitude towards my research supervisor and mentor, **Prof. Giuseppe Resnati** for introducing me to the fascinating field of supramolecular chemistry and crystal engineering. His guidance, support and encouragement have been crucial throughout the course of my work. I am thankful to him for the freedom he gave me to work independently.

Besides my supervisor, I am grateful to **Prof. Pierangelo Metrangolo** for his constant guidance and encouragement. It was indeed a good experience working with him. Besides excellent academic support, his friendly nature has had a great influence in my research work.

I express my sincere thanks to **Prof. Makoto Fujita**, Department of applied chemistry, University of Tokyo for giving me an opportunity to work in his well-established research group for three months as a visiting research student. Special thanks to Dr. Daishi Fujita and his research group who have helped and supported me with my research project over the period in Tokyo.

I specially thank Dr. Tullio Pilati, Prof. Giancarlo Terraneo, Dr. Gabriella Cavallo, Prof. Francesca Baldelli Bombelli and Maurizio Ursini for their guidance, encouragement and constructive feedback.

I am grateful to our research collaborators, Prof. Roberto Gobetto (University of Turin), Prof. Carlo Nervi (University of Turin), Prof. Alceo Macchioni (University of Perugia), Prof. Albertus P. H. J. Schenning (Eindhoven University of Technology) and Dr. Silvio Quici (CNR, Milano).

Heartfelt thanks to Prof. T.N Guru Row - My previous supervisor at Indian Institute of Science, Bangalore for introducing me to the fascinating field of chemical crystallography and for his pro-active actions in letting me enter Prof. Giuseppe Resnati and Prof. Pierangelo Metrangolo's research group as a PhD student.

I express a deep sense of gratitude to my parents and family members for their continuous support. Without their help, suggestion and motivations, this thesis would not have been possible.

Lastly, special thanks to all my NFM lab mates and friends, who have helped and supported me with my research project over the years.

Abstract

Molecular self-assembly has been well-acknowledged as one of the efficient bottom-up approache to synthesize various materials with controllable architectures and useful properties. It has clearly been proven that the formation of the well-ordered structures of self-assembled architectures can be driven by a single interaction or by the synergistic action of multiple interactions. In this thesis metal coordination, hydrogen bond (HB) and halogen bond (XB) have been used for the design and synthesis of self-assembled systems tailored to topological studies, separation processes, obtainment of supramolecular functional materials.

The first part of the thesis describes how metal coordination enables twenty four bis-pyridyl ligands (L), functionalized with an iodotetrafluorobenzene moieties, and twelve Pd(II) ions (M) to undergo in solution, a quantitative self-assembly process and to form discrete nanocages of general formula $M_{12}L_{24}$. Artificial self-assembled cages can often encapsulate guest molecules and promote unusual reactivity; the XB donor groups decorating the inside face of the obtained nanosized capsule will be used to control the nature of the guest molecule(s) encapsulated in the cage and to direct the reactivity of these molecule(s).

In the second part of the thesis, HB is employed in selective recognition and effective separation of industrially important dicarboxylic acids from either their mixtures through solid or solution phase processes. The size-matching of the interacting partners plays a major role in allowing for selective self-assembly and ensuing separation process. Specifically, we have demonstrated that bis-(trimethylammonium)alkane diiodides, a well-known class of organic salts, can reversibly encapsulate size-matching dicarboxylic acids through intermolecular HBs between the host I^- anions and the guest carboxylic OH group. The selectivity of the process is very high and very good yields of pure dicarboxylic acids can be obtained from diacids mixtures.

In the third part of the thesis XB is used to form a great variety of supramolecular architectures. Specifically, naked halide anions have been used to form several halogen bonded networks with different and fascinating topologies. A library of supramolecular anionic networks showing Borromean interpenetration has been prepared by self-assembly of crypt-222, several metal or ammonium halides, and bis-homologous α,ω-diiodoperfluoroalkanes (DIPFA's). In addition to this, XB is used to assess the proton localization in the product that hydrogen iodide forms with crypt-111, a proton sponge with unique and useful protonation kinetics. Finally, the XB driven self-assembly of alkoxystilbazole methacrylate with series of diiodoperfluorocarbons is shown to afford monotropic LCs possessing smectic A phases.

Table of contents

Chapter 1

An Introductory Note

1.1. Background

Modern science and technology is largely based on the exploration and application of special functional materials[1] in many disciplines such as electronics,[2] surface science[3] and medicine.[4] Consequently, understanding the interactions of atoms and molecules with each other is hot and timely area of interest and it impacts in many disciplines. One of the outcome of the interactions of atoms is the formation of small molecule is the prototype example. At the same time atoms and molecules can also interact through non-reactive channel to afford adducts of different site with different properties. In the latter case where in a covalent bond is neither formed nor broken, a non-covalent interaction is a driving force recognized as early as hundred and fifty years ago by J. D. Van der Waals to reformulate the equation of state real gases[5] and now they are accepted to play an irreplaceable role in molecular recognition, self-assembly, reactivity and catalysis, crystallization and biomolecules structure and functions.[6-8] Importantly non-covalent interactions are typically involved in the so named 'bottom-up' approach, i.e. molecular self-assembly technique. Beneath the cooperation of multiple non-covalent interaction to the development of novel materials, natural and synthesized building blocks are autonomously organized to produce marvelous architectures with novel structure and functional properties.[9] Inspired from natural systems,[10] nowadays self-assembly (via non-covalent interactions and metal coordination) have been granted as a powerful approach to generate complex arrangements ranging from nanoscale to macroscale.[11] In this chapter, the basic concept of non-covalent interaction and molecular self-assembly process for the preparation of complex topological system towards recognition and separation are detailed.

1.2. Supramolecular chemistry

The initial steps paving the way to *supramolecular chemistry* date back to the 19th century when some basic ideas of fundamental relevance to the topic were introduced. Specifically, Alfred Werner in 1893 developed the concept of coordination chemistry,[12] and one year later the lock-and-key concept was introduced by Emil Fischer in 1894.[13] The word "supramolecule"[14] possibly appeared in literature in 1937, when K. L. Wolf and co-workers introduced the word "Ubermolekul" to depict the dicarboxylic acids dimers formed under the control of intermolecular interactions. However, the concept of supramolecular chemistry was framed after its present structure only in 1979 when, after a systematic and huge number of examples indicating the consequence of non-covalent interactions, Jean-Marie Lehn defined supramolecular chemistry as the "chemistry beyond the molecule".[15] Molecular chemistry

covers the chemistry of covalent bonds and being the target of theoretical and experimental efforts for more than hundred years, we have witnessed the design and formation of more and more complex molecules obtained through elaborate strategies focused on forming and breaking covalent bonds in a controllable and accurate manner. Differently, supramolecular chemistry concentrates on the use of non-covalent interactions in order to self-assemble chemical entities with a precision in the sub-nanometer scale. The aim is to obtain materials with pre-established chemical and physical properties. A variety of reversible intermolecular interactions may be used in the recognition event between the molecules (or, more general, the complementary interacting sites). Thus supramolecular chemistry pursuing the control over the process of molecular (self-)assembly via non-covalent interactions, it combines in a unique and useful way to some key-features: specificity, selectivity, reversibility, directionality, and cooperativity.

Despite the key-role played by non-covalent interactions in chemistry and biology of living systems, synthetic chemists recently began to purposefully use these weak interactions. Supramolecular chemistry draws inspiration from nature's precise use of non-covalent interactions, and aims at using these weak, intermolecular forces to control chemical structure and reactivity.

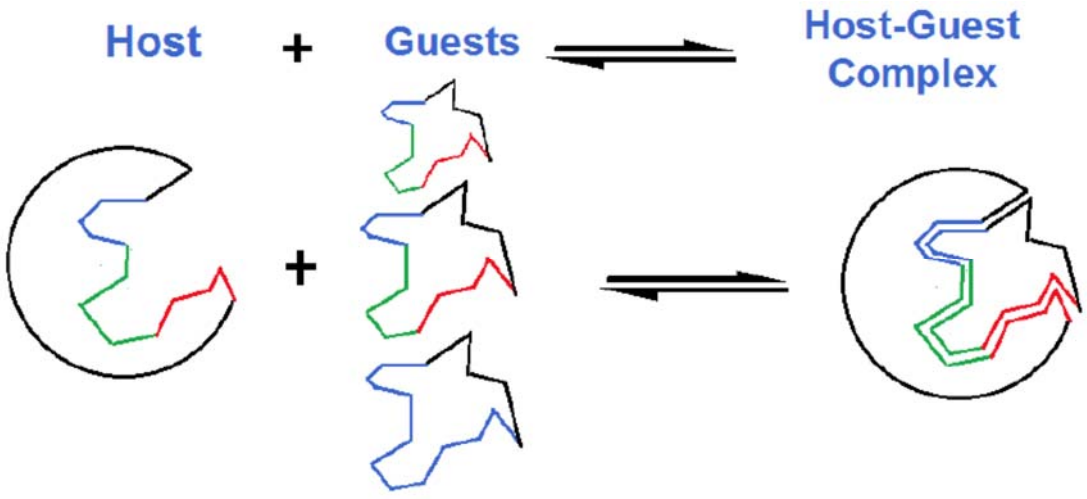

Figure 1.1 Cartoon representation of molecular recognition and assembly through non-covalent interactions in host-guest chemistry. The host moiety has several recognition sites (in different size and color) and they match the complementary groups in the guest moiety; recognition can be mediated by the same or different type of non-covalent bonding; specificity and selectivity in the recognition can thus be mediated by both geometric chemical features.

The term **"host-guest chemistry"** is generally used to designate the establishment of multiple non-covalent bonds between a large and structurally concave organic molecule (the host) and one or more simple molecules or ions (the guest), which will be accommodated inside the host cavity[16] (Fig. 1.1).

The excellent skills of many groups of organic chemists throughout the world resulted in the production of a large variety of synthetic hosts with different size, geometry, binding sites, portals and chemical and physical properties. A prototype host is a molecule having a large and functionalized cavity: cyclodextrins[17] (CD), cucurbiturils[18] (CB), calixarenes[19] and some organic/metal organic frameworks[20] are well established examples of hosts and they can attractively interact with cationic, anionic or neutral substrates of guest molecules.

A landmark in the development of supramolecular chemistry was the discovery of crown ethers.[21] These systems were first introduced in 1967 by Pedersen who reported that cyclic compounds consisting of ethylene oxide repeating units can selectively accommodate alkali metals such as sodium and potassium cations (Fig. 1.2). Interactions between metal cations and oxygen atoms in crown ethers act as a driving force for the metal complexation in the macrocycle, namely the number of coordinating oxygen atoms, is responsible for the selectivity in cation recognition. While the selective recognition of ions is a fundamental function in a living system, selective cation recognition by synthetic compounds had not been reported before the discovery of crown ethers. Therefore, this discovery was a starting point not only in the fields of molecular recognition and supramolecular chemistry, but also in the field of biomimetic chemistry. A huge variety of functionalized crown ethers have been described and a large library of compounds with diverse structures, solubilities, conformational flexibilities etc., are available. The most recent additions to this library includes stimuli responsive and adaptive crown ethers.[22] Interestingly, the formation of host-guest complexes between crown ethers and organic ammonium cations were used for the preparation of molecular machines such as molecular elevators and molecular shuttles.[23]

After the discovery of crown ethers, Lehn *et al*. synthesized cryptands, which contain a "double-cyclic" crown ether structure[24] enabling for effective and selective capture of different cations, selectivity mainly resulting from the size of the cavity defined by the cyclic array. Interestingly, this complexation behavior recalls the encapsulation of potassium ions by the antibacterial agent valinomycin.

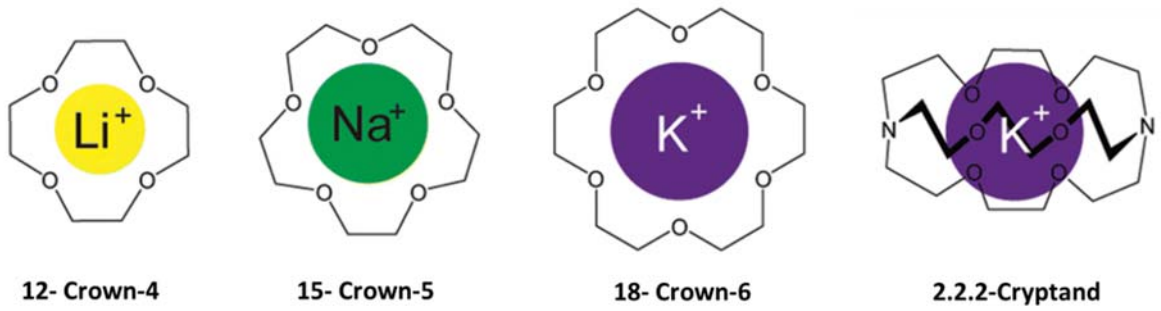

Figure 1.2 Chemical structures of simple crown ether⊂metal cation and 2.2.2.-cryptand ⊂potassium cation complexes.

In order to secure high affinity and selectivity during the host-guest recognition process, the host must have binding sites which are complementary to those of the guest(s), both in relation to their intrinsic properties (interacting donor/acceptor abilities, namely number and type of complementary sites) and their geometric features (shape, distances and angles at the binding sites and in its surrounding).

After these seminal studies, an enormous amount of studies target molecular recognition phenomena pursuing high affinity and selectivity in the binding of both charged and neutral guests. The impact of these studies encompasses nearly any field of chemistry and related disciplines. For instance, the understanding and control of recognition and assembly phenomena are of paramount importance in homogeneous and heterogeneous catalysis, for understanding biological processes (ranging from enzymatic activity to DNA base pairing),[25] in the design of functional supramolecular systems (for example, molecular motors[26] and sensors[27]) in the production of intelligent systems for waste management.[28]

A basic principle of any molecular regulation processes in biological and artificial system asks that chemical information is transmitted properly and conscientiously. Structural and electronic features in pairing molecules must enable for their 3-dimensional complementarity in terms of all properties characterizing the partners, e.g., geometric and steric aspects, electrostatic and hydrophobic parameters, single or multiple binding sites allowing for non-covalent bonds formation. Such supra-molecular self-assembly is a highly dynamic process and often involves flexible, conformational and induced fit phenomena which allow the optimization of the binding by maximizing all contributing components, spanning the maximization of the non-covalent interactions strength and the minimization of internal surface areas not saturated via adduct formation. The single or multiple non-covalent bonds formed selectively during the recognition process usually give a major contribution to the specificity of the binding of a given molecule with respect to analogous structures.

The use of molecular recognition principles to gather information on biological phenomena, in relation to catalysis, transport, signaling, etc., is a rather established field. More recently, molecular recognition principles are being used also in separation science and storage processes. For instance, adequate molecular recognition may help to obtain chemical entities in pure form and a high selectivity and can also enable for enhanced loading capacity and productivity of the purification process. As an example, by exploiting the ability of intermolecular interactions to bestow specificity in the functional properties of rigid crystalline systems, protocols have been developed for the separation of chiral pharmaceuticals, [29]synthetic chemo-affinity materials[30] and key intermediates and catalysts of industrial importance.[31]

1.3. Molecular self-assembly and Crystal engineering

Crystal engineering is the understanding of intermolecular interactions in the context of crystal packing and the utilization of such understanding in the design of new solids with desired physical and chemical properties (Fig. 1.3). In other words, the goal is to create functional solid systems by assembling molecular units into extended molecular structures. Over the past 50 years the chemistry behind the development of organic functional materials has progressively shifted its focus from the well-documented methodologies based on covalent synthesis toward approaches based on supramolecular synthesis. Many different self-assembly strategies have been proposed, and new supramolecular systems endower with quite different useful properties have been obtained. It was thus possible to obtain efficient molecular receptors,[32] functional materials with optimized properties,[33] as well as organogels,[34] supramolecular polymers and adducts,[35] useful in molecular recognition and separation.[31] Molecular modules have been assembled under control of all the various intermolecular interactions available in the literature, namely metal coordination,[36] hydrogen bonding (HB), [37] π–π stacking[38] and hydrophobic forces.[39] In some cases self-assembly processes have been driven by one single interaction, in other cases by a balanced combination of two or more interactions. The double-stranded helical structure of DNA, perhaps the best known self-assembling structure in biological systems; exists in a double stranded helical form formed as a consequence of multiple, discreet Watson–Crick HB and π–π stacking forces between the four nucleobases.[40]

In the last decades halogen bonding (XB)[41] has also entered the toolbox available to supramolecular chemists to control recognition and self-assembly processes.

As detailed in following Chapters, our research work in this thesis focused on the use of hydrogen bond and halogen bond as the non-covalent interactions driving the self-assembly process.

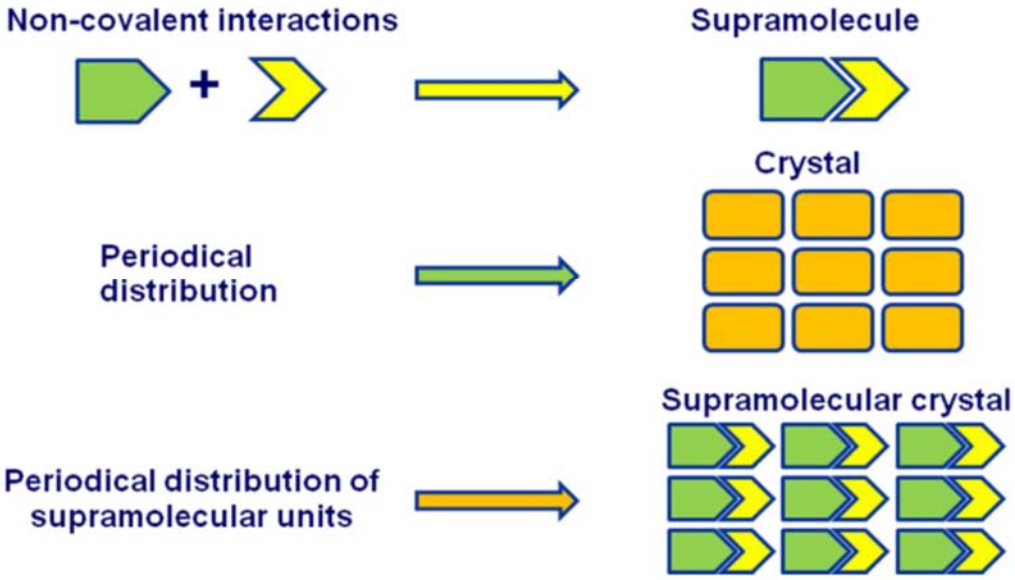

Figure 1.3 Schematic representation for the formation of supramolecular crystal.

Molecular self-assembly may be defined as the spontaneous and reversible association of molecules or ions to form larger, more complex supramolecular entities under control of the intrinsic information contained in the molecules themselves. Supramolecular assemblies represent a vast and diverse set of structures ranging in size from nanometer to millimeter and spanning systems aimed at verifying basic scientific issues and systems that perform adaptive and responsive functions in chemical and biological systems.

Self-assembly processes can be broadly classified into two main branches on the basis of the interactions driving the adducts formation: (i) *Coordination driven self-assembly phenomena,* where strong and directional transition metal−ligand bonds are responsible for tectons recognition; (ii) Those that utilize *Non-covalent interactions driven self-assembly phenomena, wherein* hydrogen bonding (HB),[38] halogen bonding (XB),[41] ion− ion,[42] π− π stacking,[38] cation−π,[43] van der Waals,[44] and hydrophobic interactions[39] are the attractive forces guiding the recognition. The two processes will be briefly discussed in the following sections.

1.4. Molecular self-assembly via coordination chemistry

The control over the structural features of the zero-, one-, two- and three-dimensional (0D, 1D, 2D, and 3D, respectively) architectures afforded by a self-assembly process is typically greater

when resorting to metal coordination than to the so-named non-covalent interactions, thanks to two distinctive features of metal coordination. First, the energies associated with metal-ligand bonds are typically in the range 15-50 kcal/mol, namely they are immediately below the energies of standard covalent bonds (ca. 60-120 kcal/mol). This allows metal coordination to frequently prevail over other interactions, possibly involving the used tectons, and to control the structure of the supramolecular architecture. Second, metal-ligand coordination typically forms very directional bondings so that it is possible to reliably predict the geometric characteristics of supramolecular architectures from the geometric characteristics of starting tectons and their binding sites. For instance, it was possible to obtain metal containing assemblies possessing specific cavities tailored to accommodate a given guest molecules and to involve it into functional transformations.

The early pioneering work reported by Lehn[45] and Sauvage[46] describes the feasibility and usefulness of coordination-driven self-assembly in the formation of infinite helicates, grids, ladders, racks, knots, rings, catenanes, rotaxanes and related species.[47] After this seminal activity, other groups have independently developed and exploited novel coordination-based paradigms for the self-assembly of discrete metallacycles and metallacages with well-defined shapes and sizes. The activity of the groups of Stang,[48] Fujita,[49] Raymond,[50] Mirkin,[51] and Cotton,[52] have been particularly remarkable. The nature of the ligands and the geometry around the metal allows to predict and design supramolecular assemblies by exploiting the opportunities offered by directional bonding,[48] molecular paneling,[49] symmetry interaction,[50] weak link[51] and dimetalic building block[52] (Fig. 1.4).

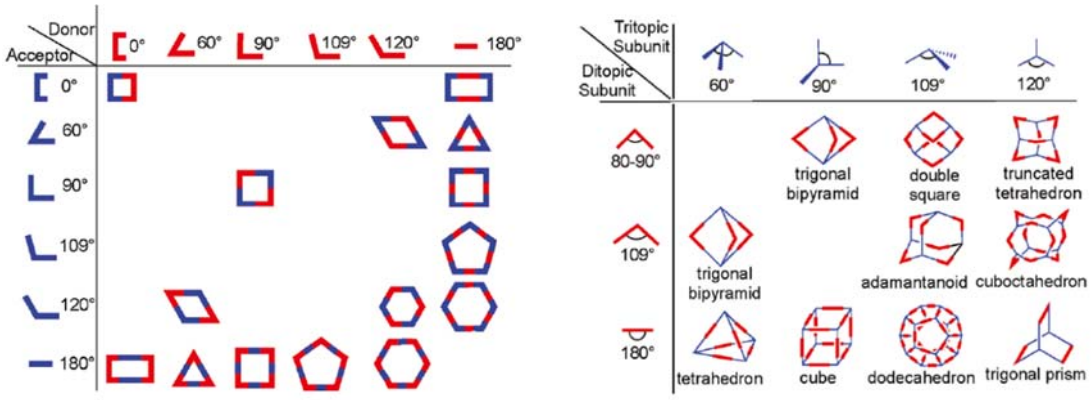

Figure 1.4 Combination of various building units for accessing convex polygons and canonical polyhedra (Left); three-dimensional architectures formed by the combination of ditopic and tritopic subunits by the directional bonding approach. (Right)

In 1991, Fujita *et al.* described the first molecular square[53] via coordination-driven self-assembly of 90° cis-protected palladium [enPdX$_2$] (en = ethylenediamine, X = Cl$^-$, NO$_3^-$ etc.,) with four linear ligands (4,4′-bipyridine) as the linker (Scheme 1.1). Subsequently many other molecular squares with larger cavities have been reported utilizing the same strategy. Pt(II) Shows a behavior analogous to Pd(II) and Pt(II)-containing molecular squares could be prepared[54] and it is interesting to observe that these squares are more stable than their palladium parents.

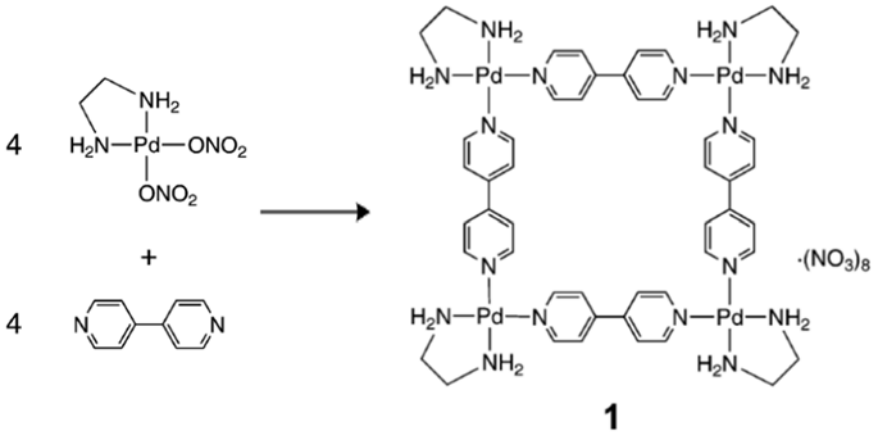

Scheme 1.1 First molecular square complexes synthesized by Fujita and coworkers.

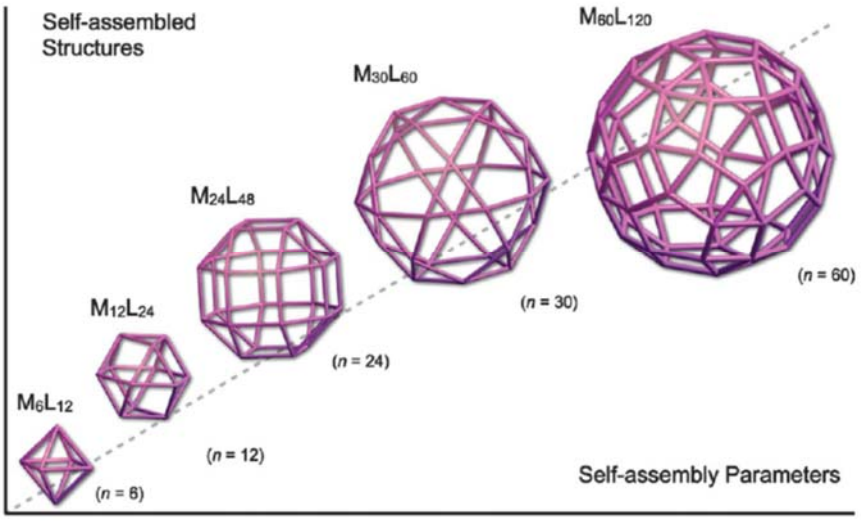

Figure 1.5 The family of roughly spherical coordination polyhedra with general formula $\mathbf{M_nL_{2n}}$, where metals (M) and bridging bis(pyridine) ligands (L) are at vertices and edges of the polyhedra, respectively.

By conveniently modifying the structure of the ligands and by choosing transition metals with different coordination geometry, an astonishingly great variety of self-assembled molecular systems were prepared (Fig. 1.5), among other squares, cages, capsules, bowls, tubes, prism and porphyrin prism.[55] In some cases the obtained cages possessed sufficiently large empty volumes in their core to uptake guests of considerable size.

In this thesis, we are describing the preparation of spherical metal coordination cages consisting of 36 components. Specifically, the obtained cages have cuboctahedron symmetry and general formula $M_{12}L_{24}$, namely they are formed on self-assembly of 12 identical metal centers (M) and 24 identical pyridine ligands (L). Self-organization of metal species and linear organic ligands is well known to form two-dimensional (2D) infinite networks wherein the ligands are spacing the nodes. In our case the formation of finite, spherical coordination networks, having a diameter of up to 7 nm, was enabled by the use of banana shaped ligand which were providing the curvature required for organizing closed systems.

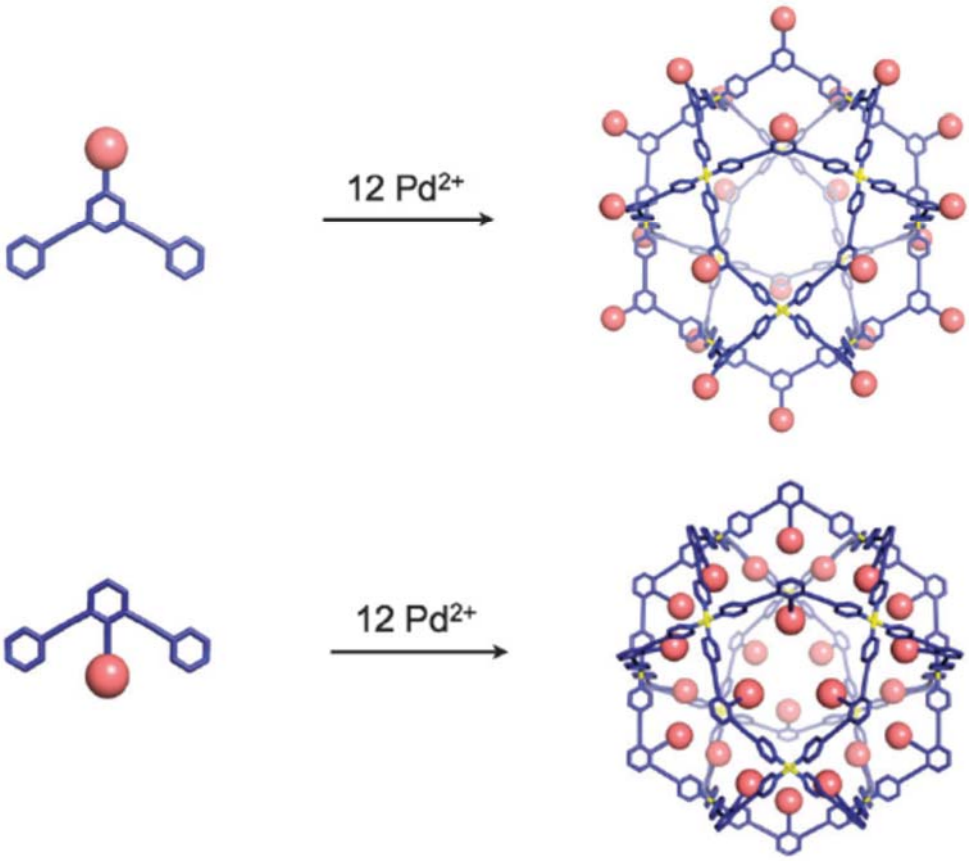

Scheme 1.2 Modification of the bis(pyridine) ligand for (a) exohedral and (b) endohedral functionalization of $M_{12}L_{24}$ spherical complexes.

In coordination cages analogous to those described here, the multi-functionalization at the inner side of the cage (endohedral functionalization[55a]) or at the outer side (exohedral

functionalization[56]) were recently obtained by using bent ligands bearing a functionalized pendant at their convex or concave side respectively (scheme 1.2). For instance, functionalization of the cage interior was made with flourous chains for fluorous- fluorous aggregation,[57] with azobenzene groups for photoisomerisation,[58] with sugars for synthesis and growth of nanoparticles,[59] and with ion gated systems for inducing coulombic interactions.[60]

1.5. Molecular self-assembly via non-covalent interactions

Noncovalent interactions include a variety of weak, reversible, and inter- or intramolecular attractive forces and they play an extremely important role in chemical and biological processes.[6-8,31] For instance, non-covalent interactions play a key role in supramolecular chemistry, self-assembly and self-organization phenomena, recognition processes and crystal engineering. The systematic study of non-covalent interaction is a forefront issue in numerous scientific research fields. While investigations on the covalent bonds, which are typically stronger than noncovalent interactions, have made available a fairly extensive set of information and reasonably detailed models are available for covalent bonds. The nature and characteristics of non-covalent interactions is still an open and debated issue. Whilst energies of non-covalent bonds (generally 0.5 – 5 kcal/mol in solution and up to 40 kcal/mol in the gas phase) are individually smaller than those of covalent bonds (80 or 100 kcal/mol for a typical C– C or C–H bond, respectively), supramolecular complexes are frequently formed thanks to the cooperative effect of many non-covalent bonds so that they are collectively enabling a fair or even high stability in these complexes. The most frequently occurring non-covalent interactions include ion-ion and ion-dipole attractions, HB, van der Waals force, and hydrophobic interaction.[37-39,42,44] Cation-π, anion-π and aurophilic interaction belongs to the group of non-covalent bondings which also received consistent attention and XB undoubtedly belong to this group too.[41,43,61,62] Recently, chalcogen bond[63] and tetrel bond[64] have also been given some interest and entered the toolbox of interactions available to the supramolecular chemist to control recognition and self-assembly processes. In this thesis HB and XB have been used to drive the self-assembly of multicomponent cocrystals and some general aspects of these interactions will be briefly discussed in the following paragraphs. A relatively longer presentation will be given for XB as it is assumed the interaction is less known to the common reader than HB.

1.5.1. Hydrogen bonding

HB is by far the most frequently occurring, studied, and exploited non-covalent interactions. According to the recent recommendation proposed by IUPAC, a HB occurs when there is evidence of bond formation between a hydrogen atom from a molecule or a molecular fragment X–H in which X is more electronegative than H, and an atom or a group of atoms in the same or a different molecule.[37,65] A typical HB may be depicted as X–H···Y–Z, where the three dots denote the bond and X–H represents the hydrogen bond donor. The acceptor may be an atom or an anion Y, or a fragment or a molecule Y–Z, where Y is bonded to Z. In some cases, X and Y are the same and X–H and H···Y distances are the same thus leading to symmetric HBs. In any event, the acceptor is an electron rich region but not limited to a lone pair of Y or π-bonded pair of Y–Z.

The HB can give rise to different patterns which can be classified on the basis of their geometric aspects (Scheme 1.3). In the simplest HB, the donor interacts with one single acceptor (Scheme 1.3, top left). But HB is a long range interaction and this makes possible that a given donor simultaneously interact with two and three acceptor hydrogen atoms (Scheme 1.3, top mid and right, respectively). Hydrogen bonds with more than three acceptors are possible in principle, but are rarely found in practice as they require very high spatial densities of acceptors. The terms simple (linear or nonlinear), bifurcated and trifurcated (or, alternatively, two-centered and three-centered), bridge, cyclic and cyclic dimers are commonly used to describe the HB arrangements (Scheme 1.3, bottom).

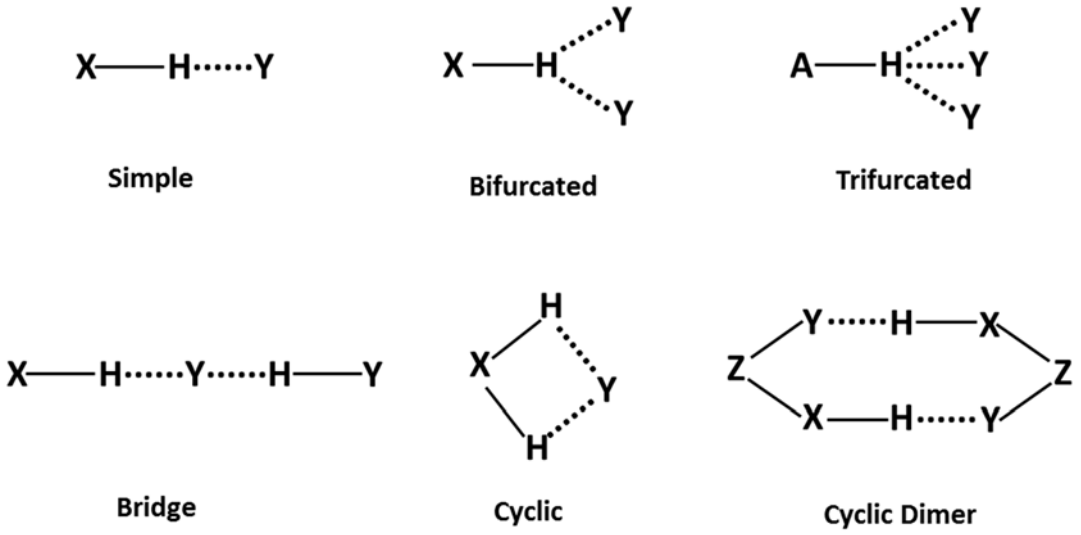

Scheme 1.3: Schematic representation of most common HB motifs.

Table 1.1 Strong, moderate, and weak hydrogen bonds following the classification of G. A. Jeffrey and G. R. Desiraju, the numerical data are guiding values only.

Hydrogen bonds, X−H•••Y−Z						
Strength	**Examples**	**X−Y (D,A)**	**H•••Y (d,A)**	**X−H•••Y (θ)**	**Energy [kcal/mol]**	**IR shift $\Delta\nu_{XH}$[Cm^{-1}]**
Very strong X−H~H•••Y	(F−H-F)	2.2−2.5	1.2−1.5	175−180	15−40	25%
Strong X−H <H•••Y	O−H•••O−H O−H•••O−H N−H•••O−H N−H•••O−H N−H•••N−H	2.6−3.0 2.6−3.0 2.8−3.0 2.7−3.1 2.8−3.1	1.6−2.2 1.7−2.3 1.8−2.3 1.9−2.3 2.0−2.5	145−180 140−180 150−180 150−180 135−180	4−15	10−25%
Weak X−H<< H•••Y	C−H•••O	3.0−4.0	2.0−3.0	110−180	< 4	< 10%

The HB strength is very dependent on the electronegative character of the acceptor and of the hydrogen atom is bound to. This strength varies typically in the range 0.2-38 kcal/mol (Table 1.1) but it can even be 40 kcal/mol, as is the case for the $F^{-}\cdots HF$ system. For practical reasons it can be useful to introduce a very qualitative classification and distinguish HBs as "weak" or "strong", and possibly also "in between" interactions. G. A. Jeffrey *et.al* described hydrogen bonds as "moderate" when associated with energies in the range 4-15 kcal/mol namely when resembling those between water molecules or in carbohydrates[66] (such interactions have also been called "normal"), HBs with energies above and below this range are termed strong and weak, respectively. Some general properties of these classes of HBs are listed in Table 1.1.

HB is an outstandingly important interaction playing a key role in physical, chemical, and biochemical processes, spanning conformational aspects of molecules in the solid, liquid and gas phases, structure and functions of organic and inorganic materials, most processes in living organisms form enzymatic catalysis to ion transport (Fig. 1.6).

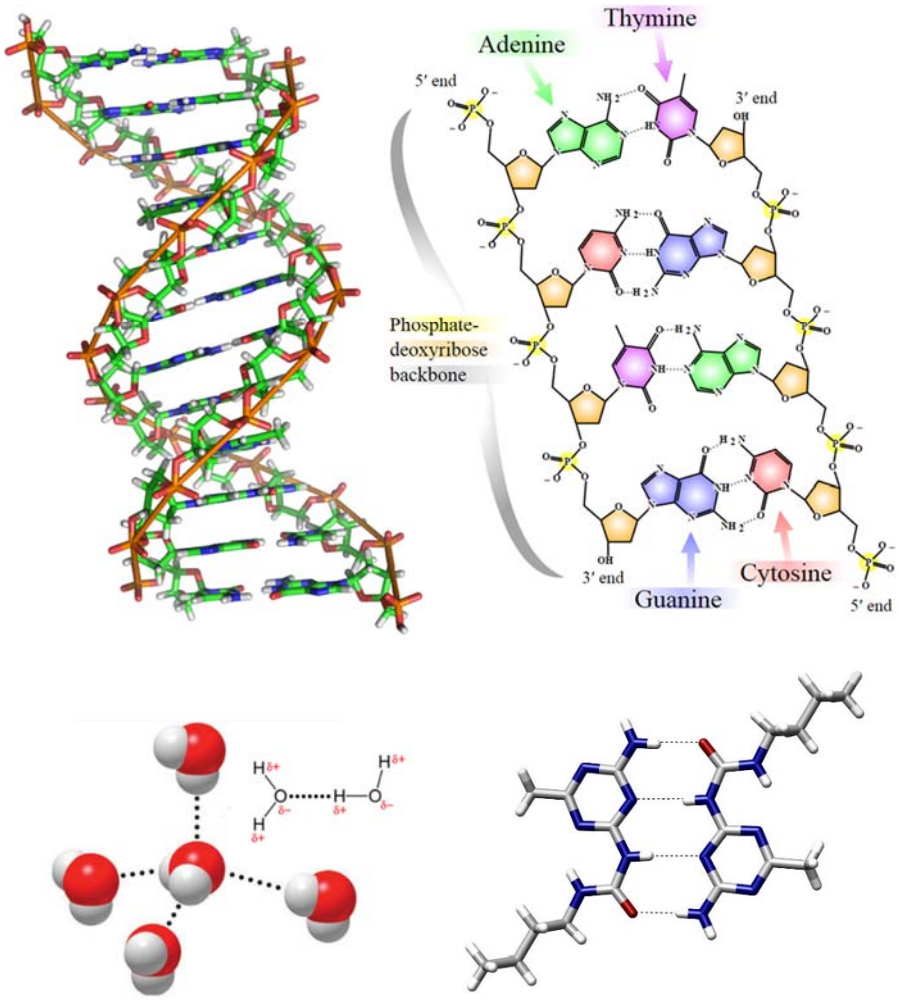

Figure 1.6 Multiple HB between two polynucleotide chains in DNA (Top); HB in water molecule (Bottom left) and a self- complementary intermolecular quadrapole HB dimer in ureido group.[67]

The typical OH···O HBs formed in water are 1.97Å long. Another example of the biochemical supramolecular structure is DNA molecule (Fig. 1.6, top view) with double helical structure composed of phosphate-deoxyribose backbone and nucleic acid bases. Under the cooperation of multiple HBs, two polynucleotide chains complement each other, and encode and transfer the genetic information in living organisms.

As a terrific case of structural study of HB and its outcomes, we can mention the organization of molecules on surfaces recently reported by N. R. Champness *et al.* [68] Later A.M. Sweetman introduced the use of dynamic force microscopy (DFM) to quantitatively map the tip-sample force field for naphthalene tetracarboxylic diimide molecules hydrogen-bonded in two-dimensional assemblies[69] (Fig. 1.7).

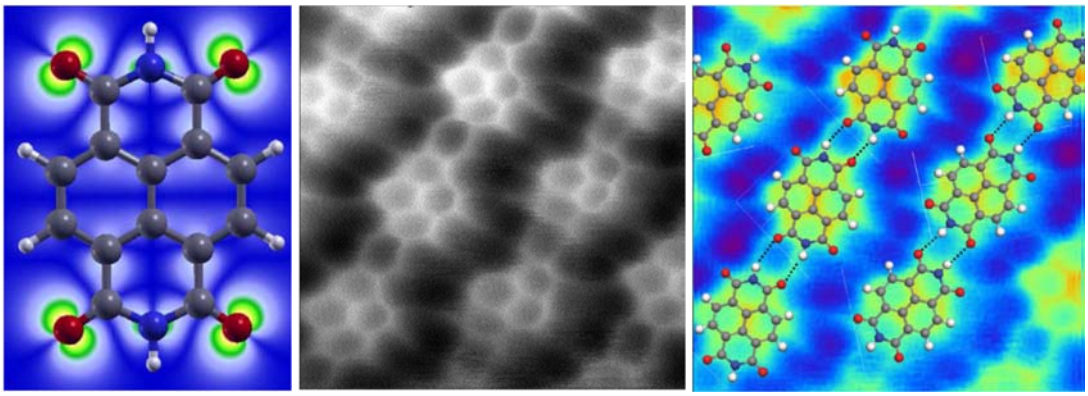

Figure 1.7 Intermolecular contrast in a 2D hydrogen-bonded assembly: Ball-and-stick model of naphthalene tetracarboxylic diimide (Left); DFM image of naphthalene diimide hydrogen-bonded on a surface (Middle) and overlay of the model of on a contrast-adjusted section of the image obtained from DFM (Right).

As a wonderful example of the sophistication in the rational design of architectures assembled *via* HB, we can discuss the supramolecular cages assembled by M. D. Ward *et al.* starting from 20 ions of three distinct species through 72 hydrogen bonds.[70] The cage is constructed from two kinds of hexagonal molecular tiles, a tris(guanidinium)nitrate cluster $(G_3NO_3]^{2+}$ and an hexa(4-sulfonatophenyl)benzene $HSPB_6^-$, joined at their edges through complementary and metrically matched N-H···O-S hydrogen bonds to form a truncated octahedron with an interior volume of 2200 cubic angstroms. This system acts as the composite building unit of a body-centered cubic zeolite-like framework able to encapsulate a wide range of charged species (Fig. 1.8).

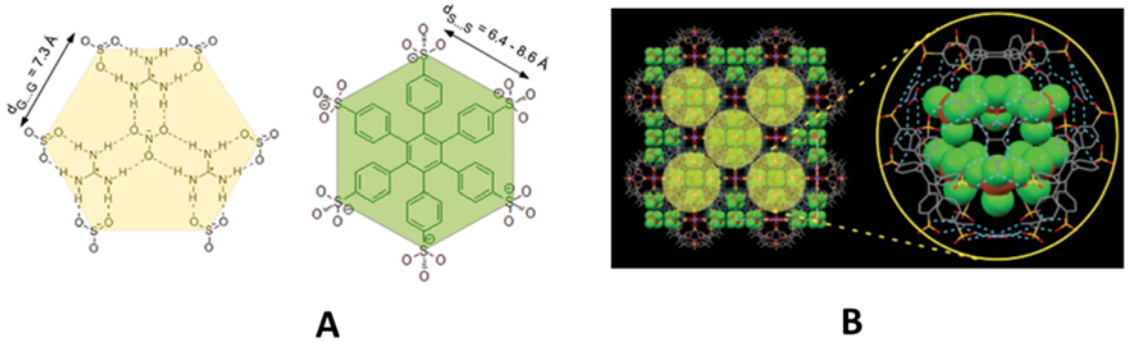

Figure 1.8 (A) Complementary $[G_3NO_3]^{2+}$ (yellow) and $HSPB_6^-$ (green) tiles assembled through HB; **(B)** encapsulation of $[FeCl_4]_1^-$ ions in a truncated octahedron system.

1.5.2. Halogen bonding

According to the recent IUPAC definition,[41b] halogen bonding (XB) *occurs when there is evidence of a net attractive interaction between an electrophilic region associated with a halogen atom in a molecular entity and a nucleophilic region in another, or the same, molecular entity.* A classic halogen bond is denoted by the three dots in R–X···Y. R–X is the XB donor, X is any halogen atom with an electrophilic region, and R is a group covalently bound to X. In some cases, X may be covalently bound to more than one group. Y is the halogen bond acceptor and is typically a molecular entity possessing at least one nucleophilic region (Fig.1. 9).

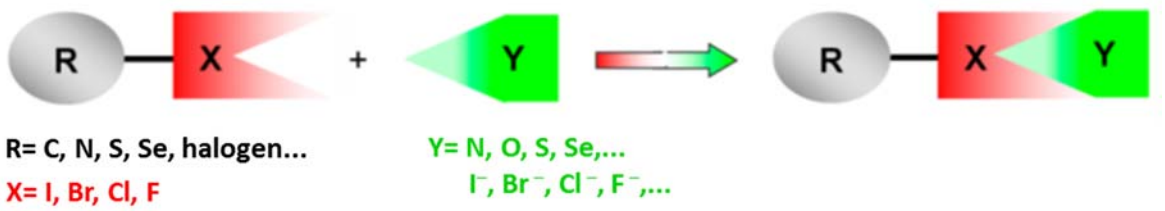

Figure 1.9 Cartoon representing XB. X is the halogen atom acting as XB donor; Y is the nucleophilic entity (XB acceptor) and can be both neutral and anionic; R is the atom/group covalently bound to the halogen.

Halogens are quite electrophilic atoms in haloorganic derivatives are commonly understood as electron rich sites so that it may seem surprising they can function as electrophilic sites. This ability more pronounced in heavy halogens, is a result of the redistribution of their electron density occurring when they form a covalent bond. In fact, in monovalent halogens the electron density, on covalent bond formation, is shifted from the region opposite to the covalent bond to the belt orthogonal to this bond. Due to this anisotropic distribution of the electron density, halogen atoms adopt an ellipsoidal shape. Electrophiles enter halogen atoms in the region (named σ-hole) of depleted electron density on the elongation of the covalent bond where the electrostatic potential is positive and nucleophiles enter in the belt orthogonal to the covalent bond where the excess of electron density results in a negative electrostatic potential (Fig. 10). Clearly, the anisotropic distribution of the electron density makes it possible for halogen atoms to behave as amphoteric sites.

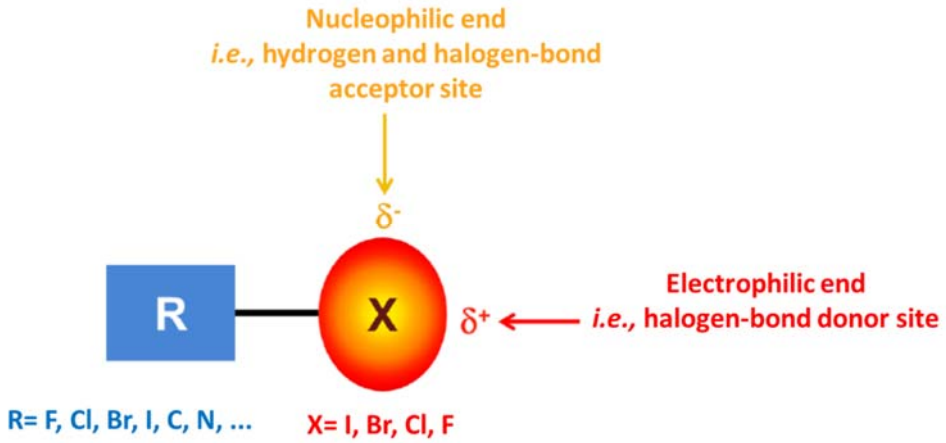

Figure 1.10 Schematic representation of the anisotropic distribution of the electron density around covalently bound halogen atoms and the pattern of the resulting interactions.

Thanks to the well localized region of positive electrostatic potential, XB is remarkably directional and the angle between the atom covalently bound to the halogen, the halogen and the entering electron rich atom usually approximates 180°.[41a, 71]

On change of the halogen atom, the strength of the XB decreases in the order of I > Br > Cl > F, in agreement with the halogen polarizability which influences the σ-hole appearance by affecting the redistribution of the electron density occurring on the halogen when covalent bond(s) are formed (Fig.1.11).

For a given halogen, the strength of the XB it can influenced by all factors that can modify its σ-hole, so stronger XBs are formed when electron withdrawing groups (e.g., fluorine atoms) are covalently bound close to the halogen.[72]

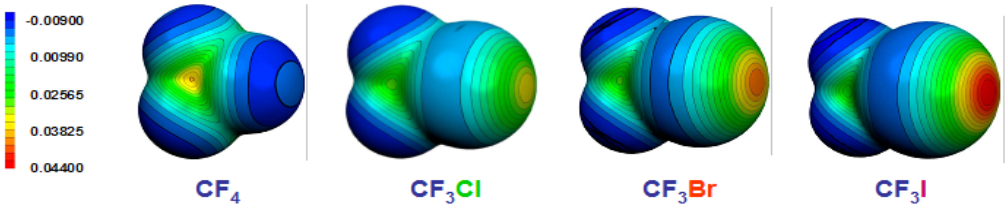

Figure 1.11 Molecular electrostatic potential, in Hartrees, at the 0.001 electrons Bohr^{-3} isodensity surface. The σ-hole gets larger and more positive moving from chlorine to iodine.

Despite the first report on the synthesis of a halogen bonded adduct dates back to 1813,[73] the term "halogen bond" has become common in the literature only in the last 15 years or so.

The complex $I_2 \cdots NH_3$, first prepared by J. J. Colin in 1813, was structurally characterized only in 1863 by F. Guthrie.[74] Landmarks in the understanding of XB have been the identification in solution of the benzene-iodine adduct reported in 1948 by H. A. Benesi and J. H. Hildebrand.[75] The description in the 1950's and 1960's of X-ray structures of dihalogen-Lewis base complexes by O. Hassel[76] investigated extensively, and in the same period, the studies of R. S. Mulliken[77] on charge transfer complexes. In the next two decades, J. M. Dumas, M. Gomel, and M. Guerin analyzed the intermolecular interactions involving haloorganics in solution and, in a review paper, they showed that the interaction features in the liquid phase parallel to those in the solid phase.[78] A. Legon's microwave studies of systems in the gas phase showed that main interaction features in adducts between dihalogens or organohalogens and oxygen or nitrogen electron donors are similar to those of analogous adducts in condensed phases.[79] P. Politzer and J. Murray, along with other researchers, revealed via extensive computational studies that the electrostatic attractions between the polarizable halogen and the electron donor plays a major role among the different forces contributing to the interaction. [80]

Data mining was also quite helpful in identifying the distinctive features of XB. An analysis of the large number of crystal structures available from the Cambridge Structural Database revealed the presence of many systems where halogens and organohalogens showed intermolecular distances shorter than the sum of the van der Waals radii of the atoms involved. These systems provided unquestionable proof of the amphoteric character of halogen atoms in dihalogens and organohalogens. Specifically, the close contacts with nucleophiles, namely electron donors such as nitrogen and oxygen atom, and with electrophiles, such as metal cations and positively charged hydrogen atoms, were both highly directional. Former interactions were preferentially on the extension of and opposite to the C–X covalent bond (C–X···nucleophile angles of 160°-180°) while latter interactions were orthogonal to the C–X bond (typically between 90° and 120°).

Thanks to the features described above, XB is a particularly attracting interaction for crystal engineers.[81] Bonding strength and directionality were particularly relevant in this respect, as they enabled to transfer the molecular information to the overall crystalline architecture, namely to reliably translate the geometry of starting tectons into the geometry of the supramolecular network. Reliable XB based synthons have been identified and successfully implemented for application spanning the preparation of receptors for anion sensing in solution,[82] of crystalline porous systems for selective inclusion,[83] co-crystals for enantiomeric mixtures resolution,[84] molecular functional and responsive materials,[85] small molecules for organo catalysis.[86] Recently, the XB driven organization of nanoparticles[87] and the XB presence

and role in protein–ligand interactions have been investigated and exploitations in drug design are being pursued.[88]

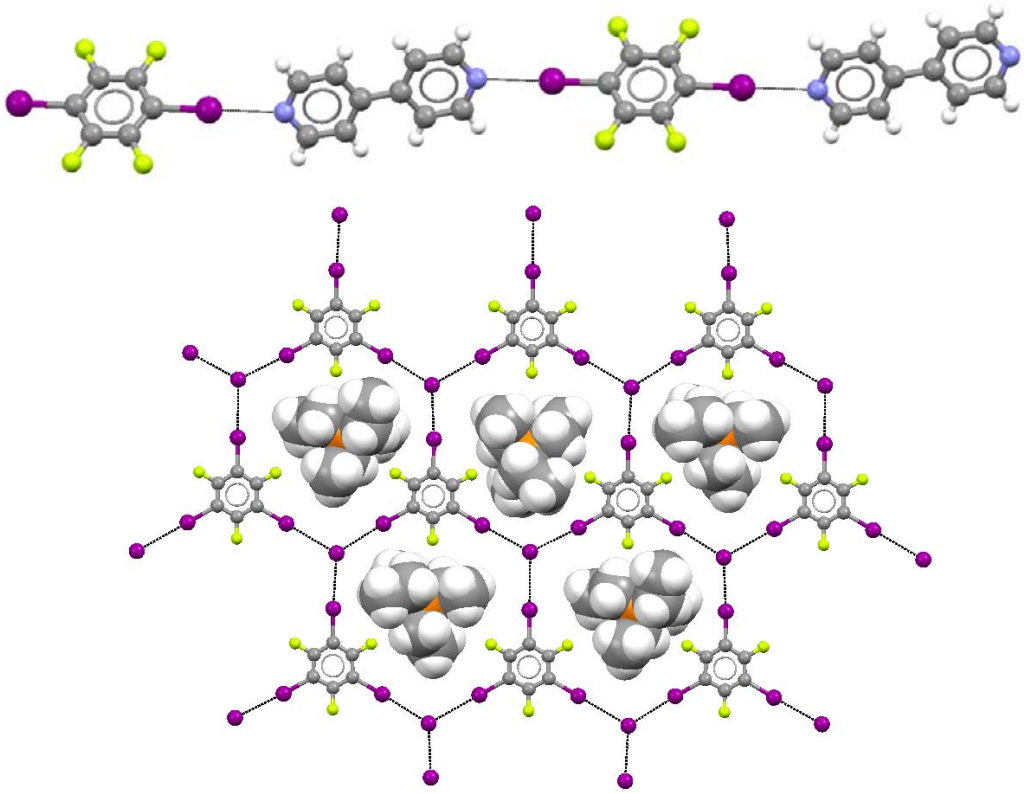

Figure 1.12 Example of 1D nets wherein 4,4'-bipyridine and 1,4-diiodotetrafluorobenzene are alternating (QIHBEO, Top); 2D network formed by tetraethylphosphonium iodide with 1,3,5-triodo-2,4,6 trifluorobenzene, iodide anions and triiodobenzene are alternating at the nodes of the net (CIZSAG, Bottom).

Being a remarkably effective tool in crystal engineering, XB allowed for the design and synthesis of many kinds of networks. Zero-, one-, two- and three-dimensional architectures have been synthesized relying on XB assisted self-assembly.[41b] A prototype example of 1D network is the linear chains between bipyridine and 1,4-diiodotetrafluorobenzene and a prototype case of 2D net is the honeycomb system formed by tetraethylphosphonium iodide with 1,3,5-triodo-2,4,6 trifluorobenzene (Fig. 1.12). Other interesting cases are described in following paragraphs.

1.6. Non-covalent interactions in porous system

Weak, intermolecular forces are difficult to observe in solution because molecular encounters are random, short-lived, and overwhelmed by collisions with the solvent while in a confined space molecules are isolated from the medium, prearranged in volumes which can work as

active sites for the encounters and time of residence of molecules in these active sites are prolonged. Moreover the restricted volume amplifies the concentrations of both donor and acceptor, while the shape of the space may favor their proper orientation for molecular interactions.

In 2009, P. Metrangolo *et al,* reported that bis(trimethylammonium)alkane diiodides, a class of dynamic organic salts well-known for their curare-like activity, can reversibly encapsulate α,ω-diiodoperfluoroalkanes (DIPFAs) through XBs between the host's I^- anions and the guest's terminal iodine atoms in a guest induced cavities[89] (Fig. 1.13). The process is highly selective for the fluorocarbon that forms an $I^-\cdots I(CF_2)_mI\cdots I^-$ superanion that is matched in length to the chosen dication. DIPFAs that are 2 to 16 carbons in length can thereby be isolated from mixtures of diiodoperfluoroalkanes by means of crystallization by using the convenient onium dication. The crystalline onium salts can also selectively capture the DIPFAs from the vapor phase in a solid-gas reaction, yielding the same product formed from solution despite a lack of porosity of the starting lattice structure. Upon heating the halogen bonded co-crystal under vacuum, DIPFAs can be evaporated off and condensed as pure compounds while the starting onium salt remains quantitatively ready for re-use. Here it is important to underline that the size matching of the interacting components is the key structural aspect for the selective binding of a given DIPFA and this approach will be successfully adopted in a different context in this thesis.

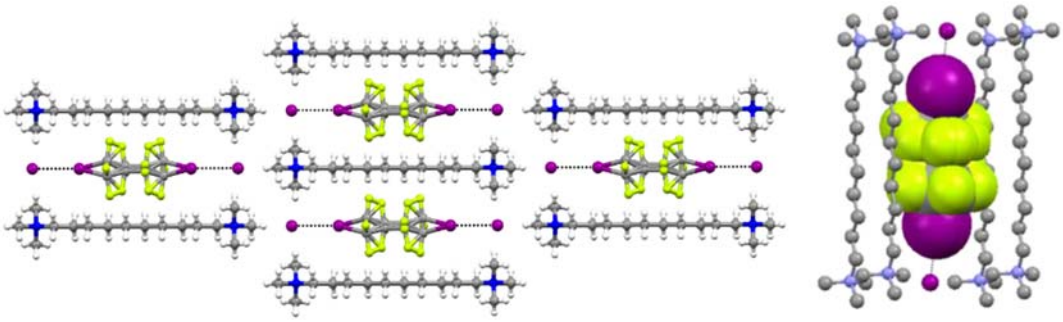

Figure 1.13 Crystal packing of the bis(trimethylammonium)decane diiodide 1,4-diiodoperfluorobutane complex viewed along the *c* axis (Left) and the same complex showing the molecular cavity defined by four alkyl dications encapsulating disordered guest molecules (Right, DIPFA in space-filling).

Taking advantage of the inducible porosity of these organic salts and applying the concept of host-guest size matching it was possible to stabilize via encapsulation some uncommon polyhalides. In 2013, G. Resnati *et al.* reported that bis(trimethylammonium)hexane diiodide traps diiodine, dibromine and dichlorine and form the rare $I_2X_2^{2-}$ tetrahalide dianion thanks to a synergistic action of HB, XB, and size matching.[90]

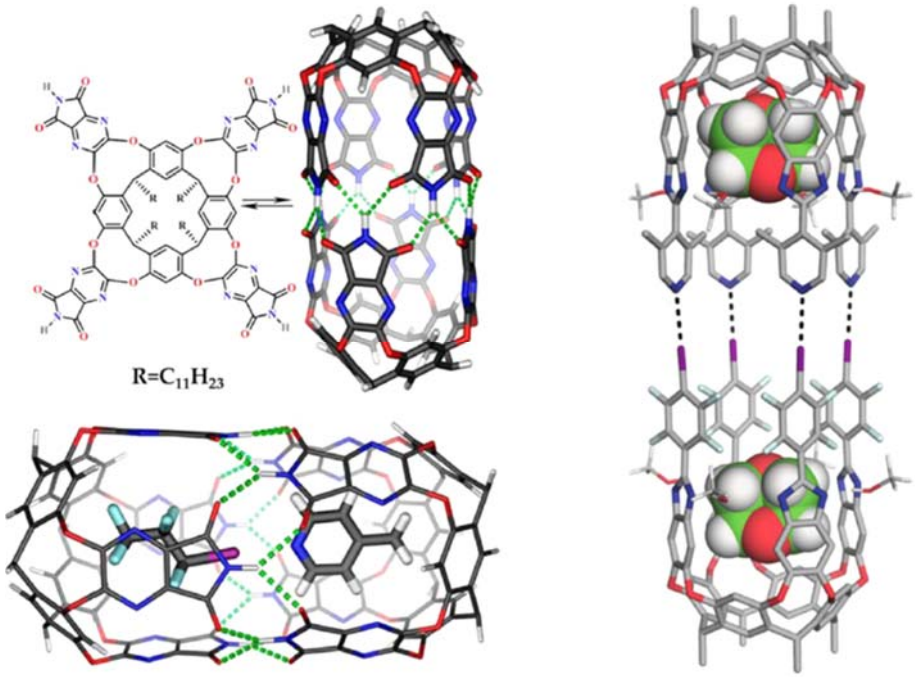

Figure 1.14 Rebek's computer-modeled dimeric capsule. (Left) and Diederich's halogen-bonded dimeric capsule encapsulated three 1,4-dioxane molecules in the cavity (Right).

The first unquestionable encapsulation of an halogen bonded adduct in confined space was reported by J. Rebek *et al.* which encapsulated an iodoperfluorocarbon-pyridine dimer in the capsule formed, thanks to the pairing of two cavitands[91] (Fig. 1.14, left). In 2015 F. Diederich and K. Rissanen drove the formation of supramolecular capsules via well-defined XBs by decorating resorcin[4]arene cavitands with polarized halogen atoms for dimerization with tetra(4-pyridyl) resorcin[4]arene cavitands.[92] Thanks to a four-point interaction successfully encapsulated 1,4-dioxane and 1,4-dithiane as a guests (Fig. 1.14, right).

M. Fujita's self-assembled cages were shown to be capable to encapsulate different molecular guests, such as DNA duplexes[93] and fluorous nanodroplets.[57] Fujita's cage was able to accommodate various XB donors, and in all cases iodine atoms were at the portals of the cage, thus allowing for the formation of XBs with either NO_3^- anions or H_2O molecules as demonstrated by using single-crystal X-ray diffraction and ^{19}F NMR techniques[94] (Fig. 1.15). Encapsulation of polyfluorinated compounds in a confined space may gain extra stability through the self-aggregation/segregation of the fluorinated guests. A similar approach based on anion coordination was employed by B. Wu and coworkers to encapsulate $CFCl_3$, a banned freon, in a tetragonal cage.[95] The freon encapsulation was further stabilized by weak Cl···π contacts as confirmed by the crystal structure analysis. High-resolution ESI-MS and NMR experiments confirms the formation of inclusion complex even in solution. The successful

approaches for polyfluorinated compounds recognition probably reveals new principles and guidelines for designing novel molecular receptors for analogous compounds.

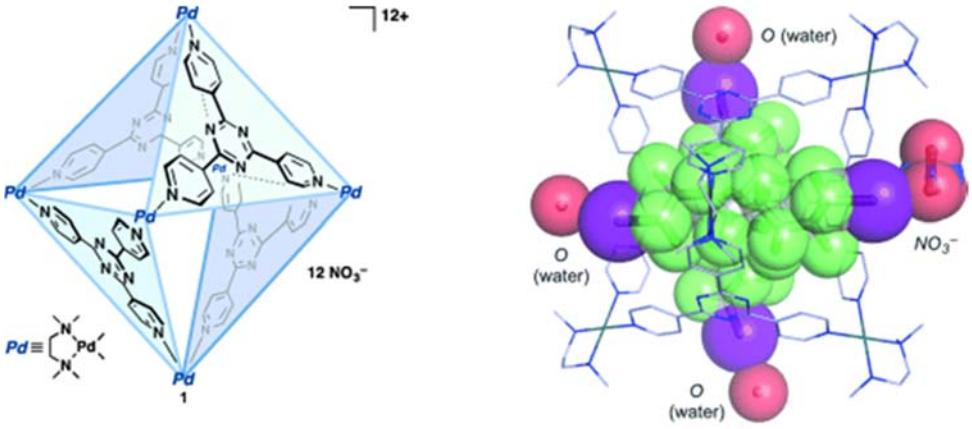

Figure 1.15 Molecular structure of Fujita's self-assembled metal coordination cage (left). Single-crystal X-ray structure of the encapsulated 1,8-diiodoperfluorooctane in Fujita's cavity. Two molecules of the XB acceptor are hosted inside the cage and pinned in their positions by XBs with nitrate anions and water molecules at the portal of the cage. Diiodoperfluorooctane molecules, NO_3^- anions, and H_2O molecules are in space-filling (Right).

Molecules confinement in a cage may enable for unique and particularly useful outcomes. As described above, it may confer unprecedented stability to caged species and allow for the preparation of poorly stable species. Importantly, as recently exemplified by J. N. H Reek *et al.*, it can also mimic the substrate binding at the active site of an enzyme and enable for reactions acceleration. Reek reported that self-assembled $M_{12}L_{24}$ nanospheres containing 24 endohedral guanidinium groups, which function as hydrogen-bond donor motifs, can strongly bind sulfonate groups and weakly bind carboxylate moieties.[96] This difference in binding strategies allows the selective inclusion of sulfonate-containing gold catalysts and, at the same time, carboxylate-functionalized substrates are pre-organized in close proximity to these catalysts by weaker hydrogen bonding in the same nanosphere. This pre-organization effect leads to enormous enhanced reaction rates in the cyclization reaction of acetylenic acids into enol lactone (Fig. 1.16).

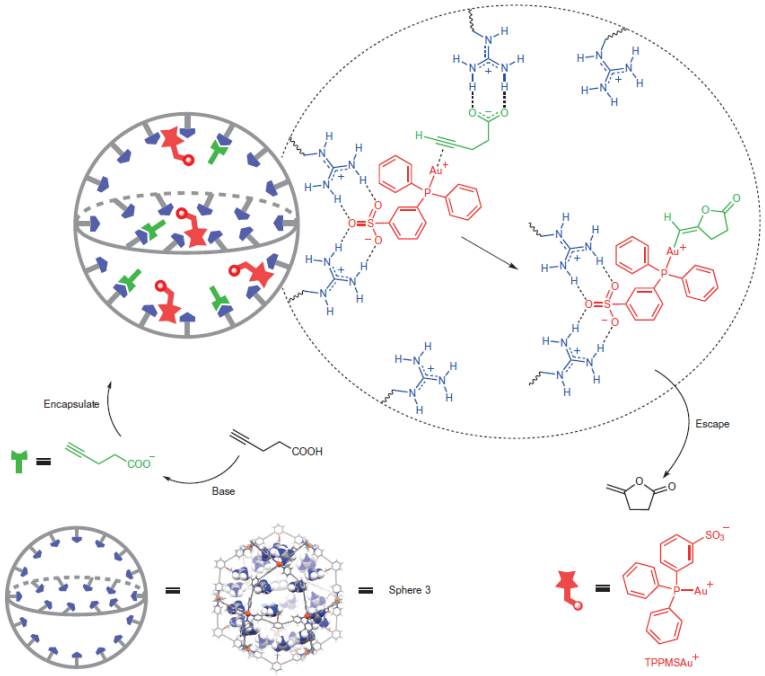

Figure 1.16 Schematic representation of the base-triggered catalytic gating process in a spherical cage. The gold (I) catalysts (drawn in red) are located in the sphere. Once the substrate (in black) is deprotonated the anionic substrate (in green) enters the sphere which pre-organize it close to the catalyst via HB to the guanidine-binding site (displayed in blue). After rapid conversion of the substrate, the neutral cyclic product leaves the sphere.

1.7. Mechanically-interlocked Molecular Architectures (MIMAs)

As molecular analogues of the keychain loop, mechanically-interlocked molecular architectures refer to those molecular systems composed of two or more components that cannot be separated from each other for mechanical reasons namely that are connected as a consequence of their topology. Mechanically interlocked molecular architectures have received considerable attention because of their topologically interesting structures and their potential application to molecular machines as well as molecular guest recognition and sensing.[97] There are a great number of these architectures, as among other, catenanes, rotaxanes, molecular knots, and molecular Borromean rings[98] (Fig. 1.17).

The synthesis of interlocked materials have defied chemists, who have overcome the early low yielding statistical and covalent approaches, by using template directed protocols relying on, for example, metal−ligand coordination,[99] hydrogen bonding,[100] argentophilic[101] and π−π stacking interactions,[102] all these approaches being used under both kinetic and thermodynamic control.

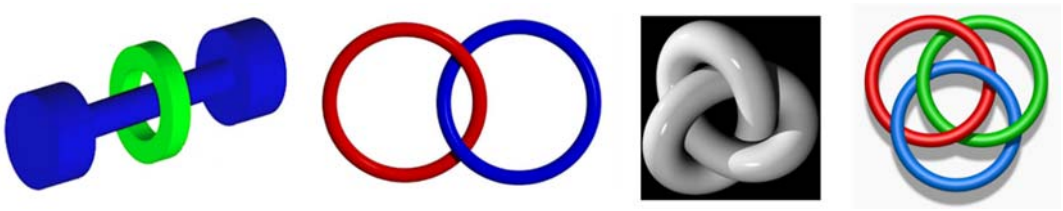

Figure 1.17 Examples of mechanically-interlocked molecular architectures: rotaxanes, catenanes, molecular knots and molecular Borromean rings (from left to right).

1.7.1. Borromean Rings:

As a historic symbol of strength in unity, Borromean rings (BRs) have raised major interest in topological chemistry not only due to their aesthetic beauty, but also due to their greater structural complexity.[103] Borromean rings consist of three rings, no two of them are interlocked, but taken together they are inseparable. The first example of Borromean rings in chemistry was reported by N. C. Seeman *et al.* in 1997 as a part of his interest in manipulation of the topological properties of DNA.[104] Some years later J. F. Stoddart *et al.* reported the first chemical synthesis of a molecular discrete Borromean ring via an all-in-one assembly strategy (Fig. 1.18).[105]

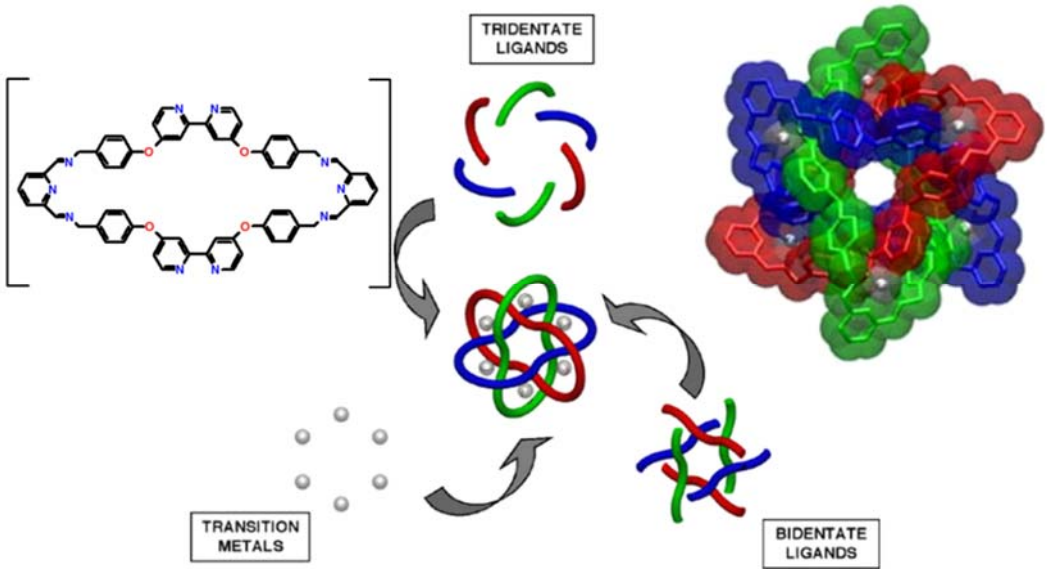

Figure 1.18 Schematic representation of Stoddart's approach to molecular Borromean ring by using a bidentate and tridentate ligand self-assembling with transition metals (all-in-one assembly strategy).

The unique entanglement of the three rings of a Borromean system preventing rings separation makes it possible to fabricate a variety of 1-D, 2-D, or 3-D networks with diversified

structural geometry but all showing Borromean interpenetration. Most examples of Borromean entanglement consist in three translationally related and infinite 2D networks which entangle in a 2D → 2D fashion. Frequently these infinite Borromean networks are based on two-dimensional (6,3) networks with undulating character and the presence of large empty frames in Borromean networks seems to be an essential requirement to have the entanglement. Coordination chemistry has been quite frequently used for the self-assembly of Borromean systems, but also HBs, argentophilic and π−π stacking interactions have been used, possibly in combination with coordination chemistry, to facilitate the formation and/or stabilization of the Borromean motif.

As described in previous sections, XB has proven to be a reliable and versatile tool for the self-assembly of a great variety of supramolecular architectures, last but not least Borromean networks. Specifically, we have already described that halide anions are very good XB acceptors and were successfully used to generate several halogen bonded networks with different topologies.[41b,106] The first purely halogen bonded supramolecular Borromean rings was described in 2006 by P. Metrangolo and G. Resnati via the self-assembly of crypt-222, potassium iodide, and α,ω-diiodoperfluoroalkanes.[107] K^+ cations are cryptated and the electron donor ability of I^- anions is boosted. These anions behave as tridentate XB acceptors and interact with three different diiodoperfluoroalkyl chains which work as bidentate and telechelic XB donors. Infinite (6,3) nets are formed where I^- anions are sitting at the vertexes of the hexagonal frames and diiodoperfluoroalkanes are forming the sides. Three such nets show Borromean entanglement supported by XB.

1.9. Reference

1. (a) C. R. Kagan and C. B. Murray, *Nat Nano.*, 2015, **10,** 1013-1026; (b) J. Liu, N. P. Wickramaratne, S. Z. Qiao and M. Jaroniec, *Nat Mater.*, 2015, **14,** 763-774; (c) M. J. Webber, E. A. Appel, E. W. Meijer and R. Langer, *Nat Mater.*, 2016, **15,** 13-26; (d) C. N. R. Rao, A. K. Sood, K. S. Subrahmanyam and A. Govindaraj, *Angew. Chem. Int. Ed.*, 2009, **48,** 7752-7777.
2. (a) Y. Li, *Acc. Chem. Res.*, 2012, **45,** 723-733; (b) M. Khazaei, M. Arai, T. sasaki, C. Y. Chung, N. S. venkataramanan, M. estili, Y. Sakka and Y. Kawazoe, *Adv. Funct. Mater.*, 2013, **23,** 2185-2192.
3. (a) Z. Nie and E. Kumacheva, *Nat Mater.*, 2008, **7,** 277-290; (b) L. Bartels, *Nat Chem.*, 2010, **2,** 87-95.

4. (a) X. Qian, X. H. Peng, D. O. Ansari, Q. Y. Goen, G. Z. Chen, D. M. Shin, L. Yang, A. N. Young, M. D. Wang and S. Nie, *Nat Biotech.*, 2008, **26,** 83-90; (b) K. Baek, I. Hwang, I. Roy, D. Shetty and K. Kim, *Accounts of Chemical Research,* 2015, **48,** 2221-2229.
5. J. D. Van Der Waals, *J Stat Phys.*, 1979, **20,** 200-244.
6. D. Strmcnik, K. Kodama, D. Van Der Vliet, J. Greeley, V. R. Stamenkovic and N. M. Marković, *Nat Chem.*, 2009, **1,** 466-472.
7. X. Li, Y. Gao, C. E. Boott, M. A. Winnik and I. Manners, *Nat Commun.*, 2015, **6,** 1-8.
8. D. N. Reinhoudt and M. Crego-Calama, *Science,* 2002, **295,** 2403-2407.
9. (a) T. Gunnlaugsson, *Nat Chem.*, 2016, **8,** 6-7; (b) J. M. Lehn, *Science,* 2002, **295,** 2400-2403.
10. M. Sarikaya, C. Tamerler, A. K. Y. Jen, K. Schulten and F. Baneyx, *Nat Mater.*, 2003, **2,** 577-585.
11. (a) G. M. Whitesides and M. Boncheva, *Proceedings of the National Academy of Sciences*, 2002, **99,** 4769-4774; (b) Y. Kim, B. Yeom, O. Arteaga, S. J. Yoo, S. G. Lee, J. G. Kim and N. A. Kotov, *Nat Mater.*, 2016, **15,** 461-468.
12. A. Werner, *Zeitchr.Anorg.Chem.*, 1893, **3,** 267-330.
13. E. Fisher, *Ber.Deutsch.Chem.Ges.*,1894, **27,** 2985-2993.
14. K.L. Wolf, H. Frahm and H.Harms, *Z.Phys.chem.*,1937, **36,** 237-242.
15. (a) J. M. Lehn, *Pure Appl.Chem.*, 1979, **51,** 979-997; (b) J. M. Lehn, *Science,* 1993, **260,** 1762-1763.
16. (a) D. C. Zhongab and T. B. Lu, *Chem. Commun.*, 2016, **52,** 10322-10337; (b) H. J. Schneider and A. K. Yatsimirsky, *Chem. Soc. Rev.*, 2008, **37,** 263-277.
17. G. Crini, *Chem. Rev.*, 2014, **114,** 10940-10975.
18. (a) J. W. Lee, S. Samal, N. Selvapalam, H. J. Kim and K. Kim, *Acc. Chem. Res.*, 2003, **36,** 621-630; (b) J. Lagona, P. Mukhopadhyay, S. Chakrabarti and L. Isaacs, *Angew. Chem. Int. Ed.*, 2005, **44,** 4844-4870; (c) L. Isaacs, *Acc. Chem. Res.*, 2014, **47,** 2052-2062.
19. (a) A. Ninagawa and H. Matsuda, *Makromol. Chem.*, *Rapid Commun.*, 1982, **3,** 65-67; (b) Y. Nakamoto and S. I. Ishida, *Makromol. Chem.*, *Rapid Commun.*, 1982, **3,** 705-707; (c) D. R. Stewart and C. D. Gutsche, *J. Am. Chem. Soc.*, 1999, **121,** 4136-4146.
20. (a) A. I. Cooper, *Angew. Chem. Int. Ed.*, 2012, **51,** 7892-7894; (b) S. Yang, A. J. Ramirez-Cuesta, R. Newby, V. G. Sakai, P. Manuel, S. K. Callear, S. I. Campbell, C. C. Tang and M. Schröder, *Nature Chemistry*, 2015, **7,** 121-129.

21. (a) C. J. Pedersen, *J. Am. Chem. Soc.*, 1967, **89,** 7017-7036; (b) R. M. Izatt and J. J. Christensen, Synthetuc Multidentate Macrocyclic Compounds, Academic Press, New York, 1978.
22. S. Shinkai, T. Minami, Y. Kusano and O. Manabe, *J. Am. Chem. Soc.*, 1983, **105,** 1851-1856.
23. (a) F. M. Raymo and J. F. Stoddart, *Chem. Rev.*, 1999, **99,** 1643-1664; (b) J. D. Badjic´, V. Balzani, A. Credi, S. Silvi and J. F. Stoddart, *Science*, 2004, **303,** 1845-1849.
24. B. Dietrich, J. M. Lehn and J. P. Sauvage, *Tetrahedron Lett.*, 1969, **10,** 2885-2888.
25. (a) C. J. Suckling, *Cell. Mol. Life Sci.*, 1991, **47,** 1093-1095; (b) W. E. Stites, *Chem. Rev.*, 1997, **97,** 1233-1250.
26. A. M. Brouwer, C. Frochot, F. G. Gatti, D. A. Leigh, L. Mottier, F. Paolucci, S. Roffia and G. W. H. Wurpel, *Science*, 2001, **291,** 2124-2128.
27. (a) A. P. Umali, S. E. LeBouef, R. W. Newberry, S. Kim, L. Tran, W. A. Rome, T. Tian, D. Taing, J. Hong, M. Kwan, H. Heymann and E. V. Anslyn, *Chem. Sci.*, 2011, **2,** 439-445; (b) A. T. Wright, E. A. Anslyn, *Chem. Soc. Rev.*, 2006, **35,** 14-28.
28. (a) B. A. Moyer, L. H. Delmau, C. J. Fowler, A. Ruas, D. A. Bostick, J. L. Sessler, E. Katayev, G. D. Pantos, J. M. Llinares, A. Hossain, S. O. Kang and K. Bowman-James, *Adv. Inorg. Chem.*, 2006, **59,** 175-204; (b) A. Rajbanshi, B. A. Moyer, R. Custelcean, *Cryst. Growth Des.*, 2011, **11,** 2702-2706.
29. A. Rocco, S. Fanali, J. Sep. Sci. 2009, **32**, 1696-1703.
30. B. Preinerstorfer, M. Lammerhofer and W. Lindner, *J. Sep. Sci.*, 2009, **32,** 1673-1685.
31. K. Uzarevic, I. Halasz, I. ilovic, N. Bregovic, M. Rubcic, D. M. Calogovic, and V. Tomisic, *Angew. Chem. Int. Ed.*, 2013, **52,** 5504-5508.
32. (a) P. D. Beer and P. A. Gale, *Angew. Chem.*, 2001, **113,** 502-532; *Angew. Chem. Int. Ed.*, 2001, **40,** 486-516; (b) F. P. Schmidtchen, *Chem. Soc. Rev.*, 2010, **39,** 3916-3935.
33. (a) M. Gsnger, J. H. Oh, M. Knemann, H. W. Hffken, A. M. Krause, Z. Bao and F. Wurthner, *Angew. Chem. Int. Ed.*, 2010, **49,** 740-743; (b) M. D. Allendorf and V. Stavila, *CrystEngComm.*, 2015, **17,** 229-246.
34. S. J. James, A. Perrin, C. D. Jones, D. S. Yufit and J. W. Steed, *Chem. Commun.*, 2014, **50,** 12851-12854.
35. J. F. Xu, Y. Z. Chen, D. Wu, L. Z. Wu, C. H. Tung and Q. Z. Yang, *Angew. Chem. Int. Ed.*, 2013, **52,** 9738-9742.
36. B. H. Northrop, H. B. Yang and P. J. Stang, *Chem. Commun.*, 2008, 5896-5908.

37. (a) T. Steiner, *Angew. Chem. Int. Ed.*, 2002, **41,** 48-76; (b) P. Tanphibal, K. Tashiro and S. Chirachanchai, *Soft Matter*, 2016, **12,** 486-491.
38. S. K. Burley and G. A. Petsko, *Science*, 1985, **229,** 23-28.
39. (a) W. Li, I. Kanyo, C.H. Kuo, S. Thanneeru and J. He, *Nanoscale*, 2015, **7,** 956-964; (b) C. D. Ma, C. Wang, C. A. Velez, S. H. Gellman and N. L. Abbott, *Nature*, 2015, **517,** 347-350.
40. S. Li, V. R. Cooper, T. Thonhauser, B. I. Lundqvist and D. C. Langreth, *J. Phys. Chem. B*, 2009, **113,** 11166-11172.
41. (a) G. Cavallo, P. Metrangolo, R. Milani, T. Pilati, A. Priimagi, G. Resnati and G. Terraneo, *Chem. Rev.*, 2016, **116,** 2478-2601; (b) G. R. Desiraju, P. S. Ho, L. Kloo, A. C. Legon, R. Marquardt, P. Metrangolo, P. Politzer, G. Resnati and K. Rissanen, *Pure Appl. Chem.*, 2013, **85,** 1711-1713.
42. A. S. Umar, V. E. Oberacker, J. A. Maruhn and P.G. Reinhard, *Physical Review C*, 2012, **85**, 1-4.
43. A. S. Mahadevi and G. N. Sastry, *Chem. Rev.*, 2013, **113,** 2100-2138.
44. Z. Wu, J. Liu, Y. Li, Z. Cheng, T. Li, H. Zhang, Z. Lu and B. Yang, *ACS Nano.*, 2015, **9,** 6315-6323.
45. J. M. Lehn, VCH: Weinheim, Germany, 1995.
46. J. P. Sauvage and C. D. Buchecker, Eds. Wiley-VCH: Weinheim, Germany, 1999.
47. (a) J. E. Beves and D. A. Leigh, *Nat. Chem.*, 2010, **2,** 708-710; (b) L. Fang, M. A. Olson, D. Benítez, E. Tkatchouk, W. A. Goddard III and J. F. Stoddart, *Chem. Soc. Rev.*, 2010, **39,** 17-29; (c) S. Durot, F. Reviriego and J. P. Sauvage, *Dalton Trans.*, 2010, **39,** 10557-10570; (d) J. A. Faiz, V. Heitz and J. P. Sauvage, *Chem. Soc. Rev.*, 2009, **38,** 422-442; (e) J. D. Crowley, S. M. Goldup, A. L. Lee, D. A. Leigh and R. T. McBurney, *Chem. Soc. Rev.*, 2009, **38,** 1530-1541; (f) V. Balzani, A. Credi and M. Venturi, *Chem. Soc. Rev.*, 2009, **38,** 1542-1550; (g) J. F. Stoddart, *Chem. Soc. Rev.*, 2009, **38,** 1802-1820; (h) B. Champin, P. Mobian and J. P. Sauvage, *Chem. Soc. Rev.*, 2007, **36,** 358-366; (i) J. P. Sauvage, *Chem.Commun.*, 2005, 1507-1510; (j) S. Bonnet, J. P. Collin, M. Koizumi, P. Mobian and J. P. Sauvage, *Adv. Mater.*, 2006, **18,** 1239-1250; (k) C. D. Buchecker, B. X. Colasson and J. P. Sauvage, *Top. Curr. Chem.*, 2005, **249,** 261-283; (l) M. Ruben, J. Rojo, F. J. Romero-Salguero, L. H. Uppadine and J. M. Lehn, *Angew. Chem. Int. Ed*., 2004, **43,** 3644-3462.
48. (a) P. J. Stang, *J. Org. Chem.*, 2009, **74,** 2-20; (b) R. Chakrabarty, P. S. Mukherjee and P. J. Stang, *Chem. Rev.*, 2011, **111,** 6810-6918.

49. (a) M. Fujita, M. Tominaga, A. Hori and B. Therrien, *Acc. Chem. Res.*, 2005, **38,** 369-378; (b) M. Fujita, K. Umemoto, M. Yoshizawa, N. Fujita, T. Kusukawa and K. Biradha, *Chem. Commun.*, 2001, 509-518.
50. (a) D. L. Caulder and K. N. Raymond, *Acc. Chem. Res.*, 1999, **32,** 975-982; (b) D. L. Caulder, C. Bruckner, R. E. Powers, S. Konig, T.N. Parac, J. A. Leary and K.N. Raymond, *J. Am. Chem. Soc.*, 2001, **123,** 8923-8938.
51. (a) C. G. Oliveri, P. A. Ulmann, M. J. Wiester and C. A. Mirkin, *Acc. Chem. Res.*, 2008, **41,** 1618-1629; (b) N. C. Gianneschi, M. S. Masar III and C. A. Mirkin, *Acc. Chem. Res.*, 2005, **38,** 825-837.
52. (a) F. A. Cotton, C. Lin and C. A. Murillo, *Proc. Natl. Acad. Sci.*, 2002, **99,** 4810-4813; (b) F. A. Cotton, C. Lin and C. A. Murillo, *Acc. Chem. Res.*, 2001, **34,** 759-771.
53. M. Fujita, J. Yazaki and K. J. Ogura, *J. Am. Chem. Soc.*, 1990,**112,** 5645-5647.
54. D. Fujita, A. Takahashi, S. Sato and M. Fujita, *J. Am. Chem. Soc.*, 2011, **133,** 13317-13319.
55. (a) M. Tominaga, K. Suzuki, T. Murase, and M. Fujita, *J. Am. Chem. Soc.*, 2005, **127,** 11950-1195; (b) N. Takeda, K. Umemoto, K.Yamaguchi and M. Fujita, *Nature*, 1999, **398,** 794-796; (c) S. Y. Yu, T. Kusukawa, K. Biradha, and M. Fujita, *J. Am. Chem. Soc.*, 2000, **122,** 2665-2666; (d) T. Yamaguchi, S. Tashiro, M. Tominaga, M. Kawano, T. Ozeki and M. Fujita, *J. Am. Chem. Soc.*, 2004, **126,** 10818-10819; (e) K. Kumazawa, K. Biradha, T. Kusukawa, T. Okano and M. Fujita, *Angew. Chem. Int. Ed.*, 2003, **42,** 3909-3913; (f) N. Fujita, K. Biradha, M. Fujita, S. Sakamoto and K. Yamaguchi, *Angew. Chem. Int. Ed.*, 2001, **40,** 1718-1721.
56. M. Tominaga, K. Suzuki, M. Kawano, T. Kusukawa, T. Ozeki, S. Sakamoto, K. Yamaguchi and M. Fujita, *Angew. Chem. Int. Ed.*, 2004, **43,** 5621-5625.
57. S. Sato, J. Iida, K. Suzuki, M. Kawano, T. Ozeki and M. Fujita, *Science*, 2006, **313,** 1273-1276.
58. T. Murase, S. Sato and M. Fujita, *Angew. Chem. Int. Ed.*, 2007, **46,** 5133-5136.
59. T. Ichijo, S. Sato and M. Fujita, *J. Am. Chem. Soc.*, 2013, **135,** 6786-6789.
60. C. J. Bruns, D. Fujita, M. Hoshino, S. Sato, J. F. Stoddart and M. Fujita, *J. Am. Chem. Soc.*, 2014, **136,** 12027-12034.
61. A. Robertazzi, F. Krull, E. W. Knapp and P. Gamez, *CrystEngComm.*, 2011, **13,** 3293-3300.
62. H. Schmidbaur and A. Schier, *Chem. Soc. Rev.*, 2012, **41,** 370-412.

63. M. E. Brezgunova, J. Lieffrig, E. Aubert, S. Dahaoui, P. Fertey, S. Lebègue, J. G. Ángyán, M. Fourmigué and E. Espinosa, *Cryst. Growth Des.*, 2013, **13,** 3283-3289.
64. A. Bauz, T. J. Mooibroek and A. Frontera, *Angew. Chem.*, 2013, **125,** 12543-12547.
65. E. Arunan, G. R. Desiraju, R. A. Klein, J. Sadlej, S. Scheiner, I. Alkorta, D. C. Clary, R. H. Crabtree, J. J. Dannenberg, P. Hobza, H. G. Kjaergaard, A. C. Legon, B. Mennucci and D. J. Nesbitt, *Pure Appl. Chem.*, 2011, **83**, 1637-1641.
66. G. A. Jeffrey, Oxford University Press, Oxford, 1997.
67. F. H. Beijer, H. Kooijman, A. L. Spek, R. P. Sijbesma and E. W. Meijer, *Angew. Chem. Int. Ed.*, 1998, **37,** 75-78.
68. A. G. Slater, L. M. A. Perdigão, P. H. Beton and N. R. Champness, *Acc. Chem. Res.*, 2014, **47,** 3417-3427.
69. A.M. Sweetman, S. P. Jarvis, H. Sang, I. Lekkas, P. Rahe, Y. Wang, J. Wang, N.R. Champness, L. Kantorovich and P. Moriarty, *Nat. Commun.,* 2014, **5**, 1-7.
70. Y. Liu, C. Hu, A. Comotti and M. D. Ward, *Science*, 2011, **333,** 436-440.
71. P. Metrangolo, H. Neukirch, T. Pilati and G. Resnati, *Acc. Chem. Res.*, 2005, **38,** 386-395.
72. G. Valerio, G. Raos, S. V. Meille, P. Metrangolo and G. Resnati, *J. Phys. Chem. A.*, 2000, **104,** 1617-1620.
73. J. J. Colin, *Sur l'iode. Ann. Chim.,* 1814, **91**:252-272.
74. F. J. Guthrie, *Chem. Soc.*, 1863, **16**, 239-244.
75. H. A. Benesi and J. H. Hildebrand, *J. Am. Chem. Soc.*, 1949, **71**, 2703-2707.
76. O. Hassel, *Science*, 1970, **170**, 497-502.
77. R. S. Mulliken and W. B. Person, Wiley-Interscience, New York, 1969
78. J. M. Dumas, H. Peurichard and M. Gome, *J. Chem. Res.*, 1978, **2,** 54-57.
79. A. C. Legon, *Chem. Eur. J.*, 1998, **4,** 1890-1897.
80. (a) T. Brinck, J. S. Murray and P. Politzer, *Int. J. Quantum Chem.*, 1992, **44,** 57-64; (b) J. S. Murray, K. Paulsen and P. Politzer, *Indian Acad. Sci.*, 1994, **106,** 267-275.
81. C. B. Aakeröy, N. R. Champness and C. Janiak, *CrystEngComm.*, 2010, **12,** 22-43.
82. G. Cavallo, P. Metrangolo, T. Pilati, G. Resnati, M. Sansotera and G. Terraneo, *Chem. Soc. Rev.*, 2010, **39,** 3772-3783.
83. K. H. Chung, J. Park, K. Y. Kim, J. K. Yoon, H. Kim, S. Han and S. J. Kahng, *Chem. Commun.*, 2011, **47,** 11492-11494.
84. A. Farina, S. V. Meille, M. T. Messina, P. Metrangolo, G. Resnati and G. Vecchio, *Angew. Chem. Int. Ed.*, 1999, **38,** 2433-2436.

85. A. Priimagi, G. Cavallo, P. Metrangolo and G. Resnati, Accounts of chemical research, 2013, **46,** 2686-2695.
86. F. Kniep, S. H. Jungbauer, Q. Zhang, S. M. Walter, S. Schindler, I. Schnapperelle, E. Herdtweck and S. M. Huber, *Angew. Chem. Int. Ed.*, 2013, **52,** 7028-7032.
87. T. Shirman, T. Arad and M. E. Van Der Boom, *Angew. Chem. Int. Ed.*, 2010, **49,** 926-929.
88. E. Parisini, P. Metrangolo, T. Pilati, G. Resnati and G. Terraneo, *Chem. Soc. Rev.*, 2011, **40,** 2267-2278.
89. P. Metrangolo, Y. Carcenac, M. Lahtinen, T. Pilati, K. Rissanen, A. Vij and G. Resnati, *Science*, 2009, **323,** 1461-1464.
90. J. M. Rujas, L. Meazza, G. K. Lim, G. Terraneo, T. Pilati, K. D. M. Harris, P. Metrangolo and G. Resnati, *Angew. Chem. Int. Ed.*, 2013, **52,** 13444-13448.
91. M. G. Sarwar, D. Ajami, G. Theodorakopoulos, I. D. Petsalakis and J. Rebek, *J. Am. Chem. Soc.*, 2013, **135,** 13672-13675.
92. (a) O. Dumele, N. Trapp and F. Diederich, *Angew. Chem. Int. Ed.*, 2015, **54,** 12339-12344; (b) N. K. Beyeh, F. Pan and K. Rissanen, *Angew. Chem.*, 2015, **127,** 7411-7415.
93. T. Sawada and M. Fujita, *J. Am. Chem. Soc.*, 2010, **132,** 7194-7201.
94. H. Takezawa, T. Murase, G. Resnati, P. Metrangolo and M. Fujita, *Angew. Chem. Int. Ed.*, 2015, **54,** 8411-8414.
95. D. Yang, J. Zhao, Y. Zhao, Y. Lei, L. Cao, X. J. Yang, M. Davi, N. D. S. Amadeu, C. Janiak, Z. Zhang, Y. Y. Wang and B. Wu, *Angew. Chem. Int. Ed.*, 2015, **54,** 8658-8661.
96. Q. Q. Wang, S. Gonell, S. H. A. M. Leenders, M. Dürr, I. I-Burmazović and J. N. H. Reek, *Nature chemistry*, 2016, **8**, 225-230.
97. (a) A. R. Pease , J. O. Jeppesen , J. F. Stoddart, Y. Luo , C. P. Collier and J. R. Heath, *Acc. Chem. Res.*, 2001, **34**, 433-444; (b) W. R. Browne, B. L. Feringa, nature nanotechnology, 2006, **1,** 25-35.
98. J. P. Sauvage, and C. D. Buchecker, eds., John Wiley & Sons, 2008.
99. K. S. Chichak, S. J. Cantrill, A. R. Pease, S. H. Chiu, G. W. V. Cave, J. L. Atwood and J. F. Stoddart, *Science*, 2004, **304,** 1308-1312.
100. Y. B. Men, J. Sun, Z. T. Huang and Q. Y. Zheng, *Angew. Chem. Int. Ed.*, 2009, **48,** 2873-2876.
101. L. Dobrzanska, H. G. Raubenheimer and L. J. Barbour, *Chem. Commun.*, 2005, 5050-5052.
102. M. P. Suh, H. J. Choi, S. M. So and B. M. Kim, *Inorg. Chem.*, 2003, **42,** 676-678.

103. S. J. Cantrill, K. S. Chichak, A. J. Peters and J. F. Stoddart, *Acc. Chem. Res.*, 2005, **38,** 1-9.

104. C. D. Mao, W. Q. Sun and N. C. Seeman, *Nature,* 1997, **386,** 137-138.

105. K. S. Chichak, S. J. Cantril, A. R. Pease, S. H. Chiu, G. W. V. Cave, J. L. Atwood and J. F. Stoddart, *Science,* 2004, **304**, 1308-1312.

106. R. Liantonio, P. Metrangolo, T. Pilati and G. Resnati; *Crystal Growth & Design,* 2003, **3,** 355-361.

107. R. Liantonio, P. Metrangolo, F. Meyer, T. Pilati, W. Navarrini and G. Resnati, *Chem. Commun.,* 2006, 1819-1821.

Chapter 2

Self-assembled $M_{12}L_{24}$ spherical cages to study the halogen-bonding complexes in confined space

2.1. Introduction

The self-assembly of giant polyhedral complexes from a large number of small components is currently one of the most exciting challenges in chemistry, and allows the bottom-up control of chemical structures on the nanoscale.[1] As already described in chapter 1 coordination driven transition metal–ligand self-assembly provides a highly efficient and powerful approach to discrete giant structures, and several groups have been intensively studying the self-assembly of coordination polyhedra with framework topologies that are described by Platonic or Archimedean solids.[2-4] By utilizing the four-coordinate transition metals (M) and divalent bridging ligands (L), a series of M_nL_{2n} regular/semi-regular polyhedra, in which four edges meet at every vertex, can be formed with geometrically restricted n values of 6, 12, 24, 30 and 60.[5] The bent angle of the ligand component determines the n value of the polyhedra where the angle around 125° gives $M_{12}L_{24}$ (n=12) structures and those of around 135° result in $M_{24}L_{48}$ (n=24) structures.[6]

Exo and endo-functionalization of $M_{12}L_{24}$ metallocages can be achieved by the attachment of a functional moiety on the convex and concave side of a building blocks respectively. This positions the chemical groups on the periphery and interior side of the resulting self-assembled supra-structures. Initially M. Fujita and co-workers have designed a number of $Pd_{12}L_{24}$ exo-functionalized molecular spheres decorated with different functional groups on the surface by simply attaching the desired moiety to the convex dipyridyl ligands.[7] The attachment of saccharide groups at the periphery led to saccharide-coated $Pd_{12}L_{24}$ molecular spheres that form aggregates upon interaction with proteins.[8]

Subsequently the same authors assembled a variety of discrete, endo-functionalized $Pd_{12}L_{24}$ molecular spheres by combining 12 naked Pd(II) ions with 24 bis-4-pyridyl ligands bearing two acetylene spacers in the assembling components.[9] The presence of these spacers enables for larger cavity space as compared to that in exohedral $Pd_{12}L_{24}$ cages assembled using dipyridyl ligands. The acetylene spacers prevent the ligands from adopting unfavorable nonplanar conformations, which are caused by steric repulsion, occurring in the absence of the spacer, between the pyridyl groups and the core benzene ring. The large cavities of the $Pd_{12}L_{24}$ molecular spheres allow for the introduction of a variety of pendant functional moieties at the interior surface.

The well-defined nanoscale cavities of these functionalized assemblies have helped in the understanding and demonstration of interesting properties otherwise not observable under standard conditions. The interactions between the cage and the guests are primarily

hydrophobic in nature and these artificial cavities have encapsulated various guest molecules and promoted unusual reactivity. At the same time, the nature of the organic ligand may preclude the incorporation of appended functional groups. For example, the attachment of perfluoroalkyl chains generated a fluorous nanophase within the cavity, allowing it to solubilize perfluoroalkane molecules and their solubility can be tuned by varying the length of the pendant perfluoroalkyl chains.[10] In addition to this, lining the inner surface with extended aromaticity increased solubility of fullerenes,[11] the presence of methyl methacrylate units enabled for the radical polymerization,[12] the use of sugar residues allowed for high degree of control over the size and shape of formed nanoparticles,[13] the tethering of azobenzene chromophore ensued effective photoisomerization processes.[14]

Halogens are typically positioned on molecular surfaces and are thereby easily available for involvement in molecular recognition processes. As described in Chapter 1, the halogen bonding (XB) is a fascinating non-covalent interaction and has attracted considerable interest in several fields.[15] The presence of electron withdrawing groups at the vicinity of the XB-donor site increases its Lewis acidity and consequently the interaction strength. In particular fluorination of the molecular backbone of certain halogenated building blocks enhances their ability to work as XB-donors, giving rise to particularly strong interactions.[16] Moreover, the fluorous phase manifests distinct solubilizing properties relative to aqueous and hydrocarbon organic phases and therefore proves useful for a range of separation,[17] purification,[18] and catalyst-immobilization techniques.[19] In particular, organic synthesis using the fluorous phase has developed rapidly in recent years[20] because of its high compatibility with environmentally benign chemistry. Nanometer-scale fluorous environments can be attained within vesicles, micelles, or dendrimers that in turn may dissolve in aqueous or organic solvents; however, the phases are often poorly defined physically and structurally.[21]

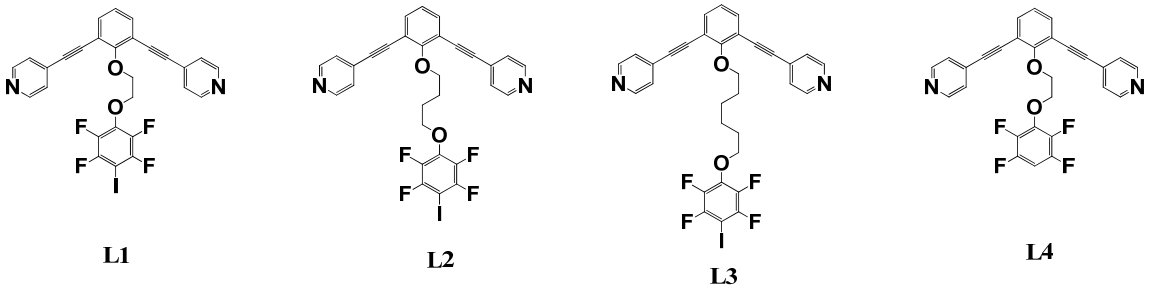

Figure 2.1 Structural formulas of the ligands **L1-L4** used for the coordination driven self-assembly of cafes with a fluorinated and XB-donor core.

In this chapter, we report endohedral functionalized cages obtained from bidentate pyridyl ligands L bearing a iodotetrafluorobenzene moiety, a well-known XB-donor group. Upon mixing Pd(II) ions (M) and convenient bidentate ligands (L), $M_{12}L_{24}$ coordination nanocages self-assembled having the XB donor moiety in the cage core. As a consequence of the well-defined host framework, the XB-donor functionalized structure could be well analyzed by NMR spectroscopy, CSI-TOF mass analysis, and X-ray crystallography.

2.2. Results and discussion

The bent ligands **L1-L4** used in this study as precursor of cages $M_{12}L_{24}$ are listed in Fig. 2.1. The different chain lengths of these ligands (**L1, L2** and **L3**) offer control over the internal occupancy of the cage core in order to control and tune guest uptake and lock. Ligands **L1-L4** were prepared by multistep organic synthesis, where the pyridyl groups were introduced by Sonogashira cross-coupling followed by Mitsunobu reactions to attach the XB-donor (**L1-L3**) or hydrofluorocarbon (**L4**) groups to the concave side of the dipyridyl units (Chap.7 Sec.7.1.2). The ligand **L4** has also been incorporated into $M_{12}L_{24}$ assemblies and was chosen because its backbone is isostructural with XB-donor ligands **L1-L3**. A comparison of the behavior of $M_{12}L_{24}$ cages from ligands **L1-L3** and **L4** will enable for assessing the XB role in guest inclusion.

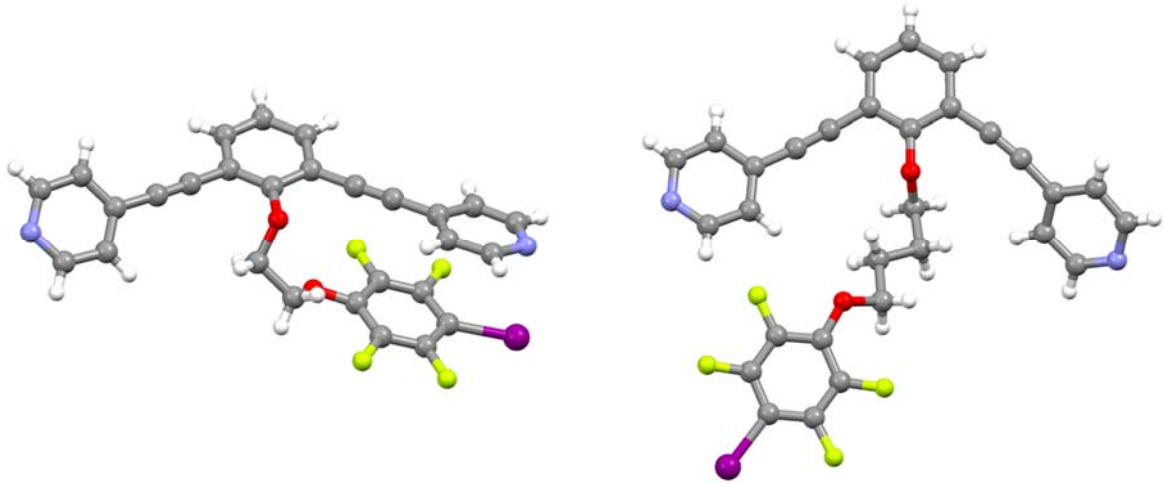

Figure 2.2 Crystal structure (Mercury 3.8, ball and stick representation) of the synthesized ligand **L1**(left) and **L 2**(Right); Color code: Grey, carbon; green, fluorine; red, oxygen; blue, nitrogen; white, hydrogen; magenta, Iodine.

Before the preparation of self-assembled cages, we established the structure in the solid of ligands **L1** and **L2** via single crystal X-ray analysis in order to check the ability of iodine to

work as XB-donor. Crystal structure of the ligands **L1** and **L2** are given in Figure 2.2 and the crystallographic data collection and structural refinements are described in experimental section (Chap.7 Sec.7.1.6). In both cases crystal packing is dominated by intramolecular XB between the pyridyl nitrogen and iodotetrafluoro moiety (Fig. 2.3), were the N···I distances are 2.897 Å and 2.950 Å in **L1** and **L2**, respectively. This behavior is consistent with the surface electrostatic potential for the diiodotetrafluorobenzene moieties[22] of 168.9 kJmol^{-1}. The two pyridyl rings in the four prepared ligands are in 1,3 position on the central benzene ring and the structure of **L1** and **L2** confirms that they form an angle of approximately 120-122°, the characteristic value required for the formation of $M_{12}L_{24}$ spherical cage structures.[6]

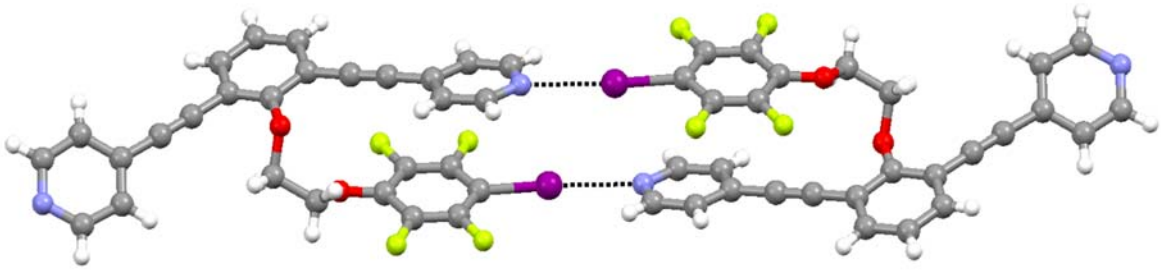

Figure 2.3 Intramolecular XB (N···I distance 2.897 Å) between the pyridyl nitrogen and iodotetrafluoro moiety in ligand **L1** (color codes as same as in Figure 2); the black dots indicates the XB.

The self-assembly of a $Pd_{12}L_{24}^{24+}$ coordination sphere (Fig. 2.4) has been achieved by treating ligands **L1-L3** with 0.5 equivalent of $Pd(BF_4)_2$ for 4 hours at 60 °C in polar organic solvents, such as $MeNO_2$ and Me_2SO.

The formation of a single self-assembled product was indicated by ^{1}H NMR spectroscopic analysis (Fig. 2.5). The line broadening and downfield shifts of the hydrogen PyHa and PyHb signals (approximate ΔδPyHa=0.78 ppm and ΔδPyHb= 0.35 ppm) are characteristic of the coordination of the pyridine brings to the Pd(II) ion. Observation of only one set of proton signals indicates the equivalency of all the ligands in the complex; this is consistent with a complex of cuboctahedral symmetry in which all edges are equivalent.

An exactly similar procedure was followed for the preparation of hydrofluorinated cage **L4**, the ^{1}H NMR and diffusion NMR (^{1}H, ^{1}H DOSY) studies proves the formation of the self-assembled spherical cages (Chap.7 Sec.7.1.3).

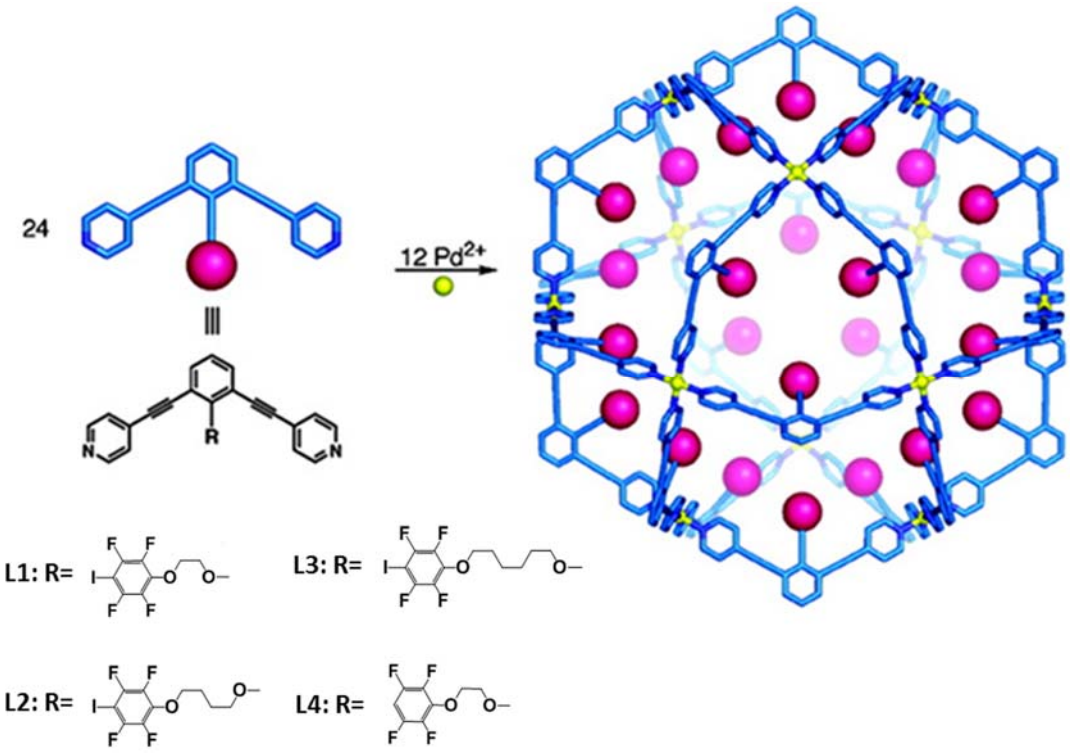

Figure 2.4 Self-assembly of $M_{12}L_{24}$ spherical complexes with 24 endohedral XB- donor group (**L1-L3**) and hydrofluorinated group (**L4**).

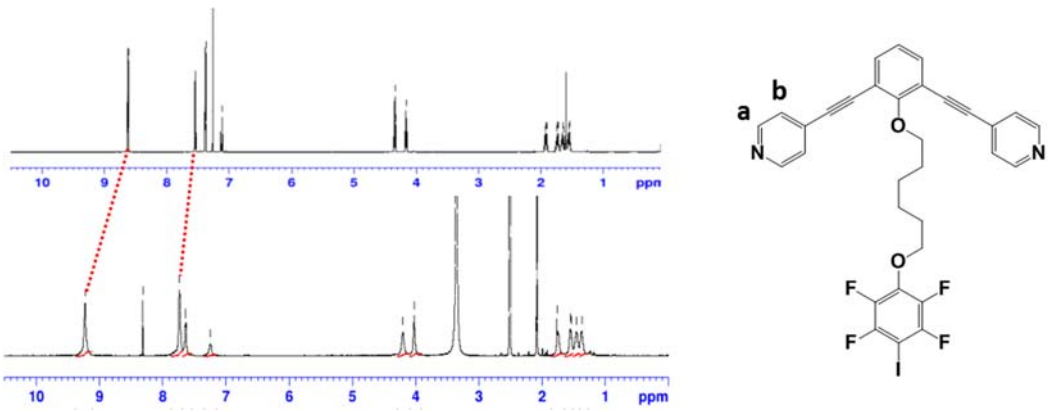

Figure 2.5 Comparison of the ^{1}H NMR spectra (600 MHz, DMSO-d6, 298 K) of ligand **L3** as pure compound (Top) and in the self-assembled cage (Bottom). Right: chemical structure of ligand **L3** with indication of probes for downfield shifts monitoring of the hydrogens (PyHa and PyHb) on reaction with Pd(II).

The ^{1}H, ^{1}H DOSY NMR spectroscopy is a useful tool for verifying presence of the giant coordination $M_{12}L_{24}$ assembly because the massive spherical complexes typically diffuse much more slowly than their uncomplexed parent ligands.

DOSY spectra of $Pd_{12}L1_{24}$ and $Pd_{12}L2_{24}$ with their corresponding ligands, in DMSO-d_6 at 298 K is reported in Figure 2.6 and Experimental section 7.22. The observation of a single diffusion band in each case supports the conclusion that the self-assembly of these molecular flasks is quantitative. The diffusion coefficient D of ligand **L1**, 2.88×10^{-10} m^2 s^{-1}, log D = –9.54, decreased in magnitude upon complex formation, 5.62×10^{-11} m^2 s^{-1}, log D = –10.25 (Fig. 2.6). This value is comparable to values of previously reported cuboctahedral $M_{12}L_{24}$ complexes.[5] The strong signals in the region of 1.5 to 3.5 ppm is the representative peaks for methyl protons of acetonitrile, water and DMSO-d_6 respectively.

Similarly $Pd_{12}L2_{24}^{24+}$, $Pd_{12}L3_{24}^{24+}$ and $Pd_{12}L4_{24}^{24+}$ diffuse almost one order of magnitude slower (4.79×10^{-11} m^2 s^{-1}, log D = –10.32, and 3.55×10^{-11} m^2 s^{-1}, log D = –10.45 and 3.16×10^{-11} m^2 s^{-1}, log D = –10.50, respectively) than their parent ligands **L2**, **L3** and **L4** (1.58×10^{-10} m^2 s^{-1}, log D = –9.80 and 1.90×10^{-10} m^2 s^{-1}, log D = –9.72, and 2.51×10^{-10} m^2 s^{-1}, log D = –9.6, respectively) in DMSO-d_6 (Chap. 7 Sec. 7.1.5).

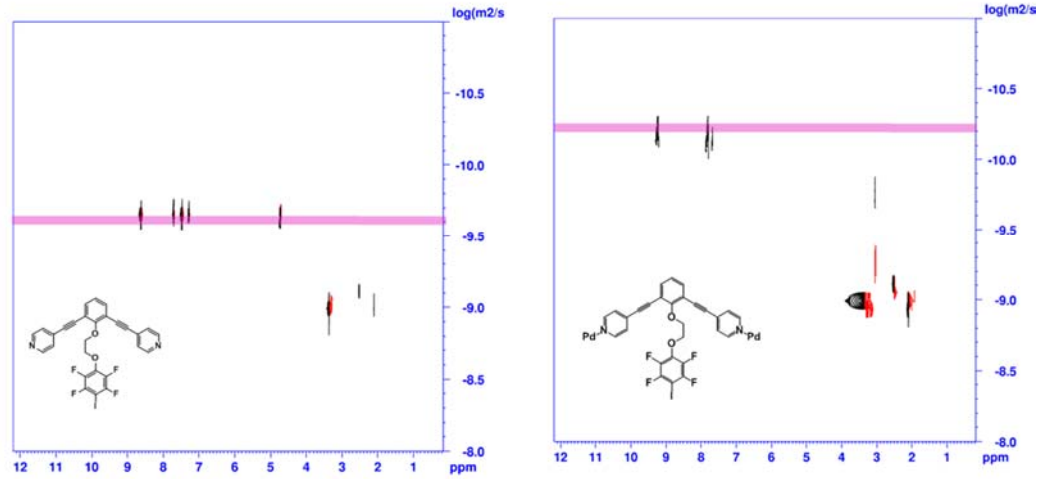

Figure 2.6 Diffusion-ordered NMR spectroscopy (DOSY, 500 MHz, DMSO-d_6, 300 K); diffusion coefficient D of ligand (Left) and spherical cage (Right).

The molecular weights and formula of selected represented complexes **L1** and **L3**, as well as their exclusive formation, were clearly confirmed by cold-spray ionization mass spectrometry (CSI-MS). From the solution of complex **L1** and **L3**, a series of prominent peaks for $[Pd_{12}L_{24}(BF_4)_{24-n}]^{n+}$ (n=13 and 14) were observed with very high resolution (>25000). The calculated monotropic mass for the complex of **L1** having the formula $(C_{19}H_{15}N_2O_2F_4I)_{24}$ $Pd_{12}(BF_4)_{11}$ is 16964.14 Da with fragment of 1304.93 Da (charge balance of 13) and these values exactly match with the experimental average mass 16975.75 Da calculated from the solution fragment of 1305.62 (Fig. 2.7, top). Very similar results were obtained from the self-

assembled solution of **L3**: the calculated monotropic mass for $(C_{32}H_{27}N_2O_2F_4I)_{24}$ $Pd_{12}(BF4)_{10}$ is 18222.64 Da (with the fragment of 1301.6 Da, charge balance of 14) and these values well match with the experimental average mass 18235.50 Da calculated with the fragment of 1302.62 Da (Fig. 2.7, bottom).

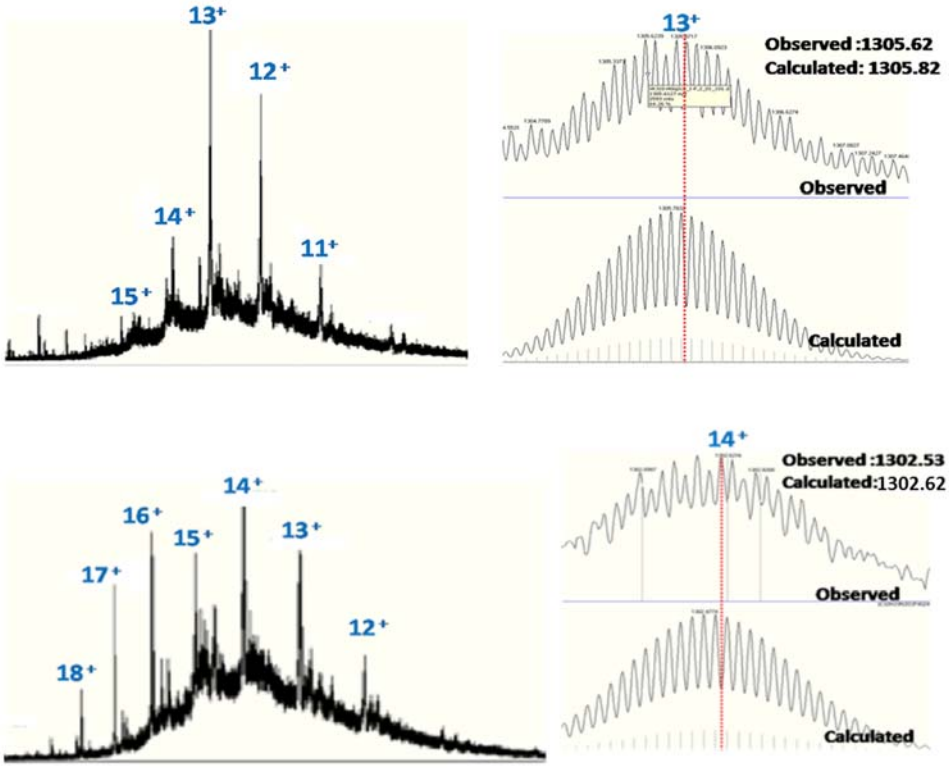

Figure 2.7 CSI-MS of spherical complex **L1** (Top) and **L3** (Bottom) with the assignment of the observed and simulated isotopic patterns.

2.2.2. Molecular Modelling studies of $M_{12}L_{24}$ spherical cages

Due to some general difficulty in atomistic (supra)molecular self-assembly simulation, only few attempts have been reported that go further in rationalizing the principles of chemical design. In this study, we used the Material Studio Complete package to model, in gas phase, our $M_{12}L_{24}$ spherical complex and we succeeded in observing a spontaneous formation of the spherical shaped $M_{12}L_{24}$ cages starting from random initial placement of metal ions and synthesized ligands. The dimensionality and internal volume of the molecular flasks with respect to the different chain length of ligand **L1-L3** were examined before beginning the chemical design of the molecular cages. The diameter of the cage is approximately 38-39 Å in all three cages and most of the attached iodotetraflurobenzene pendants point towards the center of the cage and tremble inside the cavities, very few pendants pointing outside. The space filling

modeling of the molecular cages **L1-L4** (Fig. 2.8) shows that non minor empty space is present inside the flask and is available for potential hosting several medium sized guest moieties. The space fill representation of molecular dynamic simulated structure of spherical complex **L3** has given in fig.2.8.

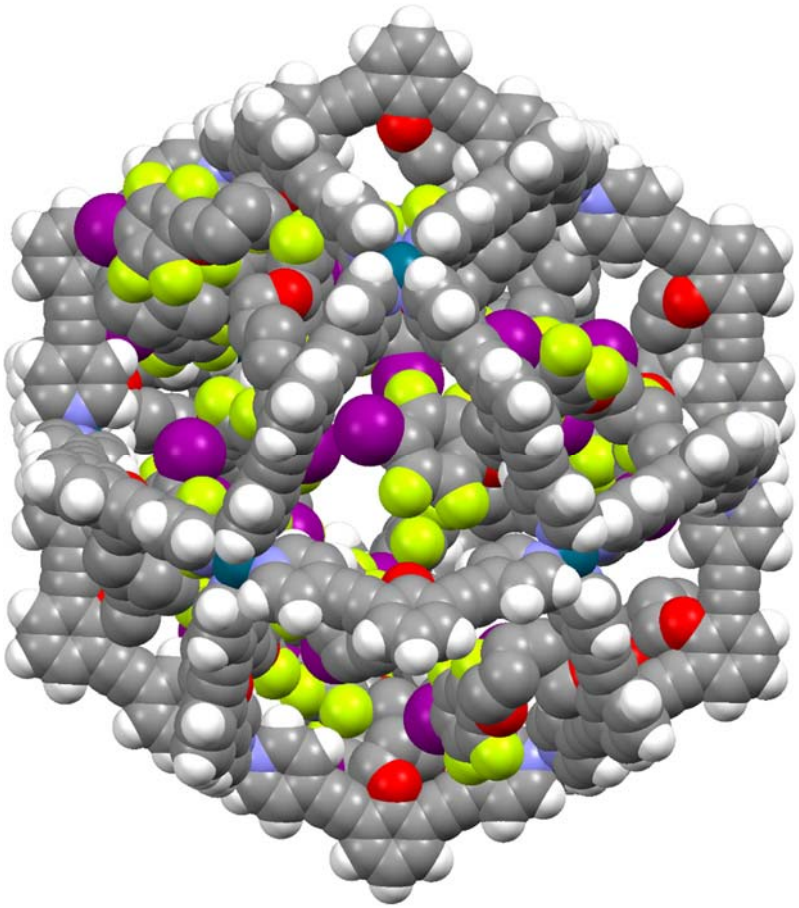

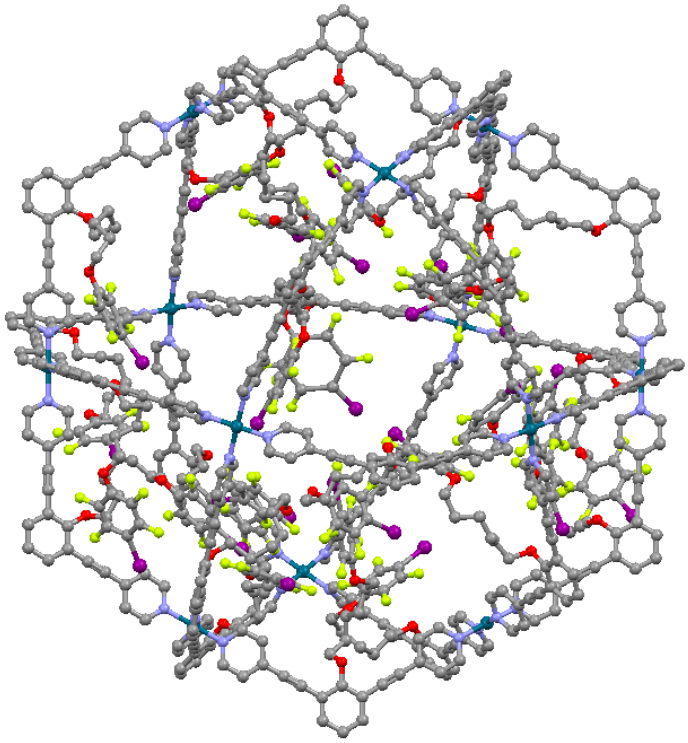

Figure 2.8 Space filling (top) and ball and stick representation (bottom) of molecular dynamic simulated structure of spherical complex obtained by using pyridine-capped bidentate ligand **L3** and Pd(II) ions; color code: Grey, carbon; green, fluorine; red, oxygen; blue, nitrogen; white, hydrogen; magenta, iodine; moss-green, palladium; in the ball and stick representation hydrogen atoms are omitted for clarity.

2.3. Conclusion

Weak intermolecular forces are difficult to observe in solution because the molecular encounters are random, short-lived, and overwhelmed by the solvent. In confined spaces especially cages the encounters are prolonged, prearranged, and isolated from the medium. The $M_{12}L_{24}$ cages functionalized with 24-fold endohedral XB-donor and fluorinated motifs were prepared to study the XB based intermolecular interactions in a confined space. The molecular modelling studies of all the synthesized nanocages shows the presence of enough space for guest uptake. Cold-spray ionization mass spectrometry, ^{1}H and diffusion NMR experiments prove the formation and stability of the giant coordination cages. The unambiguously confirmation of the formation of $M_{12}L_{24}$ spherical cages in solid state via single crystal X-ray analysis is under study. Artificial self-assembled cages can often encapsulate guest molecules and promote unusual reactivity. XB-donor sites enable for strong and directional interactions and fluorinated residues are associated with unique phase properties; both XB-donor sites and

fluorinated residues partially fill the cage interior and the useful opportunities offered by such residues in a confined space are under study.

2.4. References

1. P. A. Gale and J. W. Steed, Supramolecular Chemistry: From Molecules to Nanomaterials, Wiley, 2012.
2. (a) M. Fujita, D. Oguro, M. Miyazawa, H. Oka, K. Yamaguchi and K. Ogura, *Nature*, 1995, **378,** 469-471; (b) D. L. Caulder, R. E. Powers, T. N. Parac and K. N. Raymond, *Angew. Chem. Int. Ed.*, 1998, **37,** 1840-1843; (c) B. Moulton, J. Lu, A. Mondal and M. J. Zaworotko, *Chem. Commun.*, 2001, 863-864.
3. (a) W. Meng, B. Breiner, K. Rissanen, J. D. Thoburn, J. K. Clegg and J. R. Nitschke, *Angew. Chem. Int. Ed.*, 2011, **50,** 3479-3483; (b) X.-S. Wang, M. Chrzanowski, W.-Y. Gao, L. Wojtas, Y.-S. Chen, M. J. Zaworotko and S. Ma, *Chem. Sci.*, 2012, **3,** 2823-2827.
4. (a) M. M. J. Smulders, I. A. Riddell, C. Browne and J. R. Nitschke, *Chem. Soc. Rev.*, 2013, **42,** 1728-1754; (b) M. Fujita, M. Tominaga, A. Hori and B. Therrien, *Acc. Chem. Res.*, 2005, **38,** 369-378.
5. K. Harris, D. Fujita and M. Fujita, *Chem. Commun.*, 2013, **49,** 6703-6712.
6. H. Yokoyama, Y. Ueda, D. Fujita, S. Sato and M. Fujita, *Chem. Asian J.*, 2015, **10,** 2292-2295.
7. M. Tominaga, K. Suzuki, M. Kawano, T. Kusukawa, T. Ozeki, S. Sakamoto, K. Yamaguchi and M. Fujita, *Angew. Chem. Int. Ed.*, 2004, **43,** 5621-5625.
8. M. Ikemi, T. Kikuchi, S. Matsumura, K. Shiba, S. Satoa and M. Fujita, *Chem. Sci.*, 2010, **1,** 68-71.
9. (a) D. K. Chand, K. Biradha and M. Fujita, *Chem. Commun.,* 2001, 1652-1653; (b) M. R. Wasielewski, *J. Am. Chem. Soc.*, 2008, **130,** 4277-4284.
10. S. Sato, J. Iida, K. Suzuki, M. Kawano, T. Ozeki and M. Fujita, *Science,* 2006, **313,** 1273-1276.
11. K. Suzuki, K. Takao, S. Sato and M. Fujita, *J. AM. Chem. Soc.*, 2010, **132,** 2544-2545.
12. T. Murase, S. Sato and M. Fujita, *Angew. Chem. Int. Ed.*, 2007, **46,** 1083.
13. (a) K. Suzuki, K. Takao, S. Sato and M. Fujita, *Angew. Chem. Int. Ed.*, 2011, **50,** 4858-4861; (b) T. Ichijo, S. Sato and M. Fujita, *J. Am. Chem. Soc.*, 2013, **135,** 6786-6789; (c) K. Suzuki, S. Sato and M. Fujita, *Nature chemistry*, 2010, **2,** 55-29.
14. T. Murase, S. Sato and M. Fujita, *Angew. Chem. Int. Ed.*, 2007, **46,** 5133-5136.

15. (a) G. Cavallo, P. Metrangolo, R. Milani, T. Pilati, A. Priimagi, G. Resnati and G. Terraneo, *Chem. Rev.*, 2016, **116,** 2478-2601.
16. G. Valerio, G. Raos, S. V. Meille, P. Metrangolo and G. Resnati, *J. Phys. Chem. A.*, 2000, **104,** 1617-1620.
17. (a) A. Studer, *Science*, 1997, **275,** 823-826. (b) J. Yoshida and K. Itami, *Chem. Rev.*, 2002, **102,** 3693-3716; (c) J. A. Gladysz, D. P. Curran, I. T. Horva´ th, Eds., Handbook of Fluorous Chemistry, *Wiley-VCH*, 2004.
18. (a) A. Studer, P. Jeger, P. Wipf and D. P. Curran, *J. Org. Chem.*, 1997, **62,** 2917-2924; (b) W. Zhang, *Tetrahedron*, 2003, **59,** 4475-4489.
19. (a) I. T. Horvath and J. Rabai, *Science*, 1994, **266,** 72-75; (b) I. T. Horvath, *Acc. Chem. Rev.*, 1998, **31,** 641-650.
20. P. Kirsch, Modern Fluoroorganic Chemistry, *Wiley-VCH*, 2004.
21. (a) M. P. Krafft, *Adv. Drug Delivery Rev.*, 2001, **47,** 209-228; (b) J. G. Riess, *Tetrahedron*, 2002, **58,** 4113-4131; (c) K. C. Hoang and S. Mecozzi, *Langmuir*, 2004, **20,** 7347- 7350.
22. C. B. Aakerçy, M. Baldrighi, J. Desper, P. Metrangolo and G. Resnati, *Chem. Eur. J.*, 2013, **19,** 16240-16247.
23. K. Yamaguchi, *J. Mass Spectrom.*, 2003, **38**, 473-490.

Chapter 3

Supramolecular size-matching hosts for solubility enhancement and separation of dicarboxylic acid mixtures

3.1. Introduction

The development of molecular functional materials[1] able to capture, separate, and later release guest species is an ongoing research topic both in academia and industry,[2] and thanks to their technologically relevant properties, these materials have found applications in separation processes, [3] gas storage, [4] catalysis, [5] chemical sensors and energy-saving researches. [6]

During the past years the main strategy to target these materials has been through the construction of rigid metal organic frameworks[7] (MOFs) or porous coordination polymers[8] (PCPs), which by their nature are molecular architectures with voids to capture guest molecules.[9] The success of this approach lies in the rigidity of the architecture obtained by the use of suitable building blocks (*metals and linkers*), which prevents the formation of close-packed systems promoting the development of cavities or channels for the reversible uptake and release of guest species.

However, permanent porosity is not a mandatory pre-requisite for solid systems showing guest-capture properties.[10] In fact, it has been observed that nonporous crystalline system can have transient dynamic behavior so that the host molecular structure can reorganize its crystal lattice in response to the presence of a selectively recognizable guest.[11] In other words, a process of mutual induced fitting can occur. Nonporous solids able to absorb and release small molecules in a controllable and selective fashion are quite rare and less investigated than MOFs and PCPs. Nevertheless, some recent studies have highlighted the potential related to these dynamic abilities and have promoted these materials to the status of efficient separating tool even for complex mixtures.

In this framework, in 2009 it has been demonstrated that bis(trimethylammonium) alkane diiodides (**1**), a class of nonporous organic salts, can efficiently absorb selectively and separate a mixture of α,ω-diiodoperfluoroalkanes (DIPFAs) which are key industrial intermediates and catalysts in the synthesis of various fluorochemicals and fluoropolymers.[12] The recognition phenomena was driven by the halogen bonding[13] (XB) occurring between the I^- anions of the host ammonium salt and the terminal iodine atoms on perfluorinated guest. The preferential molecular recognition of a given DIPFA was due to the enhanced electrostatic binding strength in the ionic lattice wherein the size of the halogen-bonded superanion $I^-\cdots I(CF_2)_mI\cdots I^-$ matched that of the dicationic alkyl chain in the diammonium unit. The selective guest adsorption controlled by the size complementarity of the modules in the host−guest structure (size-matching rule) was general and occurred both in solution and solid-

gas process. The dynamic behavior of bis(trimethylammonium)alkane dihalide salts was also exploited to trap shorter guest molecules such as diiodine and to stabilize rare mixed tetrahalide anions.[14]

All these results suggest two important perspectives: (I) the bis(trimethylammonium)alkane diiodide salts are a simple and very versatile class of solid organic systems able to display a transient dynamic porosity; (II) the selective guest adsorption can be efficiently pursued by means of a self-assembly approach wherein selectivity is related to programmed size complementarity between the host and guest modules.[15] Motivated by these evidences and following the strategies of a supramolecular approach we decided to further challenge the specific ability of the bis(trimethylammonium)alkane diiodide salts **1** in reversible uptake and release of dicarboxylic acids **2** and **3**, namely guest species which are of high-value and technological relevance in many industrial[16] and biological applications.[17] The most intriguing challenges for separation of diacid mixtures is to have isomeric or non-isomeric components with similar boiling points so that some conventional separation methods cannot be successfully applied. Recently K. Uzarevic et al. reported the flexible polyamine host as an exceptional receptor for maleic acid even with large excess of competitive acids.[18]

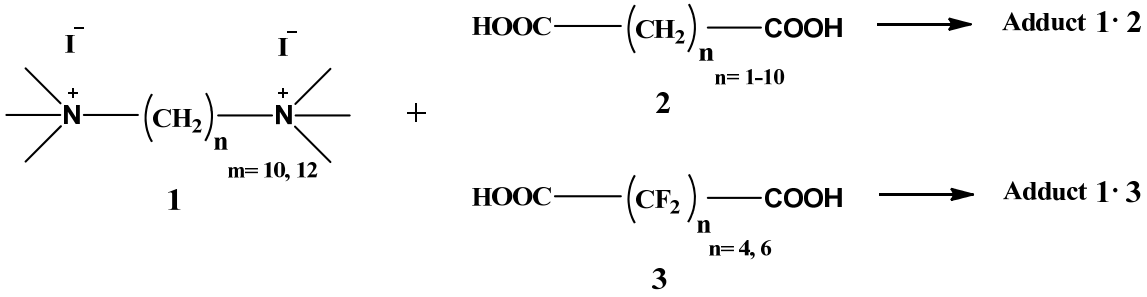

Scheme 3.1 Synthesis of supramolecular complexes **1-m·2-n** and **1m·3n** (m and n are the number of carbon atoms spacing the two nitrogen atoms in diammonium salts **1** and the two carboxylic residues in diacids **2** or **3**, respectively).

In this chapter we report that the nonporous hosts **1** react with size matching dicarboxylic acids **2** and **3** (Scheme 3.1). The supramolecular complexes **1-m·2-n** and **1-m·3-n** are formed through intermolecular hydrogen bonding[19] between the I^- anions of the hosts and guest carboxylic OH group. The process is highly effective for separating in pure form of dicarboxylic acid chain that forms an $I^{-}\cdots HOOC–(CH_2/CF_2)_n–COOH\cdots I^{-}$ superanion that

matches in length to the chosen dication. Selectivity in the formation of stable supramolecular complexes is driven by size matching[20] of the interacting host-guest moieties.

3.2. Results and discussion

Good quality crystals suitable for single crystal X-ray structural analysis of pure **1-10** and **1-12** were obtained through slow isothermal evaporation of acetonitrile solutions. Both compounds crystallized in anhydrous form wherein the anion-cation interactions dominate the crystal structure. Some hydrogen bonds are also present between the iodide ions and the methyl and methylene protons of the neighboring cation. Carbon atoms along the methylene chain spacing the nitrogen atoms adopt both gauche and trans conformations and the hydrocarbon chains are slightly twisted in morphology (Fig. 3.1).

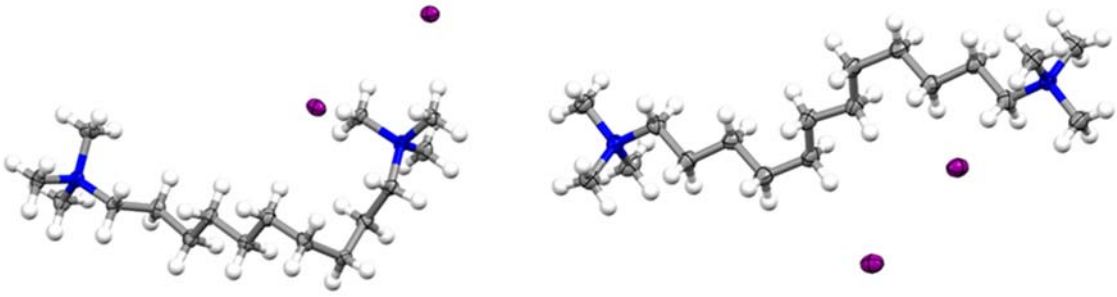

Figure 3.1 ORTEP view of supramolecular hosts **1-10** (decamethonium iodide, left) and **1-12** (of dodecamethonium iodide, right). ORTEPS were drawn at 50% probability level at 100 K). Color codes: grey, carbon; blue, nitrogen; white, hydrogen; magenta, iodine.

Based on the literature,[12] the N^+–N^+ intramolecular distance in crystalline derivatives of **1-10** wherein the compound is adopting an all-trans arrangement is 13.965 Å. In order to exploit the potential of the size-matching principle in driving selective self-assembly processes, we attempted to crystallize **1-10** with adipic acid **2-4**. In fact, the expected separation between the two acidic protons in **2-4** is 8.771 Å, as established from the pure compound in all-*trans* conformation (Refcode GLURAC02), the Pauling anionic radius of iodide anion is 2.16 Å, and a supramolecular anion wherein two iodide anions are pinning the two acidic hydrogen atoms in **2-4** would be *ca*. 15 Å long. The size difference between this supramolecular anion and decamethonium would be safely within the value enabling for an efficient and selective self-assembly process under size-matching control.[12] Specifically, decamethonium iodide **1-10** and adipic acid **2-4** were separately dissolved in dichloromethane (DCM)-methanol (MeOH)

solutions (9:1 ratio of the two solvents) and upon mixing the two solutions at room temperature, the 1:1 supramolecular cocrystal **1-10·2-4** crystallized in a quantitative yield and purity. The melting point of the cocrystal was different from the starting individual tectons **1** and **2** providing a preliminary indication for the formation of a new two component supramolecular compound rather than a mechanical mixture (Chap.7 section7.2.2.2). Moreover, IR spectroscopy reveals that ν_{O-H} stretchings were blue shifted with respect to pure diacids suggesting HB formation (Chap. 7 section 7.2.2.2, 7.2.2.3).

Single-crystal X-Ray analysis of the complex **1-10·2-4** afforded detailed information on its structure and confirmed our initial observations described above. The difference in distance between the two N atoms of **1-10** in the complex is within 1 Å of the iodide ions spacing in the superanion $I^{-}\cdots HOOC–(CH_2)_4–COOH\cdots I^{-}$ (Δ = difference between N^{+}---N^{+} and I^{-}---I^{-} separations = 0.98 Å; Table 3.1, Fig. 3.2A; Chap. 7.2.6, Fig. 7.2.4). Four dication units sit parallel to each other and define a rectangular parallelepiped shaped cavity that encapsulates one unit of diacid **1a**. The diacid sits nearly parallel to the cations defining the cavity and is trapped in its position by strong hydrogen bonding between two I^{-} ions and the two acidic protons (O–H···I^{-} 2.666 Å, Fig. 3.2A). Interestingly, on changing solvents from polar to apolar (DCM-$CHCl_3$ solutions rather than DCM-MeOH solutions), a different polymorphic structure of **1-10·2-4** cocrystal was obtained wherein the diacid **2-4** is nearly perpendicular to **1-10** units but the hydrogen bonded supramolecular anion $I^{-}\cdots HOOC–(CH_2)_4–$ $COOH\cdots I^{-}$ remains unaltered in the system (Chap.7 Fig. 7.2.6 and 7.2.7). This suggests that the strong O–H···I^{-} hydrogen bonding between **1-10** and **2-4** (C–O···I^{-} 3.423 Å, O–H···I^{-} 2.647 Å, C–O···I^{-} angle 122.04°) plays a major role in the self-assembly of the two components.

Table 3.1 Selected distance and angles in supramolecular complexes formed under size-matching control (as obtained by single crystal structural analysis at 90 K). Distances A and B are the separation of the two nitrogen atoms in a onium dication and of the two iodide anions in a supramolecular anion, respectively.

Adduct	Distance A $^{+}N(CH_2)_n N^{+}$ (Å)	Distance B $I\cdots HOOC(CH_2/CF_2)_n COOH\cdots I$ (Å)	Δ(B-A) (Å)	Distance $I^{-}\cdots O$ (Å)	Angle $I^{-}\cdots O$-C
1-10·2-4	14.003	14.989	0.986	3.474	120.56
1-12·2-6	16.565	17.549	0.984	3.473	121.12
1-10·3-4	13.029	14.093	1.064	3.298	119.02
1-12·2-3·$2H_2O$	16.602	17.972	1.370	3.414	124.27

To test the generality of the size-matching hypothesis, we challenged dodecamethonium iodide **1-12**, the bis-homologue of **1-10**, with suberic acid **2-6** , the bis-homologue of **2-4**, on the assumption that the relative metric of the interacting units remains unchanged in the two systems. The single crystal X-ray structure of cocrystal **1-12·2-6** reveals that the crystal lattices is strictly analogous to that of **1-10·2-4** complex as a quite similar $I^{-}\cdots HOOC–(CH_2)_6–COOH\cdots I^{-}$ trimer is present ($\Delta = 0.984$ Å; Table 3.1, Chap. Fig. 7.2.5). Interestingly, two of the unit cell dimensions are nearly the same in **1-10·2-4** and **1-12·2-6**, indicating similar packing in those two directions, and the third dimension is greater in the latter cocrystal as it is related to the starting tectons lengths. On varying solvent polarity (namely by using DCM-$CHCl_3$ solvent mixtures), no new polymorphic architecture was obtained when starting from **1-12** and **2-6**. Finally, for all obtained cocrystals, experimental powder XRD patterns of bulk material and patterns simulated from single crystal structures were quite similar (Chap.7 Sec. 7.2.2, 7.2.3 and Fig.7.2.10, 7.2.11), thus confirming the purity of all batches.

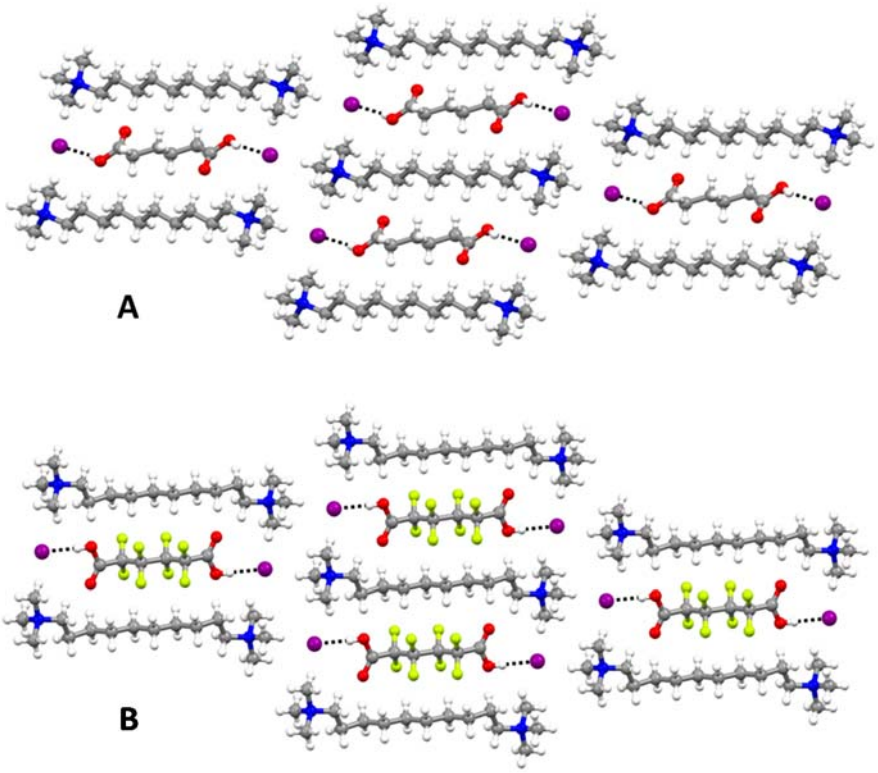

Figure 3.2 Crystal packing of supramolecular size matching complexes: **(A)** decamethonium iodide/adipic acid complex **1-10·2-4**; **(B)** decamethonium iodide octafluoro adipic acid complex **1-10·3-4**; Colour codes: grey, carbon; blue, nitrogen; white, hydrogen; red, oxygen; green, fluorine; magenta, iodine.

We reasoned that when interacting with bisonium iodides **1**, perfluorodicarboxylic acids **3** would afford cocrystals similar to those given by their hydrocarbon parents. In fact, we expected that the ability of perfluorocarboxylic acids to form stronger hydrogen bonding than their hydrocarbon parents, would enable the O–H···I$^-$ supramolecular synthon to drive the self-assembly process and counterbalance the tendency of perfluoroalkyl chains to segregate from hydrocarbon moieties, namely to induce a unique crystal packings. Indeed, crystallization of **1-10** with octafluoroadipic acid **3-4** from DCM-MeOH solutions (9:1 ratio) afforded the cocrystal **1-10·3-4** and X-ray structural analysis of this system confirmed the overcoming role of the O–H···I$^-$ supramolecular synthon and the size-matching principle. The perfluorinated diacid **3-4** is encapsulated parallelly in a rectangular shaped cavity and the hydrogen bonded and supramolecular anion I$^-$···HOOC–$(CF_2)_4$–COOH···I$^-$ is preserved in the cocrystal (Δ = 1.036 Å, Table 3.1 and Fig. 3.2B). It is interesting to observe that, as a confirmation of the mutual adapting of the interacting partners in order to optimize the overall crystal packing, the reduced length of **3-4** with respect to **2-4** translates into a more compressed conformation of **1-10** in **1-10·3-4** than in **1-10·2-4** in order to enable an effective uptake of the diacid in the self-sorted parallelepiped cavity.

We also challenged dodecamethonium iodide **1-12** with perfluorosuberic acid·**3-6** and the formation of cocrystal **1-12·3-6** was suggested by melting point analysis and by ^{1}H and ^{19}F NMR spectroscopy in the presence of an hydro-fluorinated external standard (to determine the 1:1 ratio of the starting tectons). Moreover, the characteristic shifting of carboxylic OH stretching frequency in infrared spectroscopy suggested the presence of the O–H···I$^-$ supramolecular synthon, but the poor crystallinity of the complex prevented from performing a single crystal X-ray analysis (Chap. 7, Sec. 7.2.2.2, 7.2.7 and Fig. 7.2.13).

To further assess how robust the size-matching principle was in controlling or affecting self-assembly processes, the supramolecular hosts **1-10** and **1-12** were challenged with mis-matching dicarboxylic acids in solution crystallization and milling reactions as well. Importantly, IR spectroscopy, melting point analysis, and DSC results on selected couples show that mismatching diacids do not form any complexes with host molecules, but on adding small amount of water to an equimolar mixture of dodecamethonium iodide **1-12** and adipic acid **2-4** a cocrystal was formed. Crystallographic analysis shows that two iodide anions are close to positive nitrogen atoms similar to **1-12·2-6** and adipic acid being shorter than suberic acid, the size-matching controlled self-assembly of the onium dication **1-12** with the diacid **2-4** is secured by two water molecules which are appended via hydrogen bonds to the adipic tecton. A supramolecular hydrogen bond donor **2-4·2H$_2$O** is formed whose length nicely matches the I$^-$-

--I ¯ separation in **1-12** and the cocrystal **1-12·2-4·2H₂O** is formed which has an overall architecture similar to **1-12·2-6**. In fact, **2-4·2H₂O** is pinned at its endings by two iodide anions via hydrogen bonds, the supramolecular anion $I^{-}\cdots HOOC–(CH_2)_3–COOH\cdots 2(H_2O)\cdots I^{-}$ is given (O–H···I⁻ distance is 2.490 Å, Δ = 1.37 Å, Table 3.1) which sits within a cage formed by four dodecamethonium iodides **1-12** (Fig. 3.3A and 3.3B).

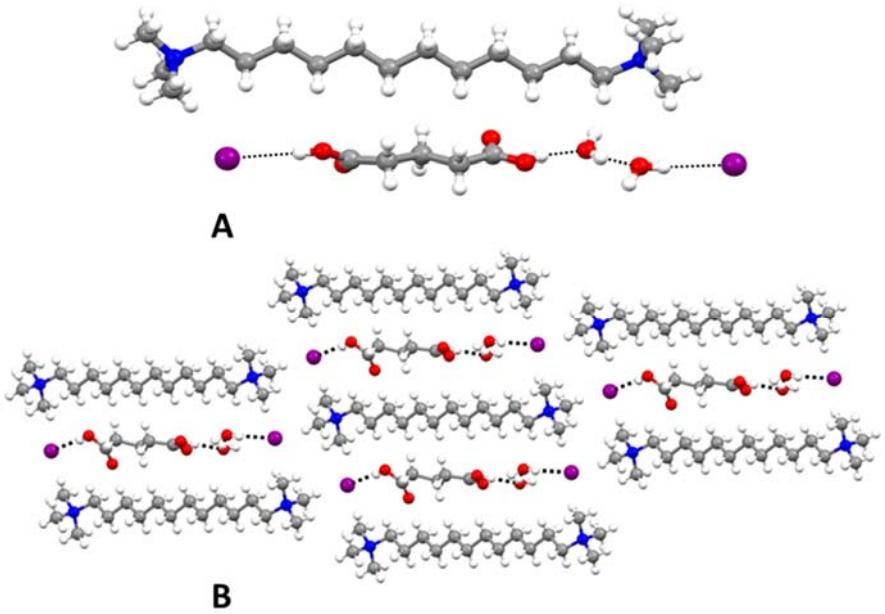

Figure 3.3 Representation (Mercury 3.8; ball and stick) of the complex **1-12·2-4·2H₂O**: **(A)**: Size-matching of onium dication and superanion of adipic acids **2-4** with two water molecules, this hydrogen bonded trimer being pinned at its endings by two iodide anions; **(B)**: Partial view of the crystal packing evidencing the cage formed by four dications and accommodating the supramolecular dianion. Colour codes: grey, carbon; blue, nitrogen; white, hydrogen; red, oxygen; magenta, iodine.

In solution, the existence of host-guest binding interaction between hosts **1** and guests **2** and **3** is proven by NMR titration experiments.[22] In order to better characterize such interactions in solution, we took advantage of nuclear Overhauser effect, ^{1}H NOSEY, and its heteronuclear version, ^{19}F, and ^{1}H HOSEY NMR spectroscopy. These techniques, were recently established as effective tools to obtain detailed information on non-covalent interactions.[23]

In diluted solutions of dications **1**·and diacids **2**, NOE contact between protons of **1** and guest's **2** internal-CH_2 moieties are absent, indicating that the concentration of such adduct, under the adopted experimental conditions, is below the ^{1}H NOSEY detection threshold (Chap. 7, Fig. 7.2.16).

Differently, when **1-12** and **3-6** are mixed in CD_2Cl_2:CD_3OD (10:1) and in 60 and 50 mM concentrations at 298 K, H/F intermolecular Overhauser contacts are observed, namely clear indications of association are obtained. In particular, fluorine atoms of perfluorosuberic acid **3-6** interact with all protons of **1-12**, with different relative intensities. It is interesting to note that fluorine interacts very strongly with the internal methylene units (arbitrary intensity 1.0, Chap. 7, Fig. 7.2.17), much less with the CH_2 in the β position with respect to the nitrogen (relative intensity 0.29) and even less with α-CH_2 (relative intensity 0.19). This observation is compatible with an adduct in solution wherein the chains of **3-6**, and expectedly of **2-6**, are parallel to the onium chains, as observed in the solid state. On the other hand, also the F/NMe_3^+ is intense (relative intensity 0.89). Such a contact can be explained with the presence of a different structure in which the chain of **1-12** is perpendicular to that of **3-6**. The relative intensities, 1:0.89, are a good estimation of the concentration ratio between the two structures.

Similar results were observed in ^{19}F, ^1H HOSEY NMR spectrum of a solution containing **1-10** and **3-4** in CD_2Cl_2/CD_3OD (10/1) at 298 K (Fig. 3.4, Chap. 7, Fig. 7.2.18). In this case, the relative concentration between the parallel and the perpendicular adducts is 1:1.14.

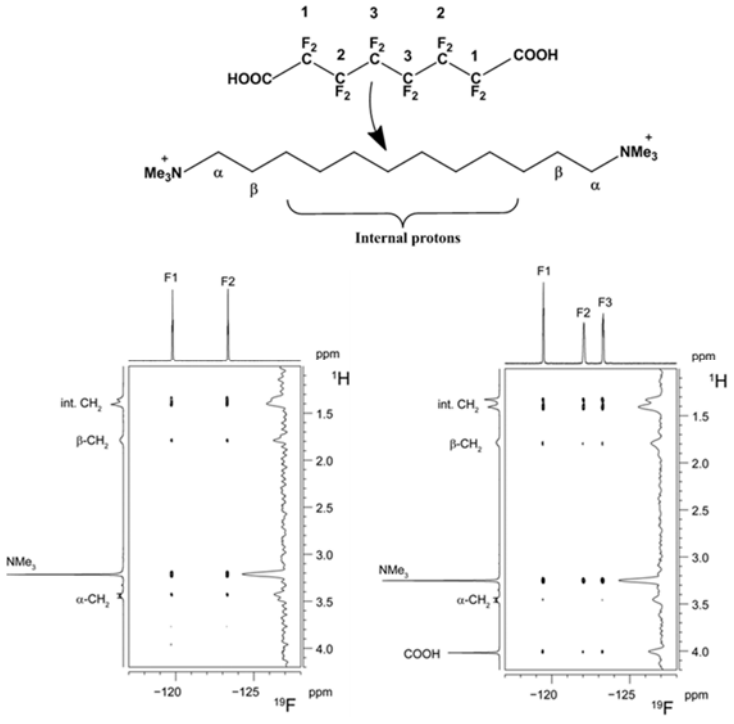

Figure 3.4 TOP: Schematic representation of expected H/F intermolecular Overhauser contacts in complex **1-12·3-6**; Bottom left side: ^{19}F, ^1H HOSEY NMR spectra of solutions containing **1-10** and **3-4** CD_2Cl_2/CD_3OD (10/1) at 298 K; Bottom right side: ^1H HOSEY NMR spectra of solutions containing **1-12** and **3-6** in CD_2Cl_2/CD_3OD (10/1) at 298K.

Interestingly, when the same experiment are conducted in different solvents (e.g., pure CD_3OD or D_2O), the qualitative pattern of the contacts remains the same, but difference exist in their relative intensities, being 1:0.51 in CD_3OD and 0.48 in D_2O. Likely, the parallel adduct is favoured in polar solvents because it minimizes the exposure of hydrophobic chains to the polar solvent.

The association constants between **1** and **3** were determined by ^{19}F NMR titrations considering the changes in the α-fluorine nuclei –(CF_2COOH) signals. The association constant of **3-4** with **1-10** and **3-6** with **1-12** in CD_2Cl_2/CD_3OD (10/1) is 12.1 ± 0.6 M^{-1} and 19 ± 1 M^{-1} respectively (Fig. 3.5, Chap 7. section 7.2.7.2, Fig. 7.2.21 and 7.2.22).

The stoichiometry of the adduct formed by onium iodide **1** with diacids **3** were studied by pulsed-gradient spin-echo (PGSE) NMR spectroscopy.[24] The hydrodynamic volume (V_H) of **3-6** resulted to be 331 Å^3 and on adding an excess of **1-12** (63 mM), V_H of **3-6** becomes 685 Å^3 confirming once again the association between the two moieties. Since the van der Waals volume of **3-6** is 405 Å^3, the hydrodynamic volume of the adduct **1-12·3-6** would be approximately 730 Å^3. Therefore, an experimental hydrodynamic volume of 685 Å^3 is well compatible with a formation of 1:1 adduct (Chap 7. Sec. 7.2.7.3)

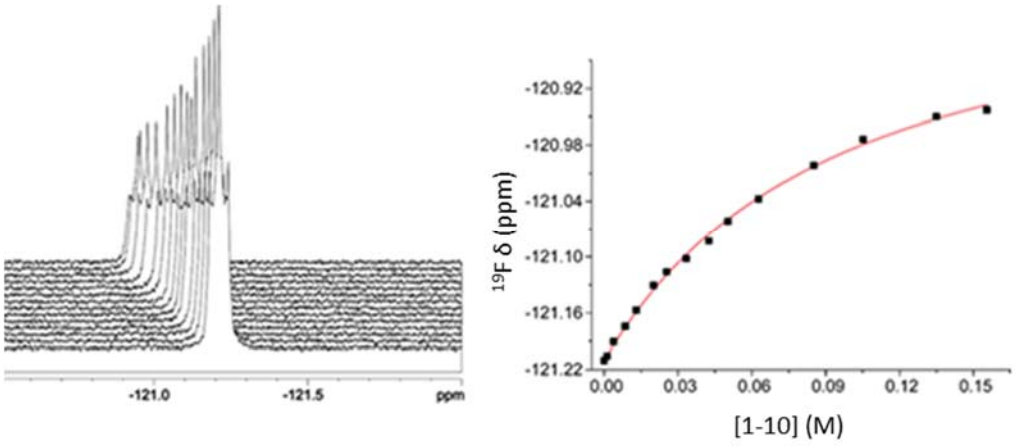

Figure 3.5 Left: Stacked spectra of **3-4** (the signal due to α-fluorine nuclei, -C*F*$_2$COOH, is shown) at increasing concentrations of **1-10** in CD_2Cl_2/CD_3OD 10/1. Right: Trend of the chemical shift of the α-fluorine nuclei (-C*F*$_2$COOH) of **3-4** (c = 13.7 mM) with [**1-10**] in CD_2Cl_2/CD_3OD 10/1. The limit value of δ (fitted) is -120.789 ± 0.031 ppm, the value of K_a is 12.1 ± 0.6 M^{-1}.

Interestingly, solubility experiments of pure individual diacids **2** and **3** and the respective supramolecular complexes with matching onium dications **1** reveal that the solubility of diacids increases tremendously on coupling with size-matching hosts (Chap. 7, Sec. 7.2.8,

table 7.2.11), namely, for instance, the molar solubility of **1-10·2-4** is much greater than **2-4** and the solubility of **1-12·2-6** is much greater than **2-6.**

In order to exploit the solubility enhancement enabled by the preferential self-assembly driven by the components size-matching, we performed competitive crystallization experiments by adding a solution containing one equivalent of a given pure onium dication **1** to a solution obtained by dissolving one equivalent of several dicarboxylic acids **2** (chain length of C4-C10). The aim was to separate a given diacid, namely the size-matching diacid, out of the diacids mixture by preferentially precipitating the mismatching diacids thanks to the increased solubility of a given diacid experiences in the presence of the size-matching onium dication. In other words, the onium dication forms a complex only with the size-matching diacid and its solubility is increased while the mismatching diacids remain uncomplexed and their solubility remains low (Chap. 7 section 7.2.9).

For instance, a solution of one equivalent of onium dication **1-10** in a mixture of acetonitrile:methanol (8:2 ratio) was added to a solution of diacids **2-4**, **2-6**, and **2-8** (one equivalent each) in the same solvent mixture. On slow evaporation of the solvent at room temperature a precipitate was formed. Evaporation was stopped and the mixture was filtered. When the mass of the precipitate was 5% more than the mismatching diacids (3-4 days), ^{1}H NMR spectroscopy, powder X-ray diffraction, melting point analysis, mass spectrometry, and, importantly, HPLC analysis showed that the solid filtrate was an equimolar mixture of the mismatching diacids **2-6** and **2-8** (~95% purity), the only detectable impurity being the matching cocrystal **1-10·2-4**. The same analytical techniques showed that evaporation of the supernatant afforded **1-10·2-4** as a pure compound (> 99%) (Fig. 3.6, Chap. 7, Sec.7.2.9 Fig. 7.2.26-27).

A similar experiment was carried by adding one equivalent of onium dication **1-12** to the solution of one equivalent each of **2-6**, **2-8**, **2-10** in acetonitrile:methanol (8:2). After 4 days, the precipitate was an equimolar mixture of mismatching diacids **2-8** and **2-10**, and the complex **1-12·2-6** was obtained from the filtrate, the purity of both batches being quite similar to those of the previous experiment. A series of analogous experiments with mixtures of diacids with different chain length are described in the experimental section (Chap. 7, Sec.7.2.9.1).

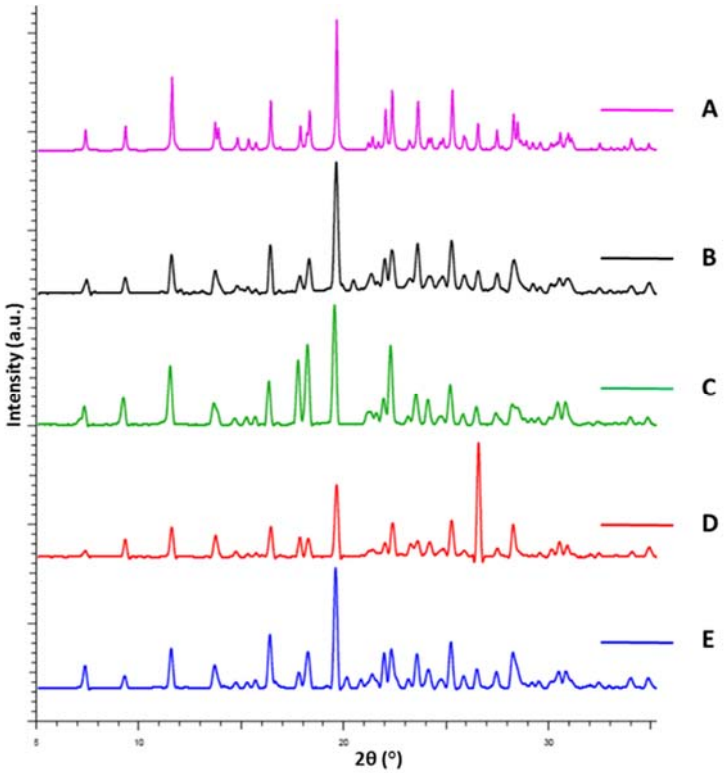

Figure 3.6 Comparison of PXRD patterns of **1-10·2-4** obtained using different experimental conditions; (A): Simulated powder pattern from single crystal structure (90 K); (B): Experimental pattern of pure cocrystals formed from solution crystallization; (C): Experimental pattern of cocrystals **1-10·2-4** separated from a mixture of **2-4, 2-6** and **2-8**; (D): Experimental pattern of cocrystals **1-10·2-4** separated from a mixture of **2-4, 2-8** and **2-10**; (E): Experimental pattern of cocrystals **1-10·2-4** separated from a mixture of **2-4, 2-6** and **2-7**.

The structures of **1-10** and **1-12** described above show that onium dications **1** are not porous materials as pure solids, but we assumed they might behave as dynamically porous systems when challenged with diacids and we tested this hypothesis by milling experiments (Chap. 7 section 7.2.2.2). The host **1** was ground with an equimolar amount of the respective matching dicarboxylic acids **2** via neat grinding (NG) or liquid assisted grinding (LAG, methanol or acetonitrile were used) and both procedures afforded the expected cocrystals in quantitative yields. With this in mind we performed competitive milling experiments (NG, LAG) by mixing one equivalent of **2-4**, **2-5**, **2-6**, **2-7**, **2-8** and **2-9** with one equivalent of potential host **1-10**. IR spectroscopy, DSC, melting point, and powder x-ray analysis discloses the selective and quantitative formation of **1-10·2-4** complex (Fig. 3.7, Chap. 7 section 7.2.2.2, Fig. 7.2.13-16).

The dynamically porous[15] character of onium dications **1** with respect to linear dicarboxylic acids is thus proven. It is also shown that the size-matching of the cation and the supramolecular anion enables for selective recognition of the matching diacid not only in solution but also in

the solid. In both cases a new opportunity for the separation of linear diacids mixtures into pure components become accessible, in the liquid thanks to the increased solubility of the matching diacids, in the solid thanks to its selective uptake in a solid-solid reaction.

Having established the possibility to obtain selectively cocrystals of a given linear dicarboxylic acid starting from a diacids mixture both in solution and in the solid, we examined how to recover the size-matching diacids from the respective complexes **1·2**. A protocol was developed based on the formation of an halogen bonded cocrystal formation.

As already reported, bis(trimethylammonium)alkane diiodides **1** give cocrystals with α,ω-diiodoperfluoroalkanes **4** on halogen bonds formation between iodine atoms of perfluoroalkanes (XB donor sites) and iodide anions (XB acceptor sites). The process can be highly selective once again thanks to the importance of the cation-supramolecular anion size-matching. In fact, when the $I^-\cdots I^-$ separation in the trimeric and halogen bonded anion $I^-\cdots I–(CF_2)_n–I\cdots I^-$ is within 1 Å of the $N^+\cdots N^+$ separation in the onium dication, the co-crsystal is much less soluble and melts at much higher temperatures than cocrystals formed by shorter or longer diiodoperfluoroalkanes. This implies that the size-matching and halogen bonded cocrystal **1·4** is particularly stable system and it might be formed not only on reaction of **4** with pure **1**, but also on reaction of **4** with the size-matching and hydrogen bonded cocrystal **1·2**. In other words, the high melting and poorly soluble cocrystal **1·4** could be obtained from the low melting and highly soluble cocrystal **1·2** as the halogen bond donor **4** substitutes for the hydrogen bond donor **2**, the trimeric anion $I^-\cdots I–(CF_2)_n–I\cdots I^-$ is formed and replaces the trimeric anion $I^-\cdots HOOC–(CH_2)_n–COOH\cdots I^-$ in the cavity identified by four onium dications.

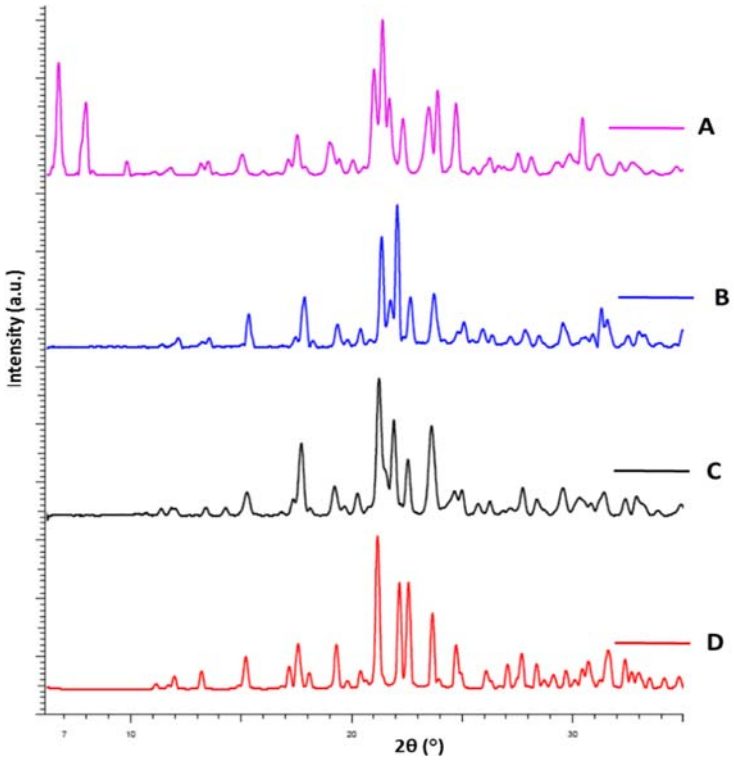

Figure 3.7 Comparison of simulated and experimental PXRD patterns of **1-10·2-4** obtained using different experimental conditions; (A): Experimental powder pattern of **2-4**, **2-5**, **2-6**, **2-7**, **2-8** and **2-9** diacids mixture; (B): Experimental pattern of separated cocrystals **1-10·2-4** from mixture of **2-4**, **2-5**, **2-6**, **2-7**, **2-8** and **2-9**; (C): Experimental pattern of pure cocrystals formed via milling experiments; (D): Simulated powder pattern of **1-10·2-4** from single crystal structure (90 K).

Indeed, on addition of a chloroform solution of one equivalent of 1,4-diiodooctafluorobutane **4-4** to a chloroform-methanol solution (9:1) of one equivalent of cocrystal **1-10·2-4**, a white solid precipitated almost immediately. Melting point, IR spectroscopy, ^{1}H and ^{19}F NMR, and powder XRD analysis of filtered precipitate indicate the formation of pure cocrystal **1-10·4-4** in nearly quantitative yields. When the chloroform-methanol solvent mixture was partially evaporated at room temperature so that the mass of the filtered crystalline solid was 5% greater than the stoichiometric mass of **1-10·4-4**, evaporation of the surnatant afforded adipic acid with <99% purity. A similar experiment was performed by adding a chloroform solution of 1,6-diiodoperfluorohexane **4-6** to a chloroform:methanol solution of cocrystal **1-12·2-6** and pure cocrysal **1-12·4-6** (~95%) and pure suberic acid 2-6 were recovered from the filtered precipitate and evaporated surnatant (Fig. 3.8). The pure form of the separated dicarboxylic acids were obtained by evaporation of $CHCl_3$:MeOH solution under the reduced pressure, the separated acids were further fully characterised by Melting point, IR spectroscopy and powder XRD analysis (Chap. 7, Sec. 7.2.11.1, Fig. 7.2.35-39).

The robust liberation of the guest prompted us to study the reverse process, namely, the uptake of DIPFA vapours by the solid bis (trimethylammonium) alkane derivatives. Practical application of the selective guest exchange would benefit from solvent free environment. We placed the cocrystal **1-10·2-4** and **1-12·2-6** to expose to the vapours of matched DIPFA **4-4** and **4-6** respectively in a sealed vessel at ambient pressure and temperature for 7 days. The **1·2** complex was isolated from surrounding liquid DIPFAs but at the same time it allowed to access the corresponding vapours. Once again melting point, IR spectroscopy and PXRD analysis indicated that dicarboxylic acids **2-4** and **2-6** was completely replaced in this gas-solid reaction by the matched DIPFA **4-4** and **4-6** in respective complexes (Chap. 7, Sec. 7.2.11.1, Fig. 7.2.40 and 7.2.41).

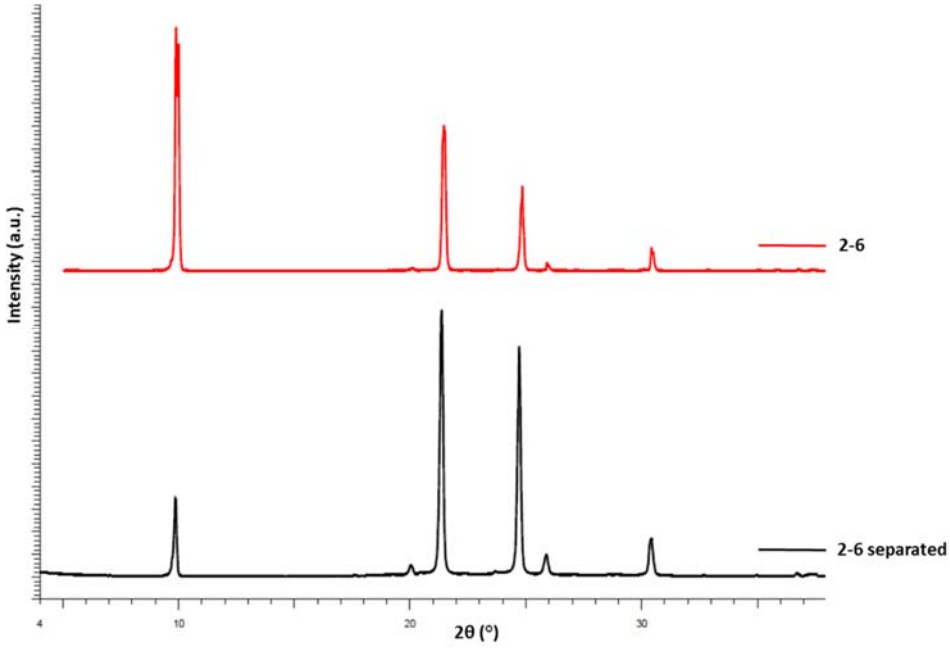

Figure 3.8 Comparison of PXRD patterns of pure suberic acid **2-6** (top, red trace) and suberic acid covered from cocrystal **1-12·2-6** upon treatment with 1,6-diiodoperfluorohexane **4-6** (bottom, black trace).

We have developed a second strategy to recover the dicarboxylic acids **2** from respective size-matching cocrystals **1·2** and once again it is based on the substitution of halogen bonded supramolecular anions for hydrogen bonded supramolecular anions, specifically the outstandingly stable I_3^- species[25] replaces the $I^-\cdots HOOC–(CH_2)_n–COOH\cdots I^-$ supraanions. This methodology gives the advantage of using low cost and environmental friendly materials and is thus more tailed for possible industrial and large scale separations. Specifically, on addition of two equivalents of molecular iodine to the methanol solutions of one equivalent of **1-10·2-4**

or **1-12·2-6**, brownish crystals were obtained after partial evaporation of the solvent and single crystal X-ray analysis of selected crystals confirmed the selective formation of the bis triiodide of **1-10** and **1-12**, respectively (Chap. 7, Fig. 7.2.9). Interestingly, in **1-12·2I_3^-** the two I_3^- match in length the $N^+\cdots N^+$ separation in dication **1-12**. Both starting from **1-10·2-4** and from **1-12·2-6**, when the filtered brown solid had a mass 5% greater than the stoichiometric mass of the respective triiodide salt, adipic and suberic acid were recovered from the supernatant with <99% purity.

3.3. Conclusion

To summarise we have shown that the bis(trimethylammonium)alkane diiodide salts are a simple and very versatile class of organic solids which display a transient dynamic porosity to absorb/exchange and release small molecules in a controllable and selective fashion. The dicationic host **1** readily forms a supramolecular complex with size-matching dicarboxylic acids both in solution or solid state. X-ray structure of pure bis-(trimethylammonium)alkane diiodides and of their cocrystals suggests that once the size-matching dicarboxylic acid forms hydrogen bonds with iodide anions, the $I^-\cdots HOOC–(CH_2/CF_2)_n–COOH\cdots I^-$ trimer functions as a supramolecular template to enact size complementarity between the host and guest modules. The combined use of HB and XB enabled for the selective uptake of the diacid guest and for its quantitative recovery, both processes occurring via self-assembly processes. The size-matching controlled formation of cocrystals allows for selective solubility variation of dicarboxylic acids and provides a new direction for selective recognition and separation.

The gas-solid reactions often entail profound transformations of the chemical and physical nature of the solid materials and rarely are of practical use. In the present case, the full reversibility of the process, whereby dicarboxylic acids can first be selectively complexed out of a mixture and then quantitatively removed by using vapors of DIPFAs, yields pure dicarboxylic acid and a reusable ionic scaffold. Beyond the practical potential for separating mixtures of bis-homologous dicarboxylic acids, the application of this purification method to other classes of compounds can be envisioned.

3.4. References

1. A. Thomas, *Angew. Chem. Int. Ed.*, 2010, **49,** 8328-8344.

2. (a) B. D. Chandler, G. D. Enright, K. A. Udachin, S. Pawsey, J. A. Ripmeester, D. T. Cramb and G. K. H. Shimizu, *Nature materials.*, 2008, **7,** 229-235; (b) I. Tokarev and S. Minko, *Adv. Mater.*, 2010, **22,** 3446-3462.
3. Z. R. Herm, B. M. Wiers, J. A. Mason, J. M. van Baten, M. R. Hudson, P. Zajdel, C. M. Brown, N. Masciocchi, R. Krishna and J. R. Long1, *Science*, 2013, **340,** 960-964.
4. J. A. Mason, M. Veenstrab and J. R. Long, *Chem. Sci.*, 2014, **5,** 32-51; (b) A. J. Graham, D. R. Allan, A. Muszkiewicz, C. A. Morrison and S. A. Moggach, *Angew Chem.*, 2011, **123,** 11338-11341.
5. (a) Z. Zhang, Y. Chen, S. He, J. Zhang, X. Xu, Y. Yang, F. Nosheen, F. Saleem, W. He and X. Wang, *Angew. Chem. Int. Ed.*, 2014, **53,** 12517-12521; (b) L. Meng, Q. Cheng, C. Kim, W.Y. Gao, L. Wojtas, Y.S. Chen, M. J. Zaworotko, X. P. Zhang and S. Ma, *Angew. Chem. Int. Ed.*, 2012, **51,** 10082-10085.
6. B. Chen, Y. Yang, F. Zapata, G. Lin, G. Qian and E. B. Lobkovsky, *Adv. Mater.*, 2007, **19,** 1693-1696.
7. (a) Y. C. Tan and H. C. Zeng, *Chem. Commun.*, 2016, **52,** 11591-11594; (b) B. Volosskiy, K. Niwa, Y. Chen, Z. Zhao, N. O. Weiss, X. Zhong, M. Ding, C. Lee, Y. Huang and X. Duan, *ACS Nano*, 2015, **9,** 3044-3049.
8. (a) A. Trewin and A. I. Cooper, *Angew. Chem. Int. Ed.*, 2010, **49,** 1533-1535; (b) Y. Zhang and S. N. Riduan, *Chem. Soc. Rev.*, 2012, **41,** 2083-2094.
9. (a) A. J. Graham, D. R. Allan, A. Muszkiewicz, C. A. Morrison and S. A. Moggach, *Angew Chem.*, 2011, **123,** 11338-11341; (b) D. J. Wales, J. Grand, V. P. Ting, R. D. Burke, K. J. Edler, C. R. Bowen, S. Mintova and A. D. Burrows, *Chem. Soc. Rev.*, 2015, **44,** 4290-4321.
10. C. Serre, C. M. Draznieks, S. Surble, N. Audebrand, Y.Filinchuk and G. Ferey, *Science*, 2007, **315,** 1828-1831.
11. (a) S. Horike, S. Shimomura and S. Kitagawa, *Nat. Chem.,* 2009, **1,** 695-704; (b) T. K. Maji, R. Matsuda and S. Kitagawa, *Nat. Mater.*, 2007, **6,** 142-148; (c) S. B. Choi, H. Furukawa, H. J. Nam, D. Y. Jung, Y. H. Jhon, A. Walton, D. Book, M. O'Keeffe, O. M. Yaghi and J. Kim, *Angew. Chem.*, 2012, **124,** 8921-8925; (d) N. K. Mal, M. Fujiwara and Y. Tanaka, *Nature,* 2003, **421,** 350-352.
12. P. Metrangolo, Y. Carcenac, M. Lahtinen, T. Pilati, K. Rissanen, A. Vij and G. Resnati, *Science*, 2009, **323,** 1461-1464.
13. (a) G. Cavallo, P. Metrangolo, R. Milani, T. Pilati, A. Priimagi, G. Resnati and G. Terraneo, *Chem. Rev.*, 2016, **116,** 2478-2601; (b) G. R. Desiraju, P. S. Ho, L. Kloo, A. C.

Legon, R. Marquardt, P. Metrangolo, P. Politzer, G. Resnati and K. Rissanen, *Pure Appl. Chem.*, 2013, **85,** 1711-1713.

14. J. M. Rujas, L. Meazza, G. K. Lim, G. Terraneo, T. Pilati, K. D. M. Harris, P. Metrangolo and G. Resnati, *Angew. Chem. Int. Ed.*, 2013, **52,** 13444-13448.
15. S. J. Dalgarno, P. K. Thallapally, L. J. Barbour and J. L. Atwood, *Chem. Soc. Rev.*, 2007, **36,** 236-245.
16. (a) F. Zhang, C. H. Huang and T. W. Xu, *Ind. Eng. Chem. Res.*, 2009, **48,** 7482-7488; (b) C. Liu, F. Liu, J. Cai, W. Xie, T. E. Long, S. R. Turner, A. Lyons and R. A. Gross, *Biomacromolecules,* 2011, **12,** 3291-3298; (c) A. Kçckritz and A. Martin, *Eur. J. Lipid Sci. Technol.*, 2011, **113,** 83-91; (d) S. H. Malca, S. D. Kuhnel, L. V. Venegas, E. A. Seifert, B. M. Nestl and B. Hauer, *Chem. Commun.*, 2012, **48,** 5115-5117.
17. (a) U. Heudorf, V. M. Sundermann and J. Angerer, *Int. J. Hyg. Environ. Health.*, 2007, **210,** 623-634; (b) G. Mingrone, L. C. Gissey and K. Macé, *Br. J. Clin Pharmacol.*, 2012, **75,** 671-676.
18. K. Uzarevic, I. Halasz, I. ilovic, N. Bregovic, M. Rubcic, D. Matkovic-Calogovic, and V. Tomisic, *Angew. Chem. Int. Ed.,* 2013, **52,** 5504-5508.
19. T. Steiner, *Angew. Chem. Int. Ed.*, 2002, **41,** 48-76.
20. M. W. Hosseini and J. M. Lehn, *J. Am. Chem. Soc.*, 1982, **104,** 3525-3527.
21. A. Dey, P. Metrangolo, T. Pilati, G. Resnati, G. Terraneo and I. Wlassics, *Journal of Fluorine Chemistry*, 2009, **130,** 816-823.
22. F. Ulatowski, K. Dąbrowa, T. Bałakier and J. Jurczak, *J. Org. Chem.,* 2016, **81,** 1746-1756.
23. (a) G. Ciancaleoni, R. Bertani, L. Rocchigiani, P. Sgarbossa, C. Zuccaccia and A. Macchioni, *Chem. Eur. J.,* 2015, **21,** 440-447; (b) L. Rocchigiani, G. Ciancaleoni, C. Zuccaccia and A. Macchioni, *J. Am. Chem. Soc.*, 2014, **136,** 112-115.
24. (a) R. N. Carballal, E. F. Megia, C. Jimenez and R. Riguera, *Nat. Prod. Rep*., 2011, **28,** 78-98; (b) A. Kuhn, S. Narayanan, L. Spencer, G. Goward, V. Thangadurai and M. Wilkening, *Phys. Rev. B.*, 2011, **83,** 94302.
25. J. Lin, J. M. Rujas, P. Metrangolo, T. Pilati, S. Radice, G. Resnati and G. Terraneo, *Cryst. Growth Des.,* 2012, **12,** 5757-5762.

Chapter 4

Halogen Bonding in Cryptated Salts

Section 1

Halogen bonded Borromean networks by design: Topology invariance and metric tuning in a library of multi-component systems

4.1.1. Introduction

To control the topological features of self-assembled systems is a key issue in many different fields related to basic sciences[1] and applicative technologies.[2] An example from application oriented studies is to avoid interpenetration and form metal organic frameworks[3] (MOFs) or covalent organic frameworks[4] (COFs) with large voids, both compound classes being promising materials for gas storage[5] and sensing,[6] mixtures separation,[7] and catalysis.[8] An example from basic investigations, is the development of heuristic principles to control the supramolecular connectivity in catenanes,[9] rotaxanes,[10] and knots,[11] the field having contributed strongly, during the last decade or so, to the terrific progresses in the design of recognition and self-assembly processes in solution and in the solid.

The Borromean rings[12] (Fig. 4.1.1 left) constitute a particularly fascinating patterns of topological entanglement[13] where complexity, structural integrity, and aesthetic beauty are present in the final architecture. The distinctive topological feature of Borromean links lies in their intrinsic mode of interpenetration: Three mutually disjoint closed curves form a link, yet no two rings are linked, but if anyone is cut, the other two are free to separate.

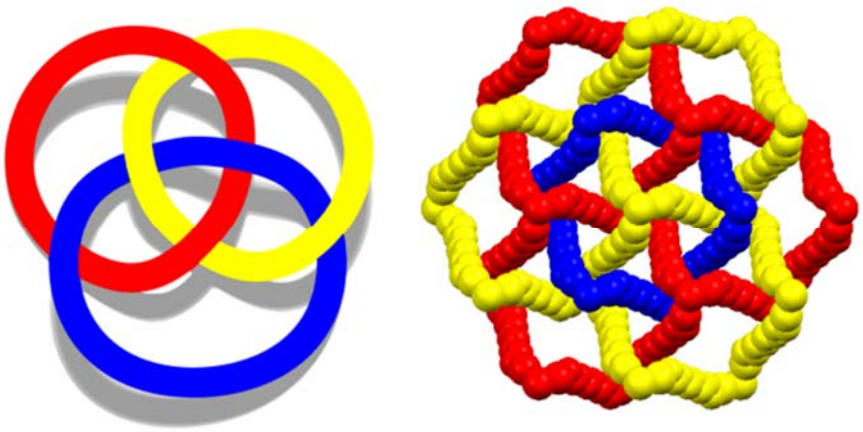

Figure 4.1.1 Left: Schematic view of discrete Borromean ring. Right: Partial view (Mercury 3.8, space-filling) of the three honeycomb nets present in the cocrystal **1·2f·3d.** Red, yellow, and blue colors differentiate the three translationally related nets showing Borromean entanglement. Supercations $K^+ \subset 1$ are omitted for clarity.

This complex interwoven structure has inspired scientists from varied backgrounds[14] and the first formation of discrete molecular Borromean rings was realized in 1997 by the effective manipulation of a DNA sequence.[15] Subsequently, nanoscale Borromean rings were prepared by Stoddart *et al.* through the use, in concert, of metal coordination, supramolecular

and dynamic covalent chemistry.[16] Infinite Borromean networks are frequently[17] based on two-dimensional (6,3) networks with undulating character.[18] It seems that the presence of large empty frames in Borromean networks is an essential requirement to have the entanglement.[19] Coordination chemistry[16d,20] has frequently driven the formation of non-trivial links, Borromean systems included. Also hydrogen bonds,[21] argentophilic[22] and π–π interactions[23] have been used, possibly in combination with coordination chemistry, to facilitate the formation and/or stabilization of the Borromean motif.

Halogen bond (XB)[24] has consolidated its role as a powerful tools in crystal engineering.[25] The available halogen bonded synthons are very diversified and both neutral and ionic motifs have been used to achieve a great variety of supramolecular architectures.[26] Halide anions have been recognized as very good XB acceptors and have been used to form several halogen bonded networks with different topologies.[27] For instance, self-assembly of bromide or chloride anions with carbon tetrabromide affords acentric adamantanoid networks presenting interesting non-linear optical properties[28] and chloride anion effectively templated redox-active ferrocene catenanes in solution and surface-confined environment.[29]

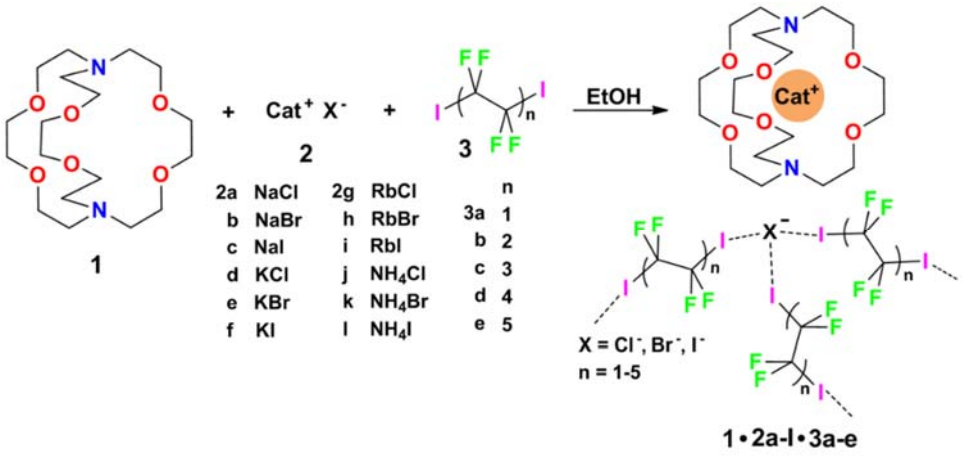

Figure 4.1.2 Starting chemical species **1**, **2a-l**, and **3a-e** and schematic representation of the structural units in corresponding cocrystals **1·2a-l·3a-e**. A pattern of three XBs around the anion is depicted as it is the by far most common arrangement in the library (it is present in twenty eight of the thirty one X-ray structures).

Some years ago we have demonstrated that self-assembly of 4,7,13,16,21,24-hexaoxa-1,10-diazabicyclo[8.8.8]hexacosane (crypt-222, **1**), potassium iodide (**2f**), and α,ω-diiodoperfluoroalkanes (**3a-d**) lead to the cocrystals **1·2f·3a-d** (Fig. 4.1.2).[30] K^+ cations are cryptated by **1** and the electron donor ability of I^- anions is boosted. These anions behave as

tridentate XB acceptors and interact with three different diiodoperfluoroalkyl chains **3a-d** which work as bidentate and telechelic XB donors. (6,3) Nets are formed where I^- anions are sitting at the vertexes of the hexagonal frames and diiodoperfluoralkanes are forming the sides (Fig. 4.1.3). In all four cocrystals these honeycomb nets produce layers which alternate with hydrocarbon layers formed by $K^+\subset$crypt-222 and iodide anions sit at the layers interface. While in **1·2f·3a,b** the fluorous layer contains a single honeycomb net, in **1·2f·3c,d** it contains three (6,3) nets showing Borromean entanglement supported by XB (Fig. 4.1.1, right).

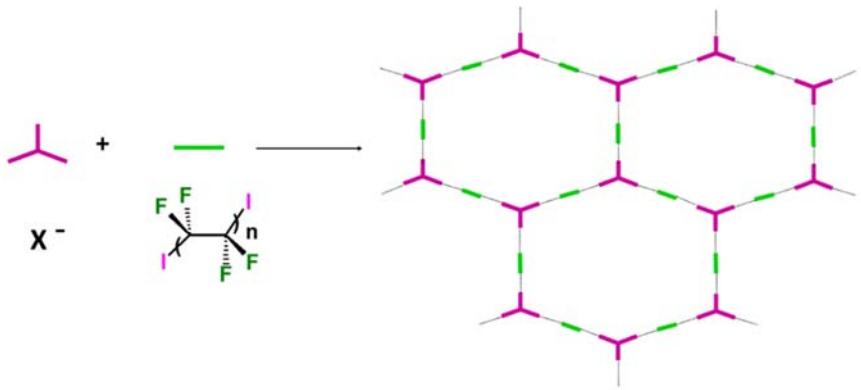

Figure 4.1.3 Schematic representation of the XB driven self-assembly of diiodoperfluoroalkanes **3** with halide anions to form supramolecular anions with (6,3) topology wherein anions are the nodes and diiodoalkanes the sides of the hexagonal frames.

Cocrystals **1·2·3** are obtained on self-assembly of three different chemical species (*i.e.*, cryptand **1**, salts **2**, and diiodoperfluoroalkanes **3**) and four components (*i.e.*, **1**, the cation and anion from salts **2**, and **3**) which can be varied independently. The numerous possibilities to vary the composition of these tetra-component cocrystals offer a unique opportunity to pursue the design and preparation of a library of different cocrystals wherein the halogen bonded supramolecular anions show Borromean entanglement. The challenge to prepare a library of cocrystals with Borromean interpenetration is a case of a quite general problem, *i.e.*, how to change the composition of a multi-component and self-assembled system while maintaining unmodified its topology. It was expected that the change of only some of the dimensional and electronic characteristics in the items of a library of cocrystals **1·2·3** are compatible with the formation of nets showing Borromean entanglement. In other words, we expected that cocrystals "similar" to **1·2f·3c,d** or **1·2f·3a,b** would afford (6,3) nets with or without Borromean interpenetration, respectively. In order to assess the chemical meaning of such similarity, we prepared a library of cocrystals **1·2·3** containing Na^+, or K^+, or Rb^+, or NH_4^+ cations, Cl^-, or

Br^-, or I^- anions, and two-, or four-, or six-, or eight-, or ten-carbon diiodoperfluoroalkanes **3** (Fig. 4.1.2).

Different anions and cations give rise to XBs and electrostatic attraction between opposite ions (the two strongest interactions in cocrystals **1·2·3**) endowed with quite different strength. This was allowing us to assess the relevance of the bonding features in determining the connectivity and the interpenetration in the formed cocrystals. In other words, this was allowing us also to assess if the Borromean interpenetration tolerates non minor differences in the strength of interactions driving the cocrystals self-assembly.

As to the metric of cocrystals **1·2·3**, our working hypothesis was that if the presence of large and void frames in a network is a prerequisite for its Borromean entanglement, diiodoperfluoroalkanes **3** were very promising candidates for obtaining a library of Borromean (6,3) cocrystals **1·2·3**. **3a-e** Are expected to be the anions spacers in supramolecular anionic networks of cocrystals **1·2·3** (Fig.4.1.3) and are also expected to behave as rigid and rod-like moieties,[31] as it is typically the case for perfluoroalkyl derivatives. **3a-e** Are thus assumed to function as the most influential component in determining the metric of the networks. One or more of them were expected to be tailored to reliably afford (6,3) networks sized for Borromean interpenetration independent of the cation and anion nature and a library of Borromean cocrystals **1·2·3** should be accessible.

The structures of obtained multicomponent cocrystals **1·2a-l·3a-e** determined via single crystal X-ray analyses (Chap. 7 table 7.3.1.1-7.3.1.5) were numerous enough to map in the detail the overall architectural landscape as a function of the cocrystal composition and to identify the boundaries of the compositional space compatible with (6,3) net formation and Borromean entanglement (Table 4.1.1). Borromean entanglement is present in twelve of the obtained cocrystals and this topology was formed starting from all four cations, all three anions, and only two of the five diiodoperfluoroalkanes **3** which have been used. This proves that the architectural features responsible for the Borromean entanglement in cocrystals **1·2·3** are robust enough to hold up *some variability in both the XB donor and acceptor modules, namely in both the metric and bonding features of the cocrystals*. Considering the different relative effect that the change of the diiodoperfluoroalkane, the cation, or the anion has on metrics and bondings in cocrystals **1·2·3**, it can be generalized that *bonding, namely energetic, features play a less influential role than metrics in determining the topology of the multi-component systems under study*. These conclusions may hold true for other multi-component systems and they may work as general heuristic principles when pursuing the preparation of multi-component cocrystals having the same topology but different composition.

4.1.2. Results and discussion

4.1.2.1. Preparation of cocrystals 1·2a-l·3a-e.

To correlate reliably the structural differences in **1·2a-l·3a-e** cocrystals with differences in the starting components, our preliminary experiments aimed at optimizing experimental conditions for the preparation of our cocrystals. The aim was to secure that the structure of the obtained systems was largely independent of the experimental conditions. This was enabling us to draw general, robust, and safe conclusions on the composition *vs.* cocrystal topology relationships.

We selected five sets of starting tectons as representative of different possible self-assemblies; the two sets **1**/**2a**/**3a** and **1**/**2b**/**3b** were expected to afford non-Borromean adducts for similarity with already reported cocrystals **1·2f·3a,b**, while the three sets **1**/**2c**/**3d**, **1**/**2h**/**3c**, and **1**/**2j**/**3d** were expected to afford Borromean adducts. We first monitored, with NMR technique, ethanol solutions containing the pure tectons mentioned above in 1:1:1.5 ratio, namely the stoichiometry of a (6,3) network. ^{1}H and ^{19}F spectra of these solutions after some hours at room temperature, confirmed cation cryptation occurred quite rapidly under adopted conditions (Chap. 7, paragraph 7.3.1.3). We then evaporated solutions wherein the **1**:**2**:**3** ratio was 1:1:1.5, 1:1:2, and 1:1:1 in order to assess how dependent the formed cocrystal was on the adopted stoichiometry. These studies have been performed on a set of four systems. DSC and powder X-ray analyses of the cocrystals (isolated at 25% ca. conversion) proved that, within the tested compositional range, the formed cocrystal was not affected by the solution stoichiometry (Chap. 7, section 7.3.1.4 and 7.3.1.5). We finally tried cocrystals formation starting from 1:1.5 molar solutions of cation⊂crypt-222 halides and diiodoperfuoroalkanes. The analytical techniques mentioned above showed that the cocrystals formed after this protocol (at 25% ca. conversion) were the very same as in previous experiments where pure tectons **1**, **2**, and **3** were mixed in 1:1:1.5 ratio.

Slow isothermal evaporation of the solvent from ethanol solutions of pure **1**, **2**, and **3** in 1:1:1.5 ratio was thus chosen as the standard protocol to prepare all the cocrystals. After 3-7 days at room temperature, colorless crystals were formed and IR analyses showed that $\nu_{C\text{-}H}$ stretchings were blue shifted with respect to pure starting **1** (typically at 2810-2970 cm^{-1} rather than at 2710-2940 cm^{-1}), consistent with the presence of cation⊂crypt-222 halides (Chap. 7, section 7.3.1.6). The presence of diiodoperfluoroalkanes in the isolated cocrystals was proven, among others, by the $\nu_{C\text{-}F}$ stretching peaks in the 1085-1200 cm^{-1} region. These peaks were red shifted, compared to pure tectons **3**, suggesting involvement in XB formation.⊂crypt-222 halides (**1·2**). These data indicate that, in all fifty two cases under study, halogen bonded

cocrystals **1·2·3** were formed wherein the α,ω-diiodoperfluoroalkanes **3a-e** are the XB donors and the anion of cryptated salts **1·2a-l** are the acceptors.[33] Melting points were different from starting tectons **1**, **2**, and **3** and from respective cation⊂crypt-222 halides **(1·2)**. These data indicate that, in all fifty two cases under study, halogen bonded cocrystals **1·2·3** were formed wherein the α,ω-diiodoperfluoroalkanes **3a-e** are the XB donors and the anion of cryptated salts **1·2a-l** are the acceptors.

Table 4.1.1. Digits in the table are the number of cocrystals **1·2·3** wherein the supramolecular anion adopts a non-interpenetrated (6,3) topology (green), a Borromean interpenetrated (6,3) topology (red), and other topologies (blue) as a function of cationic (upper five lines) and anionic components (lower five lines) and of α,ω,-diiodoperfluoroalkanes **3** (columns).

Cocrystals component	Non-Interpenetrated (6,3) networks		Borromean interpenetrated (6,3) networks		Other topologies	
	3a; 3b	**3c; 3d**	**3a; 3b**	**3c; 3d**	**3a; 3b**	**3c; 3d**
Na^+	3; 1	2; -	-; -	-; 1	-; 1[a]	1[b]; 1[c]
K^+	1; 1	-; -	-; -	1; 3	-; -	2[b]; 1[d]
Rb^+	-; -	-; 1	-; -	2; 1	-; -	1[b]; -
NH_4^+	1; -	-; -	-; -	1; 3	-; 1[a]	1[b]; -
Total	**10**		**12**		**9**	
Cl^-	1; -	-; -	-; -	-; 2	-; 1[a]	4[b]; -
Br^-	1; 1	1; 1	-; -	1; 2	-; -	1[b]; 1[c]
I^-	3; 1	1; -	-; -	3; 4	-; 1[a]	-; 1[d]
Total	**10**		**12**		**9**	

[a] (4,4) Network. [b] Ribbon of squares. [c] Pearl necklace.
[d] Oligomers formed by 1,10-diiodoperfluorodecane **3e**.

Thirty one out of the fifty two **1·2·3** adducts afforded samples suitable for single crystal X-ray analyses. Five cocrystals, specifically **1·2f·3a-d** and **1·2c·3a** had already been reported[30a, 33] and the remaining twenty six structures are discussed here.

4.1.2.2. Description of selected crystal structures.

4.1.2.2.1. General features. The well-known tendency of crypt-222 to encapsulate the medium sized cations used here accounts for the presence of cation⊂crypt-222 units in all determined structures.

Diiodoperfluoroalkanes, the sides of the supramolecular anionic networks, function as bidentate and telechelic XB donors in all cocrystals but **1·2f·3e** where some diiododecane units work as monodentate XB donors.

Halide anions, the network nodes, function as tetradentate XB acceptors in (4,4) nets (2 cocrystals) and in the discrete units present in **1·2f·3e**. Halide anions work as tridentate XB acceptors in all other systems (namely in those showing the presence of (6,3) networks (twenty two cocrystals), ribbons of juxtaposed squares (five cocrystals), and pearl-necklace arrangements (one cocrystal).

XB and the electrostatic attraction between cations and halide anions are strong interactions in cocrystals **1·2·3** and affect their structure, but also segregation[34] of fluorous and hydrocarbon components is ubiquitous and highly influential in determining the overall crystal packings. Fluoroalkyl chains segregate from cryptated cations in by far the majority of the cocrystals and halide anions typically sit at the interface of segregated domains. For instance, alternating fluorocarbon and hydrocarbon layers are formed by the discrete adducts of **1·2f·3e** (Chap. 7, Fig. 7.3.1.10), the pearl-necklaces of **1·2b·3d** (Chap. 7, Fig. 7.3.1.11), and all (6,3) networks (Chap. 7, Fig. 7.3.1.12).

4.1.2.2.2. Non interpenetrated (6,3) networks. Ten cocrystals adopt this topology which is the second most common in the prepared library (Table 4.1.1). Eight out of these ten systems are formed by **3a** and **3b**, the short chain diiodoperfluoroalkanes. Remarkable similarities exist in all ten structures (Chap. 7, Fig. 7.3.1.13-16) and cocrystals formed by sodium chloride, bromide, and iodide (**2a**, **2b**, and **2c**, respectively) with diiodotetrafluoroethane **3a** will be analyzed here in the details.

Similar to analogous systems,[27] XBs are approximately on the extension of the C-I covalent bond, as expected for strong XBs (C-I···X^- angles span the range 167.81°-179.58°). I···X^-···I Angles are 76.68°, 74.60°, and 72.16° in **1·2a·3a**, **1·2b·3a**, and **1·2c·3a**, respectively, and the resulting pyramidal arrangement around halides determines an egg tray shape in the (6,3) nets. The larger angle associated with the smaller halide allows for framing cavities of relatively constant size on halide change and the importance of this issue will be discussed in details in one of the following paragraphs. Cryptated cations are sitting in these cavities. Fluorous layers in these systems formed by short-chain diiodoperfluorocarbons, always contain a single honeycombs net.

4.1.2.2.3. (6,3) Networks with Borromean interpenetration

This topology is found in twelve cocrystals, namely this is the most frequently occurring topology in the library (Table 4.1.1).

The packings of all these cocrystals are nearly isostructural (Fig. 4.1.4), ten cocrystals being in the *P*-3 space group. Notably, this space group is adopted also by the Borromean cocrystal **1·2j·3d** where a water molecule completes the first coordination sphere[36] of the chloride. A water molecule is present also in the coordination sphere of the bromide cocrystal **1·2h·3c**, and this confirms that the tendency of **3c**,**d** to form Borromean (6,3) networks is quite robust. XB features parallel to those described above for non-interpenetrated (6,3) nets (Chap. 7, Fig. 7.3.1.12-16). For instance, C-I···X$^-$ angles are quite linear and I···X$^-$···I angles decrease when the weight of the halide increases (I···X$^-$···I angles in **1·2j·3d**, **1·2k·3d**, and **1·2l·3d**, are 83.15°, 78.73°, 74.92°, respectively). Moreover, the I···Br$^-$ separation in **1·2k·3d** (326.1 pm which corresponds to a normalized contact[36] *Nc* of 0.83) is longer than the I···Cl$^-$ separation in **1·2j·3d** (310.8 pm, *Nc* = 0.82) but shorter than the I···I$^-$ one in **1·2l·3d** (347.3 pm, *Nc* = 0.84). This scale parallels the relative size of the different anions and is consistent with theoretical studies in the gas phase[37] and some experimental studies[38] in solution showing that, with a given XB donor, Cl$^-$ gives shorter and stronger XB than Br$^-$ which gives shorter and stronger XB than I$^-$.

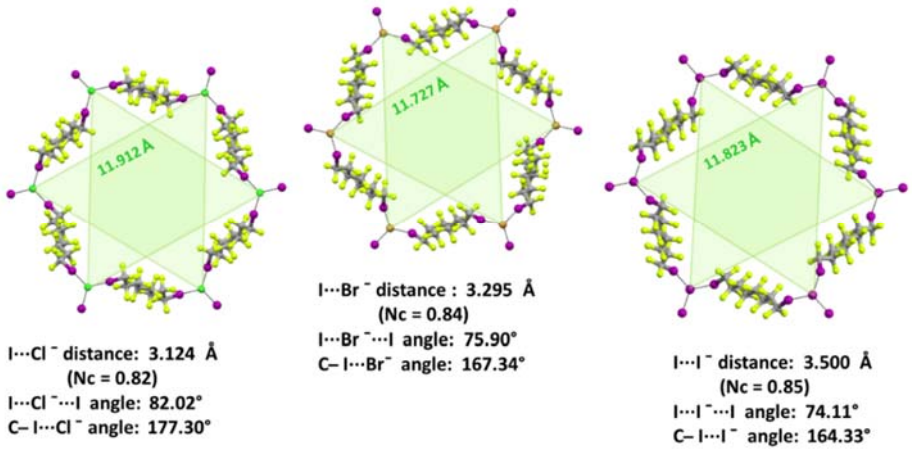

Figure 4.1.4 Ball and stick representation (Mercury 3.8) of one hexagonal frame of the honeycomb net formed by diiodooctane **3d** with potassium chloride **1·2d·3d** (left), bromide **1·2e·3d** (mid), and iodide **1·2f·3d** (right). Semitransparent green triangles connect halide anions which are on the same side of the fluorous layer. Some key structural features are reported. Color codes: Light green, fluorine; green, chlorine; brown, bromine; purple, iodine; grey, carbon.

In Borromean systems a fluorous layer is formed by three translationally related honeycomb nets which entangle in a 2D → 2D fashion (Figs.4.1.5 and 4.1.6). The chair-like shape of hexagonal frames, resulting from the pyramidal geometry at halide nodes and responsible for the egg tray arrangement of single nets, creates conditions for interpenetration. The typical stiffness of perfluoroalkyl chains,[31] forming the sides of the hexagonal rings, helps in maintaining the large polymeric mesh of hexagonal frames which is a prerequisite for entanglement of three honeycomb nets.

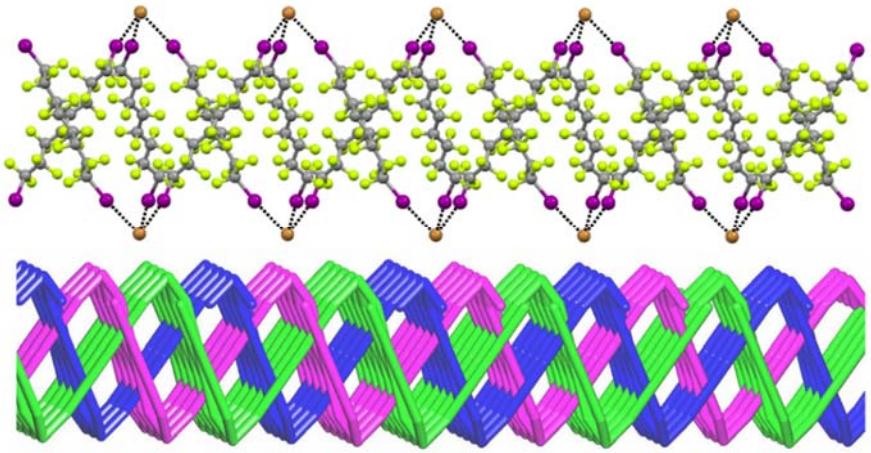

Figure 4.1.5 Top: Partial representation along the crystallographic *a*-axis (Mercury 3.8, ball and stick) of one undulating honeycomb net in **1·2e·3d**. XBs are in black dotted lines. Colour codes as in Fig.4.1.4. Bottom: Schematic view (approximately along the *a* axis) of three entangled (6,3) networks in the same compound; three different colours have been used for the three different nets.

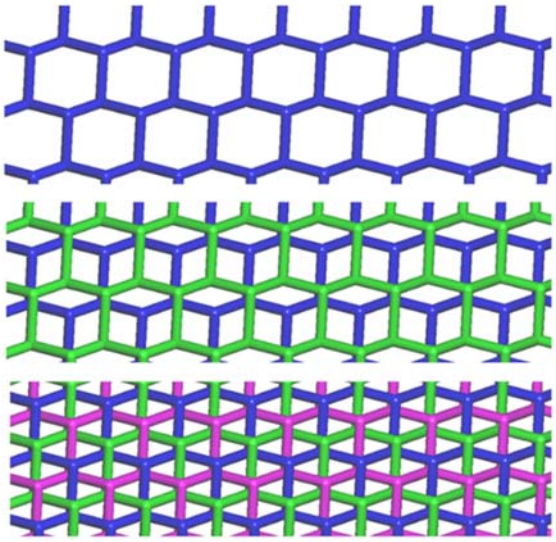

Figure 4.1.6 Superimposition of three honeycomb nets, viewed along the *c* axis, evidencing their Borromean interpenetration in **1·2e·3d**. Top: View of one honeycomb net; mid: A second net (green) is superimposed evidencing that the nets are not interlaced; bottom: The third net (violet) is added and it interlaces the other two as typical for Borromean systems.

The electrostatic attraction between cations and halide anions is a strong interaction in **1·2·3** cocrystals. On cation and anion change the separation of these charged species in the packing undergoes minor changes and the overall crystal packing remains quite constant. The convenient sizing of the cavities of the honeycomb grid is enabled primarily by the size of diiodoperfluoroalkane **3** and is tuned by the flexibility around the node of the hexagonal units. In fact, on X^- change, minor changes are observed in $X^-\cdots X^-$ separations (they are 11.823, 11.727, and 11.912 Å in **1·2f·3d**, **1·2e·3d**, and **1·2d·3d**, respectively), $K^+\cdots K^+$ separations (they are 7.194, 7.163, and 7.202 Å for the same derivatives as above), and $X^-\cdots K^+$ separations (they are 6.939, 6.913, and 7.126 Å for the same cocrystals as above). Differently, I···X^-···I angles show remarkable variability when X^- changes (they are 73.08° in **1·2f·3d**, 75.92° in **1·2e·3d**, and 82.02° in **1·2d·3d**). These geometric features help in rationalizing the topological invariance in the Borromean systems on components change. Chloride anion is the smallest anion of the **1·2d-f·3d** series and consistent with its ability to form strong XBs,[37,38] XBs in the chloride cocrystal **1·2d·3d** are shorter than in other halide cocrystals **1·2e,f·3d**. In **1·2d·3d** the assembly of hexagonal units large enough to enable interpenetration takes place by flattening the hexagonal frame relative to **1·2e,f·3d** namely by widening I···X^-···I angles which, for the chloride, are 82°, the widest angle of the series **1·2d-f·3d**. In other words, the increased separation of perfluoroalkyl chains resulting from widening of the angles at the nodes in **1·2d·3d** counterbalances hexagonal frames contraction resulting from the small chloride size and the short XBs it forms. For the same reasons I···Br^-···I angles are smaller than I···I^-···I angles. The isostructurality in the Borromean networks thus results from a fine balance between synthons size, strength, and flexibility (Fig.4.1.7).

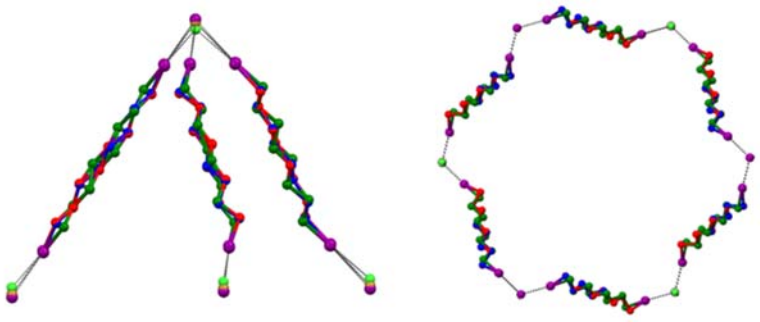

Figure 4.1.7 Left: Superimposition of the trigonal nodes in **1·2d·3d**, **1·2e·3d**, and **1·2f·3d**, evidencing isostructurality. Fluorocarbon chains of modules **3d** are green colored in **1·2d·3d** cocrystal, blue colored in **1·2e·3d**, and red colored in **1·2f·3d**, fluorine atoms are omitted; iodide, bromide, and chloride anions

are purple, brown, and green, respectively. Right: Superimposition of one hexagonal unit of **1·2d·3d**, **1·2e·3d**, and **1·2f·3d**. XB are black dotted lines. Color codes as left.

4.1.2.2.4. Other topologies. The overall architecture of pearl necklace **1·2b·3d** shows some similarities with Borromean architectures, for instance halide anions function as tridentate and pyramidal XB acceptors in both topologies. Indeed, cocrystal **1·2b·3d** can be understood as a frustrated Borromean system (Fig. 4.1.8, Chap. 7, Fig. 7.3.1.17 and 7.3.1.18) as anions positions in **1·2b·3d** are quite similar to Borromean systems. The specific connectivity of the networks nodes in **1·2b·3d** is the result of the very unusual conformation adopted by diiodooctane modules. In fact two *gauche* torsion angles are found along two of the crystallographically independent diiodoperfluorooctyl chains of **1·2b·3d** while perfluoroalkyl chains typically adopt a distorted anti-periplanar and zig-zag arrangement.[31] The reduced length of the perfluoroalkyl chain possibly prevents the connectivity of the nodes enabling for the formation of large frames and Borromean interpenetration.

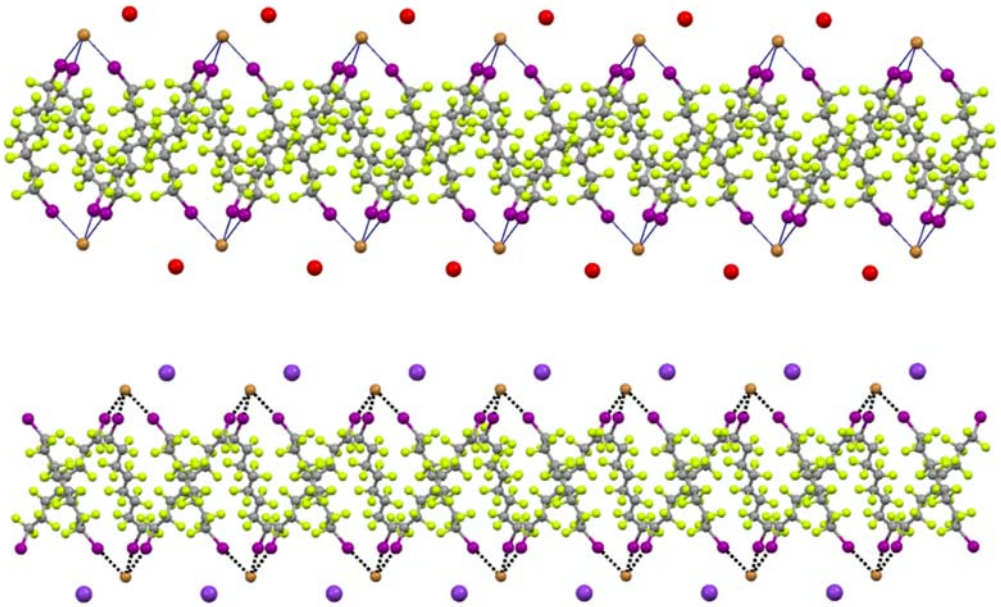

Figure 4.1.8 Representation along the *b* axis (Mercury 3.8, ball and stick) of one fluorous layer and adjacent cations layers formed by diiodoperfluorooctane **3d** with cryptated sodium bromide (**1·2b·3d**, top) or potassium bromide (**1·2e·3d**, bottom). The structural similarity of the pearl necklace (top) and Borromean system (bottom) are apparent. Crypt-222 molecules have been omitted for sake of clarity. Color codes: Grey, carbon; green, fluorine; brown, bromine; purple, iodine; red, sodium; violet, potassium.

In the five cocrystals wherein linear ribbons are present (Fig. 4.1.9), the ratio of starting tectons **1**, **2**, and **3** is 1:1:1.5 and halide anions function as tridentate XB acceptors, once again as in Borromean nets. These ribbons are formed by juxtaposed squares having anions at vertexes, diiodoperfluoroalkanes at sides, and cations hosted in the squares. The topology observed in these structures is related to the nearly planar and T shaped geometry adopted by the anions (Fig. 4.1.9). In all five structures the XB donor is the diiodoperfluorohexane **3c** while the cation can be anyone of the four used in this paper and the anion either a chloride or a bromide This confirms that the combined action of the size of the diiodoperfluoroalkane modules **3** and the flexibility, namely the angles, at the nodes is quite influential for the topology adopted by supramolecular anions.

Finally, in **1·2a·3b**, **1·2l·3b**, and **1·2f·3e** halide anions function as tetradentate XB acceptors. In the first cocystal anions are connected into square and planar (4,4) networks hosting one cryptated cation at the center of the square frame (Chap. 7, Fig. 7.3.1.19). Similar but undulated (4,4) networks are present in **1·2l·3b** while in **1·2f·3e** iodide anions adopt a distorted tetrahedral geometry and assemble well defined supramolecular anions through short I···X XBs. These supraanions further interact each other to give infinite chains via lousy C─I···I─C XBs (Chap. 7, Fig. 7.3.1.20 and 7.3.1.21).

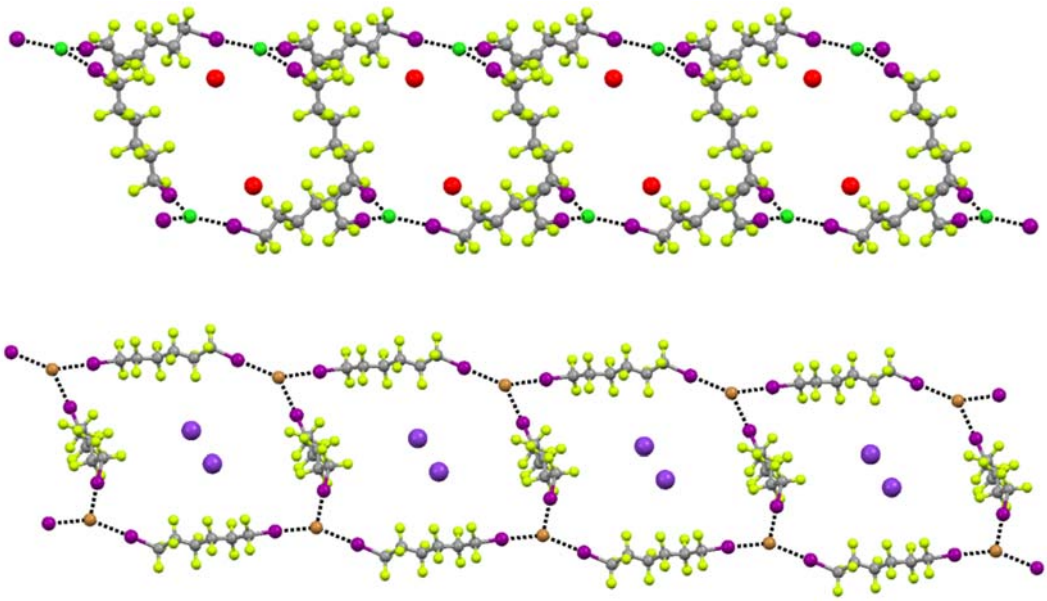

Figure 4.1.9 Representation (Mercury 3.8, ball and stick) of one ribbon of squares formed by diiodoperfluorohexane **3c** and cryptated sodium chloride (**1·2a·3c**, top) and potassium bromide (**1·2e·3c**, bottom). Crypt-222 molecules have been omitted for sake of clarity. Color codes: Grey, carbon; light green, fluorine; green, chlorine; brown, bromine; purple, iodine; red, sodium; violet, potassium.

4.1.2.3. Topology of cocrystals 1·2·3 as a function of starting components.

4.1.2.3.1. Cryptated cation. All the four cations populate the two most common topologies of the supramolecular anions, *i.e.*, the (6,3) networks showing Borromean entanglement and the non-interpenetrated (6,3) networks (Table 4.1.1). This is consistent with the fact that the cation nature, while indirectly affecting the topology of the supramolecular anion in cocrystals **1·2·3** *via* the cation-anion electrostatic attraction, is not the decisive element in determining such topology.[39]

A detailed comparison of the topologies of halogen bonded supramolecular anions in sets of cocrystals containing given cations but different anions and/or diiodoperfluorocarbons, further indicate that the size of the cation influences the metric of the cocrystals but it does not affect it to the point to be the most influential factor for the topology adopted by the halogen bonded supramolecular anion. For instance, Na^+⊂crypt-222, the smallest cryptated cation in the examined series,[39] affords a supramolecular anion with Borromean interpenetration (*i.e.*, **1·2c·3d**) only when the large iodide anion is the XB acceptor and the long diiodoperfluorooctane **3d** is the XB donor. Smaller XB acceptors, namely bromide and chloride anions, and shorter XB donors, *e.g.*, diiodoperfluoroalkanes **3c** or **3b**, form non-interpenetrated (6,3) networks (*e.g.*, **1·2a·3c**, **1·2b·3c**, and **1·2c·3b**) when self-assembling with Na^+⊂crypt-222.

In general, cations are very effective in determining recognition phenomena and the structure of templated systems,[40] but the data described above consistently prove that in our systems, Borromean interpenetration appears only when the formation of hexagonal frames with large enough meshes is secured by the synergistic action of the size of the cation, the anion, and the diiodoperfluoroalkane, the size of the diiodoalkane playing the most influential role.

4.1.2.3.2. Halide anion

In general, different anions can span quite different sizes, shapes, and coordination spheres[41] and they can template correspondingly different self-assembled structures. Sizes of halide anions vary from 119 to 206 pm (from fluoride to iodide anions when having octahedral coordination) but they are all spherical, namely they have no major directional preference in their coordination spheres. Different halides can drive the formation of different structures when involved in electrostatic interactions, metal coordination, and hydrogen bonding,[42] but, more frequently, they behave similarly.[11b,43] The same holds when halogen bonding is the driving force of the self-assembly.[27,44] It is thus not surprising that all the three anions populate the two more common topologies of the supramolecular anion in cocrystals 1·2·3. The overall

Borromean topology being poorly sensitive to the anion change, imply that *the architectural features responsible for the Borromean entanglement are robust enough to hold up some variability in the XB acceptor module.*

A pro-active role of halide anions in the formation of Borromean interpenetrated systems is related to their spherical nature which allows the I···X⁻···I angles to be wider for lighters halides in order to slightly flatten the (6,3) networks and to counterbalance the smaller size of the hexagonal frames formed by lighter halides. For instance, the I···X⁻···I angles are 73.47° for the iodide cocrystal **1·2l·3d**, 78.73° for the bromide **1·2k·3d**, and 83.15 for the chloride **1·2j·3d**. In this way, the egg tray shaped supramolecular anion contains cavities conveniently sized for Borromean entanglement.

In the four cocrystals **1·2a·3c**, **1·2d·3c**, **1·2g·3c**, and **1·2j·3c** wherein chloride anion is pairing with diiodoperfluorohexane **3c**, the supramolecular anions are ribbons of squares (Fig. 4.1.9). In general, no chloride salt forms Borromean systems on self-assembly with diiodohexane **3c**. This might be rationalized by considering that the flexibility described above at the halide nodes of supramolecular anions is not effective enough to afford adequately sized honeycomb frames on self-assembly of chloride anions, *i.e.*, the smallest used halide, with diiodohexane **3c**, *i.e.*, the shortest diiodoalkane able to give Borromean (6,3) nets. In contrast, flexibility can afford adequately sized honeycomb frames on self-assembly of chloride anions with the longer diiodoperfluorooctane **3d** (as it is the case in **1·2d·3d** and **1·2j·3d).**[45]

4.1.2.3.3. Diiodoperfluoroalkane

The structure of the supramolecular anion in cocrystals **1·2·3** is decidedly dependent on the used diiodoperfluoroalkane. As reported in Table 4.1.1, the different XB donors **3** populate in a different way the three topological groupings. For instance, all the five cocrystals formed by diiodoethane **3a** show non-interpenetrated (6,3) networks while diiodooctane **3d** gives rise to one non-interpenetrated (6,3) network, one (4,4) network, one ribbon of squares, and eight Borromean systems. Diiodoperfluoroalkanes **3a-e** are quite similar in relation to their supramolecular bonding features (*i.e.*, the XBs they are involved in) and they differentiate each other for their respective size. As perfluoroalkyl chains are stiff moieties which typically adopt a distorted anti-periplanar and zig-zag arrangement,[31] the five XB donors **3** are rod-like molecules in nearly all cocrystals **1·2·3** and the structural difference between two bis-homologues **3** translates into a change in the separation between the terminal iodine atoms of 22-24 pm ca.[31a,b] *This change seems particularly influential in determining the topology adopted by the supramolecular anion.*

The presence of large cavities in a network is a prerequisite for Borromean entanglements. The size of the diiodoperfluorocarbon, which is the side of the network meshes, is the most important parameter in determining the meshes metric. The diiodobutane **3b** and the diiododecane **3e** are the outer borders of the metric window enabling Borromean interpenetration. In other words, the former compound is too short and the latter one is too long for forming (6.3) networks enabling Borromean interpenetration. Eight of the twelve systems showing this entanglement are formed by diiodoperfluorooctane **3d**, namely its length seems better tailored to Borromean entanglement than diiodohexane **3c**.

While the presence of fluorine atoms in tectons **3** does not contribute directly to the formation of Borromean systems, *e.g.*, by forming specific attractive interactions or by determining the size of the cavities in the supramolecular anions, fluorine gives major indirect contributions to such a formation. First, the presence of fluorine enables compounds **3** to dependably function as rigid and rod-like tectons and thus to determine unvaryingly the spacing metric of halide anions. Second, it boosts the XB donor ability of iodine atoms and allows them to reliably drive the formation of supramolecular and halogen bonded anions. Strong and regularly linear XBs are formed. This interaction directionality translates the tectons geometry into self-assembled architectures geometry, namely halide anions are typically pinned on the elongation of the diiodoperfluoroalkanes molecular axis. Third, the presence of fluorine atoms favors the formation of layers containing more than one supramolecular anionic network, a prerequisite for interpenetration. This is due to the fact that perfluoroalkyl derivatives have a strong tendency to segregate, and this tendency increases with the length of the fluoroalkyl chain.[46] Interpenetration of the supramolecular anionic networks of a given layer is a way to increase segregation of their fluorous component while fulfilling the space filling requirements. Interestingly, thirteen cocrystals **1·2·3** contain interpenetrated supramolecular anions, one of them is formed by diiodobutane **3b**, four by diiodohexane **3c**, and eight by diiodooctane **3d**. The relative frequency of interpenetration clearly parallels the relative tendency of diiodoperfluoroalkanes **3** to segregate[47] and the indirect relevance of fluorine to Borromean interpenetration is confirmed.

4.1.3. Conclusions

Very few reports describe Borromean systems obtained by design[16] as most cases of this entanglement have been identified via topological analyses of structures in the Cambridge

Structural Database.[19] This highlights the great challenge related to the design and obtainment of this topology.

Molecular interpenetration and entanglement are common phenomena in natural and human-made systems, spanning DNA and self-assembled coordination polymers.[1,2,9-11] While the engineering of the benefits of these structural features in a system is still beyond the routine approach, the design and control of these features are particularly hot and timely in several fields of chemistry. We have reported here the XB driven self-assembly of a small library of nearly isostructural cocrystals containing supramolecular anionic networks endowed with Borromean interpenetration. XB has been confirmed as a reliable tool in the rational construction of entangled supramolecular assemblies with sophisticated topologies.[48] The reported results contribute to the field of anion-templated assembly of interpenetrated and interlocked structures, a field that has strongly contributed to some recent progresses of supramolecular chemistry.[29,44,49]

Borromean networks have been obtained starting from all the four used cations, all the three used anions, but only the diiodoperfluorohexane **3c** and -octane **3d**. These results confirm the working hypotheses that some of the α,ω-diiodoperfluoroalkanes would regularly afford (6,3) networks with frames sized to enable for Borromean interpenetration and that this can occur independent from the used cation and anion.

Two key structural features of diiodoperfluoroalkanes **3** for the obtainment of the Borromean systems are: a) the rigid and rod-like character of diiodoperfluoroalkyl derivatives **3**, this character enabling **3c**,**d** to space halide anions after a dependable and useful metric; b) the tendency of perfluoroalkyl motifs to segregate from hydrocarbon motifs, this tendency favoring the formation of fluorous layers containing more than one anionic network and the Borromean entanglement of these networks. A third structural feature which also contributes to the library preparation is the spherical character of halide anions, which helps in adjusting the geometry of XBs around the halides, namely in tuning the degree of pyramidalization at the nodes of the networks in order to form honeycomb frames with the convenient size.

In conclusion, the change of cations and anions in cocrystals **1·2·3** substantially affects the bonding features, namely the energetic aspects, in the self-assembled systems while it causes minor modifications of their metrics. On the other hand, the change of the diidoperfluoroalkane is the most influential element for the metric of cocrystals **1·2·3** and has a minor effect on cation-anion attraction and on XB, the two strong interactions in the cocrystals. Borromean interpenetration has been observed starting from all four cations, all three anions and only two of the five diiodoperfluoroalkanes. It thus seems that the metric features plays a

more influential role than energetic features in determining the topology of the tetra-component cocrystals described here. The applicability of this heuristic principle in the design and synthesis of other multi-component systems might be general and the usefulness of this principle in the self-assembly of crypt-111 (*i.e.*, 4,10,15-trioxa-1,7-diazabicyclo[5.5.5]heptadecane), halide derivatives, and diiodoperfluoroalkanes is under assessment.

4.1.4. References

1. (a) Y. Inokuma, T. Ukegawa, M. Hoshino and M. Fujita, *Chem. Sci.*, 2016, **7**, 3910–3913; (b) M. Frank, M. D. Johnstone and G. H. Clever, *Chem. Eur. J.*, 2016, **22,** 1-23; (c) H. S. Scott, N. Ogiwara, K. J. Chen, D. G. Madden, T. Pham, K. Forrest, B. Space, S. Horike, J. J. Perry IV, S. Kitagawa and M. J. Zaworotko, *Chem. Sci.*, 2016, **7,** 5470-5476; (d) J. F. Ayme, J. E. Beves, C. J. Campbell and D. A. Leigh, *Angew. Chem. Int. Ed.,* 2014, **53,** 7823-7827; (e) S. Zhanga, H.-J. Suna, A. D. Hughesa, R.-O. Moussodiaa, A. Bertina, Y. Chenc, D. J. Pochanc, P. A. Heineyb, M. L. Kleind and V. Percec, *Proc. Nat. Acad. Sci.*, 2014, **111**, 9058–9063; (f) M. W. Hosseini, *Acc. Chem. Res.*, 2005, **38,** 313-323.
2. (a) R. Tang, S. Zhou, Z. Cheng, G. Yu, Q. Peng, H. Zeng, G. Guo, Q. Li and Z. Li, *Chem. Sci.*, 2016, DOI: 10.1039/c6sc02956f; (b) H. J. Sun, S. Zhang and V. Percec, *Chem. Soc. Rev.*, 2015, **44,** 3900-3923; (c) S. Y. Zhang, W. Shi, P. Cheng and M. J. Zaworotko, *J. Am. Chem. Soc.,* 2015, **137,** 12203-12206; (d) Y. Horibe, J. Yang, Y. H. Cho, X. Luo, S. B. Kim, Y. S. Oh, F. T. Huang, T. Asada, M. Tanimura, D. Jeong and S. W. Cheong, *J. Am. Chem. Soc.*, 2014, **136,** 8368-8373; (e) S. Honda, T. Yamamoto and Y. Tezuka, *J. Am. Chem. Soc.*, 2010, **132,** 10251-10253; (f) E. R. Kay, D. A. Leigh and Francesco Zerbetto, *Angew. Chem. Int. Ed.*, 2007, **46,** 72-191.
3. (a) Y. C. Tan and H. C. Zeng, *Chem. Commun.*, 2016, DOI: 10.1039/c6cc05699g; (b) B. Volosskiy, K. Niwa, Y. Chen, Z. Zhao, N. O. Weiss, X. Zhong, M. Ding, C. Lee, Y. Huang and X. Duan, *ACS Nano*, 2015, **9,** 3044-3049; (c) K. M. Choi, H. M. Jeong, J. H. Park, Y.-B. Zhang, J. K. Kang and O. M. Yaghi, *ACS Nano*, 2014, **8,** 7451-7457; (d) N. Stock and S. Biswas, *Chem. Rev.*, 2012, **112,** 933-969; (e) D. Zhao, D. J. Timmons, D. Yuan and H.-Cai. Zhou, *Acc. Chem. Res.*, 2011, **44,** 123-133; (f) O. K. Farha and J. T. Hupp, *Acc. Chem. Res.*, 2010, **43,** 1166-1175.
4. (a) S. Dalapati, E. Jin, M. Addicoat, T. Heine and D. Jiang, *J. Am. Chem. Soc.*, 2016, **138,** 5797-5800; (b) P. J. Waller, F. Gándara and O. M. Yaghi, *Acc. Chem. Res.*, 2015, **48,** 3053-3063.

5. (a) D. Alezi, Y. Belmabkhout, M. Suyetin, P. M. Bhatt, Ł. J. Weseliński, V. Solovyeva, K. Adil, I. Spanopoulos, P. N. Trikalitis, A.-H. Emwas and M. Eddaoudi, *J. Am. Chem. Soc.*, 2015, **137,** 13308-13318. (b) A. J. Graham, D. R. Allan, A. Muszkiewicz, C. A. Morrison and S. A. Moggach, *Angew Chem.*, 2011, **123,** 11338-11341.
6. (a) D. J. Wales, J. Grand, V. P. Ting, R. D. Burke, K. J. Edler, C. R. Bowen, S. Mintova and A. D. Burrows, *Chem. Soc. Rev.*, 2015, **44,** 4290-4321; (b) J.-S. Qin, D.-Y. Du, W.-L. Li, J.-P. Zhang, S.-L. Li, Z.-M. Su, X.-L. Wang, Q. Xu, K.-Z. Shao and Y.-Q. Lan, *Chem. Sci.*, 2012, **3,** 2114-2118.
7. (a) K. Raatikainen and K. Rissanen, *Chem. Sci.*, 2012, **3**, 1235-1239; (b) R. Matsuda, T. Tsujino, H. Sato, Y. Kubota, K. Morishige, M.Takata and S. Kitagawa, *Chem. Sci.*, 2010, **1,** 315-321.
8. (a) Z. Zhang, Y. Chen, S. He, J. Zhang, X. Xu, Y. Yang, F. Nosheen, F. Saleem, W. He and X. Wang, *Angew. Chem. Int. Ed.*, 2014, **53,** 12517-12521; (b) L. Meng, Q. Cheng, C. Kim, W.-Y. Gao, L. Wojtas, Y.-S. Chen, M. J. Zaworotko, X. P. Zhang and S. Ma, *Angew. Chem. Int. Ed.*, 2012, **51,** 10082-10085.
9. (a) T. Sawada, M. Yamagami, K. Ohara, K. Yamaguchi and M. Fujita, *Angew. Chem. Int. Ed.*, 2016, **55**, 4519–4522; (b) K. J. Hartlieb, A. K. Blackburn, S. T. Schneebeli, R. S. Forgan, A. A. Sarjeant, C. L. Stern, D. Cao and J. F. Stoddart, *Chem. Sci.*, 2014, **5,** 90-100; (c) N. H. Evans and P. D. Beer, *Chem. Soc. Rev.*, 2014, **43,** 4658-4683; (d) R. Hovorka, G. Meyer-Eppler, T. Piehler, S. Hytteballe, M. Engeser, F. Topic, K. Rissanen and A. Lützen, *Chem. Eur. J.*, 2014, **20**, 13253-13258.
10. (a) A. Vidonne, T. Kosikova and D. Philp, *Chem. Sci.*, 2016, **7**, 2592–2603; (b) J. D. Crowley, S. M. Goldup; A.-L. Lee; D. A. Leigh and R. T. McBurney, *Chem. Soc. Rev.*, 2009, **38**, 1539-1541; (c) J. P. Sauvage and C. D. Buchecker, *Molecular Catenanes, Rotaxanes and Knots: A Journey Through the World of Molecular Topology* Wiley-VCH, Weinheim, 1999.
11. (a) K. E. Horner, M. A. Miller, J. W. Steed and P. M. Sutcliffe, *Chem. Soc. Rev.*, 2016, DOI: 10.1039/c6cs00448b; (b) V. Marcos, A. J. Stephens, J. Jararnillo-Garcia, A. L. Nussbaumer, S. L. Woltering, A. Valero, J.-F. Lemonnier, I. J. V. Yrezabal, D. A. Leigh, *Science*, 2016, **352**, 1555-1559; (c) J. F. Ayme, J. E. Beves, C. J. Campbell and D. A. Leigh, *Chem. Soc. Rev.*, 2013, **42**, 1700-1712.
12. (a) C. D. Pentecost, N. Tangchaivang, S. J. Cantrill, K. S. Chichak, A. J. Peters and J. Fraser Stoddart, *J. Chem. Ed.*, 2007, **84**, 855-859; (b) C. A. Schalley, *Angew. Chem. Int. Ed.*, 2004, **43,** 4399-4401.

13. R. S. Forgan, J. P. Sauvage and J. F. Stoddart, *Chem. Rev.*, 2011, **111,** 5434-5464.
14. G. Natarajan, A.Mathew, Y. Negishi, R. L. Whetten and T. Pradeep, *J. Phys. Chem. C*, 2015, **119**, 27768−27785.
15. (a) C. Mao, W. Sun and N. C. Seeman, *Nature*, 1997, **386**, 137-138; (b) N. C. Seeman, *Acc. Chem. Res.*, 1997, **30,** 357-363.
16. (a) C. R. Yates, D. Benitez, S. I. Khan and J. F. Stoddart, *Org. Lett.*, 2007, **9**, 2433-2436; (b) A. J. Peters, K. S. Chichak, S. J. Cantrill and J. F. Stoddart, *Chem. Commun.*, 2005, **27**, 3394–3396; (c) K. S. Chichak, A. J. Peters, S. J. Cantrill and J. Fraser Stoddart, *J. Org. Chem.*, 2005, **70,** 7956-7962; (d) S. J. Cantrill, K. S. Chichak, A. J. Peters and J. F. Stoddart, *Acc. Chem. Res.*, 2005, **38,** 1-9; (e) K. S. Chichak, S. J. Cantrill, A. R. Pease, S. H. Chiu, G. W. V. Cave, J. L. Atwood and J. F. Stoddart, *Science*, 2004, **304,** 1308-1312.
17. Q. X. Yao, X. H Jin, Z. F. Ju, H. X. Zhang and J. Zhang, *CrystEngComm.*, 2009, **11,** 1502-1504.
18. (a) X. L. Zhang, C. P. Guo, Q. Y. Yang, W. Wang, W. S. Liu, B. S. Kang and C. Y. Su, *Chem. Commun.,* 2007, **41**, 4242-4244; (b) X. Q. Lu, M. Pan, J. R. He, Y. P. Cai, B. S. Kang and C. Y. Su, *CrystEngComm.*, 2006, **8,** 827-829.
19. (a) L. Carlucci, G. Ciani, D. M. Proserpio, T. G. Mitina and V. A. Blatov, *Chem. Rev.*, 2014, **114,** 7557-7580; (b) L. Carlucci, G. Ciani and D. M. Proserpio, *Coord. Chem. Rev.*, 2003, **246,** 247-289.
20. M. Pan and C. Y. Su, *CrystEngComm.*, 2014, **16,** 7847-7859.
21. (a) N. N. Adarsh and P. Dastidar, *Cryst. Growth Des.*, 2010, **10,** 483-487; (b) Y. B. Men, J. Sun, Z. T. Huang and Q. Y. Zheng, *Angew. Chem. Int. Ed.*, 2009, **48,** 2873-2876.
22. L. Dobrzanska, H. G. Raubenheimer and L. J. Barbour, *Chem. Commun.*, 2005, 5050-5052.
23. M. P. Suh, H. J. Choi, S. M. So and B. M. Kim, *Inorg. Chem.*, 2003, **42,** 676-678.
24. (a) G. Cavallo, P. Metrangolo, R. Milani, T. Pilati, A. Priimagi, G. Resnati and G. Terraneo, *Chem. Rev.*, 2016, **116,** 2478-2601; (b) G. Berger, J. Soubhye, F. Meyer, *Polym. Chem.,* 2015, **6**, 3559-3580C; (c) C. Robertson, R. N. Perutz, L. Brammer and C. A. Hunter, *Chem. Sci.*, 2014, **5**, 4179-4183; (d) G. R. Desiraju, P. S. Ho, L. Kloo, A. C. Legon, R. Marquardt, P. Metrangolo, P. Politzer, G. Resnati and K. Rissanen, *Pure Appl. Chem.*, 2013, **85,** 1711-1713.
25. (a) C. B. Aakeröy, T. K. Wijethunga, J. Benton and J. Desper, *Chem. Commun.*, 2015, **51**, 2425-2428; (b) P. Metrangolo·G. Resnati, T. Pilati and·S. Biella in *Halogen Bonding.*

Fundamentals and Applications; P. Metrangolo, and G.Resnati Eds.; Springer-Verlag: Berlin, Heidelberg, 2008; Vol. 126, pp 105−136.

26. (a) C. C. Robertson, R. N. Perutz, L. Brammer and C. A. Hunter, Chem. Sci, 2014, 5, 4179-4183; (b) Metrangolo, F. Meyer, T. Pilati, G. Resnati and G. Terraneo, *Angew. Chem. Int. Ed.*, 2008, **47,** 6114-6127. (c) P. Metrangolo and G. Resnati, *Chem. Eur. J.*, 2001, **7,** 2511-2519.
27. (a) J. Marti-Rujas, L. Meazza, G. K. Lim, G. Terraneo, T. Pilati, K. D. M. Harris, P. Metrangolo and G. Resnati**,** *Angew. Chem. Int. Ed.*, 2013, **52**, 13444-3448; (b) C. B. Aakeröy, M. Baldrighi, J. Desper, P. Metrangolo and G. Resnati, *Chem. Eur. J.*, 2013, **19**, 16240 – 16247; (c) P. Metrangolo, T. Pilati, G. Terraneo, S. Biella and G. Resnati, *CrystEngComm.*, 2009, **11,** 1187-1196.
28. S. V. Lindeman, J. Hecht and J. K. Kochi, *J. Am. Chem. Soc.*, 2003, **125,** 11597-11606.
29. N. H. Evans, H. Rahman, A. V. Leontiev, N. D. Greenham, G. A. Orlowski, Q. Zeng, R. M. J. Jacobs, C. J. Serpell, N. L. Kilah, J. J. Davis and P. D. Beer, *Chem. Sci.*, 2012, **3,** 1080-1089.
30. (a) R. Liantonio, P. Metrangolo, F. Meyer, T. Pilati, W. Navarrini and G. Resnati, *Chem. Commun.*, 2006, 1819-1821; (b) R. Liantonio, P. Metrangolo, T. Pilati and G. Resnati, *Cryst. Growth Des.*, 2003, **3,** 355-361.
31. (a) P. Metrangolo, T. Pilati, G. Resnati and A. Stevenazzi, *Chem. Commun.*, 2004, 1492-1493; (b) G. Gattuso, A. Pappalardo, M. F. Parisi, I. Pisagatti, F. Crea, R. Liantonio, P. Metrangolo, W. Navarrini, G. Resnati, T. Pilati and S. Pappalardo, *Tetrahedron*, 2007, **63,** 4951-4958.
32. (a) P. Cardillo, E. Corradi, A. Lunghi, S. V. Meille, M. T. Messina, P. Metrangolo and G. Resnati, *Tetrahedron*, 2000, **56,** 5535-5550; (b) M. T. Messina, P. Metrangolo, W. Navarrini, S. Radice, G. Resnati and G. Zerbic, *J. Mol. Structure*, 2000, **524,** 87-94.
33. G. Cavallo, P. Metrangolo, T. Pilati, G. Resnati, M. Ursini and G. Terraneo, *Acta Cryst. E*, 2013*,* **68,** 387-388.
34. (a) Y.-C. Wu, P. Leowanawat, H.-J. Sun, B. E. Partridge, M. Peterca, R. Graf, H. W. Spiess, X. Zeng, G. Ungar, C.-S. Hsu, P. A. Heiney and Virgil Percec, *J. Am. Chem. Soc.*, 2015, **137**, 807−819; (b) H. Takezawa, T. Murase, G. Resnati, P. Metrangolo and M. Fujita, *J. Am. Chem. Soc.*, 2014, **136**, 1786-1788.
35. K. B. James, *Acc. Chem. Res.*, 2005, **38,** 671-678.
36. The normalized contact *Nc* is defined as the ratio $D_{xy}/(rX+rY)$, where D_{xy} is the experimental distance between the halogen bonded iodine atoms X and halide anions Y

and rX and rY are the van der Waals radius for iodine and the Pauling ionic radius of the halide anion Y, respectively. *Nc* is a useful indicator of the relative interaction strength, more useful than the XB distance itself, because it allows distances between different interacting sites to be compared.

37. R. D. Walsh, J. M. Smith, T. W. Hanks and W. T. Pennington, *Cryst. Growth Des.*, 2012, **12,** 2759-2768.
38. (a) R. Tepper, B. Schulze, M. Jäger, C. Friebe, D. H. Scharf, H. Görls and U. S. Schubert, *J. Org. Chem.*, 2015, **80,** 3139-3150; (b) M. Cametti, K. Raatikainen, P. Metrangolo, T. Pilati, G. Terraneo and G. Resnati, *Org. Biomol. Chem.*, 2012, **10**, 1329-1333;(c) M. G. Sarwar, B. Dragisic, S. Sagoo and M. S. Taylor, *Angew. Chem., Int. Ed.*, 2010, **49,** 1674-1677.
39. It is interesting to observe that smaller cations seem more prone than larger cations to afford samples of cocrystals **1·2·3** suitable for single crystal X-ray analyses. The mean volumes of Na^+⊂crypt-222, K^+⊂crypt-222, Rb^+⊂crypt-222, and NH_4^+⊂crypt-222 in **1·2·3** cocrystals (measured via the volumes of polyhedra defined by the eight heteroatoms of crypt-222 **1** in cocrystals **1·2·3**) are 24.404, 28.547, 32,494, and 34.469 Å3, respectively. A correlation clearly exists between the volume of the supramolecular cation cat^+⊂crypt-222 and the volume of the non-cryptated cation afforded by salts **2**. When using **3a-d**, the same set of cocrystals was tried for all cations, but sodium, potassium, ammonium, and rubidium afforded ten, seven, seven, and five single crystalline adducts, respectively.
40. *Supramolecular Chemistry*, J. W. Steed and J. L. Atwood Eds., Second Edition; Wiley, Chichester, 2009; chap. 3, pp. 105-222.
41. (a) P. A. Gale and T. Gunnlaugsson, *Chem. Soc. Rev.,* 2010, **39**, 3595-3596; (b) *Anion Receptor Chemistry*, J. L. Sessler, P. A. Gale and W. S. Cho Eds.; *Royal Society of Chemistry:* Cambridge, UK., 2006; (c) Special Issue: Anion Coordination Chemistry II, P. A. Gale Ed., *Coord. Chem. Rev.*, 2006, **250,** 2917-3244.
42. (a) N. G. White and M. J. MacLachlan, *Chem. Sci.*, 2015, **6,** 6245-6249; (b) B. Hasenknopf, J. M. Lehn, B.O. Kneisel, G. Baum and D. Fenske, *Angew. Chem. Int. Ed.*, 1996, **35,** 1838-1840.
43. (a) T. U. Connell, S. Sandanayake, G. N. Khairallah, J. M.White, R. A. J. O'Hair, P. S. Donnelly and S. J. Williams, *Dalton Trans.*, 2013, **42,** 4903-4907; (b) M.-O. M. Piepenbrock, G. O. Lloyd, N. Clarke and J. W. Steed, *Chem. Rev.,* 2010**, 110***,* 1960-2004; (c) P. Diaz, D. Michael, P. Mingos, R. Vilar, A. J. P. White and D. J. Williams, *Inorg.*

Chem., 2004, **43,** 7597-7604; (d) D. Rais, J. Yau, D. Michael, P. Mingos, R. Vilar, A. J. P. White and D. J. Williams, *Angew. Chem. Int. Ed.*, 2001, **40,** 3464-3467.

44. For selective halide anions templated synthesis of catenane and rotaxanes under XB control see: (a) J. M. Mercurio, R. C. Knighton, J. Cookson, and P. D. Beer, *Chem. Eur. J.*, 2014, **20**, 11740-11749; (b) M. J. Langton, S. W. Robinson, I. Marques, V. Félix and P. D. Beer, *Nature Chem.*, 2014, **6,** 1039-1043; (c) A. Caballero, F. Zapata, N. G. White, P. J. Costa, V. Fèlix, and P. D. Beer, *Angew. Chem. Int. Ed.*, 2012, **51,** 1876-1880.
45. It is also interesting to observe that the heavier, namely more polarizable, the halide anion is, the more likely the obtainment of Borromean interpenetration becomes. Eight, nine, and fourteen single cocrystals **1·2·3** were obtained starting from chloride, bromide, and iodide anions, respectively, and one fourth, one third, and a half of these cocrystals present Borromean interpenetration, respectively.
46. (a) V. Ojogun, B. L. Knutson, S. Vyas and H. J. Lehmler, *J. Fluorine Chemistry*, 2010, **131,** 784-790; (b) E. D. Wolf, P. Ruelle, J. V. D Broeke, B. J. Deelman and G. van Koten, *J. Phys. Chem. B*, 2004, **108,** 1458-1466; (c) L. E. Kiss, I. Kövesdi, J. Rábai, *J. Fluorine Chemistry*, 2001, **108,** 95-109.
47. Four, eleven, and eleven cocrystal **1·2·3** have been formed by **3b**, **3c**, and **3d**, respectively. The probability to form interpenetrated anionic networks is thus 25% for **3b**, 36% for **3c**, and 73% for **3d**.
48. (a) M. C. Pfrunder, A. S. Micallef, L. Rintoul, D. P. Arnold, K. J. P. Davy and J. McMurtrie, *Cryst. Growth Des.*, 2012, **12**, 714-724; (b) P. Metrangolo, F. Meyer, T. Pilati, D. M. Proserpio and G. Resnati, *Chem. Eur. J.*, 2007, **13**, 5765-5772.
49. P. D. Beer, M. R. Sambrook and D. Curiel, *Chem. Commun.*, 2006, 2105-2117.

Section 2

Assessing hydrogen bond in $H^+ \subset$crypt-111 iodide via halogen bonded adducts formation

4.2.1. Introduction

Supramolecular chemistry, broadly the chemistry of multicomponent molecular assemblies in which the component structural units are typically held together by a variety of weak intermolecular interactions, has rapidly developed in the last decades. The concepts developed in supramolecular chemistry are increasingly used in several fields like catalysis,[1] material science,[2] surface science,[3] nanotechnology and biology.[4] In many cases supramolecular chemistry involves the design and investigation of preorganized molecular receptors that are capable of binding specific substrates with high selectivity and efficiency. Some years ago Pedersen,[5] Lehn,[6] Cram[7] and others detailed the synthesis of macrocyclic molecules specially crown ethers, cryptands, cavitands *etc*., that are able to selectively bind ions or small organic molecules via non-covalent or coordination interactions.

The crypt-111 (4,10,15-trioxa-1,7-diazabicyclo[5.5.5]hepta-decane) is a well-known bicyclic system synthesized by J. Cheney and J. M. Lehn which has attracted considerable interest due to its low nucleophilicity, high proton affinity in a selective, slow and irreversible way.[8] Recently G. Alibrandi *et.al* demonstrated the use of crypt-111 as a "molecular automatic titrator" for the determination of thermodynamic parameters.[9] Pursuant to theoretical studies, crypt-111 works as a proton sponge and with acids it forms very stable ionic complexes, this behavior being favored by the relief, occurring on protonation, of the strain due to the proximity of the lone pairs oriented towards the cavity interior.[10] 1,8-bis(dimethylamino)naphthalene (DMAN) can be considered the prototype proton sponge. The field of proton sponges covers several topics related to ''superbases'',[11] and several techniques, spanning high-resolution X-ray, neutron diffraction and NMR spectroscopy (chemical shifts and spin–spin coupling constants) have been used to tackle the different aspects of the hydrogen bonds involving N atoms of proton sponges.[12-14] With the advent of new computer architectures and more practicable implementations of electron correlated quantum chemical methods such as density functional theory (DFT), it has been feasible to apply also these tools in the design of novel proton sponges or to understand the factors responsible for enhanced nitrogen basicity.

As a complement of the well-known non-covalent interaction hydrogen bonding,[15] the halogen bonding (XB)[16] has emerged as a new powerful tool in the landscape of crystal engineering. The available halogen bonded synthons are much diversified and both neutral and ionic motifs have been used to achieve a great variety of supramolecular architectures.[17] Halide anions have been recognized as very good XB acceptors and they has been used to form several halogen bonded networks with different topologies.[18] Recently it has been proved that crypt-

222 (4,7,13,16,21,24-hexaoxa-1,10-diazabicyclo[8.8.8]hexacosane, alkali metal halides and α,ω-diiodoperfluoroalkanes invariably undergo a self-assembly process were crypt-222 encapsulates the medium sized cations, such as Na^+, K^+, Rb^+ and NH_4^+, via interactions involving the oxygen and nitrogen atoms of the cryptand so that the electron donor ability of halide anions is boosted. Halide anions behaves as tridentate XB acceptors and interacts with three different diiodoperfluoroalkyl chains which act as bidentate and telechelic XB donors and honeycomb nets are typically formed.[19] Intriguingly a comprehensive literature survey revealed that the studies of protonated crypt-111 derivatives are quite few and old. Some theoretical investigations have been reported as well as some analyses of the bahaviour in solution, but the structural studies are particularly scarce and no coordinates of protonaated crypt-111 are available in the Cambridge structure database. In this chapter we report the supramolecular synthesis, single crystal X-ray analyses, IR and ^{15}N NMR spectroscopy and DFT calculations for various halogen bonded H^+⊂crypt-111 iodide derivatives: The aim was to get structural information on the conformational preferences of the cryptand and on the preferential proton localization.

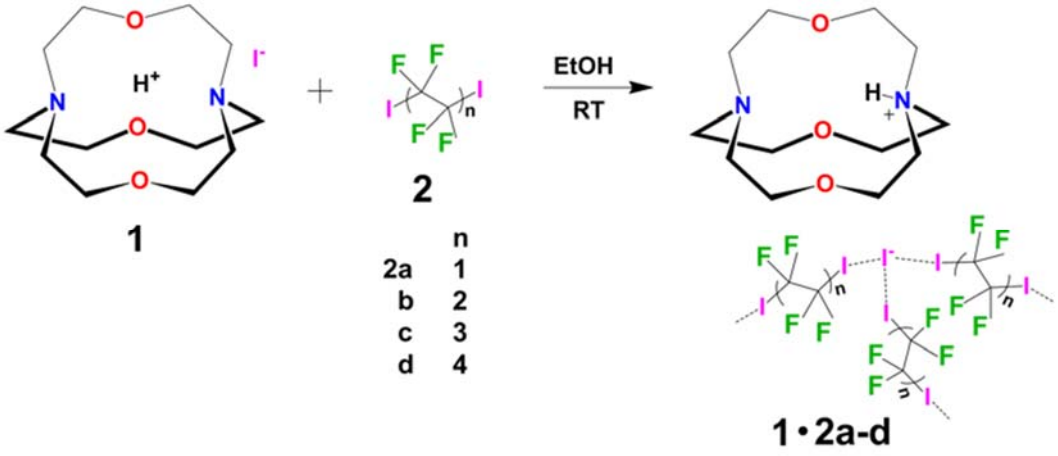

Scheme 4.2.1 Chemical formulas of starting component **1** and **2a-d**, and formed co-crystals **1a•2a-d**.

4.2.2. Results and discussion

4.2.2.1. Structural characterization of crypt-111 (1)

H^+⊂Crypt-111 iodide was prepared following already reported procedures[20] and crystals suitable for single crystal analysis were obtained through isothermal evaporation of an ethanol solution. Diffraction data for H^+⊂Crypt-111 iodide **1** and its halogen bonded cocrystals **1·2a-d** were all collected at 100 K and were good enough to allow for an assessment of the structural

details of the H^+⊂Crypt-111 moiety. Importantly, the acidic proton inside the cryptand cavity was experimentally located from the Fourier difference.

H^+⊂Crypt-111 iodide **1** crystallises in the hexagonal $P6_3/m$ space group with Z=2. The crystal shows a quite high symmetry which is related to the orientational disorder of the H^+⊂Crypt-111 moiety (in its turn associated with the mirror plane through the three oxygen). Nitrogen atoms show a distorted tetrahedral conformation (C–N–C angles 112.90°) and point their lone pair inside the cavity (Fig. 4.2.1). The cryptand adopts an endo-endo conformation (also named in-in conformation)[21] with a rugby ball shape (intramolecular N---N and O---O separations are 369.6 and 364.7 pm). Endo-exo and exo-exo conformations (in-out and out-out, respectively) have also been reported, but the endo-endo arrangement has been described as the most stable for the free cryptand and its protonated derivatives in the gas,[22] liquid,[23] and solid phases.[24]

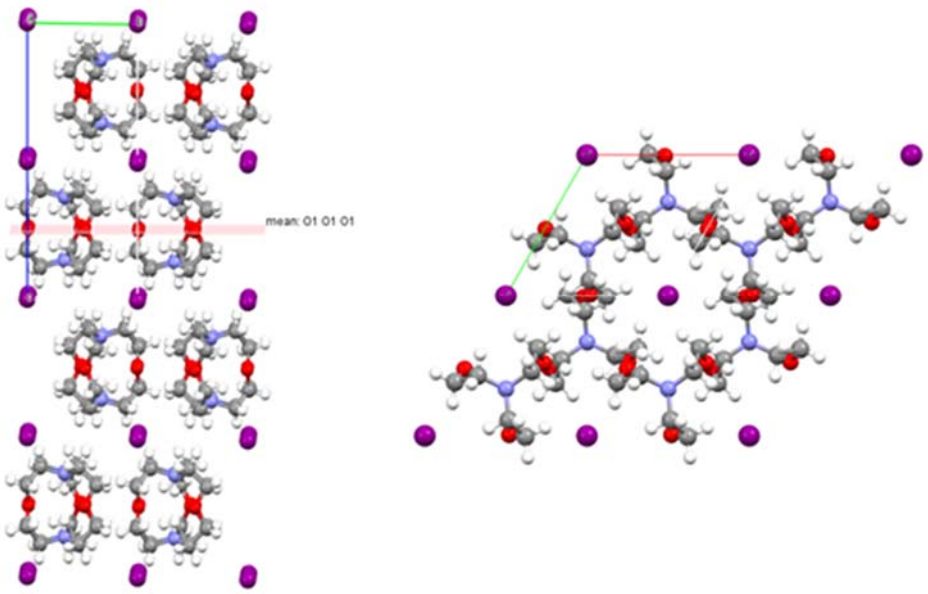

Figure 4.2.1 Partial representation (Mercury 3.8, ball and stick) of the crystal packing of H^+⊂crypt-111 iodide **1** along *c* (right) and approximately along *a* (left). The mirror through the oxygen atoms is also represented in pink. The hydrogen on nitrogen atoms correspond to a 50% occupancy. Color codes: Grey, carbon; white, hydrogen; blue, nitrogen; red, oxygen; magenta, iodine.

The best fit with the Fourier difference is obtained when the acidic hydrogen, positioned along the axis through the two nitrogen atoms, is splitted over two equipopulated positions symmetrized by to mirror through the oxygen atoms. This splitting may result from an orientational disorder of the H^+⊂Crypt-111 moiety (adopting, in the crystal, two dispositions

interchanged by the mirror through the three oxygen atoms), or from an internal hopping of the hydrogen between the nitrogen atoms. This latter possibility was considered unlikely as the barrier height for the process has been computed as high as 17 kcal/mol[25] (see onward). In order to rule out this possibility, we decided to pursue further information and analyze the co-crystals **1·2a-d** on the assumption that the expected lower symmetry of these systems might prevent orientational disorder.

Preparation: When 4,7,13,16,21,24-hexaoxa-1,10-diazabicyclo [8.8.8]hexacosane (crypt-222) cryptates the cation of alkaline halides, halogen bonded adducts are frequently obtained on self-assembly with iodoperfluorocarbons[19] and other XB donors,[26] probably as cations cryptation boosts anions electron donor ability and enables the halides to work as effective XB acceptors. We expected that iodide anion of $H^+\subset$crypt-111 iodide would show a similar behaviour. Indeed, on slow isothermal evaporation at room temperature of ethanol solutions containing cryptand **1** and bis-homologue α,ω-iodoperfluorocarbons **2a-d** in 1:1.5 ratio, the cocrystals **1·2a-d** were obtained. This starting tectons ratio was used as on self-assembly of cation$^+\subset$crypt-222 iodides with α, ω-iodoperfluorocarbons, iodide anions typically work as tridentate XB acceptors and diiodoperfluoroalkanes as bidentate XB donors.

Melting points of **1·2a-d** were sharp and different from starting tectons **1** and **2a-d** thus confirming the expected formation of supramolecular adducts rather than physical mixtures. IR spectra of **1·2a-d** showed the presence of peaks of both **1** and **2a-d** and the changes in peaks frequency and intensity were consistent with XB presence. For instance, the $\nu_{C\text{-}F}$ stretching peaks in the 1080-1200 cm^{-1} region were red shifted in **1·2a-d** compared to pure **2a-d** (e.g., peaks at 1146 and 1095 cm^{-1} in **2a** and at 1191 and1129 cm^{-1} in **2b** were at 1112 and 1082 cm^{-1} in **1·2a** and at 1178 and1116 cm^{-1} in **1·2b**) (Chap.7, Table 7.3.2.1).

4.2.2.2. Structural characterization of the supramolecular anion

Single crystal X-ray analysis show that some of the structural features of the supramolecular anions are the same in the four cocrystals **1·2a-d**, some others are common to **1·2b-d** only, these three system being very alike to each other. For instance, **1·2a-d** are all in the triclinic *P*-1 space group and Z is 2 in **1·2a** and 1 in **1·2b-d**. Two of the unit cell dimensions are nearly the same in **1·2b-d**, (*a* and *b* vary in the range 10.81-10.95 and 11.03-11.05 pm, respectively) indicating similarities in those two directions. Differently, the *c* axis increases with the perfluoroalkyl chain length and varies from 13.50 pm in **1·2b** to 16.84 pm in **1·2d**.

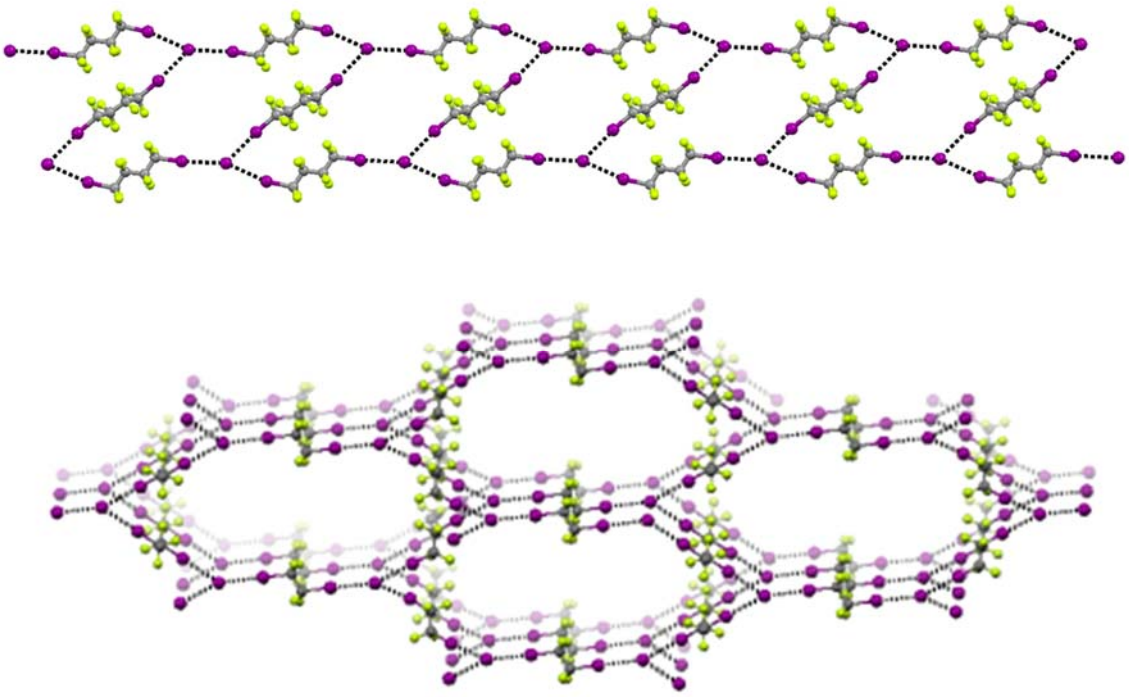

Fig. 4.2.2 Partial representation (Mercury 3.8, ball and stick) of the endless ribbon of the supramolecular anion present in **1·2b** (top) and of one of the translationally related supramolecular anions present in **1·2a** (bottom). In this latter structure the supramolecular anion is viewed approximately along the crystallographic *b* axis, which is the axis of the helical arrangement formed by XBs. Helicity is evidenced through the depth cueing representation. Color code: Grey, carbon; green, fluorine; magenta, iodine.

Along with the cation-anion electrostatic attractions, the C–I···I⁻ XBs are by far the strongest interactions in the systems and are responsible for the self-assembly of iodide **1** with diiodoperfluorocarbons **2a-d**. As expected, naked iodide ions behave as tridentate electron donors (XB acceptors) binding three different iodine atoms belonging to three distinct perfluoroalkyl chains, which work as bidentate and telechelic acceptors of electron density (XB donors). Similar to analogous systems,[19] XBs are quite short and approximately on the extension of the C─I covalent bond, as expected for strong XBs. Specifically, C─I···I⁻ angles and I···I⁻ separations span the ranges 167.80°-178.68° and 345.4-351.9 pm, respectively. These separations are longer than the average covalent I─I bond (266.6 pm) but shorter than the sum of van der Waals radius for an iodine atom (198 pm) and Pauling ionic radius for iodide ion (216 pm) (these separations correspond to normalized contacts *Nc*[27] varying from 0.83 to 0.85). The three XBs around iodide ions define a irregular-trigonal and fairly planar pattern. The three I···I⁻···I angles vary in the ranges 70.71°-77.32°, 130.30°-137.73°, and 144.16°-156.46°. The three iodine atoms halogen bonded to a given iodide anion identify a plane and in cocrystals

1·2b-d, all these planar arrays are parallel to each other and parallel ribbons of supramolecular anions are formed via juxtaposition of rhombuses where iodide anions are the vertexes and iodoperfluorocarbons the sides (Fig. 4.2.2, top).

Differently, iodine atoms in **1·2a** identify two planes nearly orthogonal to each other and helical supramolecular anions are formed. Specifically, translationally related supramolecular anions are formed wherein diiodoperfluoroethane molecules, and iodide anions, pile up along the crystallographic *b* axis and XBs bind them through a helical connectivity with six iodide, and six diiodoethane molecules, along the pitch of the helix (Fig. 4.2.2, bottom).

Perfluoroalkyl derivatives have a strong tendency to segregate from both polar and apolar compounds and this tendency increases with the length of the perfluorinated chain.[28] It is thus not surprising that in the overall crystal packing of **1·2b-d**, the fluorinated ribbons further organize into fluorinated, and neutral, layers which alternate with hydrocarbon, and charged, layers (Fig. 4.2.3).

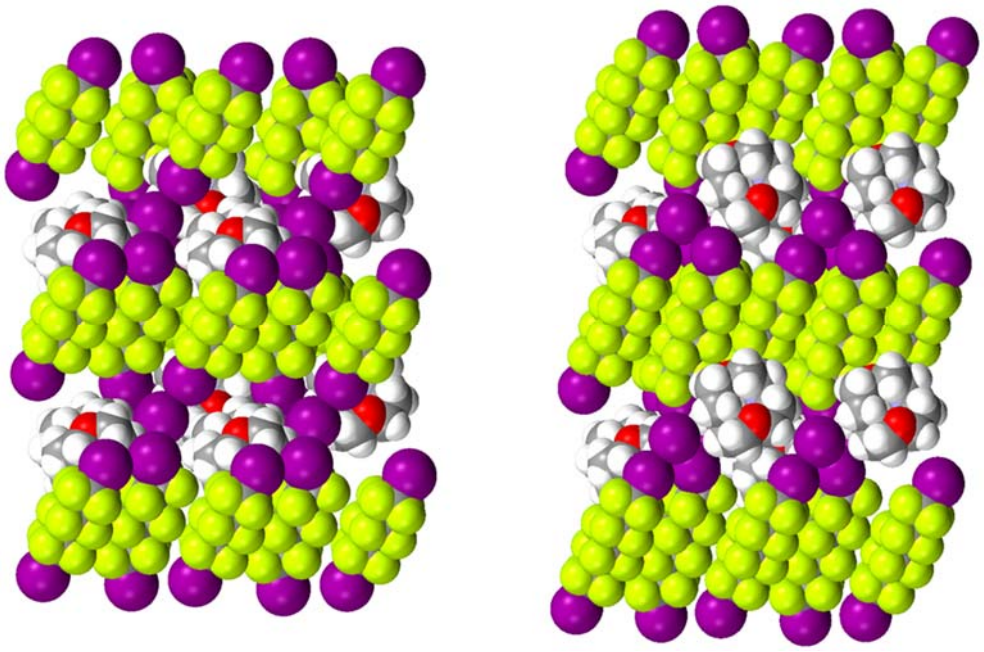

Figure 4.2.3 Space filling representation (Mercury 3.8) of the overall crystal packing of cocrystals **1·2c** (left) and **1·2d** (right) along the crystallographic *a* axis showing the segregation of supramolecular anions and the dependence of the layer thickness on the perfluoroalkyl chain length. Color code: Grey, carbon; white, hydrogen; green, fluorine; red, oxygen; blue, nitrogen; magenta, iodine.

4.2.2.3. Structural characterization of supramolecular cation $H^+\subset$crypt-111.

Some structural features of cation $H^+\subset$crypt-111 in cocrystals **1·2a-d** and in pure $H^+\subset$crypt-111 iodide **1** are similar, some others are not. The lower symmetry of cocrystals **1·2a-d**, relative

to pure **1**, parallels the lower symmetry of the contained cation $H^+\subset$crypt-111. Parallel to the halogen bonded supramolecular anion, cation $H^+\subset$crypt-111 has very similar structures in co-crystals **1·2b-d** while it shows some unique characteristics in **1·2a**. In all four cocrystals the cryptand is in the endo-endo conformation as the two nitrogen atoms adopt a distorted tetrahedral conformation (C–N–C angles span the range 111.01°-116.64°) pointing the respective lone pairs inside the cavity. In the unit cell of **1·2a** two different $H^+\subset$crypt-111 supramolecular cations are present and they both adopt a rugby ball shape more elongated than pure **1**. Differently, one single molecule is present in the unit cell of **1·2b-d** and a significantly less elongated conformation is preferred (mean values of intramolecular N---N and O---O separations are 380.5 and 349.2 pm in **1·2a** and 303.5 and 416.0 in **1·2b-d** respectively).

The Fourier difference locates the acidic hydrogen inside the cavity and 92 pm from one nitrogen atom. Three intramolecular H···O hydrogen bonds in the range 220.0-245.7 pm (corresponding to normalized contacts *Nc* in the range 0.81-0.97) pin the atom in its position in **1·2a-d** but they might also assist hydrogen hopping between the nitrogen atoms (see onward). In the more spherical cocrystals **1·2b-d**, a quite short H···N hydrogen bond (*Nc* in the range 0.77-0.80) is also present. Consistent with this model according to which the proton is covalently bonded to one nitrogen and hydrogen bonded to the other, the geometric features at the two nitrogen atoms are different from each other. C–N bond lengths in amines are typically shorter than in respective protonated derivatives and the mean values for such bond lengths at the protonated and non-protonated nitrogen atoms in **1·2a-d** are 145.6 and 149.9 pm, respectively. Protonation enhances the tetrahedral character of an amine and consistent with this general trend, the positive nitrogen in $H^+\subset$crypt-111 shows a smaller mean C–N–C angle and a greater distance from the plane through the three bonded carbon atoms than the neutral nitrogen (in one of the two independent cations in the crystal of **1·2a** these values are 112.30° *vs.* 116.33° and 42.5 *vs.* 28.2 pm, respectively) (Fig. 4.2.4, Table 4.2.1). Moreover, the proton-iodide electrostatic attraction is a strong interaction in cocrystals **1·2a-d** and it brings the iodide anion closer to the protonated nitrogen than to the neutral nitrogen (the mean value of the shortest $NH^+\cdots I^-$ and $N\cdots I^-$ distances are 464.3 and 608.1 pm, respectively). Consistent with the orientational disorder of the supramolecular cation, the two distances in crystals of pure **1** are the same and in between the values in **1·2a-d** (namely 482.1 pm).

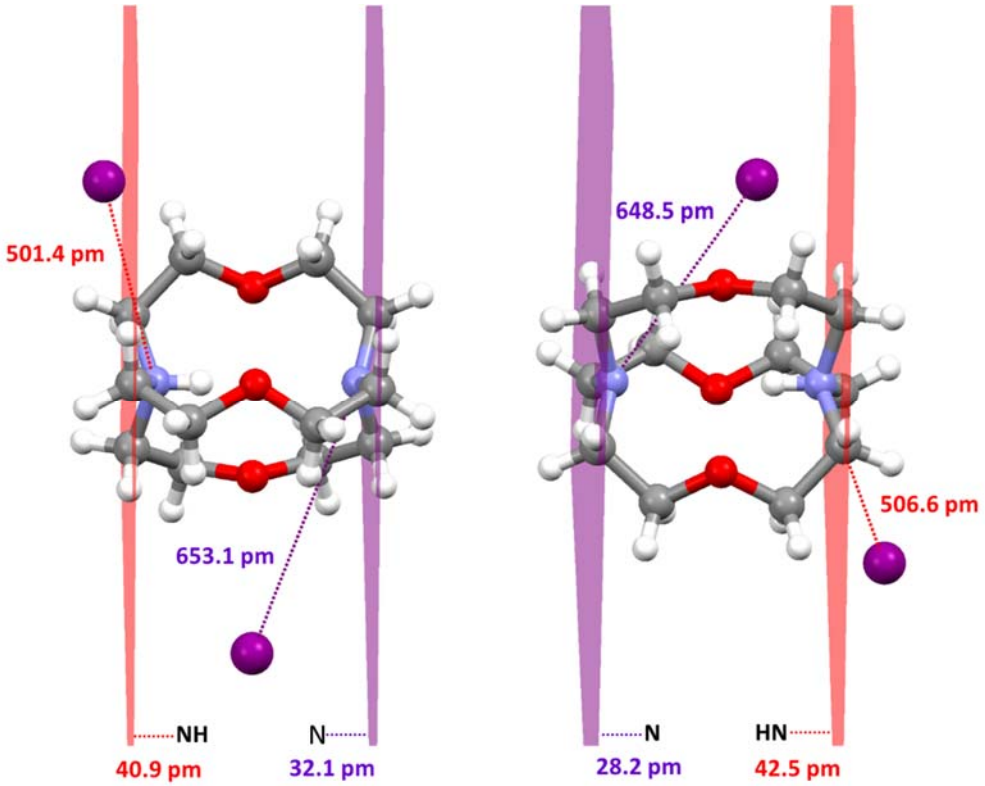

Figure 4.2.4 Ellipsoid representation (Mercury 3.8, principal ellipses are removed for clarity) of H^+⊂crypt-111 in cocrystal **1·2a** with the mean square plane through the three carbon atoms bound to the protonated (red) and non-protonated (purple) nitrogen atoms; the nitrogen-plane separations are given in the respective colours and the iodide anion closest to the two nitrogen atoms and the respective nitrogen-iodine distances are given. Color code: Grey, carbon; white, hydrogen; green, fluorine; red, oxygen; blue, nitrogen; magenta, iodine.

Table 4.2.1 Selected angles and distances in H^+⊂crypt-111 iodide (**1**) and its cocrystals **1·2b-d**. Digits in blue color refer to values of protonated bearing nitrogen atoms in complexes **1·2b-d**.

Complex	C—N—C Angle (°)[a]	N···plane$_{(C,C,C)}$ Distance (Å)	N···N Distance (Å)	N···I^- Distance (Å)
1	112.91	40.3	369.6	482.1
1·2b	**111.85**	**43.9**	303.2	**427.7**
	111.92	42.9		576.5
1·2c	**111.79**	**44.1**	302.3	**431.5**
	111.81	43.2		581.8
1·2d	**111.94**	**43.6**	304.9	**432.1**
	112.21	41.9		578.9

[a] The *given value is the mean C—N—C angle at the nitrogen atom.*

4.2.2.3. ^{15}N and ^{13}C solid-state NMR spectroscopy

Solid-state NMR (SSNMR) spectroscopy offer unique opportunities to study the structural and geometrical features of the chemical moieties along with thermodynamics.[29] Proton migration can be probed by looking at the atoms close to the interaction, namely nitrogen and carbon in systems studied here)[30] and we analysed $H^+\subset$crypt-111 iodide (1) and its halogen bonded derivatives via ^{13}C and ^{15}N SSNMR spectroscopy. The spectra of pure iodide 1 (Fig. 4.2.5) seems to indicate that the two nitrogen atoms are magnetically equivalent.

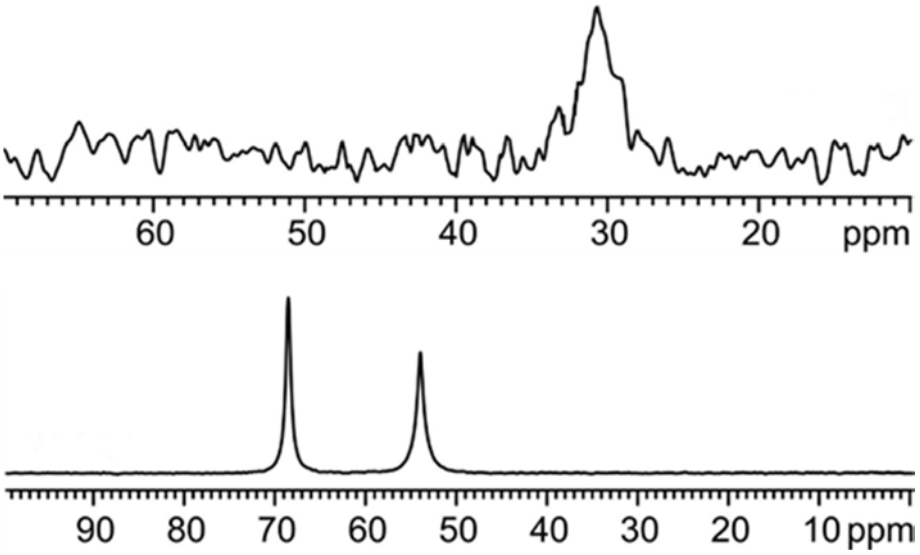

Figure 4.2.5 ^{15}N (Top) and ^{13}C (Bottom) solid-state NMR spectra of $H^+\subset$crypt-111 iodide (**1**) at 290 K.

Similarly, ^{15}N spectra of cocrystals **1·2c** and **1·2d** show a single peak at 34.844 and 35.025 ppm, respectively, suggesting that here the two nitrogen atoms are magnetically equivalent. It may be useful to contrast these results, obtained at room temperature, with indications from single crystal X-ray analysis, obtained at 100 K, and the issue is under study.

4.2.2.5. Density functional theory (DFT) calculation

DFT calculation of systems containing hydrogen-bonds or long-range weak interactions have been the subject of major attentions, among others in relation to the need to clarify self-assembly and self-organization of natural molecules, to design and optimize the functional properties of materials, to understand and control dynamic phenomena in solution, reactivity included. In order to elucidate some features of $H^+\subset$crypt-111 iodide, we performed DFT

calculations at B97-D3/aug-cc-pVDZ level. This approach, includes the D3 version of Grimme's dispersion method with the Becke-Johnson damping scheme, has been suggested to give reasonably reliable results for hydrogen-bonded system.

The optimized geometry of the protonated ligand, $H^+\subset$crypt-111, holds a nearly C_3 symmetry, with the extra proton located on the axis between the two N atoms (Fig.4.2.6) inside the cryptand cavity. The structure with the proton externally coordinated to N atom is 82.6 kJ/mol higher in energy.

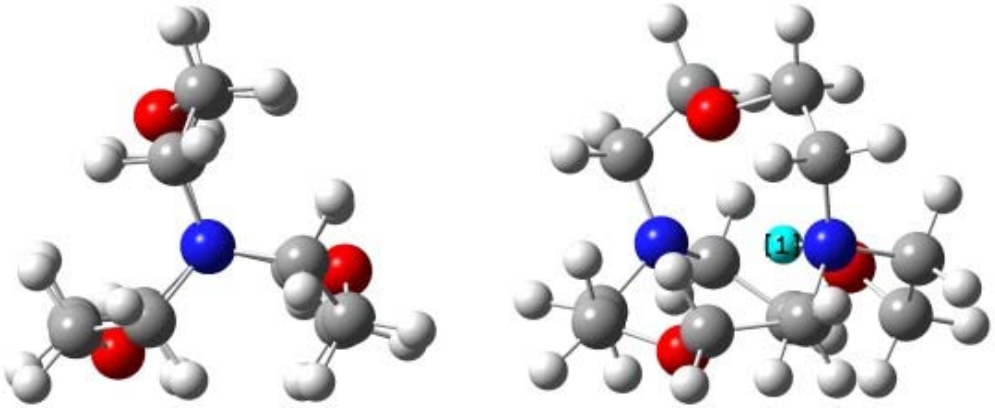

Figure 4.2.6 Axial (left) and lateral (right) view of the DFT-optimized structure of $H^+\subset$crypt-111, the acidic proton is in sky blue.

The first low-energy process identified by DFT is the expected proton transfer between the two N atoms. The transfer occurs via a process in which the molecule is "breathing", with the three flexible $–CH_2–CH_2–O–CH_2–CH_2–$ chains folding when the two N atoms get closer, and becoming more linear when N atoms get apart and the molecule relax. The transition state (TS) (Fig. 4.2.7) is stabilized by the N-H-N endo interaction, with an imaginary frequency of 1050 cm^{-1}. The TS is only 11.8 kJ/mol higher than $H^+\subset$crypt-111 and its vibrational mode is associated to the reaction coordinates that involve axial motion of the proton between the two N atoms. The low energy barrier suggests that the proton is easily transferred between the two N atoms. The value of the activation energy of $H^+\subset$crypt-111 iodide is related to the compact nature of the cell resulting in is limited space for the "breathing". The optimized cell of the halogen bonded cocrystals gives two activation energies, 11.3 and 4.2 kJ/mol for **1·2c** and 15.3 and 5.7 kJ/mol for **1·2d** respectively. The affect of XB on proton location in $H^+\subset$crypt-111 iodide cocrystals is under study.

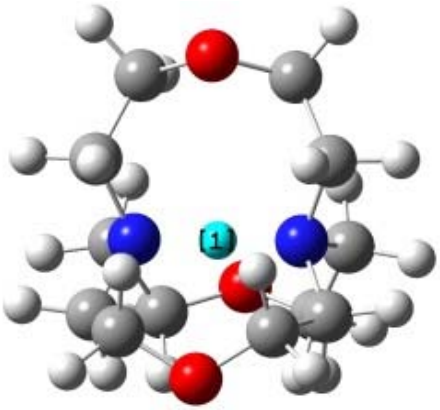

Figure 4.2.7 Transition State for the direct proton transfer between the two N atoms.

4.2.3. Conclusions

To summarise, crypt-111 and its derivatives attracted great interest due to their low nucleophilicity and very high, selective, and nearly irreversible affinity for proton. On reaction with acids, crypt-111 functions as a proton sponge: A transient exo-protonated species is formed first, then this form evolves into an endo-protonated species endowed with an exceptional stability as protonation relieves the strain induced by lone pair's proximity. Recently Alibrandi *et.al.* demonstrated the usefulness of crypt-111 in kinetic experiment of a pH sensitive reaction while the pH is changed in a controlled way. The cryptand thus functions as a "molecular automatic titrator", namely an alternative to conventional physical devices for the determination of thermodynamic parameters.[9]

The role of cation anion electrostatic attraction and I···I $^-$ halogen bonding in lowering the crystal symmetry and controlling the proton location in the supramolecular complex **1·2** has been examined. The single crystal X-ray studies, spectroscopic analysis and quantum chemical calculations of pure H^+⊂crypt-111 iodide and of its halogen bonded cocrystals with DIPFAs suggest a high degree of conformational variability in H^+⊂crypt-111 unit and this variability may be related to different locations of the acidic proton in pure H^+⊂crypt-111 iodide and in its cocrystals.

4.2.3. References

1. (a) D. G. Lee and V. S. Chang, *J. Org. Chem.*, 1978, **43,** 1532-1536; (b) D. Landini, A. Maia, F. Montanari and P. Tundo, *J. Am. Chem. Soc.*, 1979, **101,** 2526-2530.

2. (a) F. M. Raymo and J. F. Stoddart, *Chem. Rev.*, 1999, **99,** 1643-1664; (b) J. D. Badjic´, V. Balzani, A. Credi, S. Silvi and J. F. Stoddart, *Science*, 2004, **303,** 1845-1849.
3. H. Yang, B. Yuan and X. Zhang, *Acc. Chem. Res.*, 2014, **47,** 2106-2115.
4. 4. (a) J. Zhou, M. Chen, J. Xie and G. Diao, *ACS Appl. Mater. Interfaces.*, 2013, **5,** 11218-11224; (b) D. A. Uhlenheuer, K. Petkau and L. Brunsveld, *Chem. Soc. Rev.*, 2010, **39,** 2817-2826.
5. (a) C. J. Pedersen, *J. Am. Chem. Soc.*, 1967, **89,** 7017-7036; (b) R. M. Izatt and J. J. Christensen, *Synthetic Multidentate Macrocyclic Compounds*, Academic Press, New York, 1978.
6. B. Dietrich, J. M. Lehn and J. P. Sauvage, *Tetrahedron Lett.*, 1969, **10,** 2885-2888.
7. D. J. Cram, S. Karbach, Y. H. Kim, L. Baczynskyj and G. W. Kallemeyn, *J. Am. Chem. Soc.*, 1985, **107,** 2575-2576.
8. J. Cheney and J. M. Lehn, *J. Chem. Soc.*, 1972, 487-488.
9. (a) G. Alibrandi, C. L. Vecchio, G. Lando, *Angew. Chem. Int. Ed*., 2009, **48**, 6332 –6334, (b) G. Alibrandi, *Angew. Chem. Int. Ed.*, 2008, **47**, 3026-3028
10. (a) H. A. Staab and T. Saupe, *Angew. Chem. Int. Ed.*, 1988, **27,** 865-879; (b) H. A. Staab and T. Saupe, *Angew. Chem*., 1988, **100,** 895-909.
11. (a) R. W. Alder, *Chem. Rev.*, 1989, **89,** 1215-1223; (b) R. W. Alder, P. S. Bowman, W. R. S. Steele and D. R. Winterman, *Chem. Commun.*, 1968, 723-724.
12. L. Broge, I. Sotofte, C. E. Olsen and J. Springborg, *Inorg. Chem.*, 2001, **40,** 3124-3129.
13. A. Kr´ıstkova, J. R. Asher, V. G. Malkin and O. L. Malkina, *J. Phys. Chem. A*, 2013, **117,** 9235-9244.
14. R. C. Boehm, R. J. Rencsok, J. F. Harrison and T. A. Kaplan, *J. Phys. Chem.*, 1994, **98,** 6972-6979.
15. T. Steiner, *Angew. Chem. Int. Ed.*, 2002, **41,** 48-76.
16. G. R. Desiraju, P. S. Ho, L. Kloo, A. C. Legon, R. Marquardt, P. Metrangolo, P. Politzer, G. Resnati and K. Rissanen, *Pure Appl. Chem.*, 2013, **85,** 1711-1713.
17. G. Cavallo, P. Metrangolo, R. Milani, T. Pilati, A. Priimagi, G. Resnati and G.Terraneo, *Chem. Rev.*, 2016, **116,** 2478-2601.
18. (a) J. Marti-Rujas, L. Meazza, G. K. Lim, G. Terraneo, T. Pilati, K. D. M. Harris, P. Metrangolo and G. Resnati**,** *Angew. Chem. Int. Ed.*, 2013, **52**, 13444-13448; (b) P. Metrangolo, T. Pilati, G. Terraneo, S. Biella and G. Resnati, *CrystEngComm.*, 2009, **11,** 1187-1196.

19. (a) V. Kumar, T. Pilati, G. Terraneo, F. Meyer, P. Metrangolo and G. Resnati, *Chem. Sci, in press.* **DOI:** 10.1039/C6SC04478F*;* (b) G. Cavallo, P. Metrangolo, T. Pilati, G. Resnati, M. Ursini and G. Terraneo, Acta Crystallogr.,Sect.E:Struct.Rep.Online 2013, **69**, m387; (c) P. Metrangolo, F. Meyer, T. Pilati, G. Resnati and G. Terraneo, *Chem.Commun.*, 2008, 1635-1638; (d) D. B. Fox, R. Liantonio, P. Metrangolo, T. Pilati and G. Resnati *J. Fluorine Chem.*, 2004, **125,** 271-281; (e) R. Liantonio, P. Metrangolo, F. Meyer, T. Pilati, W. Navarrini and G. Resnati, *Chem.Commun.*, 2006, 1819-1821.
20. (a) P. L. Anelli, F. Montanari and S. Quici, *J. Org. Chem.*, 1985, **50,** 3453-3457; (b) R. Annunziata, F. Montanari, S. Quici and M. T. Vitali, *J. Chem. Soc.*, *Chem. Commun.*, 1981**,** 777-778.
21. G. Alibrandi, V. Amendola, G. Bergamaschi, R. Dollenz, L. Fabbrizzi, M. Licchelli and C. L. Vecchio, *Chem. Eur. J.*, 2013, **19,** 3729-3734.
22. R. Geue, S. H. Jacobson and R. Pizer, *J. Am. Chem. Soc.*, 1986, **108,** 1150-1155.
23. (a) J. Chenev, J. K. Kintzineer, J.-M. Lehn, *Nou. J. Chim.*, 1978. **2,** 41-52; (b) P. B. Smith, J. L. Dye, J. Cheney and J. M. Lehn, *J. Am. Chem. Soc.*, 1981, **103,** 6044-6048.
24. H. -J. Brugge, D. Carboo, K. V. Deuten, A. Knochel, J. Kopf and W. Dreissig, *J. Am. Chem. Soc.* 1986, **108,** 107-112.
25. R. C. Boehm, R. J. Rencsok, J. F. Harrison and T. A. Kaplan, *J. Phys. Chem.*, 1994, **98,** 6967-6971.
26. R. D. Walsh, J. M. Smith, T. W. Hanks and W. T. Pennington, *Cryst. Growth Des.*, 2012, **12,** 2759-2768.
27. The normalized contact *Nc* is defined as the ratio $D_{xy}/(rX+rY)$, where D_{xy} is the experimental distance between the halogen bonded iodine atoms X and halide anions Y and rX and rY are the van der Waals radius for iodine and the Pauling ionic radius of the halide anion Y, respectively. *Nc* is a useful indicator of the relative interaction strength, more useful than the XB distance itself, because it allows distances between different interacting sites to be compared.
28. (a) V. Ojogun, B. L. Knutson, S. Vyas and H. J. Lehmler, *J. Fluorine Chem.*, 2010, **131,** 784-790; (b) E. D. Wolf, P. Ruelle, J. V. D Broeke, B. J. Deelman and G. van Koten, *J. Phys. Chem. B.*, 2004, **108,** 1458-1466; (c) L. E. Kiss, I. K¨ovesdi and J. R´abai, *J. Fluorine Chem.*, 2001, **108,** 95-109.
29. M. R. Hansen, R. Graf and H. W. Spiess, *Acc. Chem. Res.*, 2013, **46,** 1996-2007.
30. (a) P. B. White and M. Hong, *J. Phys. Chem. B.*, 2015, **119,** 11581-11589; (b) K. Wozniak, H. He, J. Klinowski and E. Grech, *J. Phys. Chem.*, 1995, **99,** 1403-1409.

Chapter 5

Structural Characterization of New Fluorinated Mesogens Obtained Through Halogen-Bond Driven Self-Assembly

5.1. Introduction

Composed of anisotropic organic molecules, liquid crystals (LCs) are fluids exhibiting a long range order and for this reason they are often referred to as the fourth state of the matter, in between the solid and the liquid phases.[1,2] Since their discovery in the late 19th century, liquid crystals have had a profound impact on modern technology.[3] Their application in flat panel displays has paved the way to the design of a number of new electronic devices. Their exotic and unique behaviour still continues to fascinate academic and industrial researchers around the world, with actual and postulated applications well beyond the realm of flat panel displays.[4]

In recent years the self-assembly of LCs has been successfully exploited for the development of new functional nanostructured organic materials.[5–7] In such materials a well-defined hierarchical order is crucial in order to generate the desired functional properties, and the *in situ* polymerization of reactive liquid crystal monomers, in the molten phase, represents a fast and controllable process for the production of stable anisotropic polymers and networks.[8,9] Monomers containing reactive end groups such as acrylate, diene or diacetylene moiety are first aligned macroscopically in the liquid crystalline phase, then the alignment can be frozen by *in situ* polymerization induced either thermally or under UV irradiation, affording to nanostructured polymers characterized by a stable LC order over a wide temperature range.

Functional organic materials based on polymerised LC assemblies have been largely investigated for applications as membranes[10,11], drug delivery systems[4,12] optically anisotropic films [13–15], holographic materials[16], soft stimuli-responsive actuators[17–19] and sensors.[20,21] The macroscopic properties and phase structures of the resulting polymeric LC systems, and consequently their final application, are strictly related to the cross-linking density of the final network. For example, stimuli-responsive soft actuators, for application as artificial muscles, can be realized by weakly cross-linking the starting reactive mesogens.[18] The product is a liquid crystalline elastomer, where the anisotropy of the LCs and the elasticity of a rubber are combined in order to obtain actuating ability. In order to produce functional organic materials with new properties and enhanced responses, there is a need to extend the toolbox of available reactive mesogens and combine different triggers in LC materials.

As a complement of hydrogen bonding (HB), halogen bonding (XB) is emerging as a non-covalent interaction of choice in designing functional supramolecular materials.[22] According to IUPAC, the term halogen bonding refers to the non-covalent attractive interaction involving a halogen atom as the electrophilic site.[23] XB is a highly directional interaction, whose strength can be easily tuned by changing the halogen atom (XB-donor) and the electron-

withdrawing ability of the substituents in its neighbourhood.[24,25] The strength of the XB, in fact, increases with the polarizability of the halogen atom, while the presence of electron withdrawing substituents at the vicinity of the XB-donor site increases its Lewis acidity and consequently the interaction strength.[26] In particular fluorination of the molecular backbone of certain halogenated building blocks enhances their ability to work as XB-donors, giving rise to particularly strong interactions.[27] The electron-donating XB-acceptors can be either anions or neutral species possessing at least one nucleophilic region, e.g., a lone-pair-possessing heteroatom or a π-system.

Thanks to its high directionality, the XB has been applied successfully in the construction of new liquid crystalline materials.[28–30] Moreover, its high specificity for haloperfluorocarbons allowed the introduction of fluorinated modules,[31–33] overcoming the low affinity existing between perfluorocarbon and hydrocarbon compounds and opening new opportunities for exerting control over the mesomorphic phase and the functional properties of the final systems. Fluorination, in fact, represents an efficient strategy to enhance physical properties and to exert control over the supramolecular organization in liquid crystals.[34–37] Generally, the introduction of perfluorinated chains results in higher transition temperatures while the well-known tendency of perfluoroalkyl chains to segregate from hydrocarbon chains favours the formation of lamellar phases. This produces interesting charge-transport properties in ionic liquid crystals where anisotropic conduction pathways can be generated.[38,39]

Some years ago, our group has reported about the liquid crystalline behaviour of halogen-bonded trimeric complexes obtained upon self-assembly of a range of alkoxystilbazoles acting as monodentate XB-acceptors with α,ω-diiodoperfluoroalkanes or 1,4-diiodotetrafluorobenzene acting as bidentate XB-donors.[31,40] Despite the non-mesomorphic nature of the starting materials, most of the reported halogen-bonded complexes have shown liquid-crystallinity. The modularity of this approach has opened new perspectives in the engineering of liquid crystals and, liquid crystalline polymers with nematic phases have been obtained upon complexation of difunctional XB-donor and acceptor molecules,[41] while reacting an alkoxystilbazole derivative with a XB-donor molecule incorporating an azo group, supramolecular LC complexes with unique light-responsive properties have been obtained.[42]

Keen to explore the potential of XB in the formation of new reactive mesogens, on the heels of our previous results, we have prepared some new halogen bonded complexes by self-assembly of 1,4-diiodotetrafluorobenzene and α,ω–diiodoperfluoroalkanes of different chain length, with an alkoxystilbazole derivative bearing an alkoxy chain functionalized with a

terminal methacrylate group (Scheme 5.1). The formation, the structural characterization, and the mesomorphic behaviour of such materials are herein described in detail.

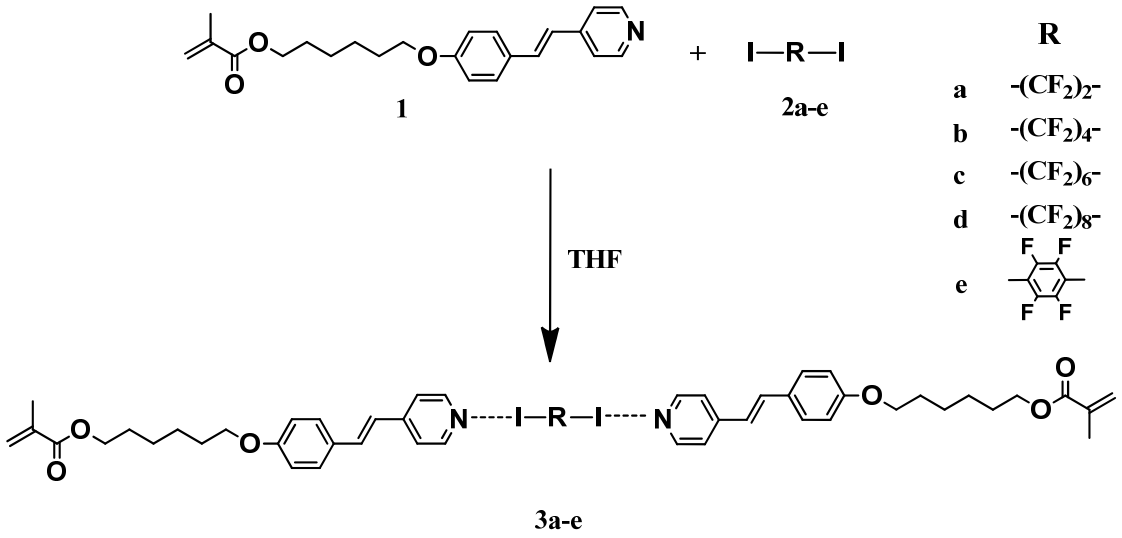

Scheme 5.1 Chemical structures of the alkoxystilbazole derivative (**1**), the diiodoperfluorocarbon modules (**2a-e**) and their halogen-bonded complexes (**3a-e**).

5.2. Results and discussion

5.2.1 Synthesis of supramolecular complexes

Diiodoperfluoroalkanes and diiodoperfluoroarenes are well-known XB donors, largely applied for the construction of numerous supramolecular structures[52–57] and liquid crystals,[29] since they form particularly short and directional interactions, thus allowing structural control over the final supramolecular complexes. From their bifunctional structures it may be expected that trimeric complexes where the fluorinated module is bridging two stilbazole derivatives **1** are obtained. Therefore, the XB-complexes **3a-e** between the stilbazole methacrylate **1** and the diiodoperfluorocarbons **2a-e** (Scheme 5.1) have been obtained by crystallizing from THF solution a 2:1 mixture of the stilbazole methacrylate and the diiodoperfluorocarbon. The successful complex formation was soon evidenced by a color change in the products. In fact both the parent stilbazole methacrylate and the diiodoperfluorocarbons are white, whereas crystals obtained from THF solutions were pale yellow implying a degree of charge transfer from the pyridine nitrogen to the σ-hole on the iodine atom.[49]

All the complexes were characterized by FTIR spectroscopy, single crystal X-ray diffraction analysis, and Polarized Optical Microscopy (POM).

5.2.2 FTIR spectroscopy

Fourier transform infrared spectroscopy (FTIR) has been applied as a simple and fast screening method to detect the occurrence of XB between the stilbazole derivative **1** and the diiodoperfluorocarbons **2**. It is well-known, in fact, that the intermolecular interaction between an electron-donor species with an electrophile affects the vibrational motions in term of intensity and shift. In pyridine-iodoperfluorocarbon complexes it has been found that the occurrence of halogen-bonding produces a blue-shift and intensity of pyridine bands decreases in the region 3000–3100 cm^{-1}, as a result of a higher positive charge on the pyridyl hydrogens in the complex, and a red-shift of the bands associated with the perfluorinated moiety, due to an increased electron density of the XB-donor.[50,51] This is clearly evident in the FTIR spectra of all the complexes described in this paper.

Table 5.1 FTIR frequency changes of the XB-acceptor (**1**) and XB-donors (**2a-e**) before and after complexation.

Sample	Pyridine ν_{C-H} stretching	Fluoroalkyl/phenyl ν_{C-F} stretching		Fluoroalkyl/phenyl δ_{C-F} bending
1	3036			
2a		1147	1096	833
3a	3040	1123	1086	826
2b		1192	1129	834
3b	3054	1175	1123	831
2c		1141	1087	833
3c	n.d. *	1115	1058	832
2d		1145	1112	838
3d	3037	-	1103	832
2e		1459		940
3e	3044	1456		934

** Upon halogen bonding the intensity of the C-H stretching vibration of pyridine ring undergoes a marked reduction and the band is not visible anymore in the spectrum of **3c.***

For instance, the ν_{C-H} absorption of the pyridine ring in the pure stilbazole methacrylate **1** at 3036 cm^{-1} becomes less intense in **3b** and is shifted to 3054 cm^{-1}, while vibrations related to diiodoperfluorobutane at 1192 cm^{-1}, 1129 cm^{-1}, and 834 cm^{-1} are red-shifted to 1175 cm^{-1}, 1123 cm^{-1}, and 831 cm^{-1} respectively upon complexation. Similarly in complex **3e** the ν_{C-H}

absorption of the pyridine ring is blue-shifted at 3044 cm^{-1} while the vibrations related to the fluorophenyl moiety at 1459 and 940 cm^{-1} for the diiodotetrafluorobenzene **3e** are red-shifted to 1456 and 936 cm^{-1}, respectively, on complexation. Selected FTIR absorption frequencies for all the complexes **3a-3e** and their individual starting components are reported in Table 5.1.

5.2.3. Single crystal X-ray analysis

Single crystals of complexes **3a-e** were grown by slow evaporation of a THF solution containing a 2:1 mixture of the stilbazole methacrylate **1** and the diiodoperfluorocarbons **2a-e**. After a period ranging from 3 to 7 days at room temperature, plate like single crystals suitable for X-ray diffraction analysis were obtained. Detailed crystallographic data for complexes **3a-e** are summarized in table 7.4.1 of experimental section chapter.

Single crystal X-ray diffraction analysis of complexes **3a-e** confirmed that in the final cocrystals, the stilbazole methacrylate **1** and the diiodoperfluorocarbon modules **2a-e** are present in a 2:1 ratio and I···N XBs are largely responsible for the self-assembly of the complementary modules **1** and **2**. The topology of the primary network is a nice example of the paradigm of the expansion of a ditopic starting module by a linear linker moiety: Each diiodoperfluorocarbon module **2** acts as a linear and ditopic XB-donor while the stilbazole methacrylate derivative **1** behaves as a strong XB-acceptor (Fig. 5.1). The geometrical parameters describing the XB contacts are reported in Table 5.2. All the XBs are quite short and linear with values similar to those reported for other halogen bonded systems involving stilbazole derivatives.[32,40,52] These feature once again confirms, the supramolecular synthon I···N is strong and reliable and that the stilbazole core on the XB acceptor module **1** is a very efficient building unit to promote the formation of halogen-bonded adducts.

Table 5.2 Described distances and angles observed in the crystal structure of co-crystals **3a-e**.

Co-crystal	N···I (Å)	N_c *	C-I···N (°)
3a	2.829	0.801	175.57
3b	2.934	0.831	173.51
3c	2.773	0.776	176.03
3d	2.759	0.781	178.19
3e	2.824	0.800	174.56

* *As a measure of the strength of XB, we define 'normalized contact' N_c as the ratio $N_c = D_{ij}/(rvdw_i + rvdw_j)$, where D_{ij} is the distance between the atoms i and j and $rvdw_i$ and $rvdw_j$ are the corresponding van der Waals radii for I and N atoms respectively.*[53]

From the crystal packing point of view it is interesting to note that although the XB donors used in the cocrystal formation are quite diverse either in structure and dimension, four perfluoroalkanes with different alkyl chain lengths and one aromatic unit respectively, the overall packing of the adducts **3a-e** shares strong similarities.

Specifically, the cocrystals **3a-d** are characterized by a stepped organization between the two stilbazoles, a direct consequence of the antiperiplanar arrangement of the perfluoromethylene groups of the XB donor (Fig. 5.1, top and Chap.7 Fig. 7.4.1). Similar organization is also observed in the cocrystal **3e**, (Fig. 5.1, bottom) where the modules **1** adopt a stepped arrangement although the core of the XB-donor is a *para*-substituted aromatic moiety. In this case the effect of the staggered arrangement is promoted by the flexibility of the XB contact. In fact, differently from all other cocrystals where the XBs take place in the plane described by the pyridyl ring of the stilbazole, in **3e** the interaction occurs out-of-plane with a distance between the iodine atom and the projection of the pyridyl ring plane of 0.89 Å. This deviation from the planarity allows for the stepped organization of the stilbazole modules in the trimer (Fig. 5.1).

Other small differences appear in the arrangement of the donor/acceptor modules in **3a-d**. For instance when the shortest XB donor **2a** is used the CF_2 unit of the chain lays on the same plane described by the pyridyl ring of the stilbazole **1**, while for all the other cocrystals the perfluoroalkyl chains are perpendicular to the plane of the pyridyl rings (Chap.7 Fig. 7.4.2).

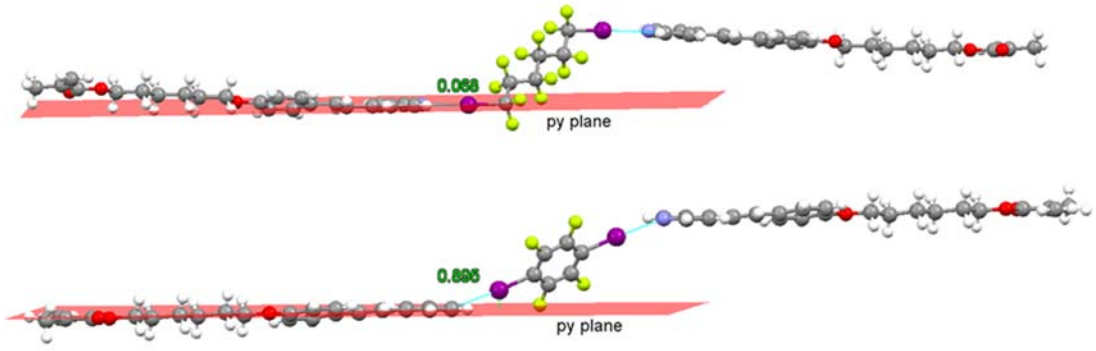

Figure 5.1 Ball-and-stick representation of the single crystal X-ray structure of complex **3c** (top) and **3e** (bottom). The stepped organization between the XB donor and acceptor in the supramolecular trimer is shown. The in-plane for **3c** and out-of-plane for **3e** XB are highlighted. The plane described by the

pyridyl ring (py plane) is shown in red and the distance between the iodine atom and the plane is reported in Å. Color codes: grey, carbon; blue, nitrogen; magenta, iodine; red, oxygen; yellow, fluorine and white, hydrogen. XB are light blue dotted lines.

It is known that perfluorocarbon and hydrocarbon compounds tend to segregate and this phenomenon is directly correlated with the number of fluorine atoms in the fluorinated moieties. This behavior becomes noticeable in the cocrystals **3b-d** where the perfluorinated units form well-defined layers fully separated by the hydrocarbon systems. For instance in **3b** the stilbazoles and the 1,4-diiodoperfluorobutane molecules are stacked in separated columns parallel to the *b* crystallographic axis (Fig. 5.2, bottom). Differently, when 1,2-diiodotetrafluoroethane **2a** and 1,4-diiodotetrafluorobenzene **2e** are used, the number of fluorine atoms is not enough to elicit the segregation and the XB-donors are surrounded by hydrocarbon units (Fig. 5.2 top, and Chap.7 Fig. 7.4.3). When present, segregation may eventually promote the formation of layered structures, *i.e.* lamellae, also in the molten phase and let us to foresee a liquid crystalline behavior.

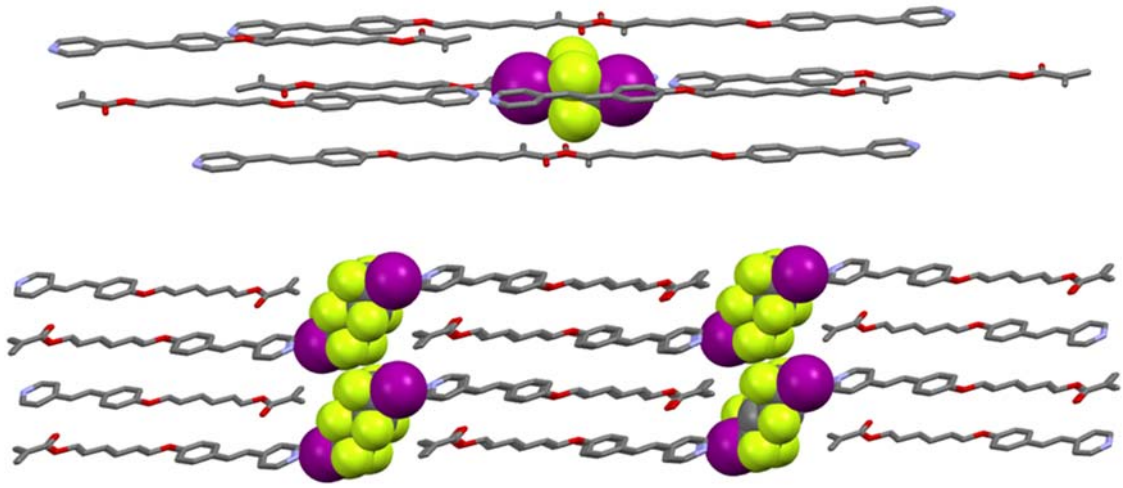

Figure 5.2 Crystal packing of complexes **3a** (top) and **3b** (bottom) showing a clear segregation between hydrocarbon and perfluorocarbon modules in complex **3b**. Hydrogen atoms have been omitted for the sake of clarity. Color codes: grey, carbon; blue, nitrogen; magenta, iodine; red, oxygen; yellow, fluorine.

Another interesting common structural feature in **3a-d** is that the stilbazoles **1** are stacked in head-to-tail fashion where the alkyl side chain of one stilbazole is sandwiched between the aromatic rings of adjacent stilbazoles and, of course, vice versa (Fig. 5. 2). In **3e** this motif is less pronounced and the stilbazole modules tend to adopt a more distorted packing.

This arrangement is a direct consequence of the angle between the two stilbazole units in the trimer.

Finally, the overall crystal packing in all the cocrystals are stabilized by weak C-H···O, H···F, and H···π short contacts occurring between adjacent stilbazoles and close perfluorinated compounds.

5.2.4. Thermal analysis

The liquid crystalline properties of complexes **3a-e** were examined by hot stage polarized optical microscopy (POM). All the starting materials are non mesomorphic and their melting points are reported in Table 5.3. On heating all the XB-complexes **3a-3e** melted directly to an isotropic liquid although at temperatures higher than the pure XB-donor and acceptors. This gives a further reliable proof that **3a-3e** are well-defined new chemical species rather than a mechanical mixture of starting modules. Moreover, these data prove that a simple one-pot co-crystallization procedure can be easily exploited to stabilize volatile perfluorinated compounds, since the occurrence of halogen bond remarkable decreases their volatility.[54]

This is remarkably taking into account the high volatility of haloperfluoroalkanes and the increasing concerns regarding their potential role as persistent and bioaccumulative organic pollutants.

On cooling from the isotropic liquid, a monotropic SmA phase appeared for complexes **3b-e**, (Fig. 5.3, Table 5.3 and Chap.7 Fig. 7.4.4) while complex **3a** decomposed soon after melting. This is because of the higher volatility of the diiodoperfluoroethane module, which upon heating evaporated from the liquid mixture. The mesogenic behavior found for **3b-e** is perfectly reproducible even after several excursions in the isotropic phase, and smectic A phases were observed over a range of 20-30°C before the material crystalized, except for **3b** whose LC phase appeared longer lived and reproducibly existed for some 45°C before crystallization occurred.

This suggests that the XB interaction survives in the liquid crystalline phase and has an appreciable strength; similar to that seen in previously reported hydrogen-bonded systems.[52] The observation of a SmA phase is consistent with XRD analysis and is a manifestation of nanophase segregation of perfluorocarbons and hydrocarbons modules.

Table 5.3 Thermal behavior of complexes **3a-e** from POM analysis.

Cocrystal	Melting point (°C)		Phase transition	T/ ˚C
	XB-Acceptor (1)	XB-Donor (2)		
3a	78	-21	Cr – I	95
3b	78	-9	Cr – I	106
			I – Sm A	80
			(Sm A – I)	97
			Sm – Cr	52
3c	78	25	Cr – I	98
			I – Sm A	82
			(Sm A – I)	94
			Sm – Cr	74
3d	78	75	Cr – I	103
			I – Sm A	81
			(Sm A– I)	95
			Sm A – Cr	65
3e	78	110	Cr – I	113
			I – Sm A	92
			(Sm A – I)	104
			Sm A – Cr	78

The reported data show that despite the non-mesomorphic nature of the starting materials, most of the halogen-bonded complexes show liquid-crystalline behavior, further confirming the effectiveness of the XB in the construction of new supramolecular mesogens.

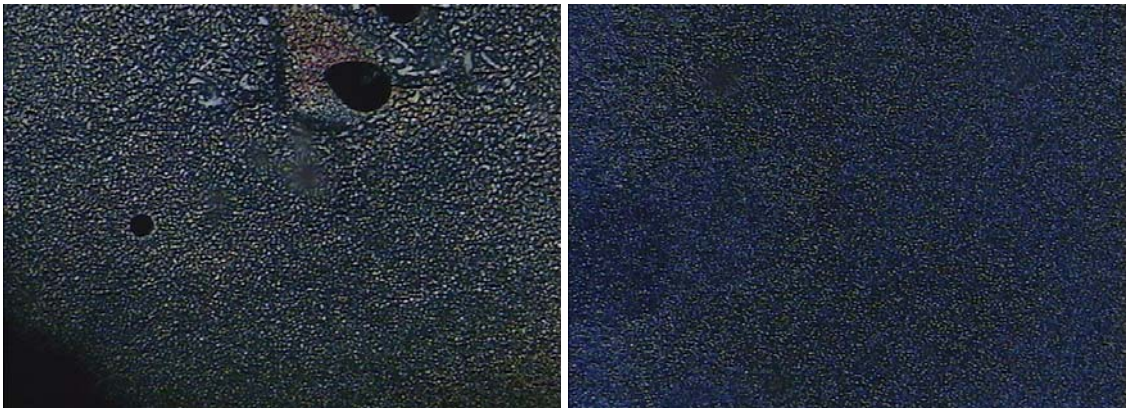

Figure 5.3 Optical textures of the smectic A phase observed on cooling from the isotropic state for complex **3d** (left; T = 81°C) complex **3e** (right; T = 92°C).

5.3. Conclusions

In summary, we have described the synthesis of new trimeric complexes obtained upon XB-driven self-assembly of 1,4-diiodotetrafluorobenzene or α,ω−diiodoperfluoroalkanes, acting as XB-donors, with an alkoxystilbazole derivative functionalized with a methacrylate terminal group, acting as XB-acceptor. Despite the non-mesomorphic nature of the starting materials, most of the halogen-bonded complexes show liquid-crystalline behavior with smectic A phases. Single crystal X-ray diffraction analysis confirmed that N···I XB interactions are largely responsible for the self-assembly of the complementary modules **1** and **2** and showed a clear segregation between perfluorocarbon and hydrocarbon molecules that perfectly agree with the lamellar phase observed in the LC state.

All the reported complexes decompose at temperatures higher than the melting points of the starting diiodoperfluorocarbons proving that an XB-driven cocrystallization can be exploited as an easy and convenient tool to stabilize volatile perfluorinated compounds.

The obtained supramolecular mesogens possess reactive groups suitable for incorporation into liquid crystalline elastomeric actuators.

5.4. References

1. H. K. Bisoyi and S. Kumar, *Chem. Soc. Rev.*, 2011, **40,** 306-319.
2. K. Goossens, K. Lava, C. W. Bielawski and K. Binnemans, *Chem. Rev.*, 2016, **116,** 4643-4807.
3. P. Kirsch and M. Bremer, *Angew. Chem. Int. Ed.*, 2000, **39,** 4216-4235.
4. J. P. F. Lagerwall and G. Scalia, *Curr. Appl. Phys.*, 2012, **12,** 1387-1412.
5. G. Fernández, *Nat. Mater.*, 2012, **12,** 12-14.
6. D. Iqbal and M.H. Samiullah, *Materials*, (Basel), 2013, **6,** 116-142.
7. B. G. Kim, S. Kim, J. Seo, N. K. Oh, W. C. Zin and S. Y. Park, *Chem. Commun.*, 2003, 2306-2307.
8. C. Bowry, Polym., Springer US, 1995, 278-304.
9. H. Thiem, P. Strohriegl, M. Shkunov and I. McCulloch, *Macromol. Chem. Phys.*, 2005, **206,** 2153-2159.
10. G. M. Bögels, H. P. C. Van Kuringen, I. K. Shishmanova, I. K. Voets, A. P. H. J. Schenning and R. P. Sijbesma, *Adv. Mater. Interfaces.*, 2015, **2,** 524.

11. D. J. Broer, C. M. W. Bastiaansen, M. G. Debije and A. P. H. J. Schenning, *Angew. Chem. Int. Ed.*, 2012, **51,** 7102-7109.
12. M. Malmsten, *Soft Matter*, 2006, **2,** 760-769.
13. S. J. Lee, J. Y. Jho and J. H. Lee, *Mol. Cryst. Liq. Cryst.*, 2015, **621,** 175-181.
14. C. D. Favre-Nicolin and J. Lub, *Macromolecules*, 1996, **29,** 6143-6149.
15. M. Okazaki, K. Kawata, H. Nishikawa and M. Negoro, *Polym. Adv. Technol.*, 2000, **11,** 398-403.
16. B. U. Theissen, S. J. Zilker, T. Pfeuffer and P. Strohriegl, *Adv. Mater.,* 2000, 12, 1698–1700
17. L. T. De Haan, J. M. N. Verjans, D. J. Broer, C. W. M. Bastiaansen and A. P. H. J. Schenning, *J. Am. Chem. Soc.*, 2014, **136,** 10585-10588.
18. J. Mamiya, *Polym. J.*, 2012, **45,** 239-246.
19. S. Petsch, B. Khatri, S. Schuhladen, L. Köbele, R. Rix, R. Zentel and H. Zappe, *Smart Mater. Struct.*, 2016, **25,** 85010.
20. D. J. Mulder, A. P. H. J. Schenning and C. W. M. Bastiaansen, *J. Mater. Chem. C.*, 2014, **2,** 6695-6705.
21. C. Ohm, M. Brehmer and R. Zentel, *Adv. Mater.*, 2010, **22,** 3366-3387.
22. A. Priimagi, G. Cavallo, P. Metrangolo and G. Resnati, *Acc. Chem. Res.*, 2013, **46,** 2686-2695.
23. G. R. Desiraju, P. S. Ho, L. Kloo, A. C. Legon, R. Marquardt, P. Metrangolo, P. Politzer, G. Resnati and K. Rissanen, *Pure Appl. Chem.*, 2013, **85,** 1711-1713.
24. P. Politzer, J. S. Murray and T. Clark, *Phys. Chem. Chem. Phys.*, 2010, **12,** 7748-7757.
25. C. B. Aakeröy, P. D. Chopade ad J. Desper, *Cryst. Growth Des.*, 2013, **13,** 4145-4150.
26. P. Politzer, J. S. Murray and T. Clark, *Chem. Life Sci.*, 2015, 19-42.
27. K. E. Riley, J. S. Murray, J. Fanfrlík, J. Řezáč, R. J. Solá, M. C. Concha, F. M. Ramos and P. Politzer, *J. Mol. Model.*, 2011, **17,** 3309-3318.
28. L. J. McAllister, C. Präsang, J. P. W. Wong, R. J. Thatcher, A. C. Whitwood, B. Donnio, P. O'Brien, P. B. Karadakov and D. W. Bruce, *Chem. Commun.*, 2013, **49,** 3946-3948.
29. D. W. Bruce,P. Metrangolo, F. Meyer, T. Pilati, C. Präsang, G. Resnati, G. Terraneo, S. G. Wainwright and A. C. Whitwood, *Chem. Eur. J.*, 2010, **16**, 9511.
30. X. Wang, F. W. Heinemann, M. Yang, B. U. Melcher, M. Fekete, A. V. Mudring, P. Wasserscheid and K. Meyer, *Chem. Commun.*, 2009, 7405-7407.
31. P. Metrangolo, C. Präsang, G. Resnati, R. Liantonio, A. C. Whitwood and D. W. Bruce, *Chem. Commun.*, 2006, 3290-3292.

32. D. W. Bruce, P. Metrangolo, F. Meyer, T. Pilati, C. Praesang, G. Resnati, G. Terraneo, S. G. Wainwright and A. C. Whitwood, *Chem. Eur. J.*, 2010, **16,** 9511-9524.
33. G. Cavallo, G. Terraneo, A. Monfredini, M. Saccone, A. Priimagi, T. Pilati, G. Resnati, P. Metrangolo and D. W. Bruce, *Angew. Chem. Int. Ed.*, 2016, 6300-6304.
34. F. Guittard, E. Taffin de Givenchy, S. Geribaldi, A. Cambon, *J. Fluor. Chem.*, 1999, **100,** 85-96.
35. M. Hird, *Chem. Soc. Rev.*, 2007, **36,** 2070-2095.
36. P. Kirsch, *J. Fluor. Chem.*, 2015, **177,** 29-36.
37. P. Kirsch, M. Lenges, A. Ruhl, F. Huber, R. D. Chambers and G. Sandford, *J. Fluor. Chem.*, 2007, **128,** 1221-1226.
38. A. Abate, A. Petrozza, G. Cavallo, G. Lanzani, F. Matteucci, D. W. Bruce, N. Houbenov, P. Metrangolo and G. Resnati, *J. Mater. Chem. A* ,2013, **1,** 6572-6578.
39. A. Abate, A. Petrozza, V. Roiati, S. Guarnera, H. Snaith, F. Matteucci, G. Lanzani, P. Metrangolo and G. Resnati, *Org. Electron.*, 2012, **13,** 2474-2478.
40. D. W. Bruce, P. Metrangolo, F. Meyer, C. Prasang, G. Resnati, G. Terraneo, A. C. Whitwood, C. Praesang, G. Resnati, G. Terraneo and A. C. Whitwood, *New J. Chem.*, 2008, **32,** 477-482.
41. J. Xu, X. Liu, T. Lin, J. Huang and C. He, *Macromolecules,* 2005, **38,** 3554-3557.
42. A. Priimagi, M. Saccone, G. Cavallo, A. Shishido, T. Pilati, P. Metrangolo and G. Resnati, *Adv. Mater.*, 2012, **24,** OP345-OP352. doi:10.1002/adma.201204060.
43. C. B. Aakeröy, S. Panikkattu, P. D. Chopade and J. Desper, *CrystEngComm.*, 2013, **15,** 3125-3136.
44. J. L. Syssa-Magalé, K. Boubekeur, P. Palvadeau, A. Meerschaut and B. Schollhorn, *CrystEngComm.*, 2005, **7,** 302-308.
45. A. Casnati, G. Cavallo, P. Metrangolo, G. Resnati, F. Ugozzoli and R. Ungaro, *Chem. Eur. J.*, 2009, **15,** 7903-7912.
46. A. Abate, S. Biella, G. Cavallo, F. Meyer, H. Neukirch, P. Metrangolo, T. Pilati, G. Resnati and G. Terraneo, *J. Fluor. Chem.*, 2009, **130,** 1171-1177.
47. M. Baldrighi, P. Metrangolo, F. Meyer, T. Pilati, D. Proserpio, G. Resnati and G. Terraneo, *J. Fluor. Chem.*, 2010, **131**, 1218-1224.
48. L. Catalano, P. Metrangolo, T. Pilati, G. Resnati, G. Terraneo and M. Ursini, *J. Fluor. Chem.*, 2016, http://dx.doi.org/10.1016/j.jfluchem.2016.07.011
49. K. Willis, D. J. Price, H. Adams, G. Ungar and D. W. Bruce, *J. Mater. Chem.*, 1995, **5,** 2195-2199.

50. B. Hawthorne, H. Fan-Hagenstein, E. Wood, J. Smith and T. Hanks, *Int. J. Spectrosc.*, 2013, 1-10.
51. Q. J. Shen and W. J. Jin, *Phys. Chem. Chem. Phys.*, 2011, **13,** 13721-13729.
52. H. L. Nguyen, P. N. Horton, M. B. Hursthouse, A. C. Legon and D. W. Bruce, *J. Am. Chem. Soc.*, 2004, **126,** 16-17.
53. A. Bondi, van der Waals Volumes and Radii, *J. Phys. Chem.*, 1964, **68,** 441-451.
54. C. B. Aakeröy, T. K. Wijethunga, J. Desper and C. Moore, *J. Chem. Crystallogr.*, 2015, **45,** 267-276.

Chapter 6

General conclusions

Supramolecular chemistry draws inspiration from Nature's precise use of noncovalent interactions, and aims at using these weak, intermolecular forces to control chemical structure and reactivity. To this end, the work presented in this thesis focuses on the systematic use of non-covalent interactions along with metal coordination to construct both simple and sophisticated supramolecular architectures tailored to selective recognition and separation processes. Some of the development topologies may work as molecular materials with unique and useful properties.

The confined space within a cage is endowed with unique properties resulting from the fact that in a restricted volume encounters are prolonged, prearranged, and isolated from the medium. In the first part of this thesis, we demonstrate the obtainment of the giant coordination cages $M_{12}L_{24}$ thanks to the solution self-assembly of twenty four bis-pyridyl ligands (L), functionalized with an iodotetrafluorobenzene moieti, and twelve Pd(II) ions (M). Cold-spray ionization mass spectrometry and ^{1}H and diffusion NMR experiments confirm the formation and stability of the giant coordination cages. Artificial self-assembled cages can often encapsulate guest molecules and promote unusual reactivity; the molecular modeling studies of all the synthesized nanocages show there is enough inside space for guest uptake. The 24-fold endohedral functionalization with halogen bond donor sites and fluorinated motifs enables for studying halogen-bonding and fluorophilicity in a confined spaces. The halogen bond donor groups decorating the inside face of the obtained nanosized capsule will be used to control the nature of the guest molecule(s) encapsulated in the cage and to direct the reactivity of these molecule(s).

In the second part of the thesis we have shown that the bis-(trimethylammonium)alkane diiodides are a very versatile class of organic solids displaying a transient dynamic porosity so that they absorb/exchange and release small molecules in a controllable and selective fashion. The reported dynamic response of these onium derivatives towards α,ω-diiodoperfluoroalkanes (DIPFAs) demonstrates their potential for separating DIPFA's mixtures via halogen bond formation, and the cavity-directed reactivity in the synthesis and interconversion of interhalogen polyanions confirms their practical usefulness. Similarly these onium derivatives readily form supramolecular and hydrogen bonded complexes with size-matching dicarboxylic acids both in solution and solid state. The X-ray structures of pure bis-(trimethylammonium)alkane diiodides and their cocrystals suggest that once the size-matching dicarboxylic acid forms hydrogen bonds with iodide anions, the $I^{-}\cdots HOOC–(CH_2/CF_2)_n–COOH\cdots I^{-}$ trimer works as a supramolecular template and enacts size complementarity between the host-guest modules. The combined use of hydrogen and halogen bonds enabled for

the selective guest uptake and its quantitative recovery, via self-assembly processes. The size-matching controlled cocrystal formation allows for selective solubility variation of dicarboxylic acids and provides a new direction for selective recognition and separation.

In the third part of the thesis, halogen-bonding based assembly is used as a reliable tool to achieve a great variety of supramolecular architectures and to design topologies endowed with useful functional properties. We describe that a library of supramolecular anionic networks showing Borromean interpenetration has been prepared by self-assembly of crypt-222, several metal or ammonium halides, and bis-homologous α,ω-diiodoperfluoroalkanes. The halogen-bonding and its directionality has been confirmed as a reliable tool which predictably translates the geometrical features of tectons into sophisticated Borromean networks. The reported results contribute to the field of anion-templated assembly of interpenetrated and interlocked structures, a field that has strongly contributed to some recent progresses of supramolecular chemistry. The change of cations and anions in cocrystals substantially affects the bonding features, namely the energetic aspects, in the self-assembled systems while it causes minor modifications of their metrics. On the other hand, the change of the diidoperfluoroalkane is the most influential element for the metric of obtained cocrystals and has a minor effect on cation-anion attraction and on XB. Obtained systems consistently indicate that the metric features plays a more influential role than energetic features in determining the topology of the tetra-component cocrystals.

The interest in crypt-111 and its derivatives is due to their low nucleophilicity and very high proton affinity. On reaction with acids, crypt-111 functions as a proton sponge: The transient exo-protonated species rapidly evolves into the endo-protonated species which is endowed with an exceptional stability as protonation relieves the strain induced by the lone pair's proximity inside the cavity. The single crystal X-ray studies, spectroscopic analysis and quantum chemical calculations of pure $H^+\subset$crypt-111 iodide and of its halogen bonded cocrystals with DIPFAs suggest a high degree of conformational variability in $H^+\subset$crypt-111 unit which may be related to different locations of the acidic proton in pure $H^+\subset$crypt-111 iodide and in its cocrystals. Some initial studies have been made to establish the role of $I\cdots I^-$ halogen bond in lowering the crystal symmetry and affecting the proton location in the supramolecular cation but further investigations are required before general conclusions are drawn on $H^+\subset$crypt-111 structure.

Finally, part of the thesis describes the synthesis of new trimeric complexes obtained upon halogen bond driven self-assembly of diiodoperfluorocarbons, acting as halogen bond

donors, with alkoxystilbazole derivatives functionalized with a methacrylate terminal group, acting as halogen bond acceptors. Despite the non-mesomorphic nature of the starting materials, most of the halogen bonded complexes show a liquid-crystalline behavior with smectic A phases. Single crystal X-ray diffraction analysis confirmed that N···I halogen bonds are largely responsible for the self-assembly of the complementary modules. A clear segregation between perfluorocarbon and hydrocarbon molecules is present and is perfectly consistent with the lamellar phase observed in the LC state. The obtained supramolecular mesogens possess reactive groups suitable for incorporation into liquid crystalline elastomeric actuators.

Chapter 7

Experimental Section

7.1 Self-assembled $M_{12}L_{24}$ spherical cages to study the halogen bonding interactions in confined space.

7.1.1. Materials and methods

Commercial HPLC-grade solvents were used without any further purification. Starting materials were purchased from Sigma–Aldrich, TCI (Europe and Japan) and Apollo Scientific. Thin layer chromatography (TLC) was performed on silica gel 60 F_{254} (E. Merck) and visualized under a UV lamp at 254 nm. Column chromatography was carried out on silica gel 60F (Merck 9385, 0.040–0.063 mm). Flash chromatography was carried with Biotage Isolrea-TM coupled with UV detector. Nuclear magnetic resonance (NMR) spectra were recorded on Bruker Avance 500 and 600 spectrometers. ^{1}H and ^{1}H DOSY NMR spectra were recorded at ambient temperature at 500 MHz, while the ^{13}C and ^{19}F spectra were recorded at ambient temperature at 400 and 600 MHz respectively. The chemical shifts are given in ppm. DMSO-*d*6, $CDCl_3$, CD_3NO_2 were used as solvents. Melting points were determined with a Reichert instrument by observing the melting and crystallizing process through an optical microscope. High-resolution mass spectra were recorded on an Agilent 6210 LC-TOF electron spray ionization (ESI) mass spectrometer. High-resolution CSI-TOF mass spectra were measured on a Bruker maXis® equipped with an auto-sample injection system. Mass spectra were processed on Bruker Data Analysis (Version 4.0 SP2) software and the simulations were performed on Bruker Isotope Pattern software.

7.1.2. Synthesis of Ligands

Synthesis of halogen bonding (XB) donor ligands

Synthesis of 1-acetoxy -2,6-dibromobenzene (V1)

The mixture of 2,6-dibromobenzene (5 g, 20 mmol) and pyridine (16.6 mL, 206 mmol) was stirred in acetic anhydride (70 mL) at 80 °C for 4 hours under nitrogen atmosphere. Reaction progress was monitored by TLC, after the complete conversion, reaction mixture was evaporated under reduced pressure and the residue was purified by recrystallization ($CHCl_3$: hexane 50:50) to give the title compound. White solid (2.28 g) in 98% yield. Melting point: 46-47 °C. ^{1}H NMR (500 MHz, $CDCl_3$) 7.56 (d, J = 8.1 Hz, 2H), 7.26 (t, J = 8.1 Hz, 1H), 2.39 (s, 3H).

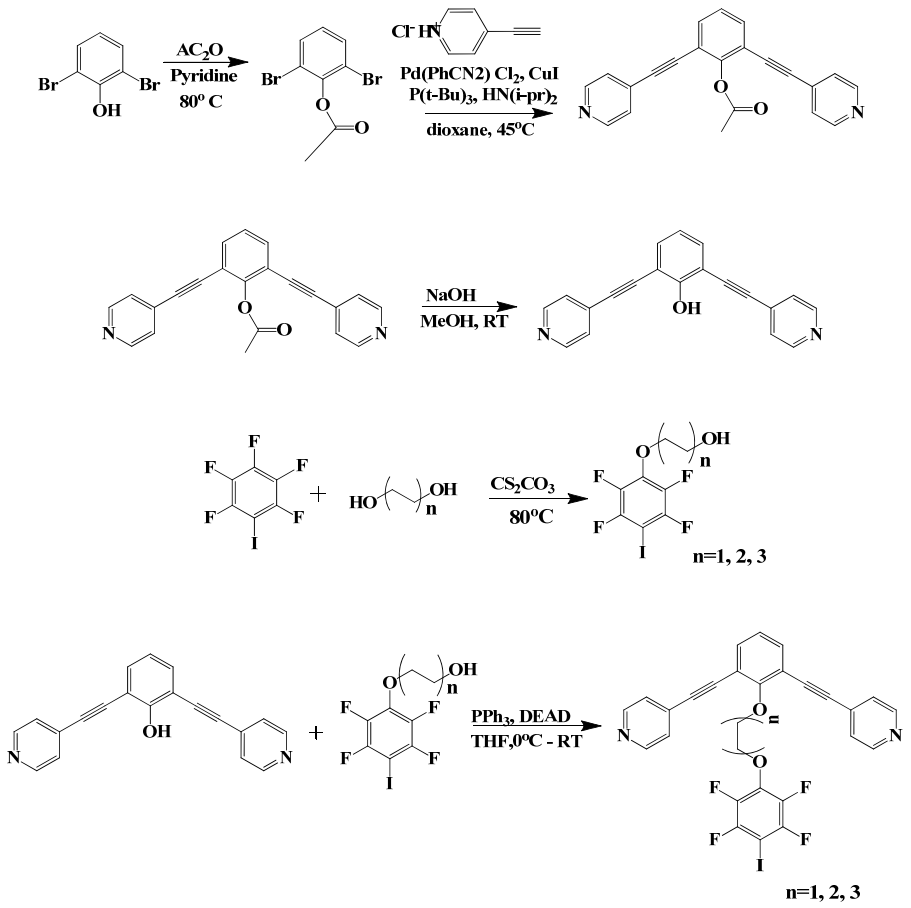

Scheme 7.1.1 Synthetic root developed for the preparation of XB donor ligands **L1-L3.**

Synthesis of 1-acetoxy-2,6-bis(4-pyridylethynyl)benzene (V2)

Tri-*t*-butylphosphine (3.39 mL, 1.36 mmol; 10% solution in hexane) and diisopropylamine (16.5 mL, 116 mmol) was added to a mixture of 1-acetoxy-2,6-dibromobenzene (3.23 g, 11.0 mmol), 4- ethynylpyridine hydrochloride (4.07 g, 29.1 mmol), $Pd(PhCN)_2Cl_2$ (253 mg, 0.660 mmol) and copper (I) iodide (76.2 mg, 0.400 mmol), and these mixture was stirred in 1,4-dioxane (40 mL) at 40° C for 12 h under argon atmosphere. The reaction mixture was diluted with ethyl acetate (200 mL) and filtered. After dilution with water (200 mL), the mixture was washed with ethylene diamine (5 mL) and extracted with ethyl acetate. The combined organic layer was dried over anhydrous sodium sulfate and evaporated under reduced pressure, and the residue was purified by column chromatography on silica gel ($CHCl_3$: methanol = 100:1).The obtained title compound as a white solid (2.9 g) yield: 81%. MP: 128 -130 °C. ^{1}H NMR (500 MHz, $CDCl_3$, 300 K); 8.63 (d, J = 6.5 Hz, 4H), 7.62 (d, J = 7.5 Hz, 2H), 7.36 (d, J = 6.0 Hz, 4H), 7.30 (t, J = 8.0 Hz, 1H), 2.44 (s, 3H). ESI-MS, positive-ion mode: m/z 353.

Synthesis of 2, 6-bis(4-pyridylethynyl)phenol (V3)

Exactly 3 M solution of NaOH (4.55 mL, 13.6 mmol) was added to 1-acetoxy-2,6-bis(4-pyridylethynyl)benzene (2.25 g, 6.65 mmol) in MeOH (85 mL), and the mixture was stirred at room temperature for 30 min. The reaction mixture was evaporated under reduced pressure, then CH_2Cl_2 (200 mL) and water (100 mL) were added to the solid. The mixture was neutralized with aqueous solution of NH_4Cl, and the product was extracted with CH_2Cl_2. The combined organic layer was dried over anhydrous sodium sulfate and evaporated under reduced pressure to give the title compound as a white solid, 1.93 g, 96% yield. MP 134.4°C. ^{1}H NMR (500 MHz, $CDCl_3$, 300 K) 8.61 (d, *J* = 5.7 Hz, 4H), 7.50 (d, *J* = 7.9 Hz, 2H), 7.35 (d, *J* = 5.9 Hz, 4H), 6.95 (t, *J* = 7.7 Hz, 1H). ESI-MS, positive-ion mode: m/z 310.

Synthesis of 4-(2,3,5,6-tetrafluoro-4-iodophenoxy) ethanol (V4)

Iodopentafluoro benzene (4.54 mL, 34 mmol), ethylene glycol (19 mL, 340 mmol) and sodium carbonate (3.96 g, 37.4 mmol) were stirred for 16 hours at 80 ºC. Reaction progress was monitored by TLC and reaction mixtures were loaded to the silica gel column chromatography (Hexane: EtOAc from 8:2 to 6:4). Yellow oil, Yield: 5.7 gram, percentage yield 60.5. ^{1}H NMR $CDCl_3$, 500 MHz) 4.30 (t, *J*= 7.6 Hz, 2H), 3.89 (t, *J*= 6.5 Hz, 2H), 2.34 (s, 1H). ^{13}C NMR: ($CDCl_3$, 400 MHz) 146.9, 142.1, 134.6, 70.1, 60.9, 59.8; ^{19}F NMR: ($CDCl_3$, 600 MHz) -121, -158. ESI-MS, positive-ion mode: m/z 336.

Synthesis of 4-(2,3,5,6-tetrafluoro-4-iodophenoxy) butanol (V5)

Iodopentafluoro benzene (0.907 mL, 6.8 mmol), 1,4 butane diol (3.1 mL, 34mmol) and cesium carbonate (2.69 g, 8.16 mmol) were stirred for 24 hours at 80 ºC. Reaction progress was monitored by TLC and reaction mixture were loaded to the silica gel column chromatography (Hexane: EtOAc from 8:2 to 6:4). Colorless oil, Yield: 1.8 gram, Yield 67%. ^{1}H NMR ($CDCl_3$, 500 MHz) 4.42 (t, *J*= 7.5 Hz, 2H), 4.33(t, *J*= 6.5 Hz, 2H), 1.89 (m, 2H), 1.59 (m, 2H); ^{13}C NMR: ($CDCl_3$, 400 MHz) 146.6, 141.8, 134.5, 69.7, 60.9, 59.7, 26.8, 25.4; ^{19}F NMR: ($CDCl_3$, 600 MHz) -121 ppm, -157 ppm. ESI-MS, positive-ion mode: m/z 365.

4-(2,3,5,6-tetrafluoro-4-iodophenoxy) hexanol (V6)

Iodopentafluoro benzene (0.907 mL, 6.8 mmol), hexane diol (3.9 g, 33mmol) and cesium carbonate (2.66g, 8.16 mmol) were stirred for 24 hours at 80ºC. Reaction progress was monitored by TLC and reaction mixture was loaded to the silica gel column chromatography (Hexae: EtOAc from 8:2 to 6:4). Yield: 5.7 gram, Percentage Yield: 68%. ^{1}H NMR ($CDCl_3$,

500 MHz) 4.30 (t, *J*= 7.4 Hz, 2H), 3.89(t, *J*= 6.6 Hz, 2H), 1.94 (m, 2H), 1.62 (m, 2H), 1.54 (m, 4H); ^{13}C NMR: ($CDCl_3$, 400 MHz) 146.9, 143.1, 134.7, 62.8, 61.7; ^{19}F NMR: ($CDCl_3$, 600 MHz) -121 ppm, -158 ppm; ESI-MS, positive-ion mode: m/z 393.

Synthesis of ligand L1 (2, 3, 5, 6-tetrafluoro-4-iodophenoxy (ethoxy1, 3phenylene) bis (ethyne-2, 1-diyl) dipyridine)

Diisopropyl azodicarboxylate (0.238 mL, 1.50mmol) was added dropwise to the mixture of 2, 6-bis (4-pyridylethynyl) phenol **V3** (0.25 g, 0.843 mmol) and 4-(2, 3, 5, 6-tetrafluoro-4-iodophenoxy) ethanol **V4** (0.425 g, 1.264 mmol) in dry THF under inert dry conditions at 0° C. The reaction mixture was further stirred in room temperature for 4 hours and diluted with $CHCl_3$ (20 mL), washed with water (15 mL) and extracted with $CHCl_3$, dried over anhydrous Na_2SO_4 and concentrated under reduced pressure.

The crude dried mixture was dissolved in ethyl acetate (5 mL) and 4 N HCl in ethyl acetate was added dropwise (2 mL). The precipitate (protonated product) is filtered off under suction pump and washed with pure ethyl acetate. The $NaHCO_3$ solution (4-6 equivalents, 20 mL) was added to the filtered solid and extracted with $CHCl_3$ (40 mL), dried over anhydrous Na_2SO_4 and concentrated under reduced pressure. Flash chromatography ($CHCl_3$: MeOH, 9:1). Product obtained: white solid, yield: 75%, 300 mg. ^1H NMR (500 MHz, $CDCl_3$, 300 K); 8.62 (d, *J*= 6.5 Hz, 4H), 7.56 (d, *J*= 7.6 Hz, 2H), 7.36 (d, *J*= 6.0 Hz, 4H), 7.15 (t, *J*= 8.0 Hz,1H), 4.42 (t, *J*= 7.9 Hz, 2H), 4.33 (t, *J*= 7.5 Hz, 2H). ^{13}C NMR: ($CDCl_3$, 400 MHz) 166.1, 150.14, 146, 143.2, 134.2, 126.1, 127.9, 80.6, 77.8, 133.6, 119.5, 111.5, 67.8, 61.2. ^{19}F NMR (600 MHz, $CDCl_3$, 300 K); 123.93 ppm, -157.0 ppm; Exact mass calculation, positive-ion mode, obtained m/z 615.0161 and calculated m/z 615.0187.

Synthesis of ligand L2 (4,4'-((2-(4-(2,3,5,6-tetrafluoro-4-iodophenoxy)butoxy)-1,3-phenylene)bis(ethyne-2,1-diyl))dipyridine)

Diisopropyl azodicarboxylate (0.238 mL, 1.50 mmol) was added dropwise to the mixture of 2, 6-bis (4-pyridylethynyl) phenol **V3** (0.25g, 0.843 mmol) and 4-(2, 3, 5, 6-tetrafluoro-4-iodophenoxy) butanol **V5** (0.461 g, 1.265 mmol) in THF at 0° C; further stirred in room temperature for 3 hours. The reaction mixture was diluted with $CHCl_3$ (20 mL), washed with water (15 mL) and extracted with $CHCl_3$, dried over anhydrous Na_2SO_4 and concentrated under reduced pressure.

The crude mixture was dissolved in ethyl acetate (5 mL) and 4N HCl in ethyl acetate (2 mL) was added dropwise. The precipitate (protonated product) is filtered off under suction

pump and washed with pure ethyl acetate. The $NaHCO_3$ solution (4-6 equivalents, 20 mL) was added to the filtered solid and extracted with $CHCl_3$ (40 mL), dried over anhydrous Na_2SO_4 and concentrated under reduced pressure. Flash chromatography ($CHCl_3$: MeOH, 9:1). Product obtained: white solid, 290 mg, yield 76%. ^{1}H NMR (500 MHz, $CDCl_3$, 300 K); 8.64 (d, *J*= 6.5 Hz, 4H), 7.41 (d, *J*= 7.6 Hz, 2H), 7.36 (d, *J*= 6.0 Hz, 4H), 7.15 (t, *J*= 8.0 Hz, 1H), 4.42 (t, *J*= 7.9 Hz, 2H), 4.33 (t, *J*= 7.5 Hz, 2H), 2.44 (m, 4H). ^{13}C NMR: (CDCl3, 400 MHz) 167.1, 150.5, 146.5, 143.6, 134.7, 126.3, 126.9, 133.6, 119.5, 111.5, 80.3, 77.6, 67.8, 61.2. 27.8. ^{19}F NMR (600 MHz, CDCl3, 300 K);-122.98 ppm, -156.8 ppm. Exact mass calculation, positive-ion mode, obtained m/z 642.9260 and calculated m/z 642.9281.

Synthesis of ligand L3 (4,4'-((2-((6-(2,3,5,6-tetrafluoro-4-iodophenoxy)hexyl)oxy)-1,3-phenylene)bis(ethyne-2,1-diyl))dipyridine)

Diisopropyl azodicarboxylate (0.180 mL, 1.230 mmol) was added dropwise to the mixture of 2, 6-bis (4-pyridylethynyl) phenol **V3** (0.20 g, 0.674 mmol) and 4-(2, 3, 5, 6-tetrafluoro-4-iodophenoxy) hexanol **V6** (0.370 g, 0.943 mmol) in THF at 0° C further stirred in room temperature for 4 hours. The reaction mixture was diluted with $CHCl_3$ (15 mL), washed with water (10 mL) and extracted with $CHCl_3$, dried over anhydrous Na_2SO_4 and concentrated under reduced pressure.

The crude mixture was dissolved in ethyl acetate (5 mL) and 4N HCl in ethyl acetate (2 mL) was added dropwise. The precipitate (protonated product) is filtered off under suction pump and washed with pure ethyl acetate. The $NaHCO_3$ solution (4-6 equivalents, 20 mL) was added to the filtered solid and extracted with $CHCl_3$ (40 mL), dried over anhydrous Na_2SO_4 and concentrated under reduced pressure. Flash chromatography ($CHCl_3$: MeOH, 9:1). Product obtained: white solid, 310 mg, yield 79%. ^{1}H NMR (500 MHz, $CDCl_3$, 300 K); 8.64 (d, *J*= 6.5 Hz, 4H), 7.41 (d, *J*= 7.6 Hz, 2H), 7.36 (d, *J*= 6.0 Hz, 4H), 7.15 (t, *J*= 8.0 Hz, 1H), 4.42 (t, *J*= 7.9 Hz, 2H), 4.33 (t, *J*= 7.5 Hz, 2H), 2.44 (m, 4H), 1.59 (m, 4H). ^{13}C NMR: ($CDCl_3$, 400 MHz) 166.9, 150.3, 145.9, 143.6, 134.5, 126.3, 127.1, 133.3, 119.7, 111.5, 80.5, 77.6, 67.6, 61.2. 27.8, 22.9. ^{19}F NMR (600 MHz, $CDCl_3$, 300 K); -123.79 ppm, -156.9 ppm. Exact mass calculation, positive-ion mode, obtained m/z 670.4720 and calculated m/z 670.4768.

Synthesis of hydrofluorinated ligand

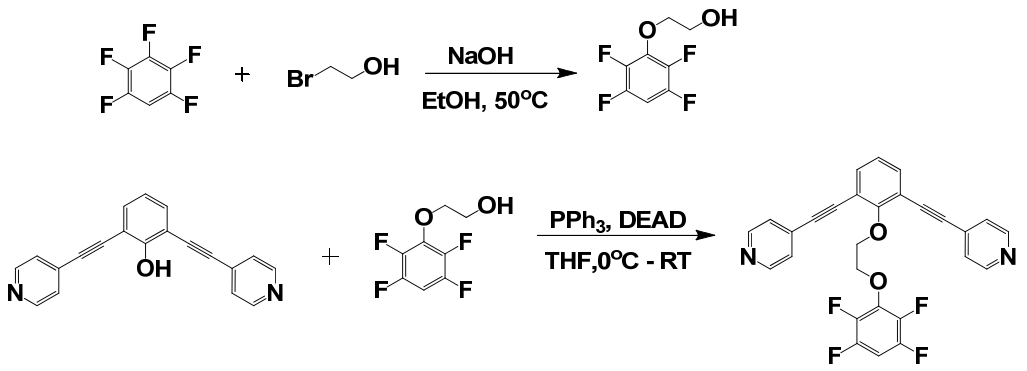

Scheme 7.1.2 Synthetic root developed for the preparation of hydrofluorinated ligand **L4**

Synthesis of 2-(2,3,5,6-tetrafluorophenoxy)ethanol (V6)

2,3,5,6 Tetrafluoro phenol (1 g, 6 mmol) was dissolved dry EtOH (8 mL) under nitrogen atmosphere for 15 minutes. NaOH (12 mm, 0.48 g) was added and stirred at 50 °C for 2 hours. 2- Bromo ethanol (0.9 mL, 12 mmol) was added dropwise to the same reaction mixture and refluxed under nitrogen for 20 hours. Cooled the reaction mixture to room temperature and removed the ethanol then diluted with 8 0mL of $CHCl_3$ and 10% NaOH solution was added (1.5 mL). Organic phase was extracted and dried over anhydrous Na_2SO_4 and concentrated under reduced pressure. Flash chromatography (Hexane: EtOAc from 8:2 varied up to 6:4). Obtained product colorless oil, yield: 57%. ^{1}H NMR (500 MHz, $CDCl_3$, 300 K); 6.10 (m, 1H), 3.89 (m, 4H), 2.34 (s, 1H). ^{19}F NMR (600 MHz, $CDCl_3$, 300 K) -143, -160. ESI-MS, positive-ion mode: m/z 210.

Synthesis of ligand L4 (4,4'-((2-(2-(2,3,5,6-tetrafluorophenoxy)ethoxy)-1,3-phenylene)bis(ethyne-2,1-diyl))dipyridine)

Diisopropyl azodicarboxylate (0.180 mL, 1.230 mmol) was added dropwise to the mixture of 2, 6-bis (4-pyridylethynyl) phenol V3 (0.20 g, 0.674 mmol) and 4-(2, 3, 5, 6-tetrafluoro phenoxy) ethanol V7 (0.22 g, 1 mmol) in dry THF at 0 °C further stirred in room temperature for 3 hours. The reaction mixture was diluted with $CHCl_3$ (15 mL), washed with water (10 mL) and extracted with $CHCl_3$, dried over anhydrous Na_2SO_4 and concentrated under reduced pressure.

The crude mixture was dissolved in ethyl acetate (5 mL) and 4 N HCl in 1-4 dioxane (2 mL) was added dropwise. The precipitate (protonated product) is filtered off under suction pump and washed with pure ethyl acetate. The $NaHCO_3$ solution (5 equivalents, 20 mL) was

added to the filtered solid and extracted with $CHCl_3$ (40 mL), dried over anhydrous Na_2SO_4 and concentrated under reduced pressure. Product obtained: brown solid, yield: 69%, 295mg. ^1H NMR (500 MHz, $CDCl_3$, 300 K); 8.62 (d, *J*= 6.5 Hz, 4H), 7.56 (d, *J*= 7.6 Hz, 2H), 7.36 (d, *J*= 6.0 Hz, 4H), 7.20 (t, *J*= 8.0 Hz, 1H). 6.10 (m, 1H), 4.42 (t, *J*= 7.9 Hz, 2H), 4.33 (t, *J*= 7.5 Hz, 2H).^{19}F NMR (600 MHz, $CDCl_3$, 300 K);- 143.92 ppm, -159.8 ppm; Exact mass calculation, positive-ion mode, obtained m/z 488.1162 and calculated m/z 488.1018.

7.1.3. Synthesis of spherical cages L1-L4

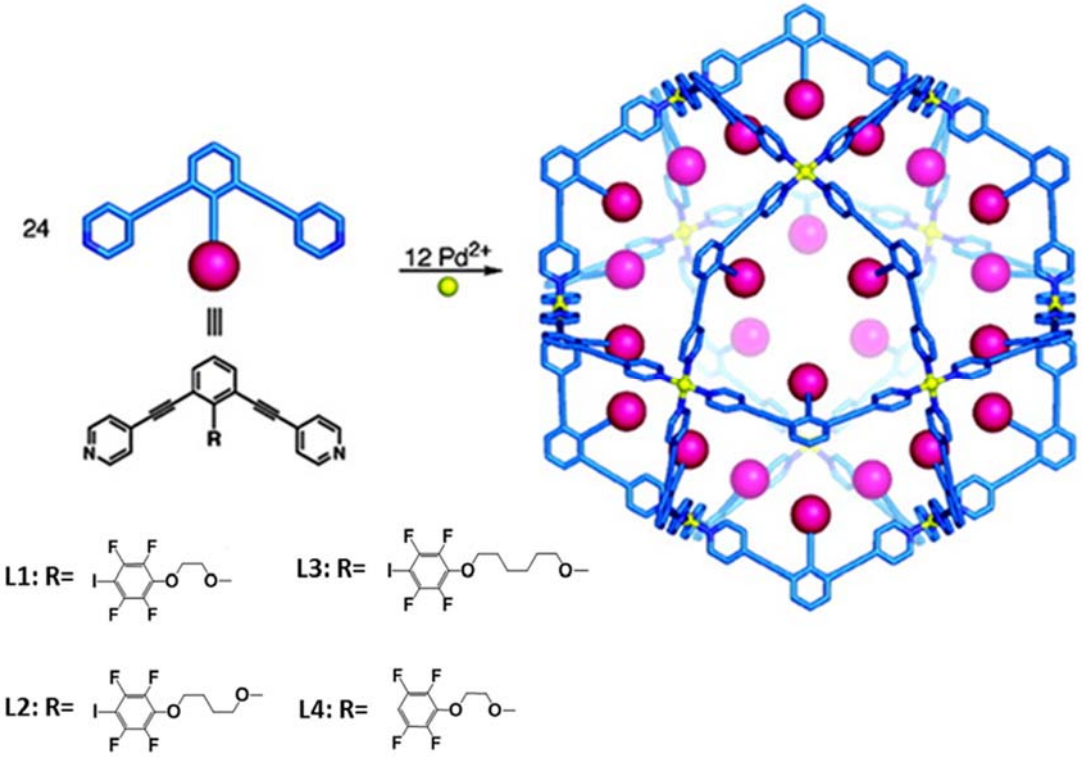

Figure 7.1.1 Self-assembly of $M_{12}L_{24}$ spherical complexes with 24 endohedral XB donor group (L1-L3) and hydrofluorinated ligand (L4)

Self-assembly of L1

Ligand **L1** (10 mg, 0.016 mmol) was treated with dimethyl sulfoxide solution of [Pd $(CH_3CN)_4$] $(BF_4)_2$ (0.8 mM, 0.8 mL) at 60° C for 3 hours. The quantitative formation of sphere for **L1** was confirmed by ^1H, ^1H DOSY NMR and CSI-TOF MS analysis. ^1H NMR (500 MHz, DMSO-*d*6, 300 K); 9.18 (br, s, 96 H), 7.76 (br, s, 96 H), 7.63 (br, s, 48 H), 7.23 (br, s, 24 H), 4.72(br, s, 48 H), 4.63 (br, s, 48 H). ^{19}F NMR (600 MHz, DMSO-*d*6, 300 K); -123.9 ppm, -157.1 ppm. High Resolution Mass: $(C_{19}H_{15}N_2O_2F_4I)_{24}$ $Pd_{12}(BF4)_{11}$; Charge balance 13

Calculated monotropic Mass: 16964.14; fragmentation: 1304.93

Calculated Average mass: 16975.75; fragmentation: 1305.82

Experimentally Obtained fragmentation: 1305.62

Self-assembly of L2

Ligand **L2** (10.7 mg, 0.016 mmol) was treated with dimethyl sulfoxide solution of [Pd (CH_3CN)$_4$] (BF_4)$_2$ (0.8 mM, 0.8 mL) at 60° C for 3 hours. The quantitative formation of sphere for **L2** was confirmed by ^{1}H and ^{1}H DOSY NMR analysis. ^{1}H NMR (500 MHz, DMSO-*d*6, 300 K); 9.21 (br, s, 96 H), 7.75 (br, s, 96 H), 7.68 (br, s, 48 H), 7.27 (br, s, 24 H), 4.29 (br, s, 48 H), 4.20 (br, s, 48 H) 1.87 (br, s, 96 H); ^{19}F NMR (600 MHz, DMSO-*d*6, 300K); -123.6 ppm, -157.0 ppm.

Self-assembly of L3

Ligand **L3** (11.3 mg, 0.018 mmol) was treated with dimethyl sulfoxide solution of [Pd (CH_3CN)$_4$] (BF_4)$_2$ (0.8 mM, 0.8 mL) at 60° C for 3 hours. The quantitative formation of sphere for **L3** was confirmed by ^{1}H, ^{1}H DOSY NMR and CSI-TOF MS analysis. ^{1}H NMR (500 MHz, DMSO-*d*6, 300 K); 9.20 (br, s, 96 H), 7.71 (br, s, 96 H), 7.62 (br, s, 48 H), 7.22 (br, s, 24 H), 4.17 (br, s, 48 H), 3.99 (br, s, 48 H), 1.74 (br, s, 48 H), 1.52 (br, s, 48 H), 1.43 (br, s, 48 H), 1.34 (br, s, 48 H). ^{19}F NMR (600 MHz, DMSO-*d*6, 300 K) -123.8 ppm, -157.5 ppm.

Mass: $(C_{32}H_{27}N_2O_2F_4I)_{24}$ $Pd_{12}(BF4)_{10}$; Charge balance 14

Calculated monotropic Mass: 18222.64; fragmentation: 1301.6

Calculated Average mass: 18235.50; fragmentation: 1302.53

Experimentally Obtained fragmentation: 1302.62

Self-assembly of L4

Ligand **L4** (7.9 mg, 0.016 mmol) was treated with dimethyl sulfoxide solution of [Pd (CH_3CN)$_4$] (BF_4)$_2$ (0.8 mM, 0.8 mL) at 60° C for 3 hours. The quantitative formation of sphere for **L3** was confirmed by ^{1}H and ^{1}H DOSY NMR analysis. ^{1}H NMR (500 MHz, DMSO-*d*6, 300 K); 9.18 (br, s, 96 H), 7.76 (br, s, 96 H), 7.63 (br, s, 48 H), 7.23 (br, s, 24 H), 6.10(br, s 24 H) 4.72(br, s, 48 H), 4.63 (br, s, 48 H). ^{19}F NMR (600 MHz, DMSO-*d*6, 300 K); -143.12 ppm, -160.1 ppm.

7.1.4. ^{1}H NMR spectra for the self-assembled complexes L1-L4

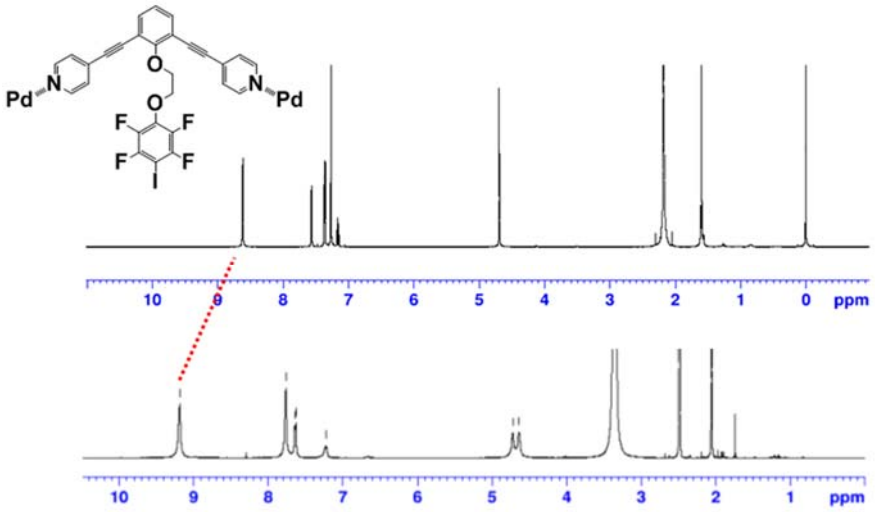

Figure 7.1.2 Comparison of ^{1}H NMR spectra of ligand **L1** and its $M_{12}L_{24}$ spherical complex. Top: ^{1}H NMR spectra of the pure ligand **L1**; Bottom: ^{1}H NMR spectra of $M_{12}L_{24}$ complex formed by self-assembly of 12 ligands (L1) and 24 palladium metals. The red dotted line shows downfield shift of protons close to the pyridyl nitrogen ring is the characteristic of the coordination of the pyridine rings to the Pd ion.

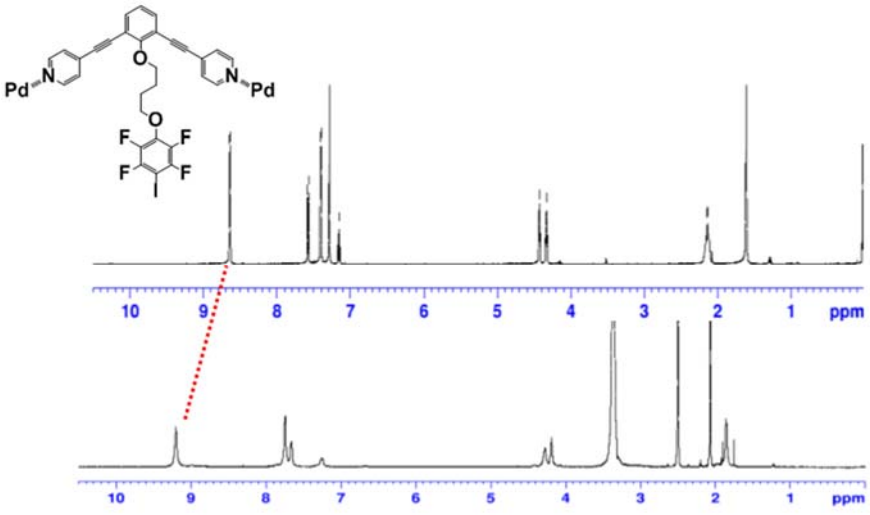

Figure 7.1.3 Comparison of ^{1}H NMR spectra of ligand **L2** and its $M_{12}L_{24}$ spherical complex. Top: ^{1}H NMR spectra of the pure ligand **L2**; Bottom: ^{1}H NMR spectra of $M_{12}L_{24}$ complex formed by self-assembly of 12 ligands (L2) and 24 palladium metals. The red dotted line shows downfield shift of protons close to the pyridyl nitrogen ring is the characteristic of the coordination of the pyridine rings to the Pd ion.

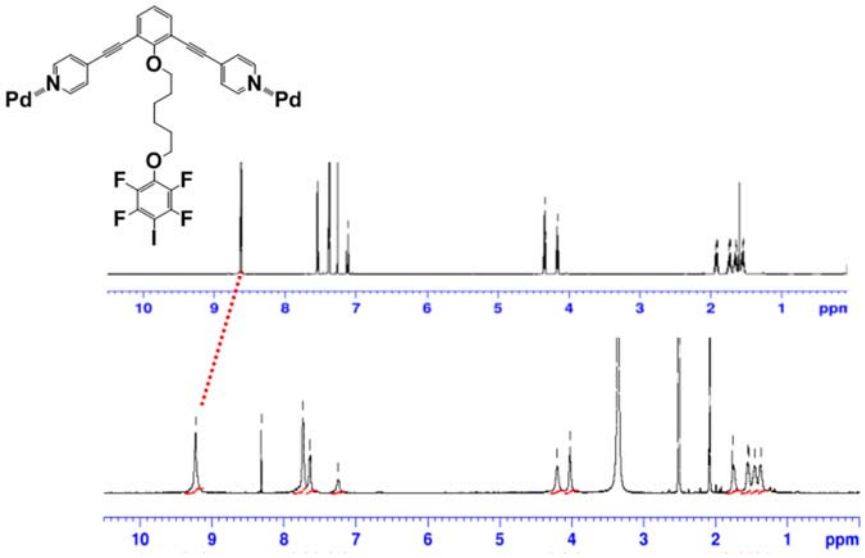

Figure 7.1.4 Comparison of ^{1}H NMR spectra of ligand **L3** and its $M_{12}L_{24}$ spherical complex. Top: ^{1}H NMR spectra of the pure ligand **L3**; Bottom: ^{1}H NMR spectra of $M_{12}L_{24}$ complex formed by self-assembly of 12 ligands (L3) and 24 palladium metals. The red dotted line shows downfield shift of protons close to the pyridyl nitrogen ring is the characteristic of the coordination of the pyridine rings to the Pd ion.

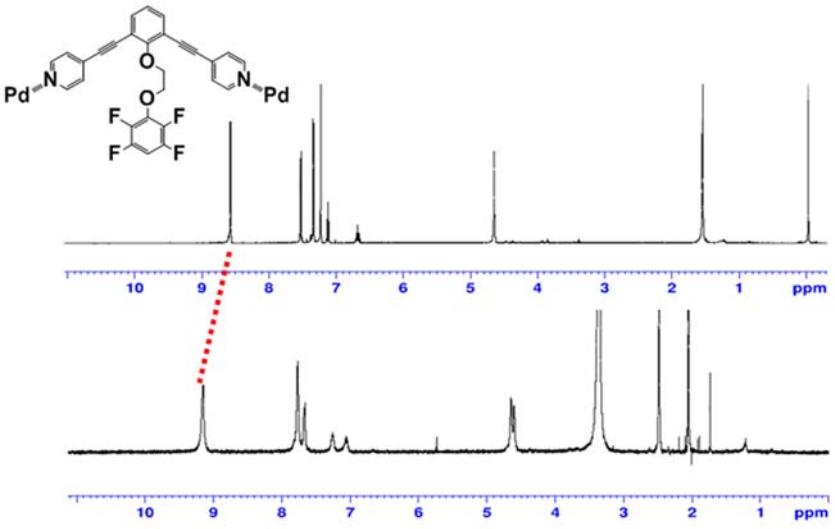

Figure 7.1.5 Comparison of ^{1}H NMR spectra of ligand **L4** and its $M_{12}L_{24}$ spherical complex. Top: ^{1}H NMR spectra of the pure ligand **L4**; Bottom: ^{1}H NMR spectra of $M_{12}L_{24}$ complex formed by self-assembly of 12 ligands (L4) and 24 palladium metals. The red dotted line shows downfield shift of protons close to the pyridyl nitrogen ring is the characteristic of the coordination of the pyridine rings to the Pd ion.

7.1.5. ^{1}H DOSY NMR spectra for the self-assembled complexes L1-L4

^{1}H DOSY NMR spectroscopy is a useful tool for verifying $M_{12}L_{24}$ assembly because the massive spherical complexes typically diffuse much more slowly than their uncomplexed parent ligands. The observation of a single diffusion band in each case supports the conclusion that the self-assembly of these molecular flasks is quantitative. The ^{1}H DOSY NMR spectra for the ligand **L1-L4** and the respective spheres were given below.

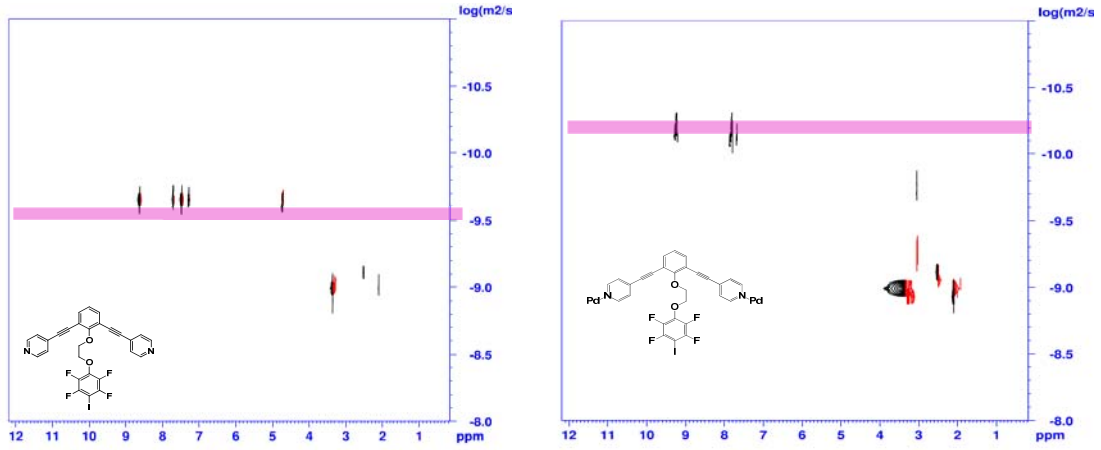

Figure 7.1.6 ^{1}H DOSY NMR spectra (600 MHz, 298 K, DMSO-*d*6) of ligand **L1** (left) and sphere $Pd_{12}L1_{24}$ (right).

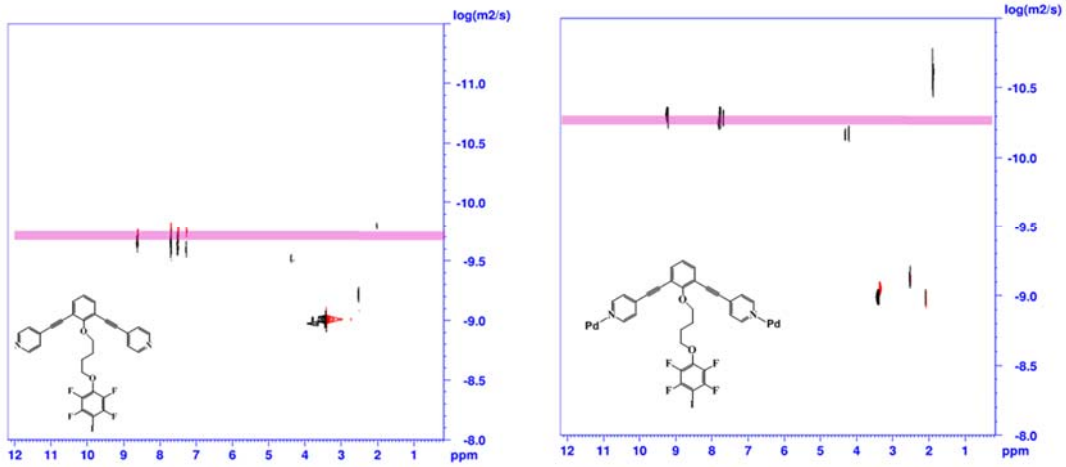

Figure 7.1.7 ^{1}H DOSY NMR spectra (600 MHz, 298 K, DMSO-*d*6) of ligand **L2** (left) and sphere $Pd_{12}L2_{24}$ (right).

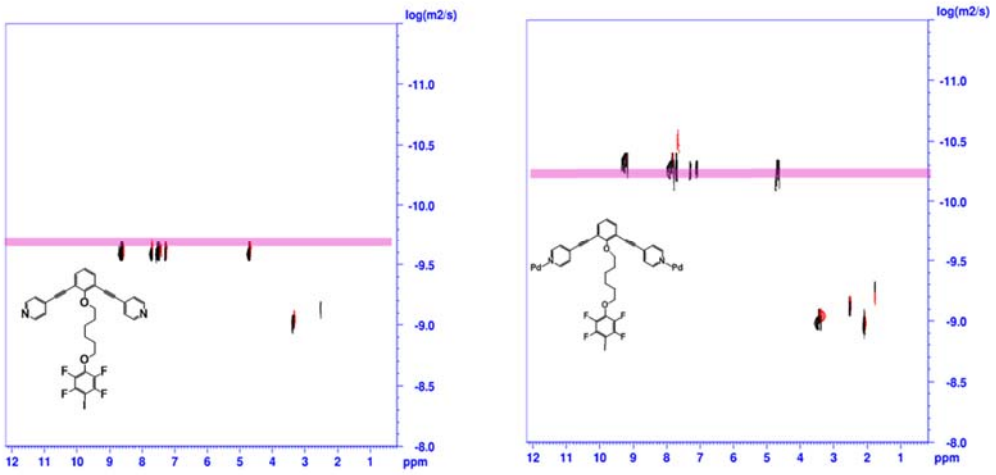

Figure 7.1.8 [1]H DOSY NMR spectra (600 MHz, 298 K, DMSO-*d*6) of ligand **L3** (left) and sphere $Pd_{12}L3_{24}$ (right)

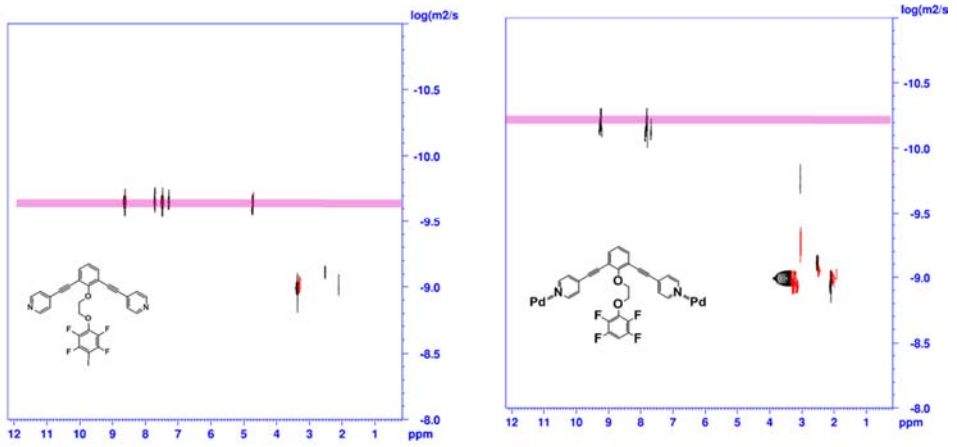

Figure 7.1.9 [1]H DOSY NMR spectra (600 MHz, 298 K, DMSO-*d*6) of ligand **L4** (left) and sphere $Pd_{12}L4_{24}$ (right)

7.1.6. Single crystal X-ray analysis

The crystals were diffracted using Mo-Kα radiation on a Bruker KAPPA APEX II diffractometer with a Bruker KRYOFLEX low temperature device. Crystal structures of the reported complexes were solved by direct method and refined against F^2 using SHELXL97[1]. Packing diagrams were generated using Mercury 3.8.[2] Intermolecular interactions were analysed with PLATON. [3] The non-hydrogen atoms were refined anisotropically and hydrogen atoms were refined using difference Fourier map or positioned geometrically.

Ligand L1 and L2 were crystallized in $CHCl_3$ solution at room temperature. After 3-5 days colourless plate shaped crystals were isolated and used single crystal analysis. The data collection, refinement and other crystallographic information details were provoided in table 7.1.1.

Table 7.1.1 Crsyallographic information table for ligand **L1** and **L2**

Name	**L1**	**L2**
Chemical formula	C_{25} H_{16} N_2 O_2 F_4 I	C_{54} H_{40} N_4 O_4 F_8 I2
Formula weight	614.34	1270.0
Crystal system, space group	Monoclinic, P21/c	Triclinic, P -1
Temperature (K)	100 K	100 K
a (Å)	11.8922(15)	10.9507(7)
b (Å)	11.1077(14)	11.0332(6)
c (Å)	18.400(2)	16.8392(12)
α(°)	90	89.803(3)
β (°)	97.730(1)	82.830(4)
γ(°)	90	84.757(3)
V (Å^3)	2408.5(5)	2010.11(12)
Z	4	1
μ (mm^{-1})	1.390	1.305
Crystal size (mm^3)	0.42, 0.34, 0.10	0.26, 0.12, 0.08
F(000)	1207.0	1278.1
Diffractometer	Bruker APEX-II CCD area detector diffractometer	
Absorption correction	Based on multi-scan	
No. of measured, independent and observed reflections	19109, 5459, 3467	28061, 11493, 9228
θ_{min} (°)	2.1	1.52
θ_{max} (°)	28.5	28.5
$R_{\_all}$, $R_{\_obs}$	0.031, 0.030	0.051, 0.031
$wR2_{\_all}$, $wR2_{\_obs}$	0.066, 0.065	0.079, 0.069
GOOF	1.034	1.049
No. of parameters	394	702
$\Delta\rho_{max}$, $\Delta\rho_{min}$ (e Å^{-3})	0.56, -0.34	2.5, -1.6

7.2. Supramolecular size-matching hosts for solubility enhancement and separation of dicarboxylic acid mixtures.

7.2.1. Materials and methods

Commercial AR grade solvents were used without any further purification for synthesis and crystallization. Starting materials were purchased from Sigma–Aldrich, TCI (Europe and Japan) and Apollo Scientific. IR spectra were obtained using a Nicolet Nexus FT-IR spectrometer equipped with UATR unit. Melting points were determined with a Reichert instrument by observing the melting and crystallizing process through a polarizable optical microscope. DSC analysis were carried out with a Mettler Toledo DSC600 hot stage (10 and 20 °C/min). NMR spectra (^{1}H and ^{19}F) were recorded at ambient temperature on a Bruker AV-400 spectrometer, at 400 MHz. All chemical shifts are given in ppm. $CDCl_3$, CD_2Cl_2, CD_3OD, CD_3CN and DMSO-d6 were used as a solvent.

7.2.2. General synthetic procedures

7.2.2.1. Synthesis of Dodecamethonium iodide (1-12)

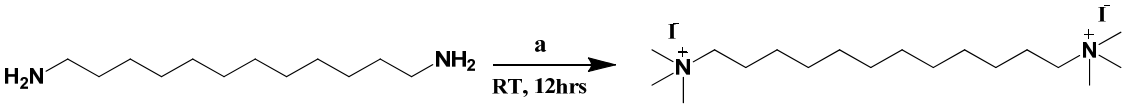

Scheme 7.2.1 Synthesis of dodecamethonium iodide; (a): 1,2,2,6,6-pentamethylpiperidine, MeI in DMF.

Procedure: 3.79 mL (61 mmol) of methyl iodide were added dropwise at ambient temperature to a mixture of dodecanediamine (1 g, 5 mmol) and 1,2,2,6,6-pentamethylpiperidine(3.60 mL, 20 mmol) in DMF (15 mL). The reaction mixture was stirred overnight at room temperature to ensure complete precipitation of the bisquaternary compound. The resulting solid was then filtered, washed with acetone and dried under vacuum to give the pure product. 82% yield, white solid, mp, 222 °C. ^{1}H NMR (400 MHz, CD_2Cl_2:CD_3OD, 10:1): δ 1.30-1.38 (m, 16H), 1.76 (m, 4H), 3.22 (s, 18H), 3.3 (m, 4H). ^{13}C NMR (400 MHz, DMSO): δ 24.8, 26.5, 29.2, 29.7, 30.6, 54.02, 66.8. ESI-MS, positive-ion mode: m/z 413 [M - I], 143 [M - 2I]. I.R. selected bands (cm^{-1}): 3003, 2913, 2848, 1461, 970, 915, 728.

7.2.2.2. Synthesis of bis-onium iodide - dicarboxylic acid cocrystals (1·2 and 1·3 cocrystals). General procedure

7.2.2.2.1. Synthesis of complexes by Crystallization: Equimolar amounts of bis (trimethylammonium) alkane diiodides (**1-10** and **1-12**) and dicarboxylic acids **2** and **3** were dissolved separately in a 1:1 mixture of methanol and acetonitrile or in a 9:1 mixture of dichloromethane and methanol. The two solutions were mixed in a small vial which was placed in a larger vial containing *n*-hexane as a second less efficient solvent and the system was sealed. *n*-Hexane was allowed to diffuse until crystals were formed; crystals were then filtered and washed with fresh solvent.

Complex of decamethonium iodide and adipic acid (1-10·2-4)

White solid, MP of complex: 187- 189 °C, Pure **1-10**: 252 °C, pure **2-4**: 153 °C, I.R. selected bands (cm^{-1}) pure **1-10**: 3486, 3431, 2952, 2858, 1630, 1474, 1475, 964, 907, 584; pure **2-4**: 2961, 1685, 1407, 1275, 1189, 915, 735; **Complex 1-10·2-4**: 3179, 2926, 2850, 1727, 1394, 1230, 1145, 905, 751.

Complex of dodecamethonium iodide and suberic acid (1-12·2-6)

White solid, MP: 188-190 °C, Pure **1-12:** 222 °C, pure **2-6:** 145 °C; I.R selected bands (cm^{-1}): Pure **1-12:** 3003, 2913, 2848, 1461, 970, 939, 915, 728; pure **2-6:** 2913, 2863, 1685, 1409, 1325, 1250, 1187, 917, 795; complex **1-12·2-6:** 3139, 3013, 2925, 2843, 1721, 1388, 1216, 1157, 962, 907, 757.

Complex of decamethonium iodide and octafluoroadipic acid: (1-10·3-4)

Brown solid, MP: 170-172 °C, Pure **1-10:** 252 °C, pure **3-4**: 131-136 °C I.R. selected bands (cm^{-1}): pure **1-10:** 3486, 3431, 2952, 2858, 1630, 1474, 1475, 964, 907, 584; pure **3-4**: 3353, 1746, 1427, 1177, 1122, 887, 832, 647, 529; complex **1-10·3-4**: 3171, , 2920, 2857, 1774, 1474, 1386, 1197, 1143, 962, 761, 639.

Complex of dodecamethonium iodide and perfluorosuberic acid: (1-12·3-6)

Brown solid, MP: 175-179 °C, Pure **1-12**: 222 °C, Pure **3-6:** 139-144 °C; I.R. selected bands (cm^{-1}): Pure **1-12:** 3003, 2913, 2848, 1461, 970, 939, 915, 728; Pure **3-6** : 3541, 1697, 1459, 1321, 1183, 1145, 637; complex **1-12·3-6**: 2936, 2864, 1774, 1476, 1388, 1208, 1141, 962, 670.

7.2.2.2.2. Solid state synthesis of complexes (Grinding and Milling experiments), General procedure

Complex formation of **1** with dicarboxylic acids **2** or **3** was performed through liquid assisted grinding and milling reactions.

Neat and liquid assisted grinding (NG and LAG): The two components were mixed in 1:1 molar ratio, and the mixture was ground using an agate mortar and pestle for 15–20 min. Complex formation was confirmed by Powder XRD, IR and melting point analysis. Alternatively, selected solvents (such as MeOH or EtOH) were added dropwise over the course of grinding. Powder XRD, IR and melting point analysis confirmed the formation of supramolecular complexes.

Selected IR frequencies and the melting points of the complexes obtained by LGA

Complex: 1-10·2-4: mp: 188- 189 °C, I.R selected bands (cm^{-1}): 3176, 2924, 2849, 1728, 1393, 1231, 1144, 906, 749.

Complex: 1-12·2-6: mp: 188- 189 °C, I.R selected bands (cm^{-1}): 3138, 3012, 2923, 1720, 1389, 1214, 1159, 961, 906, 754.

Complex: **1-10·3-4**: mp: 170-172 °C, I.R selected bands (cm^{-1}): 3168, 2916, 1770, 1473, 1387, 1197, 1142, 960, 762, 638.

Complex: 1-12·3-6: mp: 175-179 °C °C, I.R selected bands (cm^{-1}): 2936, 2862, 1772, 1472, 1388, 1208, 1144, 963, 672.

Milling Experiments:

Equimolar amounts of starting tectons were ground using Retsch MM200 ball mill operating at 25 Hz for 20-40 minutes. Typically less than 250 mg of starting compounds were placed in a steel jar (inner volume ≈5 mL) equipped with one 7 mm steel ball. Reactions were conducted in the presence of 30 μL of solvent (methanol or ethanol). PXRD patterns, IR spectra and melting point analysis were examined for all products.

Complex: 1-10·2-4: mp: 188-189 °C, I.R. selected bands (cm^{-1}): 3171, 2927, 2852, 1725, 1392, 1228, 1139, 960, 753.

Complex: 1-12·2-6: mp: 187-189 °C, I.R. selected bands (cm^{-1}): 3137, 2925, 2843, 1721, 1386, 1216, 1157, 1118, 962, 759.

Complex: **1-10·3-4** mp: 170-172 °C, I.R. selected bands (cm^{-1}): 3162, 2916, 1774, 1474, 1386, 1197, 1143, 962, 903, 639.

Complex: 1-12·3-6: mp: 175-179 °C, I.R. selected bands (cm^{-1}): 2936, 2864, 1774, 1476, 1388, 1208, 1141, 962, 607.

7.2.3. Infrared Spectroscopy: Experimental and general discussion

IR spectroscopy proved a valuable technique in the analysis of the products of selective complexation, as the bands indicative of selective acid moiety complexation were easily detected. Individual spectra of host **1** and dicarboxylic acids **2** and **3** were compared with obtained complexes in order to observe frequency changes of stretching and bending vibrations. Notably the appearance of broad band around 3100-3200 cm^{-1} in all complexes corresponds to stretching vibrations of OH group, in addition to this blue shifting of C=O stretch around 1670-1750 cm^{-1} indicates the formation of supramolecular complexes. The C-F stretching frequency changes in complex **1·3** relative to pure diacids **3** (around 1000-1400 cm^{-1}) were also monitored.

7.2.4. Thermal Analysis:

7.2.4.1. Thermogravimetric studies: The thermal behavior of complexes, pure polymethylene bismethonium iodides **1** and diacids **2** and **3** were examined with Perkin-Elmer PYRIS DIAMOND TGA7 thermogravimetric analysers. The measurements were carried out in platinum pans under synthetic air atmosphere (flow rates of 150 and 50 ml/min, respectively) with heating rates of 10 °C and 5 °C/min at a temperature range of 28–700 °C. The sample weights used in the measurements were about 2-7 mg depending on the sample. The TG curves for complex **1-10·2-4** and **1-12·2-6** are presented in Fig.7.2.1. Both supramolecular size-matching complexes starts to decompose around 180 °C before the melting point of host methonium iodides **1**.

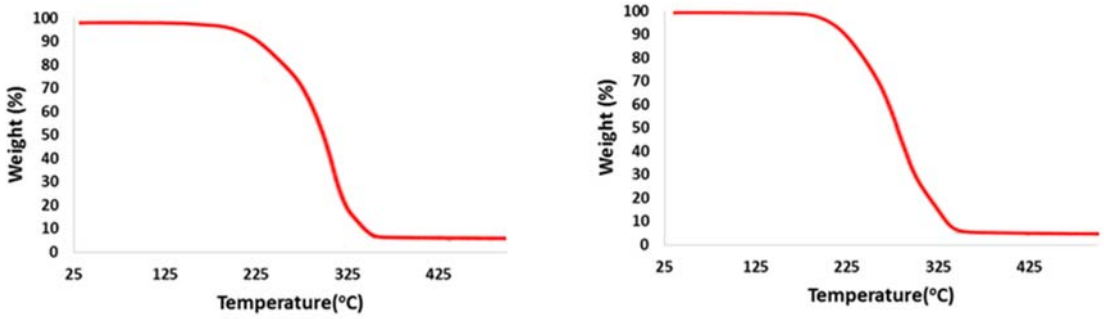

Figure 7.2.1 TG curves of complex **1-10·2-4** (left) and **1-12·2-6** (right) measured at a heat rate of 10 °C/min under flowing air atmosphere.

7.2.4.2. Differential scanning calorimetry

DSC analysis were carried out with a Mettler Toledo DSC600 hot stage (10 °C/min) under flowing nitrogen (flow rate 50 mL/min) using 50 µL sealed aluminum sample pan. The samples

were placed in a 30 μL sealing aluminum pan with capillary holes as cover-pan to minimize the free volume inside the pan and to ascertain good thermal contact between the sample and the pan. Various temperature profiles with heating rates of 3 to 10 °C/min were used to examine thermal behavior of the selected complexes. Many consecutive cycles were carried out in order to examine the melting, recrystallization and stability of the complexes. The DSC curves for complex **1-10·2-4** and **1-12·2-6 a**re presented in Fig.7.2.2.

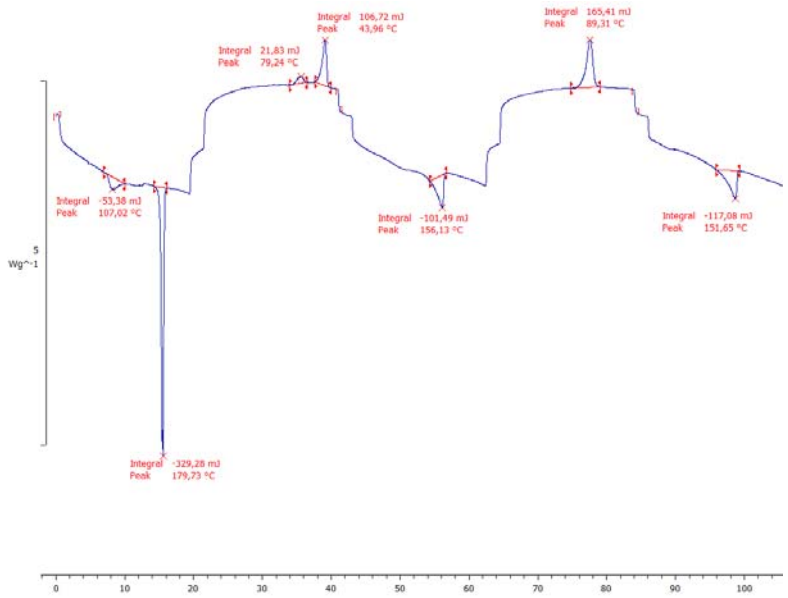

Figure 7.2.2 DSC curves of complex **1-10·2-4** measured at a heating rate of 10 °C/min under flowing nitrogen atmosphere.

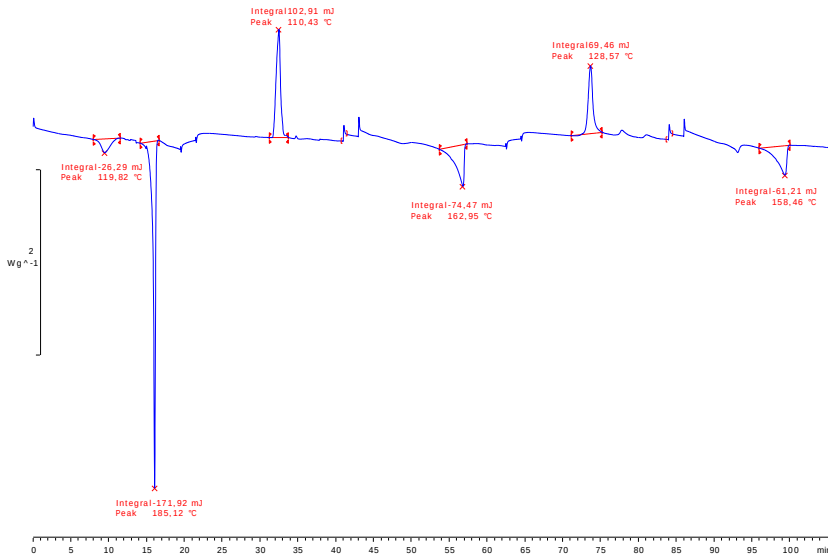

Figure 7.2.3 DSC curves of complex **1-12·2-6** measured at a heating rate of 10 °C/min under flowing nitrogen atmosphere.

7.2.5. Synthesis of mismatching complexes with water inclusion

Synthetic procedure: Equimolar amounts of **1** and mismatching dicarboxylic acids **2** were dissolved separately in a 1:1 mixture of methanol and acetonitrile. The two solutions were mixed in a small vial and approximately 20-30 μL of water were added. The same crystallization vial was placed in a larger vial containing *n*-hexane as a second less efficient solvent and sealed tightly. Volatile solvents were allowed to diffuse until crystals were formed; then crystals were filtered and washed with fresh solvent.

Complex of dodecamethonium iodide and glutaric acid water complex (1-12·2-3·2H_2O)

White solid, mp: 170-172 °C, Pure **1-12,** 222 °C, pure **2-3** 95-98 °C; I.R. selected bands (cm^{-1}): Pure **1-12**: 3003, 2915, 2848, 1463, 972, 915, 730; pure **2-3**: 2955, 2895, 1685, 1410, 1302, 1204, 913, 757 583; complex **1-12·2-3·2H_2O**: 3488, 3130, 2923, 2854, 1721, 1707, 1486, 1315, 1169, 960, 905, 657, 574.

Complex of decamethonium iodide and malonic acid water complex (1-10·2-1·2H_2O)

White solid, mp: 164-165 °C, Pure **1-10,** 252 °C, pure **2-1** 145 °C; I.R. selected bands (cm^{-1}): Pure **1-10**: 3486, 3431, 2952, 2858, 1630, 1474, 1475, 964, 907, 584; pure **2-1**: 2956, 1693, 1453, 1305, 1216, 1169, 913, 785, 649; complex **1-10·2-1·2H_2O**: 3484, 2923, 2862, 1717, 1476, 1336, 1234, 1137, 964, 909, 655, 548.

7.2.6. Crystallographic Analysis

7.2.6.1. Crystallization: Single crystals of complexes **1-10·2-4 and 1-12·2-6** were obtained on slow evaporation at room temperature of saturated solutions in methanol:acetonitrile (1:1) or dichloromethane:methanol (1:1). In case of complex **1-10·3-4**, equimolar amounts of starting tectons were dissolved in methanol:acetonitrile, obtained solutions were mixed in a small vial which was sealed in a lager vial containing CCl_4. Miss-matching complexes (**1-12·2-3** and **1-10·2-1**) were crystallized in the presence of trace amount of water. A polymorph of complex **1-10·2-4** was crystallized from acetonitrile:methanol (95:5) solvent mixture and solvents were allowed to evaporate slowly at room temperature. **1-10·4-4** and **1-12·4-6** were obtained by dissolving equimolar amounts of starting tectons in a 1:1 mixture of MeOH: $CHCl_3$. The solvent mixture was allowed to evaporate slowly at room temperature.

7.2.6.2. Single crystal X-ray diffraction analysis (SXRD)

SXRD data collection and structural refinement details were described in section 7.1.6. Crystal structure of cocrystals **1-10·2-1**, **1-12·2-3** and **1-10·3-4** showed some disorder; disorder was

particularly remarkable in cocrystal **1-10·3-4;** octafluoroadipic acid was present in two helical, distorted *all-trans* conformations having opposite handedness, fluorine atoms showed great separations, so that the whole molecules could be split and refined with few restraints on the perfluorocarbon geometry. As can be deduced by comparing ADPs of amino groups with those of the polymethylene chain carbon atoms, also these latter atoms are disordered, due to the strong interactions with the surrounding dicarboxylic acid molecules; not withstanding, the separation of these carbon atoms is too small to allow their splitting and their restrained refinement. The crystallinity of the cocrystal **1-12·3-6** was very bad and poorly diffracting, any attempt to increase the data resolution by cooling the cocrystal failed. Despite a good data sets for complex **1-10·2-1** was collected, heavy positional disorder was observed along carboxylic acid chain and water molecule, and we are unable to make a clear model to see how the water molecules interact with onium iodide and diacid units.

Table 7.2.1 Crystallographic data for individual starting host and cocrystals

Name	**1-10**	**1-12**	**1-10·2-4**
Chemical formula	$C_{128}H_{304}N_{16}I_6$	$C_{36}H_{84}N_4I_2$	$C_{22}H_{48}I_2N_2O_4$
Molecular weight	512.3	540.4	640.28
Crystal system, space group	Orthorombhic, Pbca	Monoclinic P21/c	Triclinic, P -1
Temperature (K)	100	100	100K
a (Å)	12.3675(5)	7.3528(14)	5.9573(3)
b (Å)	11.9074(5)	12.0390(20)	7.8893(4)
c (Å)	29.1864(12)	13.8150(30)	15.1736(7)
α(°)	90	90	96.235(3)
β (°)	90	92.710(20)	98.394(3)
γ(°)	90	90	92.705(2)
V (Å^3)	4298.13(3)	1221.54(12)	699.89(6)
Z	8	2	1
μ (mm^{-1})	2.923	2.576	2.272
Crystal size (mm^3)	0.27, 0.20, 0.12	0.23, 0.17, 0.10	0.22, 0.14, 0.09
F(000)	2032.0	540	332.0
Data collection			
Diffractometer	Bruker APEX-II CCD area detector diffractometer		
Absorption correction	Based on multi-scan		
No. of measured, independent and observed reflections	21485,6692, 4597	22320, 2812, 2164	16517, 5702, 4780
R_{int}	3.56	3.39	3.27
θ_{min} (°)	2.7	2.4	2.6
θ_{max} (°)	27.4	26.1	35.5
Refinement			
R_{all}, R_{obs}	0.067, 0.036	0.052, 0.034	0.043, 0.033
$wR2\_{all}$, $wR2\_{obs}$	0.064, 0.056	0.082, 0.075	0.071,0.069
GOOF	0.957	1.039	1.011
No. of parameters	187	103	139
$\Delta\rho_{max}$, $\Delta\rho_{min}$ (e Å^{-3})	0.617, -0.586	1.413, -0.895	2.023, -1.274

Table 7.2.1 Crystallographic data for individual starting host and cocrystals (continuation).

Name	**1-12·2-6**	**1-10·3-4**	**1-12·2-3·H_2O**
Chemical formula	C_{26} H_{56} I_2 N_2 O_4	C_{22} H_{40} F_8 I_2 N_2 O_4	C_{22} H_{46} I_2 N_2 O_8
Molecular weight	358.07	802.36	720.41
Crystal system, space group	Triclinic, P -1	Triclinic, P -1	Triclinic, P -1
Temperature (K)	100K	100K	100
a (Å)	5.9560(4)	5.8199(15)	5.9285(10)
b (Å)	7.8630(6)	7.923(2)	7.9181(15)
c (Å)	17.2041(15)	17.365(4)	16.765(30)
α(°)	85.155(4)	99.227(16)	85.112(9)
β (°)	82.317(4)	98.956(16)	85.047(9)
γ(°)	87.157(4)	91.652(16)	88.247(9)
V ($Å^3$)	795.02(11)	779.5(3)	780.99 (9)
Z	2	1	1
μ (mm^{-1})	2.014	1.709	2.054
Crystal size (mm^3)	0.25, 0.18, 0.10	0.13, 0.010, 0.08	0.13, 0.10, 0.02
F(000)	338.0	396.0	362
Data collection			
Diffractometer	Bruker APEX-II CCD area detector diffractometer		
Absorption correction	Based on multi-scan		
No. of measured, independent and observed reflections	10516, 3579, 2817	10218, 2863, 2322	73183, 6844, 4774
R_{int}	3.92	3,93	5.57
θ_{min} (°)	2.4	2.40	2.45
θ_{max} (°)	27.5	25.71	30.30
Refinement			
R_{all}, R_{obs}	0.057, 0.041	0.064, 0.047	0.127, 0.111
$wR2\_{all}$, $wR2\_{obs}$	0.055, 0.052	0.123, 0.115	0.295, 0.288
GOOF	0.996	1.140	1.284
No. of parameters	158	269	217
$\Delta\rho_{max}$, $\Delta\rho_{min}$ (e $Å^{-3}$)	0.899, -1.107	1.427, 0.790	4.915, -6.796

Table 7.2.1 Crystallographic data for individual starting host and cocrystals (continuation).

Name	**1-10·2-1·H_2O**	**1-10·2-4(polymorph)**
Chemical formula	C_{19} H_{40} I_2 N_2 O_4	C_{22} H_{48} I_2 N_2 O_4
Molecular weight	602.32	640.28
Crystal system, space group	Monoclinic, P 21/c	Monoclinic, P 21/n
Temperature (K)	100	100
a (Å)	14.547(3)	7.3561(10)
b (Å)	13.842(3)	21.0490(30)
c (Å)	13.404(3)	9.3110(12)
α(°)	90.00	90.000(00)
β (°)	96.434(9)	94.185(12)
γ(°)	90.00	90.000(00)
V (Å^3)	2682.0(9)	1437.86(13)
Z	4	2
μ (mm^{-1})	2.366	2.213
Crystal size (mm^3)	0.15, 0.13, 0.07	0.19, 0.21, 0.08
F(000)	1200	664
Data collection		
Diffractometer	Bruker APEX-II CCD area detector diffractometer	
Absorption correction	Based on multi-scan	
No. of measured, independent and observed reflections	83153, 7851, 5741	40253, 7288, 6786
R_{int}	4.95	3.92
θ_{min} (°)	2.04	2.4
θ_{max} (°)	30.03	27.5
Refinement		
R_{all}, R_{obs}	0.075, 0.0495	0.022, 0.020
$wR2\_{all}$, $wR2\_{obs}$	1.034	0.047, 0.046
GOOF	287	1.137
No. of parameters	66	142
$\Delta\rho_{max}$, $\Delta\rho_{min}$ (e Å^{-3})	1.212, -1.431	0.925, -1.013

7.2.6.2.1. Single crystal X-ray representations:

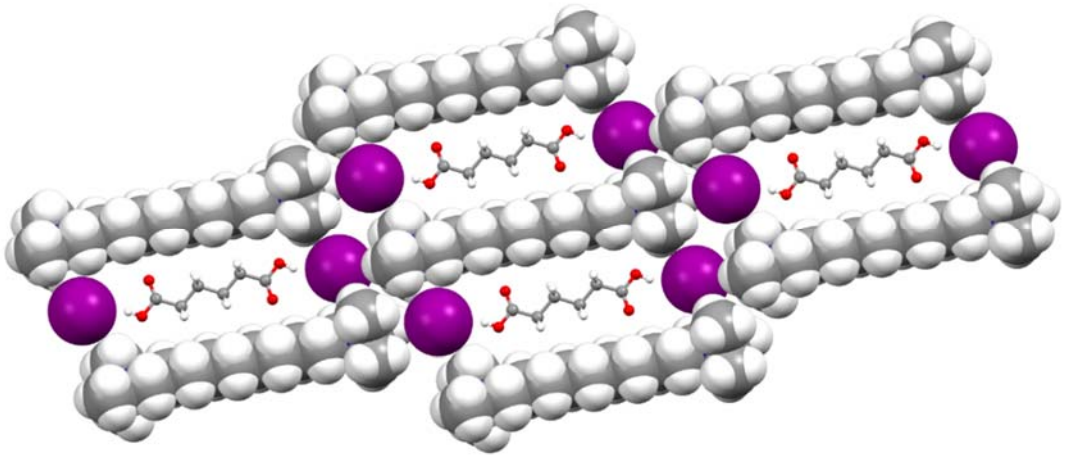

Figure 7.2.4 Crystal packing (Mercury 3.8) of the complex **1-10·2-4**. Decamethonium iodide is in space filling representation while adipic acid molecules are in ball stick to show the better confinement. Color codes: grey, carbon; blue, nitrogen; white, hydrogen; red, oxygen; magenta, iodine.

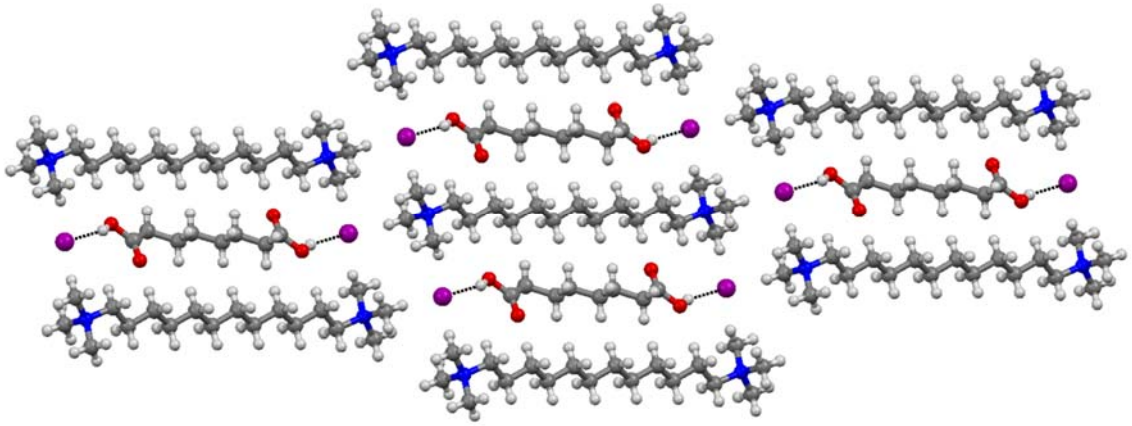

Figure 7.2.5 Crystal packing of dodecamethonium iodide-suberic acid cocrystal **1-12·2-6**. Dotted lines indicates the hydrogen bonding between host onium iodide and guest acid moiety. Color codes: grey, carbon; blue, nitrogen; white, hydrogen; red, oxygen; magenta, iodine.

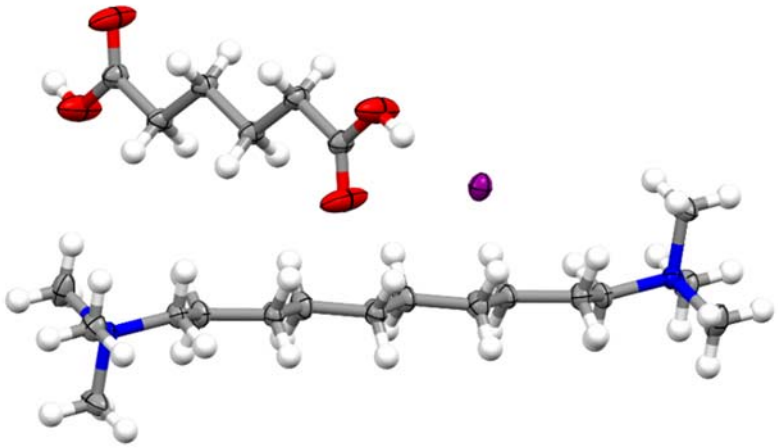

Figure 7.2.6 ORTEP view (at 60% probability level at 100 K) of the polymorph of **1-10·2-4** where guest diacids are perpendicular to the host onium iodide. Color codes: grey, carbon; blue, nitrogen; white, hydrogen; magenta, iodine.

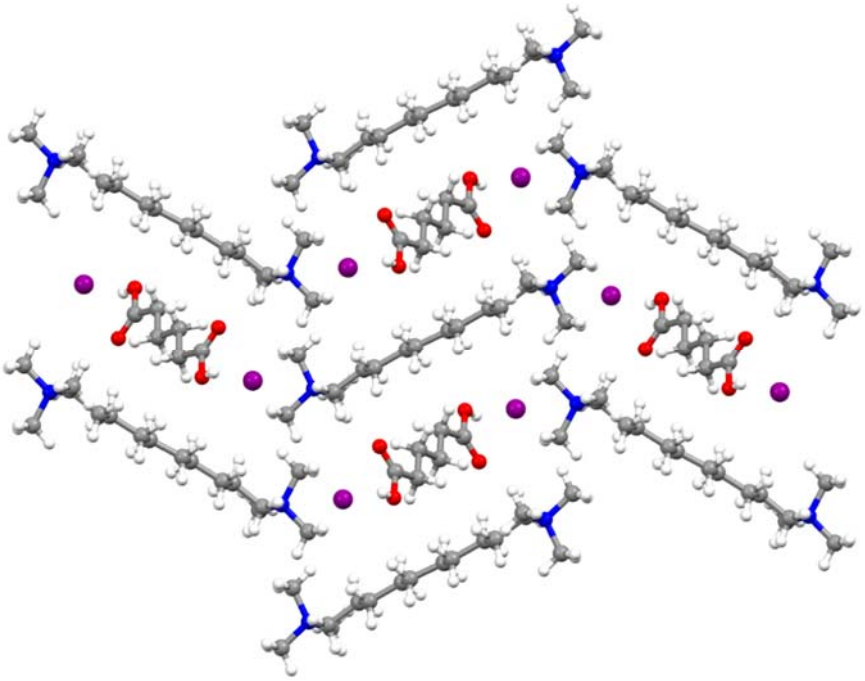

Figure 7.2.7 Partial representation of the crystal packing (Mercury 3.8, ball and stick) of the polymorph of cocrystal **1-10·2-4** where guest diacids are perpendicular to the host onium iodide. Color codes: grey, carbon; blue, nitrogen; white, hydrogen; red, oxygen; magenta, iodine.

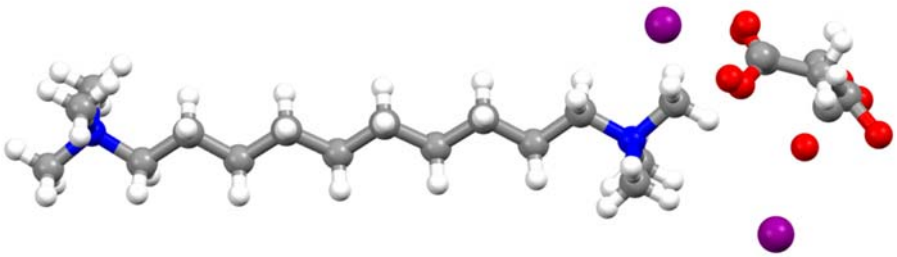

Figure 7.2.8 Crystal structure of mismatching cocrystal **1-10·2-1.** Water and malonic acid molecules are disordered, despite the good quality of the single crystal and X-ray data, we are unable to produce a clear modelling of malonic acid and water molecule due to heavy structural disorder. Color codes: grey, carbon; blue, nitrogen; white, hydrogen; magenta, iodine

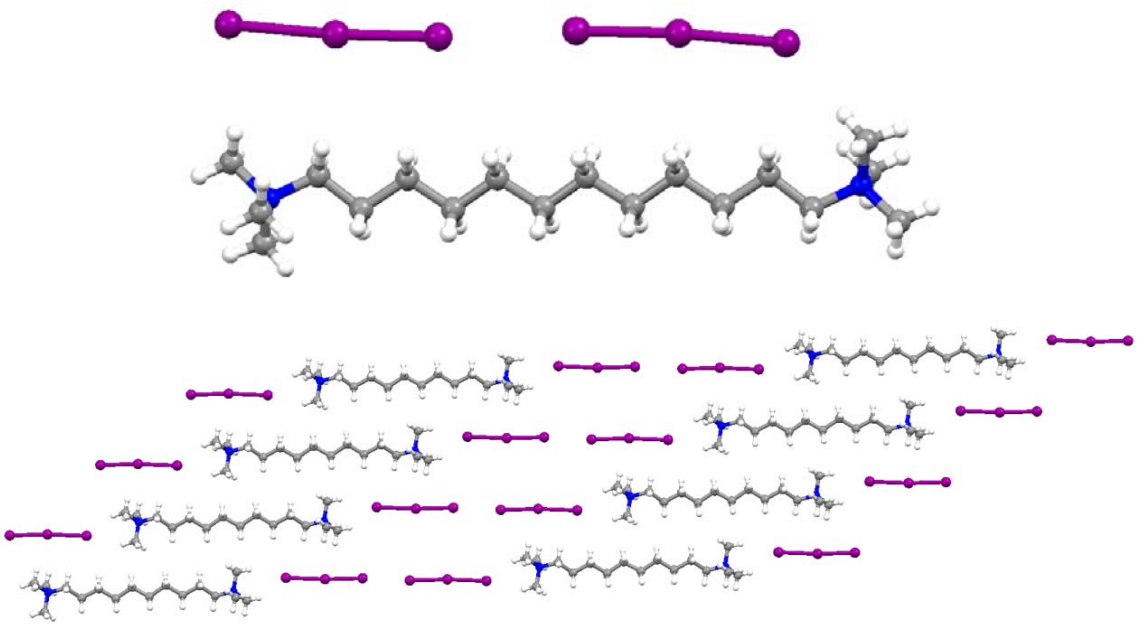

Figure 7.2.9 Crystal structure of decamethonium bis-triiodide. Top: representation of one dication and two anions units evidencing that the two I_3^- matches the length of the dication. Bottom: partial view of the overall crystal packing. Color codes: grey, carbon; blue, nitrogen; white, hydrogen; magenta, iodine.

7.2.6.3. Powder X-ray diffraction analysis:

Crystalline powder material of pure polymethylene bismethonium iodides, diacids and cocrystals was packed on borosilicate glass slides and the data sets were collected on Bruker D8 instrument at 293 K. The measurements were made in Bragg–Brentano geometry using Johansson monochromator to produce pure CuKα1 radiation (1.5406 Å; 45kV, 30mA) and

step–scan technique in 2θ range of 3.5–40°. Data were acquired from a spinning sample by X´Celerator detector in continuous scanning mode with a step size of 0.0167° using sample dependently counting times of 40 to 440 s per step.

Experimental powder X-ray diffraction (PXRD) patterns of pure onium iodides, adipic acid, their complexes and simulated patterns from the single crystal are shown below. The comparison of simulated and experimental PXRD pattern confirms the structural uniformity of bulk cocrystal samples. Few additional peaks (much weaker than the intensity gain of the main phase) are occasionally present in simulated patterns with respect to experimental patterns; this is possibly related to some structural disorder and differences in data collection temperatures.

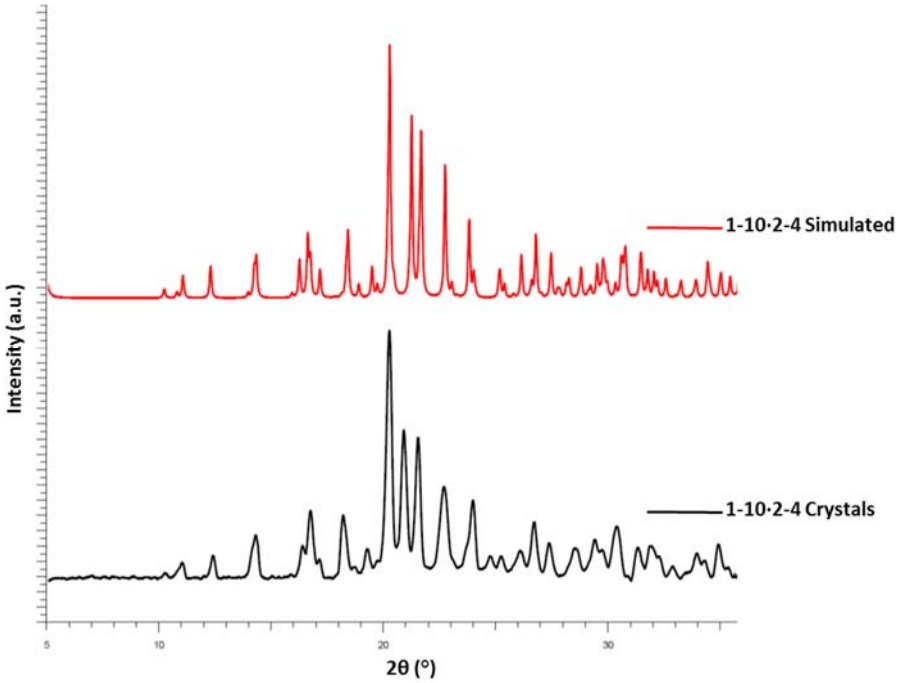

Figure 7.2.10 PXRD patterns of **1-10·2-4**: simulated (top, red trace, from single crystal structure at 90 K) and experimental (bottom, black trace, sample from solution crystallization).

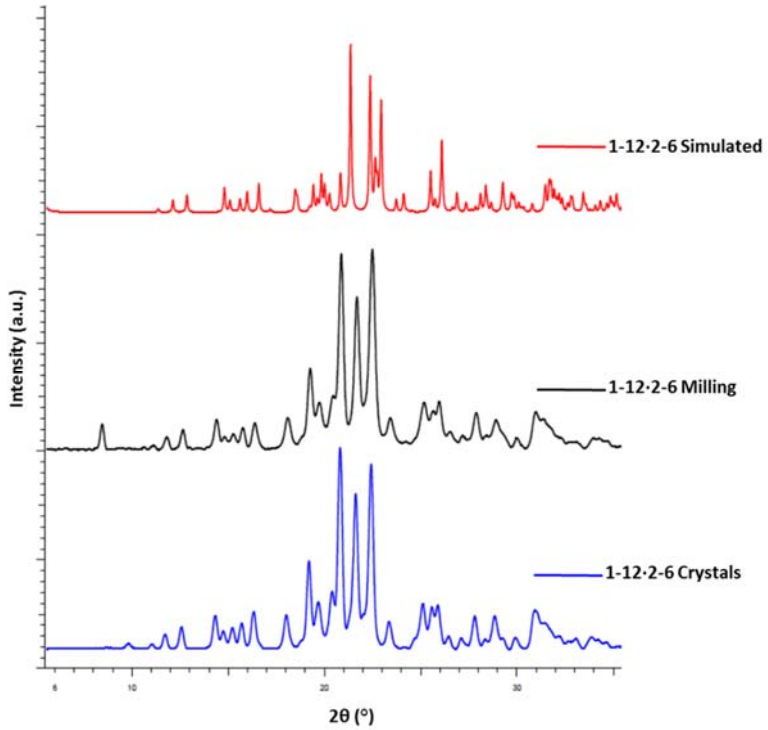

Figure 7.2.11 PXRD patterns of **1-12·2-6**: simulated (top, red trace, from single crystal structure at 90 K; experimental (mid, black trace, sample from milling reaction); experimental (bottom, blue trace, sample from solution crystallization).

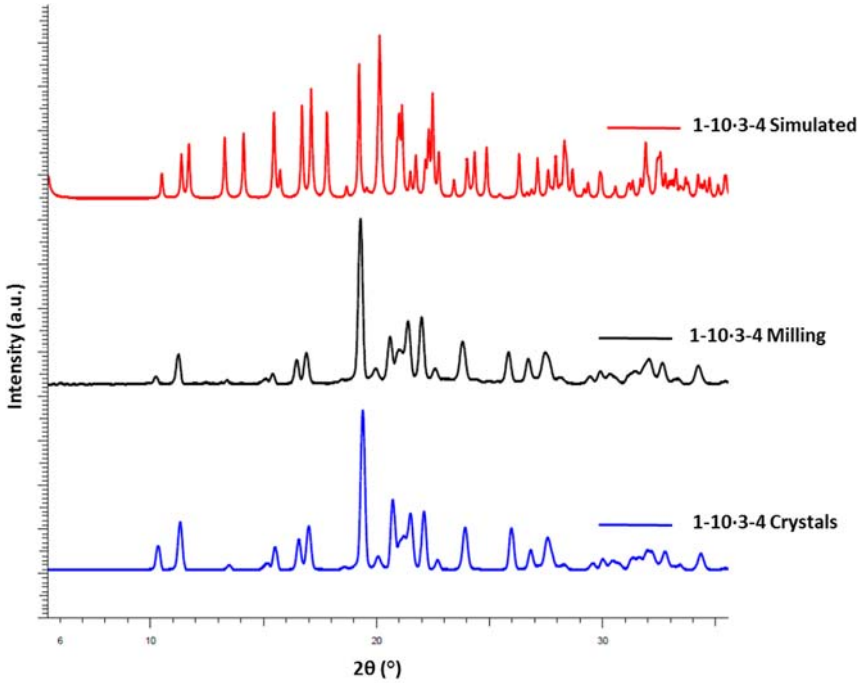

Figure 7.2.12 PXRD patterns of **1-10·3-4**: simulated (top, red trace, from single crystal structure at 90 K); experimental (mid, black trace, sample from milling reaction); experimental (bottom, blue trace, from solution crystallization).

The cocrystal **1-10·3-4** has poor crystalline property. After filtration, cocrystal **1-10·3-4** is a whitish powder which turns to yellowish after two days at room temperature and to brownish after one week. This may be related to iodide oxidation to iodine by atmospheric oxygen. As it is often the case for polyfluorinated compounds, **1-10·3-4** is a gummy plastic material at room temperature and pressure; this feature might be responsible for the fact that some peaks observed in experimental PXRD patterns, are missing in patterns simulated from single crystal structure.

On crystallizing a mixture of onium dication **1-12** and diacid **3-6**, a gummy powder with features similar to **1-10·3-4** was obtained. IR, melting point, ^{1}H and ^{19}F NMR analysis and mass spectroscopy consistently suggested the formation of hydrogen bonded cocrystal **1-12·3-6**, but we were unable to obtain any crystal good enough for single crystal X-ray analysis.

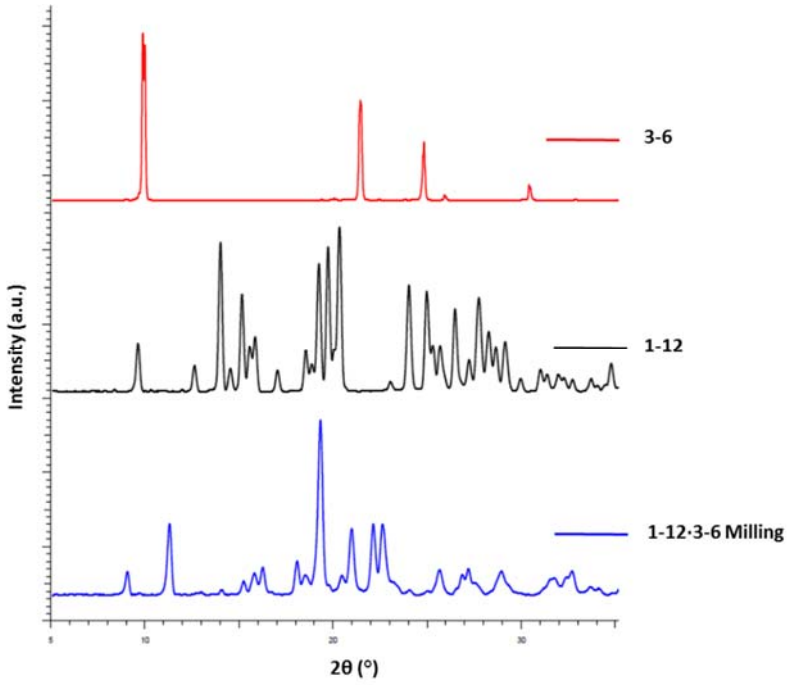

Figure 7.2.13 PXRD patterns; Top: experimental pattern of pure **3-6**; Mid: Experimental pattern of pure **1-12**; Bottom: Experimental pattern of the cocrystals **1-12·3-6** obtained from solution crystallization.

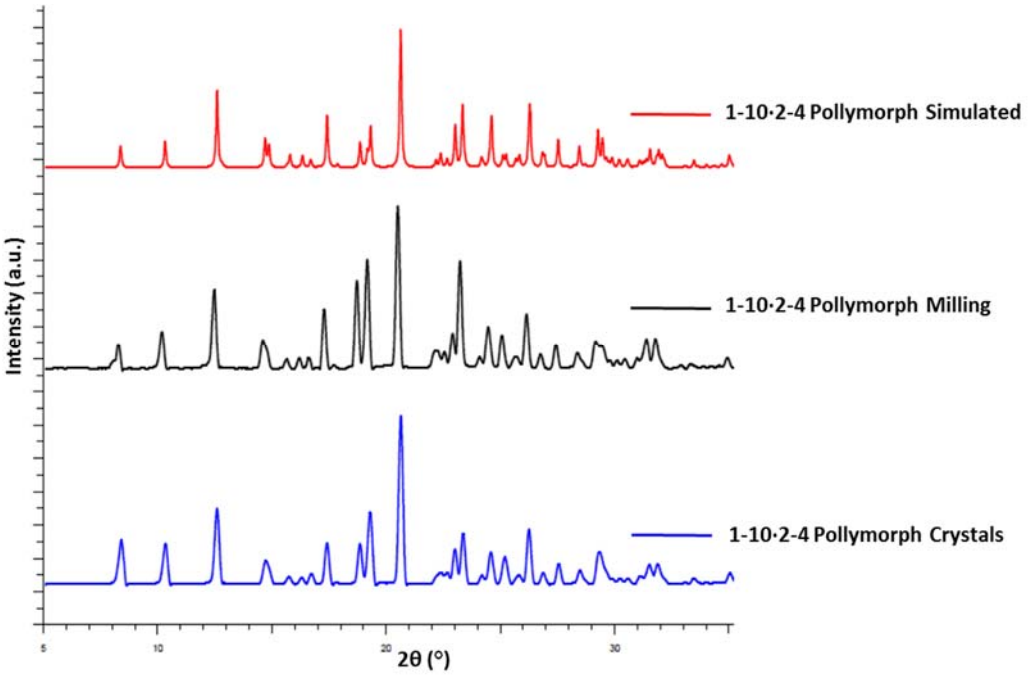

Figure 7.2.14 PXRD patterns of **1-10·2-4** polymorph wherein adipic acid is orthogonal to the onium dication; Top: simulated pattern from single crystal structure at 90 K; Mid: experimental pattern of a sample from milling reactions; Bottom: experimental pattern of a sample from solution crystallization.

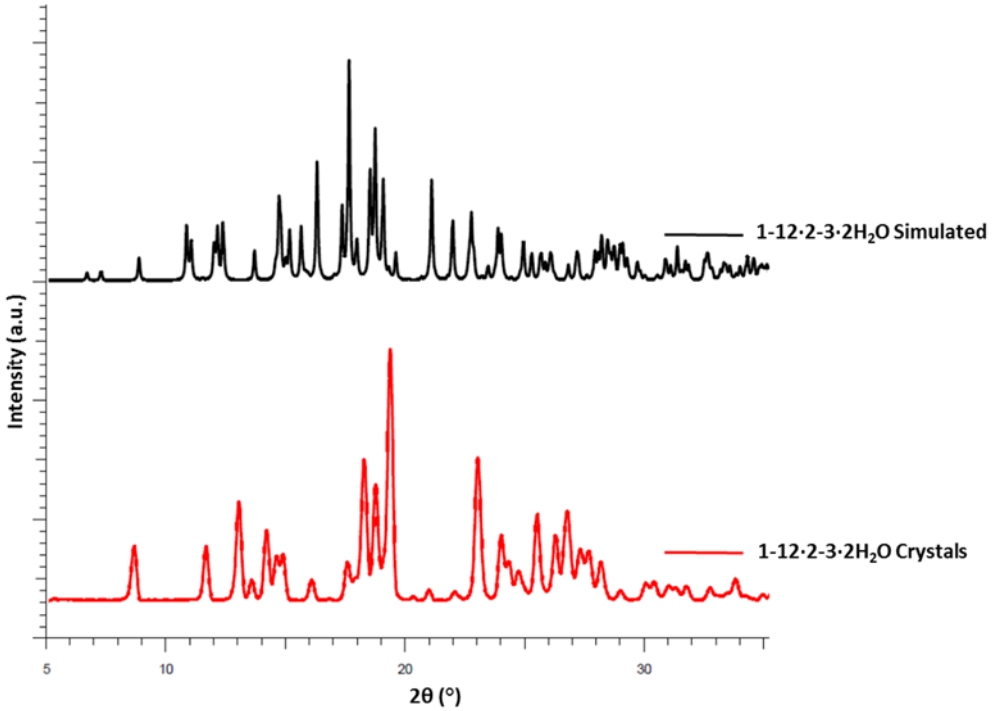

Figure 7.2.15 PXRD patterns of **1-12·2-3·H_2O**; Top: simulated pattern from single crystal structure at 90 K; Bottom: experimental pattern of a sample from solution crystallization.

7.2.7. Binding studies in solution by NMR spectroscopy

In solution, the existence of an interaction at ambient temperature between **1** and **2** or **3** is proven by ^{1}H and ^{19}F NMR titration experiments in CD_2Cl_2:CD_3OD (10:1) at room temperature. ^{1}H NMR spectra were recorded on a Bruker AV-400 spectrometer, at 400 MHz and ^{19}F spectra were recorded at ambient temperature on a Bruker AV-500; at 470.6 MHz.

7.2.7.1. Aggregation studies in solution by ^{1}H NOSEY, ^{19}F and ^{1}H HOSEY NMR technique

In solution, the existence of an interaction between **1** and **2** or **3** is proven by NMR titration experiments. In order to better characterize such an interaction in solution, we took advantage of advanced NMR technique, as nuclear Overhauser effect NMR spectroscopy (^{1}H NOSEY and its heteronuclear version, ^{19}F, ^{1}H HOSEY), which already proved to provide detailed information on non-covalent interactions.

^{1}H NOESY NMR studies

The aggregations of **2-4** with **1-10** (concentrations of 160 and 80 mM, respectively) have been studied by ^{1}H NOSEY in dichloromethane:methanol (10:1). In this case, no intermolecular NOE contacts were detected (Fig. 7.2.16). These indicates that the concentration of a possible adduct is below the ^{1}H NOSEY detection threshold. The same result was obtained in MeOD.

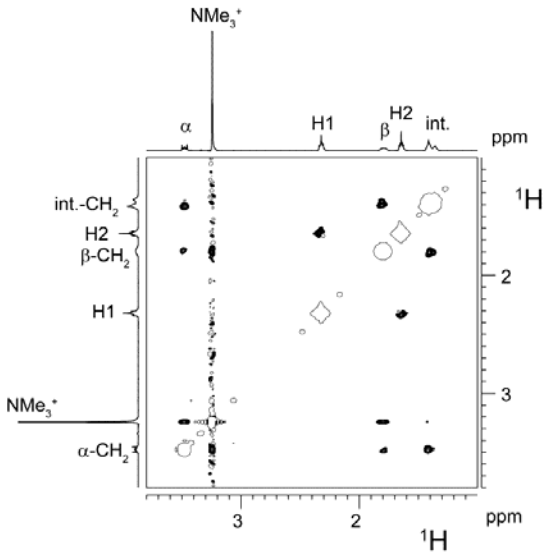

Figure 7.2.16 ^{1}H NOSEY NMR spectrum of a solution containing **2-4** (160 mM) and **1-10** (80 mM) in CD_2Cl_2:CD_3OD (10:1) at 298 K

^{19}F, ^{1}H HOSEY NMR studies

When **3-6** and **1-12** are mixed in similar concentrations (50 and 60 mM, respectively) in CD_2Cl_2:CD_3OD (10:1) at 298 K, clear indications of association came from the ^{19}F, ^{1}H HOSEY NMR spectrum (Fig. 7.2.17), where H/F intermolecular NOE contacts are observed. In particular, the fluorine atoms of the perfluorosuberic acid interact with all the protons of **1-12**, with different relative intensity.

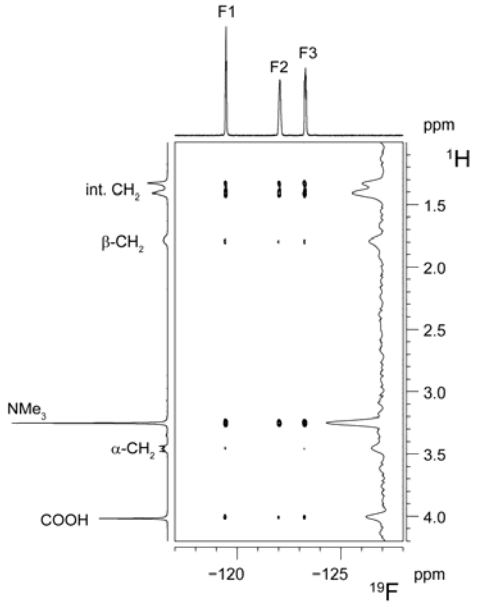

Figure 7.2.17 ^{19}F, ^{1}H HOSEY NMR spectrum of a solution containing **3-6** (50 mM) and **1-12** (60 mM) in CD_2Cl_2:CD_3OD (10:1) at 298 K.

Table 7.2.2 Normalized cross-peak relative intensities obtained from the ^{19}F, ^{1}H HOSEY NMR spectrum of a solution of **3-6** (50 mM) and **1-12** (60 mM) in CD_2Cl_2:CD_3OD (10:1) at 298 K.

	F1	F2	F3
internal -CH_2	0.90	0.87	1.00
β-CH_2	0.42	0.23	0.29
NMe_3^+	0.90	0.68	0.87
α-CH_2	0.19	0.13	0.19

Analyzing the NOE contacts and their relative intensity, normalized for the *f* factor (Table 7.2.2), it is interesting to note that the fluorine interacts very strongly with the internal methylene units, much less with the β-CH_2 and even less with α-CH_2. On the other hand the F/ NMe_3^+ contact is very intense. This pattern indicates the contemporary presence of two adducts

in solution: **1-12·3-6**‖ having the chain of **1-12** parallel to that of **3-6**, and **1-12·3-6**⊢, with the two chains perpendicular to each other.

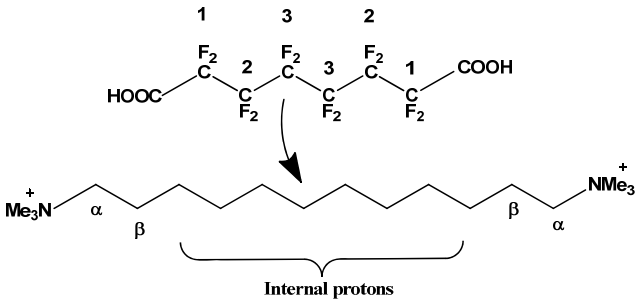

Structure **1-12·3-6**‖

astructure **1-12·3-6**⊢

Scheme 7.2.2 The arrows indicate the main NOE contacts in **1·3** supramolecular complexes.

The **1-12·3-6**‖ explains why intense F/internal-CH_2 contacts are present in solution, whereas the contacts between the fluorine and the external methylene moieties, namely α-CH_2 and β-CH_2, are very low. The latter point also suggests that there is not any horizontal shift between the two chains.

1-12·3-6⊢ explains very well the high intensity of F/NMe_3^+ contacts and the lack of selectivity between F1, F2 and F3. Interestingly, if **1-12·3-6**⊢ were the only structure in solution, no F/internal-CH_2 contacts should be detected. In other words, the NOE contacts due to the structures **1-12·3-6**‖ and **1-12·3-6**⊢ do not interfere each other and the relative intensity of F/internal-CH_2 and F/NMe_3^+ contacts can be roughly related to the respective relative concentration. In summary, the ^{19}F, ^1H HOSEY NMR spectrum of a solution containing **3-6** (50 mM) and **1-12** (60 mM) in CD_2Cl_2:CD_3OD (10:1) at 298 K can be fully explained by the presence of two structures, **1-12·3-6**‖ and **1-12·3-6**⊢ with similar concentrations.

Similar conclusions can be drawn from the ^{19}F, ^1H HOSEY NMR spectrum of a solution containing **3-4** (69 mM) and **1-10** (83 mM) in CD_2Cl_2:CD_3OD (10:1) at 298 K (Fig.7.2.18 and Table 7.2.3). Again, the F/internal-CH_2 and F/NMe_3^+ contacts have similar intensity, whereas contacts with α-CH_2 and β-CH_2 are much weaker.

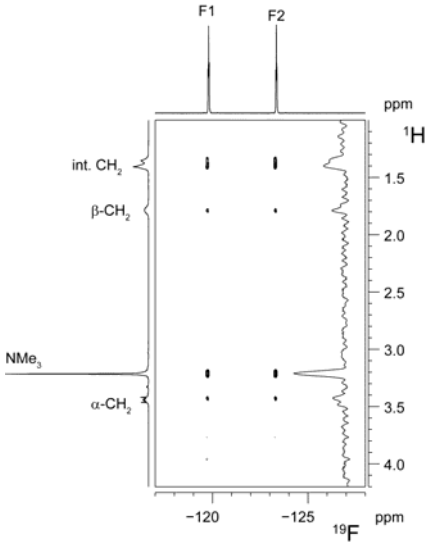

Figure 7.2.18 ^{19}F, ^{1}H HOSEY NMR spectrum of a solution containing **3-4** (69 mM) and **1-10** (83 mM) in CD_2Cl_2:CD_3OD (10:1) at 298 K.

Table 7.2.3 Normalized cross-peak relative intensities obtained from the ^{19}F, ^{1}H HOESY NMR spectrum of a solution of **3-4** (69 mM) and **1-10** (83 mM) in CD_2Cl_2:CD_3OD (10:1) at 298 K.

	F1	F2
internal -CH_2	0.80	0.83
β-CH_2	0.40	0.40
NMe_3^+	0.87	1.00
α-CH_2	0.33	0.37

In pure methanol, NOE contacts between **3-6** (53 mM) and **1-12** (28 mM) are still detectable, indicating that the aggregation process is not inhibited by polar solvents (Fig. 7.2.19, table 7.2.4). Nevertheless, the relative intensities of the contacts are. In particular, the F1/NMe_3^+ contact is considerably smaller than the F1/internal-CH_2 one (0.61 and 0.97, respectively), suggesting that the concentration of **1-12·3-6**⊢ is smaller than that of **1-12·3-6**‖. This can be explained considering that polar solvents favor hydrophobic CH/CF interactions, which are more numerous in **1-12·3-6**‖ than in **1-12·3-6**⊢.

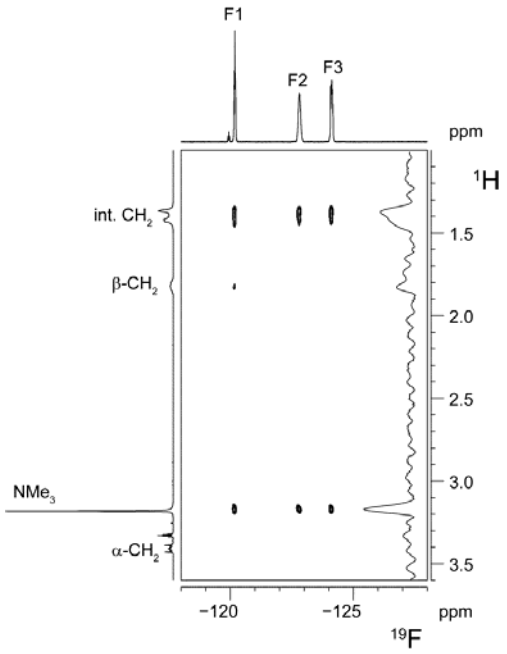

Figure 7.2.19 ^{19}F, ^{1}H HOSEY NMR spectrum of a solution containing **3-6** (53 mM) and **1-12** (28 mM) in CD_3OD at 298 K.

Table 7.2.4 Normalized cross-peak relative intensities obtained from the ^{19}F, ^{1}H HOSEY NMR spectrum of a solution of **3-6** (53 mM) and **1-12** (28 mM) in CD_3OD at 298 K.

	F1	F2	F3
internal-CH_2	0.97	1.00	1.00
β-CH_2	0.29	0.45	0.45
NMe_3^+	0.61	0.45	0.45
α-CH_2	n.d.	n.d.	n.d.

Remarkably, the solvent used for the crystallization of **1-12·3-6** is a mixture of methanol and acetonitrile, where the structure **1-12·3-6**‖ is predominant.

In water, the fluorinated acid is less soluble than in methanol. Despite this, the ^{19}F, ^{1}H HOSEY NMR spectrum of a solution containing **3-6** (6 mM) and **1-12** (17 mM) still shows intramolecular NOE contacts. The relative intensities of the F1/NMe_3^+ and F1/internal-CH_2 contact are 0.35 and 1.0, respectively, indicating that the **1-12·3-6**⊢ structure is even less important in water than in methanol, while **1-12·3-6**‖, which minimizes the exposure of hydrophobic chains to the solvent, is favored (Fig. 7.2.20, table 7.2.5).

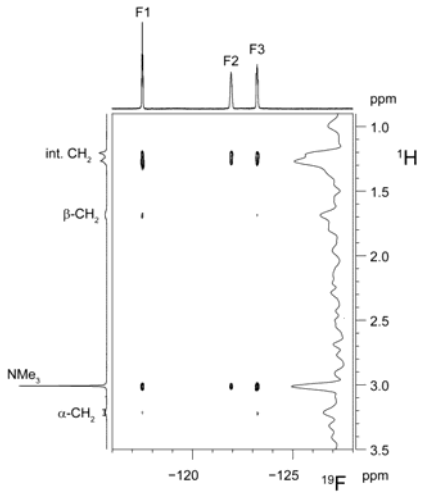

Figure 7.2.20 ^{19}F, ^{1}H HOSEY NMR spectrum of a solution containing **1-12** (17 mM) and **3-6** (6 mM) in D_2O at 298 K.

Table 7.2.5 Normalized cross-peak relative intensities obtained from the ^{19}F, ^{1}H HOSEY NMR spectrum of a solution of **1-12** (17 mM) and **3-6** (6 mM) in D_2O at 298 K.

	F1	F2	F3
internal -CH_2	1.00	0.71	0.92
β-CH_2	0.35	0.20	0.42
NMe_3^+	0.48	0.32	0.61
α-CH_2	0.29	0.32	0.31

7.2.7.2. Determination of association constants *via* ^{19}F NMR titrations

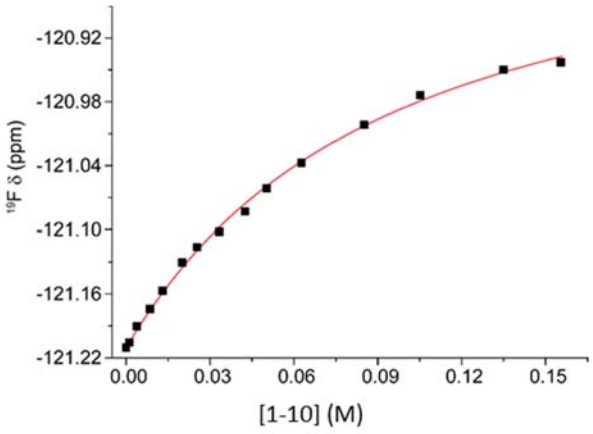

Figure 7.2.21 Trend of the chemical shift of the α-fluorine nuclei (-C*F*$_2$COOH) of **3-4** (c = 13.7 mM) with **1-10** in CD_2Cl_2:CD_3OD 10:1. The limit value of δ (fitted) is -120.789 ± 0.031 ppm, the value of K_a is 12.1 ± 0.6 M^{-1}.

Table 7.2.6 Values of the chemical shift of the α-fluorine nuclei (-C*F*$_2$COOH) of **3-4** (c = 13.7 mM) with **1-10** in CD_2Cl_2:CD_3OD 10:1.

[**1-10**] (mM)	^{19}F $\delta_{\alpha\text{-}F}$ (**3-4**) (ppm)
0	-121.2154
1.1	-121.2107
3.9	-121.1956
8.6	-121.1792
13.1	-121.1620
20.1	-121.1356
25.3	-121.1212
33.3	-121.1070
42.5	-121.0880
50.3	-121.0664
62.8	-121.0424
85.2	-121.0066
106	-120.9788
135	-120.9550
156	-120.9480

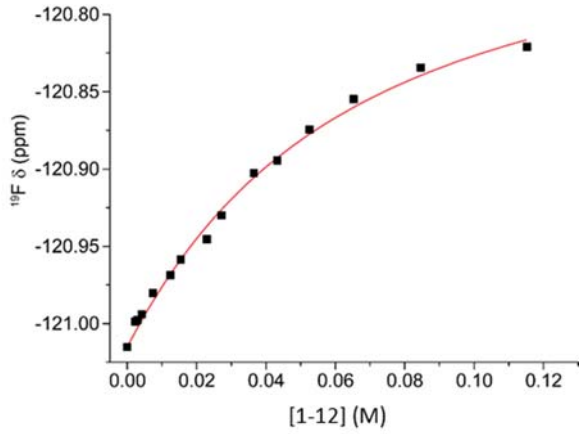

Figure 7.2.22 Trend of the chemical shift of the α-fluorine nuclei (-C*F*$_2$COOH) of **3-6** (*C* = 16.6 mM) with [**1-12**] in CD_2Cl_2/CD_3OD 10/1. The limit value of δ (fitted) is -120.716 ± 0.015 ppm, the value of K_a is 19 ± 2 M^{-1}.

Table 7.2.7 Values of the chemical shift of the α-fluorine nuclei (-C*F*$_2$COOH) of **3-6** (c = 16.6 mM) with **1-12** in CD_2Cl_2:CD_3OD 10:1.

[1-12] (mM)	^{19}F $\delta_{\alpha\text{-}F}$ (**3-6**) (ppm)
0	-121.01520
2.3	-120.9988
3.0	-120.9978
4.2	-120.9940
7.4	-120.9804
12.5	-120.9687
15.5	-120.9586
23.0	-120.9455
27.2	-120.9301
36.6	-120.9028
43.3	-120.8945
52.6	-120.8745
65.3	-120.8549
84.6	-120.8345
115.3	-120.8210

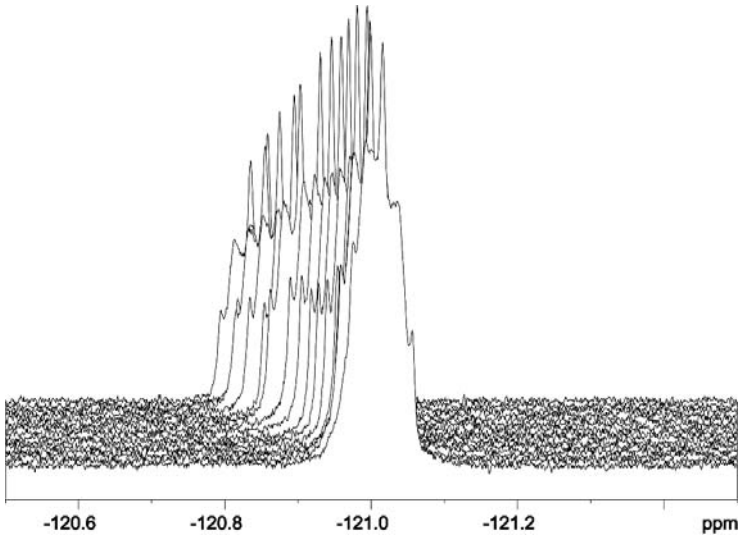

Figure 7.2.23 Stacked spectra of **3-6** (the signal due to α-fluorine nuclei, -C*F*$_2$COOH, is shown) at increasing concentrations of **1-12** in CD_2Cl_2:CD_3OD 10:1.

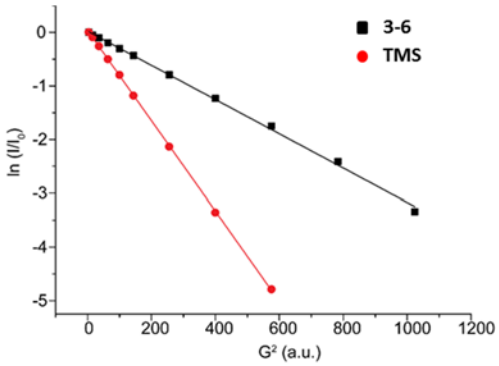

Figure 7.2.24 Logarithm of (I/I_0) versus G^2 of **3-6** (16.7 mM) in CD_2Cl_2:CD_3OD 10:1.

Table 7.2.8 Values of normalized I for the signal due to the α-fluorine nuclei (-C*F*$_2$COOH) of **3-6** (c = 16.7 mM) and TMS in CD_2Cl_2:CD_3OD 10:1 at different values of G^2 (a. u.).

G^2	$I_{\alpha\text{-}F}$ (**3-6**) (a.u.)	I(TMS) (a. u.)
4	1	1
16	0.94912	0.9097
36	0.90136	0.7717
64	0.82249	0.60503
100	0.73740	0.45077
144	0.64746	0.30582
256	0.45212	0.11779
400	0.29114	0.0348
576	0.17334	0.00833
784	0.08937	n.d.
1024	0.0354	n.d.

n.d. = not detectable

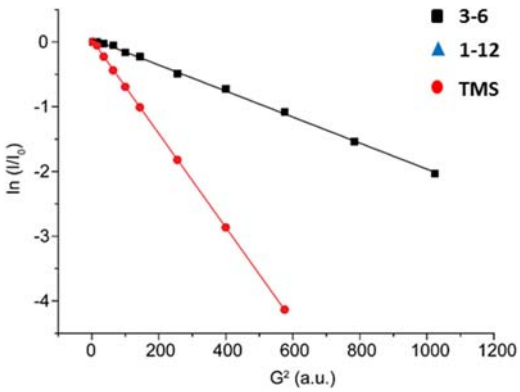

Figure 7.2.25 Logarithm of (I/I_0) versus G^2 of **3-6** (16.7 mM) and **1-12** (63 mM) in CD_2Cl_2:CD_3OD 10:1.

Table 7.2.9 Values of normalized I for the signal due to the α-fluorine nuclei (-CF_2COOH) of **3-6** (c = 16.7 mM) and TMS in CD_2Cl_2:CD_3OD 10:1 at different values of G^2 (a. u.) in the presence of **1-12** (63 mM).

G^2	$I_{\alpha\text{-}F}$ (**3-6**) (a.u.)	I(TMS) (a. u.)
4	1	1
16	0.99885	0.94731
36	0.97557	0.79635
64	0.94907	0.64490
100	0.85162	0.49978
144	0.79905	0.36345
256	0.61398	0.16136
400	0.48457	0.05678
576	0.33907	0.01595
784	0.21461	n.d.
1024	0.13088	n.d.

n.d. = not detectable

7.2.7.3. PGSE studies

The hydrodynamic volume (V_H) of **3-6** has been measured in CD_2Cl_2:CD_3OD 10:1 (t = 22 °C) using the reported methodology, and it resulted to be 331 Å^3 (Fig. 7.2.24). Adding an excess of **1-12** (63 mM), V_H (**3-6**) becomes 685 Å^3 (Fig.7.2.25), confirming once again the association between the two moieties. Since the van der Waals volume of **1-12** is 405 Å^3, the hydrodynamic volume of the adduct **1-12·3-6** would be approximately 730 Å^3. Therefore, an experimental hydrodynamic volume of 685 Å^3 is compatible with a 1:1 adduct.

Table 7.2.10 Diffusion coefficients (D_t, 10^{-10} m^2 s^{-1}), hydrodynamic radii (r_H, Å) and hydrodynamic volumes (V_H, Å^3) of **3-6** (C = 16.7 mM) in CD_2Cl_2:CD_3OD 10:1 at different concentrations of **1-12** (c, mM).

c (**1-12**)	D_t(**3-6**)	r_H(**3-6**)	V_H(**3-6**)
0	10.4	4.29	331
63	6.55	5.47	685

Experimental Details on PGSE Studies.

^{1}H and ^{19}F PGSE NMR measurements were performed by using the double stimulated echo sequence with longitudinal eddy current delay at 298 K without spinning. The dependence of

the resonance intensity (I) on a constant waiting time and on a varied gradient strength G is described by the following equation:

$$\ln\left(\frac{I}{I_0}\right) = -(\gamma\delta)^2 D_t \left(\Delta - \frac{\delta}{3}\right) G^2$$

Where I is the intensity of the observed spin echo, I_0 the intensity of the spin echo in the absence of gradient, D_t the self-diffusion coefficient, Δ the delay between the midpoints of the gradients, δ the length of the gradient pulse, and γ the magnetogyric ratio. The shape of the gradients was rectangular, their length d was 4–5 ms, and their strength G was varied during the experiments. The semi-logarithmic plots of $\ln(I/I_0)$ versus G^2 were fitted by using a standard linear regression algorithm, and a correlation factor better than 0.99 was always obtained. Different values of G, and number of transients were used for different samples.

The self-diffusion coefficient D_t, which is directly proportional to the slope m of the regression line obtained by plotting $\ln(I/I_0)$ versus G^2 was estimated by evaluating the proportionality constant for a sample of HDO (5%) in D_2O (known diffusion coefficients in the range 274–318 K) under the exact same conditions as the sample of interest. The TMS was taken as internal standard. The D_t data were treated as described in the literature in order to derive the hydrodynamic dimensions. Error propagation analysis yielded a standard deviation of approximately 3-4 % in the hydrodynamic radius.

7.2.8. Solubility Studies:

Solubility studies of dicarboxylic acids (2), onium iodides (1) and their cocrystals (1·2)

Experiments of solubility of individual components and complexes were carried out according to reported standard procedures where the solid samples are taken in a round bottom flask and measured amounts of distilled water were added. The system was then stirred at 60 ^oC for 1 hour to form a clear solution. Samples were cooled to room temperature (25 °C) and the formed precipitate was removed by filtration. The collected aqueous parts are concentrated under the reduced pressure, the remaining water was removed by vacuum before further analysis. The solubility profile of the starting individual component and cocrystals are detailed below (table 7.2.11).

Table 7.2.11 solubility profile of individual components and complexes at 25 °C.

Compound	**Solubility in g/100 mL at 25 °C**
1-10	6.8 g
1-12	5.3 g
2-4	2.4 g
2-6	0.25 g
1-10·2-4	**16.5 g (3.6 g of 2-4)**
1-12·2-6	**12.6 g (2.90 g of 2-6)**
2-1	Highly soluble
2-2	8.3 g
2-3	43 g
2-5	2.5 g
2-7	0.21 g
2-8	0.03 g
2-9	0.51 g
2-10	0.006

7.2.9. Selective binding studies of onium iodide with a series of dicarboxylic acids and separation of size matching complexes

To study the selective binding of **1** with the matching diacids **2** we have opted for the two methods described below.

7.2.9.1. Crystallization of matching acids from the mixture of dicarboxylic acids

Series dicarboxylic acids were dissolved together in acetonitrile:methanol (90:10) in 5 mL crystallization glass vial. To this solution an equivalent amount of separately dissolved matching bismethonium iodide in the same solvent mixture was added. After slow evaporation of solvents at room temperature for approximately 2-4 days the mismatching dicarboxylic acids precipitate and the remaining mother liquor contains the matching acid complexed with bismethonium salts. The precipitated dicarboxylic acids are removed by filtration. The separated filtrate is concentrated under reduced pressure and dried under high vacuum to get pure size matching complexes. Melting point, IR spectroscopy and PXRD analysis of separated complexes perfectly matches with the previously synthesized pure size-matching complexes. A series of trials for selective binding and separation of size-matching complexes by crystallization are described below (Table 7.2.12).

Table 7.2.12 Selective binding studies of diacids by crystallization at room temperature

Trial No	Dicarboxylic Acids Mixture	Added Onium Iodide	Precipitated Mismatching Acids	Content of Surnatant	Obtained Yield (matching complex)
1	*2-4* 2-6 2-8	*1-10*	2-6, 2-8	*1-10·2-4*	82%
2	*2-4* 2-8 2-10	*1-10*	2-8, 2-10	*1-10·2-4*	84%
3	*2-4* 2-6 2-7	*1-10*	2-7, 2-6	*1-10·2-4*	79%
4	*2-6* 2-4 2-8	*1-12*	2-4, 2-8	*1-12·2-6*	78%
5	*2-6* 2-5 2-7	*1-12*	2-5, 2-7	*1-12·2-6*	81%
6	*2-6* 2-8 2-10	*1-12*	2-8, 2-10	*1-12·2-6*	83%

Melting point and IR spectroscopy analysis of pure and separated complexes:

Pure* 1-10·2-4 *complex:

Melting point 187- 189° C

I.R. selected bands (cm^{-1}): 3179, 2926, 2850, 1727, 1394, 1230, 1145, 905, 751.

Trial no.1. Separated 1-10·2-4 complex from mixture of 2-4, 2-6, 2-8

Melting point 186- 189° C

I.R. selected bands (cm^{-1}): 3178, 2927, 2852, 1729, 1397, 1228, 1148, 905, 754.

Trial no.2. Separated 1-10·2-4 complex from mixture of 2-4, 2-8, 2-10

Melting point 187- 189° C

I.R. selected bands (cm^{-1}): 3177, 2924, 2856, 1729, 1398, 1232, 1152, 903, 750.

Trial no.3. Separated 1-10·2-4 complex from mixture of 2-4, 2-7, 2-6

Melting point: 187- 189° C

I.R. selected bands (cm^{-1}): 3179, 2922, 2847, 1732, 1399, 1232, 1148, 908, 749.

Pure 1-12·2-6 complex:

Melting point: 188- 190° C

I.R. selected bands (cm^{-1}): 3139, 3013, 2925, 2843, 1721, 1388, 1216, 1157, 962, 907, 757.

Trial no.4. Separated 1-12·2-6 complex from mixture of 2-4, 2-6, 2-8

Melting point: 188- 189° C

I.R. selected bands (cm^{-1}): 3132, 3015, 2927, 2847, 1722, 1391, 1214, 1163, 964, 909, 748

Trial no.5. Separated 1-12·2-6 complex from mixture of 2-5, 2-6, 2-7

Melting point: 188- 190° C

I.R. selected bands (cm^{-1}): 3134, 3012, 2923, 2840, 1716, 1390, 1212, 1159, 960, 911, 754

Trial no.6. Separated 1-12·2-6 complex from mixture of 2-6, 2-8, 2-10

Melting point: 188- 189° C

I.R. selected bands (cm^{-1}): 3142, 3015, 2928, 2851, 1725, 1390, 1219, 1167, 968, 914, 750.

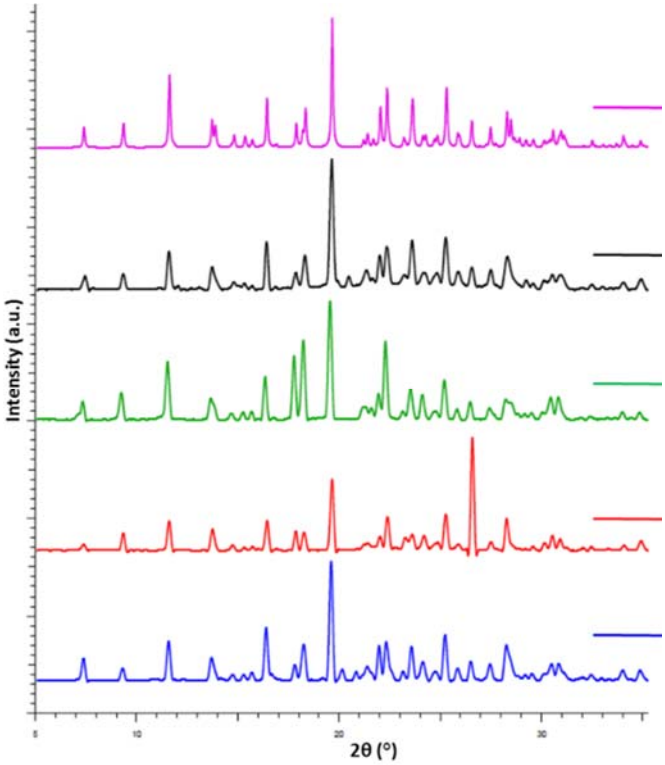

Figure 7.2.26 PXRD patterns of **1-10·2-4** prepared from pure **1-10** and mixtures of diacids **2** (table 7.2.12); Magenta: Simulated pattern from the single crystal structure at 90 K; Black: Experimental pattern of the cocrystals obtained via solution crystallization; Green: Experimental pattern of the separated matching **1-10·2-4** complexes from the mixture of **2-4, 2-6, 2-8**; Red: Experimental pattern of the separated matching **1-10·2-4** complexes from the mixture of **2-4, 2-8, 2-10**; Blue: Experimental pattern of the separated matching **1-10·2-4** complexes from the mixture of **2-4, 2-6, 2-7**.

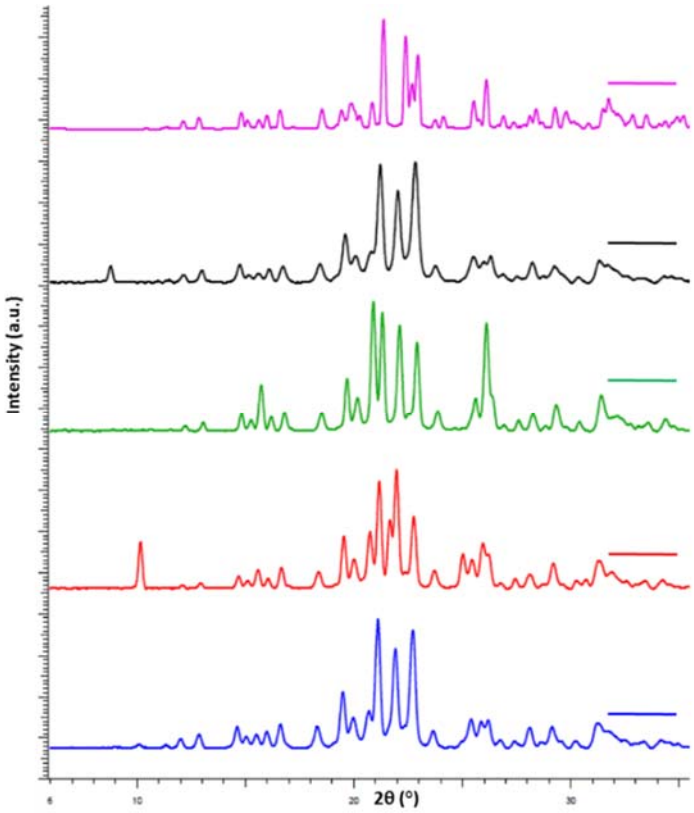

Figure 7.2.27 PXRD patterns of **1-12·2-6** obtained from pure **1-12** and from mixtures of dicids **2** (table 7.2.14); Magenta: Simulated powder pattern from the single crystal structure at 90 K; Black: Experimental pattern of the cocrystals obtained via solution crystallization; Green: Experimental pattern of the separated matching **1-12·2-6** complexes from the mixture of **2-4, 2-6, 2-8**; Red: Experimental pattern of the separated matching **1-12·2-6** complexes from the mixture of **2-5, 2-6, 2-7**; Blue: Experimental pattern of the separated matching **1-12·2-6** complexes from the mixture of **2-6, 2-8, 2-10.**

7.2.9.2. Separation of matching complex from mixture of diacids by milling reactions

Series of dicarboxylic acids **2** were added to a Retsch ball milling steel jar, the equimolar amount of size matching bismethonium iodide **1** were added. A small amount of CH_3OH was added (around 0.5 mL for total quantity of 1 g). After placing steel ball (1 mm) the system was milled for 15 minutes at 30 MHz. Melting point analysis, IR spectroscopy and powder X-ray analysis of milled mixtures clearly show the selective formation of the size matching dicarboxylic acid/methonium iodide cocrystal and mismatching diacids remain unreacted.

By keeping the concept of selective binding in mind, water was (the amount of water was chosen based on the solubility profile) added to the finely ground mixture from the ball milling and gently heated up to obtain a clear solution. The system was cooled to room temperature, the precipitated mismatching diacids were removed by filtration, while evaporation of filtrate under reduced pressure yielded the pure size-matching complexes. Once

again melting point, PXRD, IR and Mass spectroscopy analysis were carried out to assess the formation and purity of the obntained size matching cocrystals.

Table 7.2.13 Selective binding studies of diacids by crystallization in room temperature.

Trial. No	Dicarboxylic Acids Mixture	Added Onium Iodide	Precipitated Mismatching Acids	Content of Surnatant	Obtained Yield (matching complex)
1	*2-4* 2-5 2-6 2-7 2-8 2-9	*1-10*	2-5 2-6 2-7 2-8 2-9	*1-10·2-4*	82%
2	2-5 *2-6* 2-7 2-8 2-9	*1-12*	2-5 2-7 2-8 2-9	*1-12·2-6*	84%

Melting point and IR spectroscopy analysis of pure and separated complexes:

Pure 1-10·2-4 complex obtained by milling reaction

Melting point: 188-189 °C, I.R. selected bands (cm^{-1}): 3171, 2927, 2852, 1725, 1392, 1228, 1139, 960, 753.

Trial No 1. Complex 1-10·2-4 separated from the mixture of 2-4, 2-5, 2-6, 2-7, 2-8, 2-9

Melting point: 187-189 °C, I.R. selected bands (cm^{-1}): 3174, 2924, 2857, 1719, 1389, 1230, 1139, 964, 749.

Pure 1-12·2-6 complex obtained by milling reaction

Melting point: 187-189 °C, I.R. selected bands (cm^{-1}): 3137, 2925, 2843, 1721, 1386, 1216, 1157, 1118, 962, 759.

Trial No 2. Complex 1-12·2-6 separated from the mixture of 2-5, 2-6, 2-7, 2-8, 2-9

Melting point: 187-189 °C, I.R. selected bands (cm^{-1}): 3133, 2922, 2844, 1724, 1385, 1217, 1158, 1119, 963, 760.

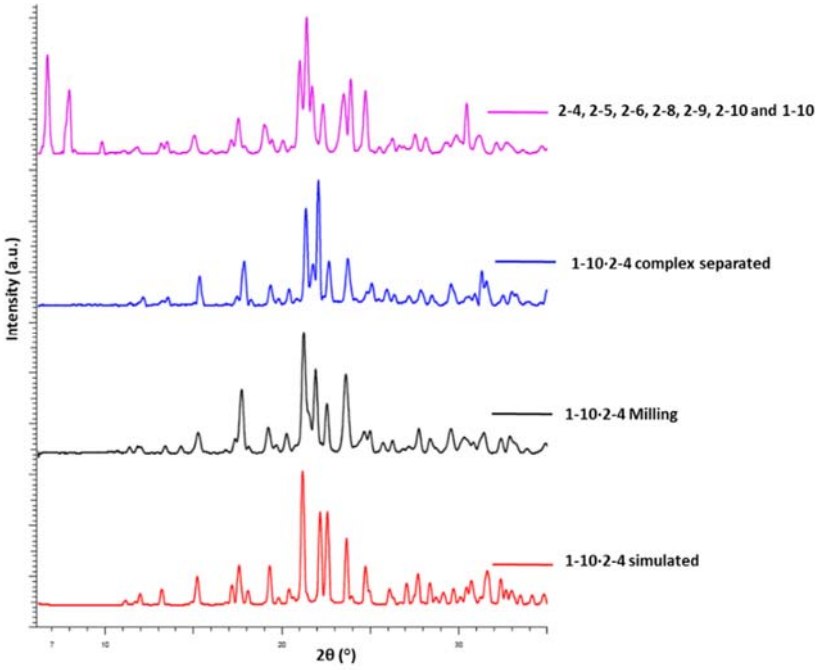

Figure 7.2.28 PXRD patterns of pure and separated **1-10·2-4** obtained by milling reaction (table 7.2.13); Magenta: Experimental pattern of the mixture of diacid **2-4, 2-5, 2-6, 2-8, 2-9, 2-10** with host **1-10**; Blue: Experimental pattern of the separated matching **1-10·2-4** cocrystals from the diacid mixtures; Black: experimental pattern **1-10·2-4** of cocrystals obtained via milling reaction; Red: Simulated powder pattern **1-10·2-4** from the single crystal structure at 90 K;

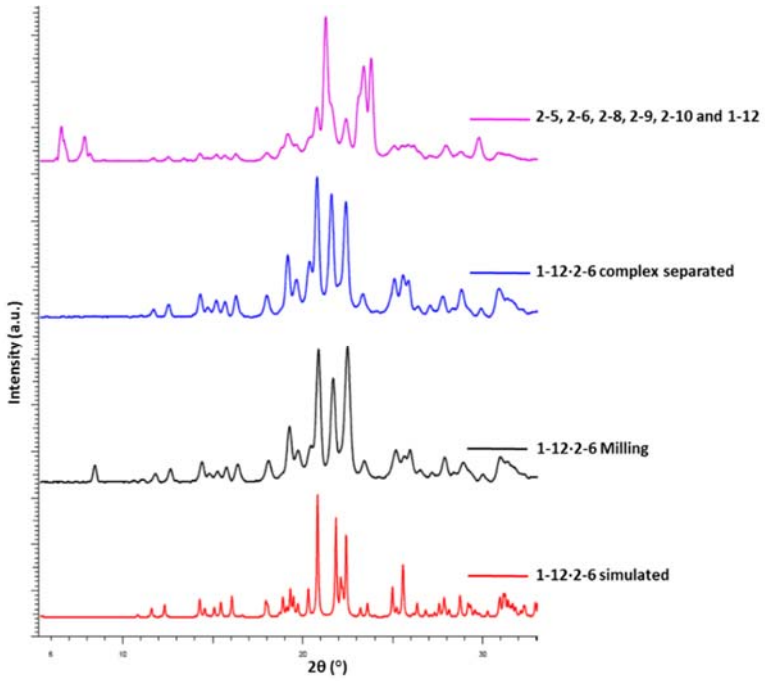

Figure 7.2.29 PXRD patterns of pure and sepaarted **1-12·2-6** obtained by milling reactions (table 7.2.13); Magenta: Experimental pattern of the mixture of diacid **2-5, 2-6, 2-8, 2-9, 2-10** with host **1-12**; Blue: Experimental pattern of the separated matching **1-12·2-6** cocrystals from the diacid mixtures;

Black: experimenatl pattern **1-12·2-6** of cocrystals obtained via milling reaction; Red: Simulated powder pattern **1-12·2-6** from the single crystal structure at 90 K.

7.2.10. Mass spectroscopy analysis of the pure and separated size matching cocrystals.

The purity of the separated size-matching cocrystals was examined by mass spectroscopy analysis; specifically, the spectrum of the cocrystal obtained from the pure matching diacid was compared with spectra of cocrystals obtained by crystallization of mixtures of diacids. All spectra were nearly identical and not even a trace amount of mismatching dicarboxylic acids was observed suggesting complete separations. Selected mass spectra for the complexes and separated diacids are given below.

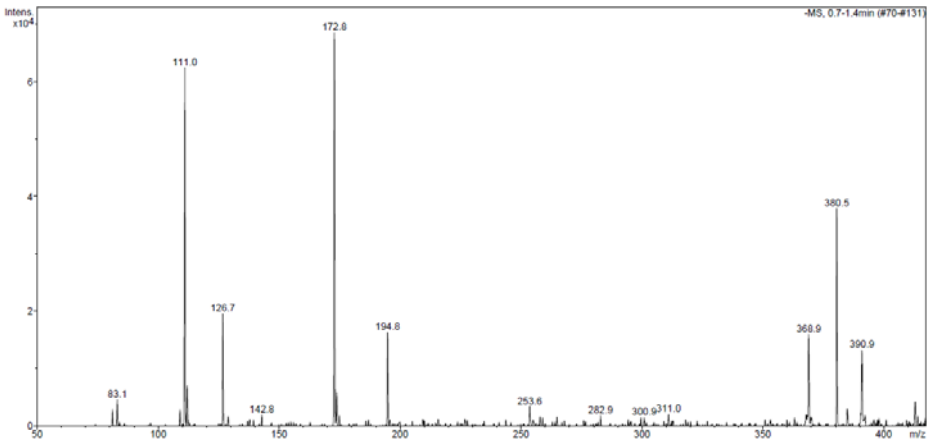

Figure 67.2.30 Mass spectrum of pure **1-12·2-6** cocrystal.

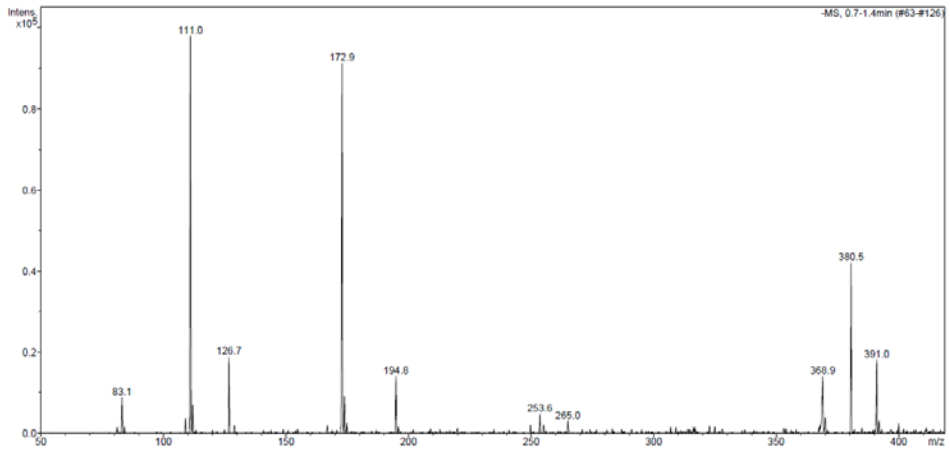

Figure 7.2.31 Mass spectrum of **1-12·2-6** cocrystal separated by crystallization from the mixture of **2-6, 2-8, 2-10**.

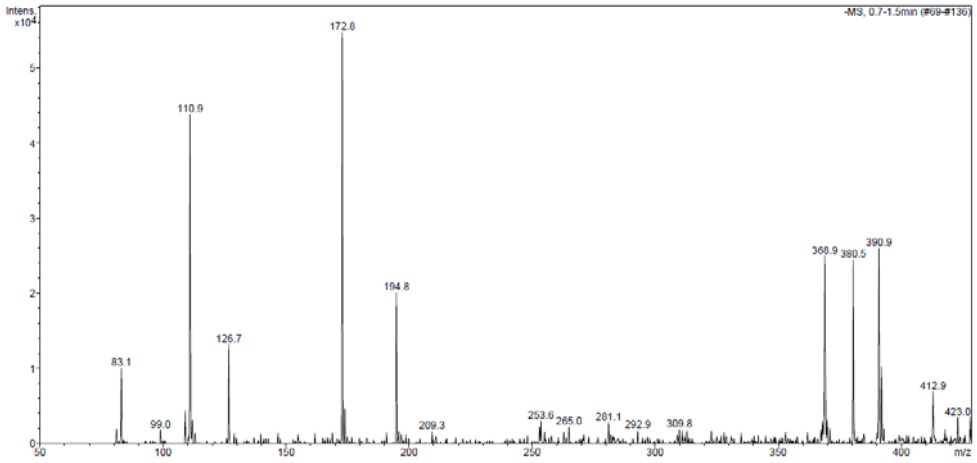

Figure 7.2.32 Mass spectrum of **1-12·2-6** cocrystal separated by milling/washing from the mixture of **2-6, 2-8, 2-10.**

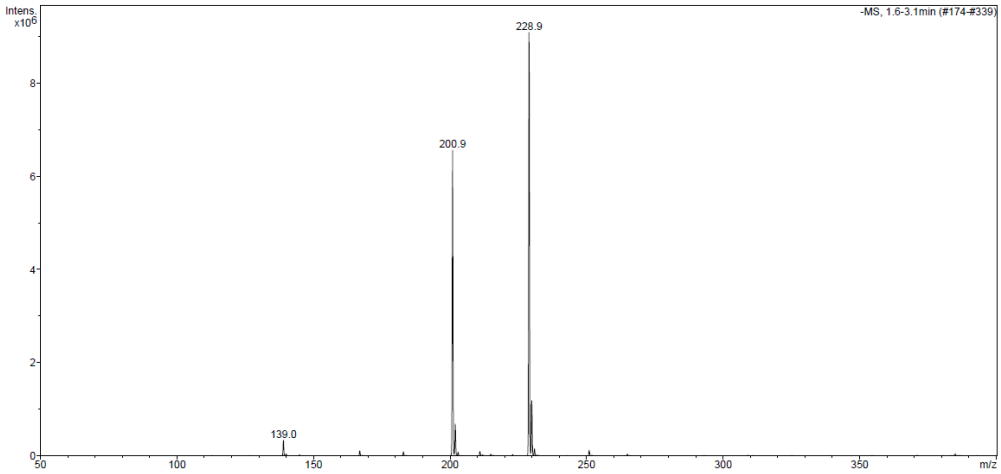

Figure 7.2.33 Mass spectrum of diacids **2-8** and **2-10** separated from crystallization procedures.

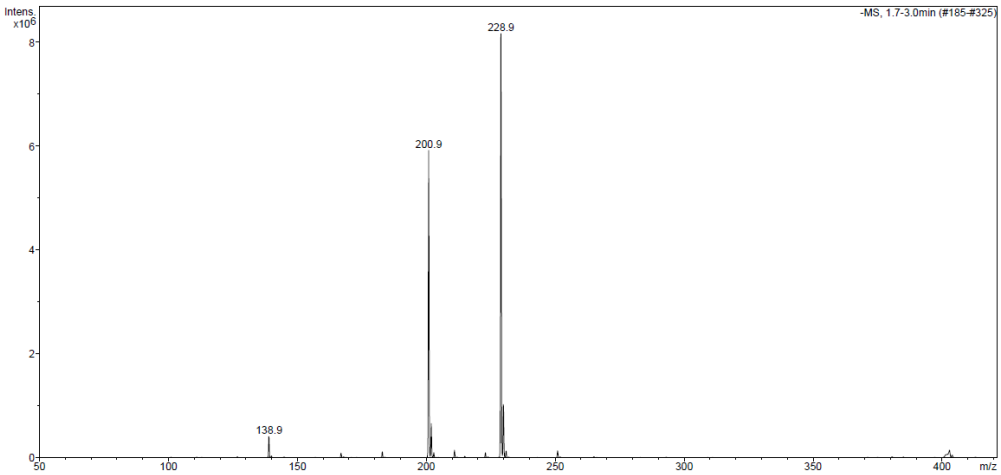

Figure 7.2.34 Mass spectrum of separated **2-8** and **2-10** diacids by milling and washing

7.2.11. Recovery of dicarboxylic acid from size-matching cocrystals

7.2.11.1. By addition of diiodoperfluoroalkanes 4 (DIPFA)

General procedure for recovery via the synthesis of 1·4 cocrystals: Equimolar amounts of size-matching diiodoperfluoroalkanes **4** (DIPFA) and cocrystal **1·2** were solubilized separately in chloroform and methanol, respectively. When these two solutions are mixed, the bismethonium iodide-DIPFA cocrystal is formed immediately as a white precipitate. This precipitate is filtered off and evaporation of surnatant affords the pure dicarboxylic acid in quantitative yields. Both precipitate and dicarboxylic acids were characterized by melting point, IR and powder XRD analysis.

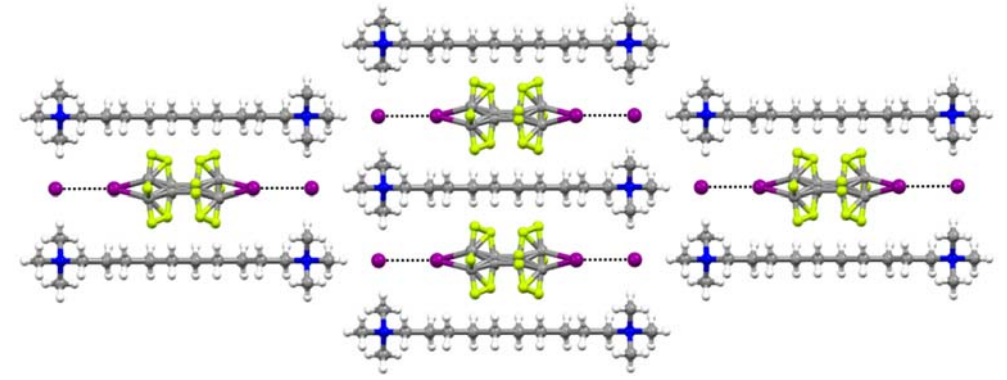

(A)

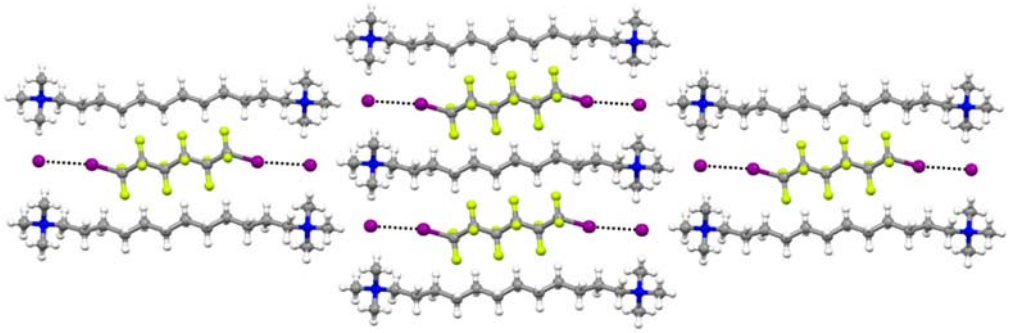

(B)

Figure 7.2.35 Crystal packing of cocrystals**1·4;** (A) decamethonium iodide with iodooctafluorobutane (**1-10·4-4**), (B) dodecamethonium iodide with diiododododecafluorohexane (**1-12·4-6**), dotted lines indicate the halogen bonding between host onium iodide and DIPFA. Color codes: grey, carbon; blue, nitrogen; white, hydrogen; red, oxygen; magenta, iodine. (*Complete SXRD data's were not collected as the compound is already reported in a previous paper, reference 12 in chapter 2 for more information about structural details*)

Recovery of 2-4 from mixture of 1-10·2-4

Matching complex **1-10·2-4** (500 mg, 0.76 mmol) and diidooctafluorobutane **4-4** (0.360 mg, 0.78 mmol) were dissolved separately in equimolar solutions of CH_3OH and $CHCl_3$, respectively. On mixing these two solutions, **1-10·4-4** precipitates almost immediately, and it

was filtered off. The filtrate were concentrated under reduced pressure in order to obtain the adipic acid **2-4** in pure form.

Pure **1-10·2-4:** Pale yellow solid, mp: 187 °C, I.R. selected bands (cm^{-1}): 3138, 3009, 2926, 2850, 1721, 1407, 1270, 1188, 919, 761; adduct **1-10·4-4:** mp: 228 °C. I.R. selected bands (cm^{-1}): 3008, 2939, 2869, 1473, 1403, 1182, 1121, 1040, 960, 759; separated **2-4,** mp: 154 °C, I.R. selected bands (cm^{-1}): 2961, 2876, 1685, 1407, 1270, 1188, 919, 732.

Recovery of 1b from mixture of 1-12·2-6:

The same protocol was used as described above for **1-10·2-4**.

Pure **1-12·2-6:** Pale yellow solid, mp: 190 °C, I.R. selected bands (cm^{-1}): 3132, 3009, 2920, 2847, 1721, 1470, 1391, 1217, 1157, 960, 900, 757, 653; adduct **1-12·4-6:** mp: 226 °C. I.R. selected bands (cm^{-1}): 3012, 2928, 2855, 1481, 1406, 1193, 1122, 1041, 964, 907, 763,730; separated **2-6:** mp: 142 °C, I.R. selected bands (cm^{-1}): 2933, 2863, 1685, 1400, 1327, 1251, 1185, 922, 678, 520.

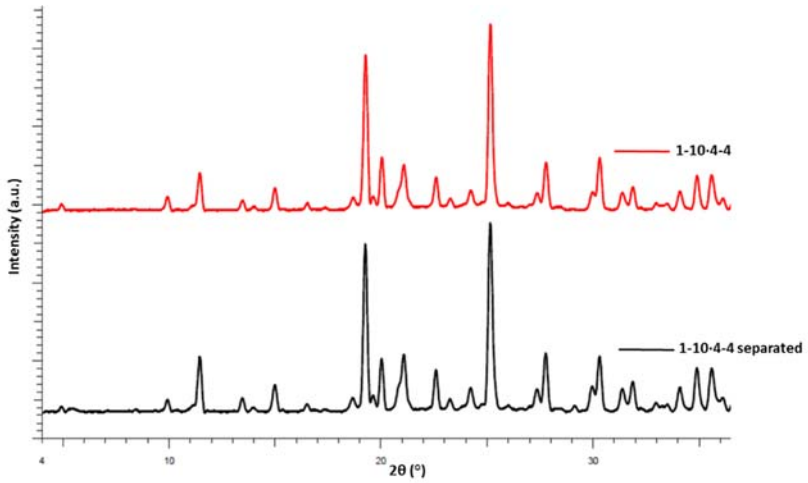

Figure 7.2.36 PXRD patterns for cocrystal **1-10·4-4** prepared from pure **1-10** and **4-4** (top, red trace) and from **1-10·2-4** and **4-4** (bottom, black trace).

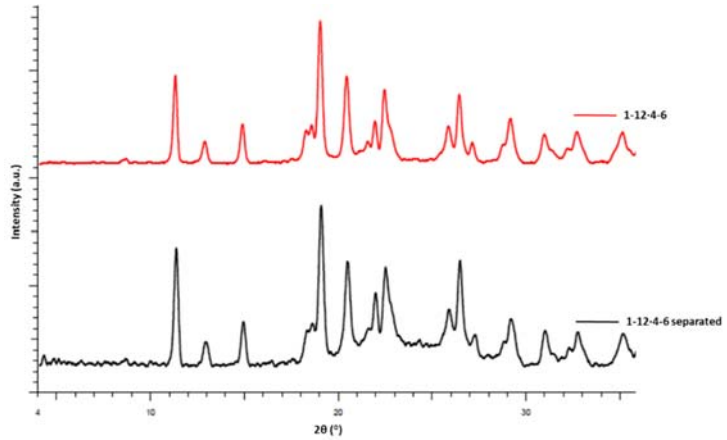

Figure 7.2.37 PXRD patterns for cocrystal **1-12·4-6** prepared from pure **1-12** and **4-6** (top, red trace) and from **1-12·2-6** and **4-6** (bottom, black trace).

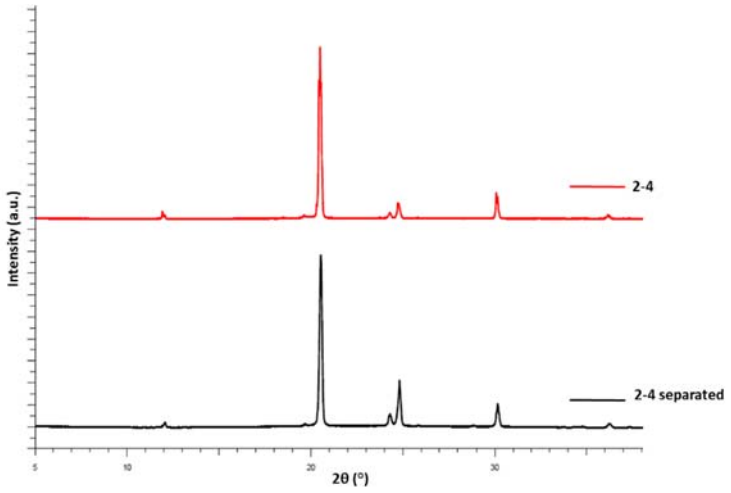

Figure 7.2.38 Comparison of PXRD patterns for the pure 2-4 with 2-4 separated from 1-10·4-4 cocrystal.

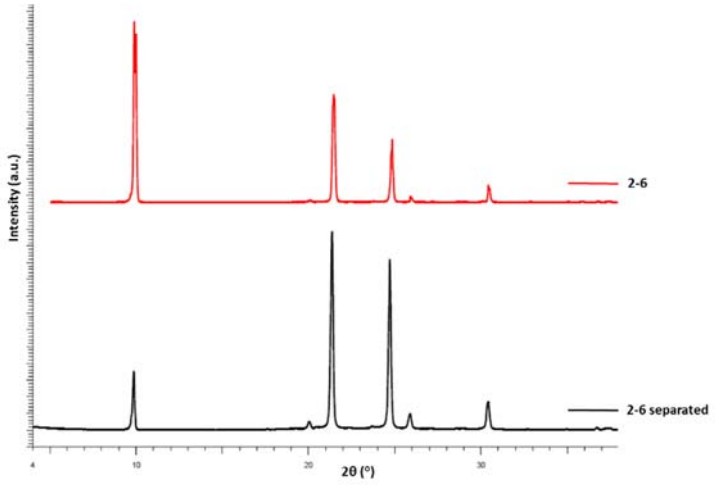

Figure 7.2.39 Comparison of PXRD patterns for the pure **2-6** with **2-6** separated from **1-12·2-6** cocrystal.

7.2.11.2. Recovery of dicarboxylic acids by gas solid reaction with diiodoperfluoroalkanes 4 (DIPFA)

Experimental procedure: Approximately 100 mg of pure **1·2** complex were placed in an open glass vial, this vial was placed in a bigger vial containing matching DIPFA and the system was sealed to allow DIPFA's vapors to diffuse into matching cocrystals. The reaction progress were monitored *via* IR spectroscopy and melting point analysis.

Expulsion of 2-4 by 4-4 in 1-10·2-4 cocrystal

Pure 1-10·2-4 cocrystal: White solid, mp: 187-189 °C, I.R. selected bands (cm^{-1}): 3179, 2926, 2850, 1727, 1394, 1230, 1145, 905, 751. Pure **1-10,** mp: 252 °C; I.R. selected bands (cm^{-1}): 3486, 3431, 2952, 2858, 1630, 1474, 1475, 964, 907, 584; Pure **2-4**: 151-153 °C, I.R. selected bands (cm^{-1}): 2961, 1685, 1407, 1275, 1189, 915, 735.

After a gas solid reaction (7 days at room temperaure): Pale brown solid; mp: one portion starts melting at 151 °C and complete melting at 220 °C. I.R. selected bands (cm^{-1}): 3006, 2951, 2864, 1692, 1427, 1279, 1184, 1125, 1038, 731, 629.

Expulsion of 2-6 by 4-6 in 1-12·2-6 cocrystal

Pure cocrystal 1-12·2-6: White solid, mp of cocrystal: 188- 190 °C, I.R. selected bands (cm^{-1}): 3139, 3013, 2925, 2843, 1721, 1388, 1216, 1157, 962, 907, 757. Pure **1-12,** mp: 222 °C; I.R. selected bands (cm^{-1}): 3003, 2913, 2848, 1461, 970, 939, 915, 728; Pure **2-6**: 145 °C, I.R. selected bands (cm^{-1}): 2913, 2863, 1685, 1409, 1325, 1250, 1187, 917, 795.

After a gas solid reaction (7 days at room temperature): Pale brown solid; mp of cocrystal: one portion starts melts at 145 °C and complete melting at 220 °C. I.R. selected bands (cm^{-1}): 3010, 2941, 2863, 1688, 1473, 1327, 1249, 1199, 1140, 1081, 959, 911, 765, 724, 682.

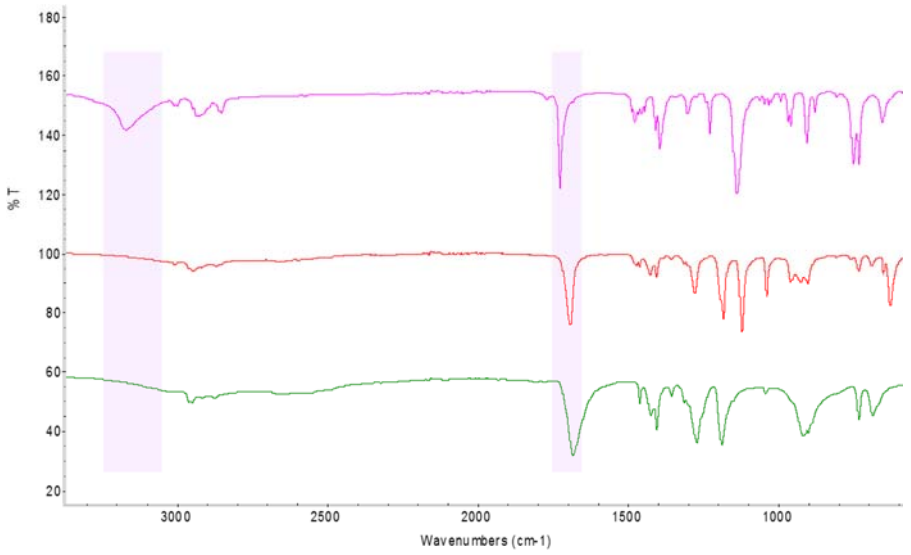

Figure 7.2.40 IR spectra (3200-600 cm^{-1} range) of crystalline **1-10·2-4** before (top, magenta trace) and after (mid, red trace) gas solid reaction with **4-4**; pure **2-4** (bottom, green trace**).**

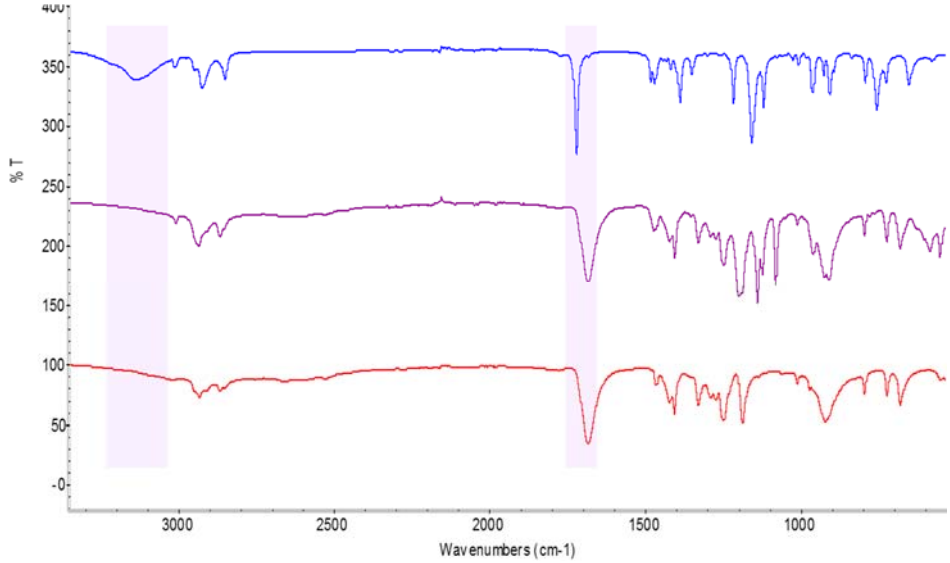

Figure 7.2.41 IR spectra (3200-600 cm^{-1} range) of crystalline **1-12·2-6** before (top, blue trace) and after (mid, violet trace) gas solid reaction with **4-6**: pure **2-6** (bottom, red trace).

7.2.12. Purity analysis by HPLC

Purity of separated matching complexes were determined by reversed-phase high-performance liquid chromatography connected with mass spectrometry (LC-MS). Because the aliphatic dicarboxylic acids lack a good ultraviolet (UV) chromophore, that's why mass spectrometry (MS) is used to achieve sensitive detection of acid moiety. The separation is performed on a Thermo Scientific Acclaim™ Organic Acid (OA, 3 μm, 2.1 × 150 mm) column with 0.1% formic acid and acetonitrile as a mobile phase.

7.3. Halogen bonding in cryptated salts

7.3.1. Halogen bonded Borromean networks by design: Topology invariance and metric tuning in a library of multi-component systems

7.3.1.1. Materials and methods

Commercial AR grade solvent (Ethanol) were used without any further purification for supramolecular synthesis and crystallization. Starting materials were purchased from Sigma–Aldrich, TCI (Europe and Japan) and Apollo Scientific. IR spectra were obtained using a Nicolet Nexus FT-IR spectrometer equipped with UATR unit. Melting points were determined with a Reichert instrument by observing the melting and crystallizing process through a polarizable optical microscope. DSC analysis were carried out with a Mettler Toledo DSC600 hot stage (10 °C/min). NMR spectra (^{1}H and ^{19}F) were recorded at ambient temperature on a Bruker AV-400 spectrometer, at 400 MHz. All chemical shifts are given in ppm. Ethanol-d_6 was used as a solvent.

7.3.1.2. Single crystal X-ray structure determination and data parameters

The crystals were diffracted using Mo-Kα radiation on a Bruker KAPPA APEX II diffractometer with a Bruker KRYOFLEX low temperature device. Crystal structures of the reported complexes were solved by direct method and refined against F^2 using SHELXL97[1]. Packing diagrams were generated using Mercury 3.8.[2] Intermolecular interactions were analysed with PLATON.[3] The non-hydrogen atoms were refined anisotropically and hydrogen atoms were refined using difference Fourier map or positioned geometrically.

Table 7.3.1.1. Crystallographic data and structure refinement parameters for cocrystals formed by crypt-222 (**1**), sodium chloride and bromide (**2a** and **2b**, respectively) and α,ω-diiodoperfluoroalkanes **3a-d**.

Structure	**1•2a•3a**	**1•2a•3b**	**1•2a•3c**
Formula	$C_{42}H_{72}Cl_2F_{12}I_6N_4Na_2O_{12}$	$C_{26}H_{36}ClF_{16}I_4N_2NaO_6$	$C_{54}H_{72}Cl_2F_{36}I_6N_4Na_2O_{12}$
Molecular formula	2(**1•2a**)•3(**3a**)	(**1•2a**)•2(**3b**)	2(**1•2a**)•3(**3c**)
Fw	1931.32	1342.61	2531.44
Crystallographic System	Trigonal	Orthorhombic	Monoclinic
Space group	*R*-3*c*	$C222_1$	$\boldsymbol{P}2_1$
a (Å)	11.4435(9)	18.7124(17)	12.3140(12)
b (Å)	11.4435(9)	20.013(2)	22.647(2)
c (Å)	84.639(7)	11.7798(10)	15.5410(15)
α (°)	90	90.00	90.00
β (°)	90	90.00	92.803(10)
γ (°)	120	90.00	90.00
V (Å^3)	9598.8(13)	4411.4(7)	4328.8(7)
T (K)	103	103	103
Z	6	4	2
ρ (g.cm^{-3})	2.005	2.022	1.942
μ (mm^{-1})	3.099	3.001	2.354
Absorption correction T_{min}, T_{max}	0.4418, 0.5849	0.3972, 0.5101	0.6644, 0.7466
Collected, independent, obs. [$I>\sigma(I)$] reflections	154667, 6540, 5800	73501, 9047, 8147	63086, 28274, 23461
R_{int}	0.036	0.030	0.030
θ_{max}	39.99	35.28	33.42
Parameters, restraints	149, 39	323, 243	1268,1434
$wR(F^2)$, $R[F^2 > 2\sigma(F^2)]$	0.0564, 0.0246	0.0673, 0.0294	0.0863, 0.0383
Goodness of fit	1.103	1.084	1.010
Δρ (min,max)	-0.9,1.7	-0.6,1.2	-0.5, 1.9
Topology of supramolecular anion	(6,3) network	(4,4) network	ribbon of juxtaposed squares
CCDC number	1505909	1505910	1505911

Structure	**1•2b•3a**	**1•2b•3b**	**1•2b•3c**	**1•2b•3d**
Formula	$C_{42}H_{72}Br_2F_{12}I_6N_4Na_2O_{12}$	$C_{42}H_{81.40}Br_2F_{17.73}I_{4.43}N_4Na_2O_{13.57}$	$C_{60}H_{90}Br_2F_{36}I_6N_4Na_2O_{15}$	$C_{60}H_{72}Br_2F_{48}I_6N_4Na_2O_{12}$
Molecular formula	2(**1•2b**)•3(**3a**)	2(**1•2b**)•2.217(**3b**)•0.783(**EtOH**)	2(**1•2a**)•3(**3c**)•3(**EtOH**)	2(**1•2a**)•3(**3d**)
Fw	2020.24	2036.81	2758.56	2920.42
Crystallographic System	Trigonal	Monoclinic	Trigonal	Triclinic
Space group	*R*-3*c*	*Cc*	*R*-3	***P***-1
a (Å)	11.5113(14)	19.7905(15)	11.4448(15)	11.4362(12)
b (Å)	11.5113(14)	11.4577(9)	11.4448(15)	11.5407(12)
c (Å)	84.749(10)	32.498(2	58.475(8)	20.084(2)
α (°)	90	90.00	90	88.409(10)
β (°)	90	97.627(10)	90	89.682(11)
γ (°)	120	90.00	120	60.533(8)
V (Å^3)	9726(2)	7303.8(9)	6633.1(15)	2306.8(4)
T (K)	103	103	103	103
Z	6	4	3	1
ρ (g.cm^{-3})	2.070	1.852	2.072	2.102
μ (mm^{-1})	4.209	3.096	3.156	3.047
Absorption correction T_{min}, T_{max}	0.2317, 0.3824	0.4800, 0.5519	0.4380, 0.5769	0.6247, 0.6958
Collected, independent, obs. [$I>\sigma(I)$] reflections	72173, 6612, 5687	148452, 30684, 26979	64013, 6979, 5994	67609, 12343, 8049
R_{int}	0.044	0.052	0.027	0.072

θ_{max}	40.11	35.07	36.52	29.23
Parameters, restraints	142, 45	323, 243	286,363	604,0
wR(F^2), R[F^2 > 2σ(F^2)]	0.0585, 0.0268	0.0633, 0.0335	0.0875, 0.0315	0.0651, 0.0343
Goodness of fit	1.103	1.058	1.073	0.920
Δρ (min,max)	-1.4,1.3	-1.5,1.1	-0.9, 1.7	-0.8, 1.3
Topology of supramolecular anion	(6,3) network	(6,3) network	(6,3) network	pearl necklace
CCDC number	1505912	1505913	1505914	1505915

Table 7.3.1.2. Crystallographic data and structure refinement parameters for cocrystals formed by crypt-222 (**1**), sodium iodide (**2c**), and α,ω-diiodoperfluoroalkanes **3c,d**. **1•2c•3a** Has already been published (*Acta Cryst.* **2013***, E68*, m387-388; refcode: AFEHAW).

Structure	**1•2c•3c**	**1•2c•3d**
Formula	$C_{56}H_{78}F_{36}I_8N_4Na_2O_{13}$	$C_{60}H_{72}F_{48}I_8N_4Na_2O_{12}$
Molecular formula	2(**1•2c**)•3(**3c**)•**EtOH**	2(**1•2c**)•3(**3d**)
Fw	2760.40	3014.4
Crystallographic System	Monoclinic	Triclinic
Space group	*C*2/*c*	***P***-1
a (Å)	20.224(2)	11.6302(6)
b (Å)	11.5766(9)	11.6788(6)
c (Å)	38.451(3)	20.1421(10
α (°)	90	88.653(3)
β (°)	101.478(9)	88.965(2)
γ (°)	90	60.148(2)
V (Å^3)	8822.3(13)	2372.1(2)
T (K)	150	103
Z	4	1
ρ (g.cm^{-3})	2.078	2.110
μ (mm^{-1})	2.952	2.77
Absorption correction T_{min}, T_{max}	0.4380, 0.5769	0.4240, 0.4939
Collected, independent, obs. [*I*> σ *(I)*] reflections	75607, 13172, 10265	134012, 14968, 1293
R_{int}	0.057	0.028
θ_{max}	30.55	31.09
Parameters, restraints	805, 1597	959, 1139
wR(F^2), R[F^2 > 2σ(F^2)]	0.1452, 0.0623	0.1557, 0.0589
Goodness of fit	1.151	1.130
Δ ρ (min,max)	-3.1,1.5	-1.6, 3.4
Topology of supramolecular anion	(6,3) network	Borromean interpenetrated (6,3) network
CCDC number	1505916	1505917

Table 7.3.1.3. Crystallographic data and structure refinement parameters for cocrystals formed by crypt-222 (**1**), potassium halides **2d-f**, and α,ω-diiodoperfluoroalkanes **3c-e**. **1•2f•3a**, **1•2f•3b**, **1•2f•3c**, and **1•2f•3d** have already been published (*Chem. Commun.* **2006**, 1819-1821; refcodes: TEHQUT, IHURAE, TEHRAA, and IHUQUX, respectively).

Structure	**1•2d•3c**	**1•2d•3d**
Formula	$C_{56}H_{78}Cl_2F_{36}I_6\ K_2N_4O_{13}$	$C_{60}H_{72}Cl_2F_{48}I_6\ K_2N_4O_{12}$
Molecular formula	2(**1•2d**)•3(**3c**)•**EtOH**	2(**1•2d**)•3(**3d**)
Fw	2609.72	2863.72
Crystallographic System	Monoclinic	Trigonal
Space group	***P***$2_1/n$	***P***-3
a (Å)	12.876(2)	11.912(2)
b (Å)	22.489(4)	11.912(2)
c (Å)	15.665(3)	20.261(4)
α (°)	90	90
β (°)	100.51(2)	90
γ (°)	90	120
V (Å^3)	4460.0(14)	2489.8(6)
T (K)	90	127
Z	2	1
ρ (g.cm^{-3})	1.943	1.910
μ (mm^{-1})	2.371	2.149
Absorption correction T_{min},T_{max}	0.6928, 1.0000	0.7541, 1.0000
Collected, independent, obs. [$I>\sigma(I)$] reflections	74973, 12998, 11656	25438, 3841, 3281
R_{int}	0.032	0.023
θ_{max}	30.00	27.49
Parameters, restraints	614, 20	304, 557
$wR(F^2)$, $R[F^2 > 2\sigma(F^2)]$	0.1186, 0.0548	0.1257, 0.0530
Goodness of fit	1.113	1.040
Δρ (min,max)	-0.8,1.9	-0.6,1.2
Topology of supramolecular anion	ribbon of juxtaposed squares	Borromean interpenetrated (6,3) network
CCDC number	1505918	1505919

Structure	**1•2e•3c**	**1•2e•3d**	**1•2f•3e**
Formula	$C_{56}H_{78}Br_2F_{36}I_6K_2N_4O_{13}$	$C_{60}H_{72}Br_2F_{48}I_6\ K_2N_4O_{12}$	$C_{48}H_{36}F_{60}I_7KN_2O_6$
Molecular formula	2(**1•2e**)•3(**3c**)•**EtOH**	2(**1•2e**)•3(**3d**)	**1•2f**•3(**3e**)
Fw	2746.38	2952.64	2804.19
Crystallographic System	Monoclinic	Trigonal	Triclinic
Space group	***P***2_1	***P***-3	***P***-1
a (Å)	12.897(2)	11.727(2)	13.976(2)
b (Å)	22.537(3)	11.727(2)	14.730(2)
c (Å)	16.022(2)	20.290(3)	21.282(3)
α (°)	90	90	100.10(2)
β (°)	99.657(16)	90	96.99(2)
γ (°)	90	120	102.38(2)
V (Å^3)	4591.0(11)	2416.5(5)	4154.8(10)
T (K)	103	127	193
Z	2	1	2
ρ (g.cm^{-3})	1.952	2.029	2.241
μ (mm^{-1})	2.952	2.986	2.843
Absorption correction T_{min},T_{max}	0.4380, 0.5769	0.8498,1.0000	0.7366, 1.0000

Collected, independent, obs. [$I>\sigma(I)$] reflections	75607, 13172, 10265	35618, 6464, 5316	92349, 23695, 12307
R_{int}	0.057	0.027	0.039
θ_{max}	30.55	34.30	30.66
Parameters, restraints	805, 1597	329, 569	1467, 3269
$wR(F^2)$, $R[F^2 > 2\sigma(F^2)]$	0. 1469, 0.0627	0.0903, 0.0337	0.1908, 0.0604
Goodness of fit	1.150	1.099	0.911
$\Delta\rho$ (min,max)	-3.1,1.5	-0.9, 1.9	-1.4,3.0
Topology of supramolecular anion	ribbon of juxtaposed squares	Borromean interpenetrated (6,3) network	infinite chain of loosely connected discrete adducts
CCDC number	1505920	1505921	1505922

Table 7.3.1.4. Crystallographic data and structure refinement parameters for cocrystals formed by crypt-222 (**1**), rubidium halides **2g-i**, and α,ω-diiodoperfluoroalkanes **3c,d**.

Structure	**1•2g•3c**	**1•2h•3c**	**1•2h•3d**
Formula	$C_{56}H_{78}Cl_2F_{36}I_6N_4O_{13}Rb_2$	$C_{54}H_{74}Br_2F_{36}I_6N_4O_{13}Rb_2$	$C_{60}H_{72}Br_2F_{48}I_6N_4O_{12}Rb_2$
Molecular formula	2(**1•2g**)•3(**3c**)•**EtOH**	2(**1•2h**)•3(**3c**)•**H$_2$O**	2(**1•2a**)•3(**3d**)
Fw	2702.46	2763.33	3045.38
Crystallographic System	Monoclinic	Triclinic	Trigonal
Space group	***P***$2_1/c$	***P***-1	***P***-3
a (Å)	18.3661(13)	20.402(6)	11.9008(12)
b (Å)	22.5367(16)	20.609(7)	11.9008(12)
c (Å)	22.0198(14)	21.141(7)	20.483(2)
α (°)	90	118.216(14)	90
β (°)	101.118(3)	118.520(14)	90
γ (°)	90	90.16(2)	120
V (Å^3)	8943.2(11)	6576(4)	2512.3(4)
T (K)	103	103	103
Z	6	3	1
ρ (g.cm^{-3})	2.007	2.093	2.013
μ (mm^{-1})	3.354	4.270	3.752
Absorption correction T_{min}, T_{max}	0.4380, 0.5769	0.5029, 0.5790	0.2548, 0.3463
Collected, independent, obs. [$I>\sigma(I)$] reflections	210518, 31976, 22078	75248, 25112, 13329	37410, 4335, 3286
R_{int}	0.054	0.091	0.035
θ_{max}	34.03	26.02	28.69
Parameters, restraints	1122, 391	1653, 1280	266, 428
$wR(F^2)$, $R[F^2 > 2\sigma(F^2)]$	0.0647, 0.0354	0.0939, 0.0562	0.2311, 0.0804
Goodness of fit	1.005	0.993	1.046
$\Delta\rho$ (min,max)	-1.1,1.4	-0.9, 1.0	-1.8, 5.7
Topology of supramolecular anion	ribbon of juxtaposed squares	Borromean interpenetrated (6,3) network	(6,3) network
CCDC number	1505923	1505924	1505925

Structure	**1•2i•3c**	**1•2i•3d**
Formula	$C_{54}H_{72}F_{36}I_8N_4O_{12}Rb_2$	$C_{60}H_{72}F_{48}I_8N_4O_{12}Rb_2$
Molecular formula	2(**1•2i**)•3(**3c**)	2(**1•2i**)•3(**3d**)
Fw	2839.30	3139.36
Crystallographic System	Trigonal	Trigonal
Space group	***P***-3	***P***-3

a (Å)	12.241(2)	12.0208(7)
b (Å)	12.241(2)	12.0208(7)
c (Å)	17.612(3)	20.2652(14)
α (°)	90	90
β (°)	90	90
γ (°)	120	120
V (Å^3)	2285.5(7)	2536.0(3)
T (K)	296	103
Z	2	1
ρ (g.cm^{-3})	2.063	2.056
μ (mm^{-1})	3.895	3.538
Absorption correction T_{min}, T_{max}	0.2592, 0.3667	0.2175, 0.3196
Collected, independent, obs. [$I>\sigma(I)$] reflections	29933, 1800, 1375	39814, 4955, 3853
R_{int}	0.040	0.030
θ_{max}	21.67	30.03
Parameters, restraints	233, 190	314, 487
$wR(F^2), R[F^2 > 2\sigma(F^2)]$	0.1399, 0.0492	0.1633, 0.0582
Goodness of fit	1.040	1.048
Δρ (min,max)	-0.7,1.1	-1.7,3.1
Topology of supramolecular anion	Borromean interpenetrated (6,3) network	Borromean interpenetrated (6,3) network
CCDC number	1505926	1505927

Table 7.3.1.5. Crystallographic data and structure refinement parameters for cocrystals formed by crypt-222 (**1**), ammonium halides **2j-l**, and α,ω-diiodoperfluoroalkanes **3a-d**.

Structure	**1•2j•3c**	**1•2j•3d**	**1•2k•3d**
Formula	$C_{56}H_{86}Cl_2F_{36}I_6N_6O_{13}$	$C_{60}H_{82}Cl_2F_{48}I_6N_6O_{13}$	$C_{60}H_{82}Br_2F_{48}I_6N_6O_{13}$
Molecular formula	2(**1•2j**)•3(**3c**)•**EtOH**	2(**1•2j**)•3(**3d**)•**H$_2$O**	**1•2k**•3(**3d**)
Fw	2567.6	2839.62	2928.54
Crystallographic System	Monoclinic	Trigonal	Trigonal
Space group	$P2_1/c$	*P*-3	*P*-3
a (Å)	18.272(2)	11.949(2)	11.9484(10)
b (Å)	22.620(3)	11.949(2)	11.9484(10)
c (Å)	22.105(3)	20.359(4)	20.449(2))
α (°)	90	90	90
β (°)	100.571(12)	90	90
γ (°)	90	120	120
V (Å^3)	8981(2)	2517.4(8)	2528.3(4)
T (K)	103	103	103
Z	4	1	1
ρ (g.cm^{-3})	1.899	1.861	1.923
μ (mm^{-1})	2.264	2.044	2.774
Absorption correction T_{min}, T_{max}	0. 3832, 0. 4986	0.5653, 0.6783	0.4074, 0.4923
Collected, independent, obs. [$I>\sigma(I)$] reflections	186042, 37032, 25785	44589, 4898, 3737	59789, 4382, 3093
R_{int}	0.044	0.037	0.032
θ_{max}	37.42	29.99	28.75
Parameters, restraints	805, 1597	212, 9	234, 89
$wR(F^2), R[F^2 > 2\sigma(F^2)]$	0.0668, 0.0343	0.1654, 0.0552	0.2638, 0.0778
Goodness of fit	1.001	1.066	1.030

$\Delta\rho$ (min,max)	-1.3,1.6	-0.9, 3.1	-1.0,1.9
Topology of supramolecular anion	ribbon of juxtaposed squares	Borromean interpenetrated (6,3) network	Borromean interpenetrated (6,3) network
CCDC number	1505928	1505929	1505930

Structure	**1•2I•3a**	**1•2I•3b**	**1•2I•3c**	**1•2I•3d**
Formula	$C_{44}H_{86}F_{12}I_8N_6O_{13}$	$C_{40}H_{40}F_{16}I_5N_3O_6$	$C_{54}H_{80}F_{36}I_8N_6O_{12}$	$C_{60}H_{80}F_{48}I_8N_6O_{12}$
Molecular formula	2(**1•2I**)•3(**3a**)	**1•2I**•2(**3b**)	2(**1•2I**) •3(**3c**)	2(**1•2I**) •3(**3d**)
Fw	2150.39	1429.11	2704.44	3004.50
Crystallographic System	Triclinic	Monoclinic	Tri gonal	Trigonal
Space group	*P*-1	*C*2/*m*	***P***-3	***P***-3_1c
a (Å)	13.6266(10)	14.369(3)	12.2742(3)	12.0821(3)
b (Å)	13.8928(10)	23.356(4)	12.2742(3)	12.0821(3)
c (Å)	19.4320(12)	13.780(3)	17.5343(5))	39.2838(10)
α (°)	99.707(3)	90	90	90
β (°)	94.565(4)	94.557(12)	90)	90
γ (°)	92.430(4)	90	120	120
V (Å^3)	3608.7(4)	4610.0(16)	2287.73(10)	4966.3(2)
T (K)	103	155	296	103
Z	2	4	1	2
ρ (g.cm^{-3})	1.979	2.059	1.963	2.009
μ (mm^{-1})	3.522	3.475	2.836	2.640
Absorption correction T_{min}, T_{max}	0.5236, 0.6131	0.2235, 0.3204	0.2526, 0.2956	0.4763, 0.5731
Collected, independent, obs. [$I>\sigma(I)$] reflections	132848, 19237, 12406	45579, 8224, 6428	25284, 2067, 1574	56452, 3981, 3098
R_{int}	0.053	0.035	0.051	0.052
θ_{max}	29.13	32.03	22.71	27.89
Parameters, restraints	896, 357	535, 306	238, 246	266, 428
$wR(F^2)$, $R[F^2 > 2\sigma(F^2)]$	0.0939, 0.0414	0.0804, 0.0367	0.1687, 0.0507	0.2083, 0.0687
Goodness of fit	1.007	1.116	1.084	1.067
$\Delta\rho$ (min,max)	-2.2,2.8	-1.6, 1.3	-0.5, 0.8	-2.0, 3.6
Topology of supramolecular anion	(6,3) network	Interpenetrated (4,4) network	Borromean interpenetrated (6,3) network	Borromean interpenetrated (6,3) network
CCDC number	1505931	1505932	1505933	1505934

7.3.1.3. NMR spectroscopy

Experiments aimed at establishing the most convenient conditions to synthesise the target library.

7.3.1.3.1. Assessment that cryptation occurs quite rapidly under adopted conditions.

Pure 4,7,13,16,21,24-hexaoxa-1,10-diazabicyclo[8.8.8]hexacosane (crypt-222, 1). ^{1}H NMR (400 MHz, Ethanol-*d*$_6$): δ, 3.70 (s, 12H) 3.63-3.66 (t, 12H), 2.71-2.73, (t, 12H).

Pure 1,2-diiodotetrafluoroethane (3a). ^{19}F NMR (400 MHz, Ethanol-*d*$_6$): δ, -57.71.

Pure 1,4-diiodooctafluorobutane (3b). ^{19}F NMR (400 MHz, Ethanol-*d*$_6$): δ, -65.11 (C*F*$_2$-I), -113.65 (C*F*$_2$CF$_2$-I).

Pure 1,6-diiododododecafluorohexane (3c). ^{19}F NMR (400 MHz, Ethanol-*d*$_6$): δ, -65.77 (C*F*$_2$-I), -113.65 (C*F*$_2$CF$_2$-I), -121.84 (C*F*$_2$ CF$_2$CF$_2$-I).

Pure 1,8-diiodohexadecafluorooctane (3d). ^{19}F NMR (400 MHz, Ethanol-*d*$_6$): δ, -66.01 (C*F*$_2$-I), -114.68 (C*F*$_2$CF$_2$-I), -121.79 (C*F*$_2$ CF$_2$CF$_2$-I), -122.68 (C*F*$_2$ CF$_2$ CF$_2$CF$_2$-I).

Solutions obtained on mixing 1, 2, and 3 in 1:1:1.5 ratio. The cryptand **1** (0.025 mmol), the halide salt **2** (0.025 mmol), and the α,ω-dioodoperfluoroalkane **3** (0.037 mmol) are added to an NMR tube containing ethanol-*d6* (0.5 mL) and the resulting system is monitored via ^{1}H and ^{19}F NMR. Spectra immediately after mixing the starting tectons (Time 0) and after 12 hours at room temperature (Time 12) are reported.

Self-assembly in solutions formed starting from crypt-222 (1), sodium chloride (2a), and 1,2-diiodotetrafluoroethane (3a). Time 0: ^{1}H NMR (400 MHz, Ethanol-*d*$_6$): δ, 3.67 (s, 12H), 3.62-3.65 (t, 12H), 2.68-2.71, (t, 12H); ^{19}F NMR (400 MHz, Ethanol-*d*$_6$): δ -57.78. Time 12: ^{1}H NMR (400 MHz, Ethanol-*d*$_6$): δ, 3.64 (s, 12H) 3.62-3.64 (t, 12H), 2.68-2.70, (t, 12H); ^{19}F NMR (400 MHz, Ethanol-*d*$_6$): δ -57.78.

Self-assembly in solutions formed starting from crypt-222 (1), sodium bromide (2b), and 1,4-diiodooctafluorobutane (3b). Time 0: ^{1}H NMR (400 MHz, Ethanol-*d*$_6$): δ, 3.68 (s, 12H), 3.63-3.66 (t, 12H), 2.69-2.72, (t, 12H); ^{19}F NMR (400 MHz, Ethanol-*d*$_6$): δ -65.21, -113.64. Time 12: ^{1}H NMR (400 MHz, Ethanol-*d*$_6$): δ, 3.68 (s, 12H) 3.63-3.65 (t, 12H), 2.69-2.71, (t, 12H); ^{19}F NMR (400 MHz, Ethanol-*d*$_6$): δ -65.21, -113.64.

Self-assembly in solutions formed starting from crypt-222 (1), sodium iodide (2c), and 1,8-diiodohexadecafluorooctane (3d). Time 0: ^{1}H NMR (400 MHz, Ethanol-*d*$_6$): δ, 3.67 (s, 12H), 3.62-3.64 (t, 12H), 2.68-2.70, (t, 12H); ^{19}F NMR (400 MHz, Ethanol-*d*$_6$): δ -66.18, -114.69, -121.79, -122.67. Time 12: ^{1}H NMR (400 MHz, Ethanol-*d*$_6$): δ, 3.67 (s, 12H) 3.62-3.64 (t, 12H), 2.68-2.70, (t, 12H); ^{19}F NMR (400 MHz, Ethanol-*d*$_6$): δ -66.18, -114.74, -121.85, -122.73.

Self-assembly in solutions formed starting from crypt-222 (1), rubidium bromide (2h), and 1,6-diiododododecafluorohexane (3c). Time 0: ^{1}H NMR (400 MHz, Ethanol-*d*$_6$): δ, 3.64 (s, 12H), 3.57-3.59 (t, 12H), 2.58-2.61, (t, 12H); ^{19}F NMR (400 MHz, Ethanol-*d*$_6$): δ -65.91, -

114.67, -121.82. Time 12: ^{1}H NMR (400 MHz, Ethanol-d_6): δ, 3.64 (s, 12H) 3.57-3.59 (t, 12H), 2.58-2.60, (t, 12H); ^{19}F NMR (400 MHz, Ethanol-d_6): δ -65.91, -114.67, -121.82.

Self-assembly in solutions formed starting from crypt-222 (1), ammonium chloride (2j), and 1,8-diiodohexadecafluorooctane (3d). Time 0: ^{1}H NMR (400 MHz, Ethanol-d_6): δ, 6.98-7.24 (t, 4H), 3.65 (s, 12H), 3.59-3.61 (t, 12H), 2.59-2.61, (t, 12H); ^{19}F NMR (400 MHz, Ethanol-d_6): δ -66.08, -114.67, -121.78, -122.66, Time 12: ^{1}H NMR (400 MHz, Ethanol-d_6): δ, 3.65 (s, 12H) 3.58-3.61 (t, 12H), 2.59-2.61, (t, 12H), NH_4 protons were a very broad signal in the range 6.9 to 7.5 ; ^{19}F NMR (400 MHz, Ethanol-d_6): δ -65.07, -114.70, -121.83, -122.70.

7.3.1.3.2. Assessment that cocrystals with the same composition are formed independent of the stoichiometry and composition of starting solution.

Ethanol solutions obtained by dissolving:

b1) the cation⊂crypt-222 halide (**1**·**2**) and the diiodoperfluoroalkane **3** in 1:1.5 ratio;

b2) the cryptand **1**, the salt **2**, and the diiodoperfluoroalkane **3** in 1:1:1.5 ratio;

b3) the cryptand **1**, the salt **2**, and the diiodoperfluoroalkane **3** in 1:1:2 ratio;

b4) the cryptand **1**, the salt **2**, and the diiodoperfluoroalkane **3** in 1:1:1 ratio;

were slowly evaporated at room temperature. After 1-4 days the formed whitish crystals (25% ca. conversion) were filtered and analyzed via ^{1}H and ^{19}F NMR.

The following sets of starting materials were used:

crypt-222 (**1**), sodium chloride (**2a**), and 1,2-diiodotetrafluoroethane (**3a**);

crypt-222 (**1**), sodium bromide (**2b**), and 1,4-diiodooctafluorobutane (**3b**);

crypt-222 (**1**), sodium iodide (**2c**), and 1,8-diiodohexadecafluorooctane (**3d**);

crypt-222 (**1**), rubidium bromide (**2h**), and 1,6-diiodododecafluorohexane (**3c**);

crypt-222 (**1**), ammonium chloride (**2j**), and 1,8-diiodohexadecafluorooctane (**3d**).

^{1}H and ^{19}F NMR of cocrystals from solution b1) are reported below for the five sets of starting material. The same spectra were obtained for cocrystals afforded by solutions b2), b3), and b4), confirming that cocrystals with the same composition are formed independent of the stoichiometry and composition of starting solution.

Cocrystals formed starting from Na^{+}⊂crypt-222 chloride (1·2a) and 1,2-diiodotetrafluoroethane (3a). ^{1}H NMR (400 MHz, Ethanol-d_6): δ, 3.67 (s, 12H), 3.61-3.64 (t, 12H), 2.67-2.70, (t, 12H); ^{19}F NMR (400 MHz, Ethanol-d_6): δ -57.80.

Cocrystals formed starting from Na^+⊂crypt-222 bromide (1·2b) and 1,4-diiodooctafluorobutane (3b). ^{1}H NMR (400 MHz, Ethanol-d_6): δ, 3.67 (s, 12H), 3.62-3.64 (t, 12H), 2.68-2.70, (t, 12H); ^{19}F NMR (400 MHz, Ethanol-d_6): δ -65.20, -113.65.

Cocrystals formed starting from Na^+⊂crypt-222 iodide (1·2c) and 1,8-diiodohexadecafluorooctane (3d). ^{1}H NMR (400 MHz, Ethanol-d_6): δ, 3.67 (s, 12H), 3.62-3.64 (t, 12H), 2.68-2.70, (t, 12H); ^{19}F NMR (400 MHz, Ethanol-d_6): δ -66.14, -114.69, -121.78, -122.67. **Cocrystals formed starting from Rb^+⊂crypt-222 bromide (1·2h) and 1,6-diiodododecafluorohexane (3c).** ^{1}H NMR (400 MHz, Ethanol-d_6): δ, 3.63 (s, 12H), 3.56-3.59 (t, 12H), 2.58-2.60, (t, 12H); ^{19}F NMR (400 MHz, Ethanol-d_6): δ -65.85, -114.68, -121.83.

Cocrystals formed starting from NH_4^+⊂crypt-222 chloride (1·2j) and 1,8-diiodohexadecafluorooctane (3d). ^{1}H NMR (400 MHz, Ethanol-d_6): δ, 3.65 (s, 12H), 3.58-3.61(t, 12H), 2.59-2.61, (t, 12H); ^{19}F NMR (400 MHz, Ethanol-d_6): δ -66.06, -114.68, -121.78, -122.67.

7.3.1.4. DSC analysis

Experiments aimed at establishing the most convenient conditions to synthesise the target library.

Assessment that the different solution stoichiometries and composition was not changing the formed cocrystal.

Thermal behaviors of all the complexes were established with a Mettler Toledo DSC600 hot stage (10 °C/min) under flowing nitrogen (flow rate 50 ml/min) using 50 µl sealed aluminum sample pans. The sealing was made by using a 30 µl aluminum pan with capillary holes as cover-pan to minimize a free volume inside a pan and to ascertain good thermal contact between sample and pan. Several heating/cooling cycles were performed to assess the reliability of the data; only one heating cycle (heating rate 10 °C/min) is reported here. DSC pictures for pure **1** and supramolecular cocrystals **1·2·3** are given below.

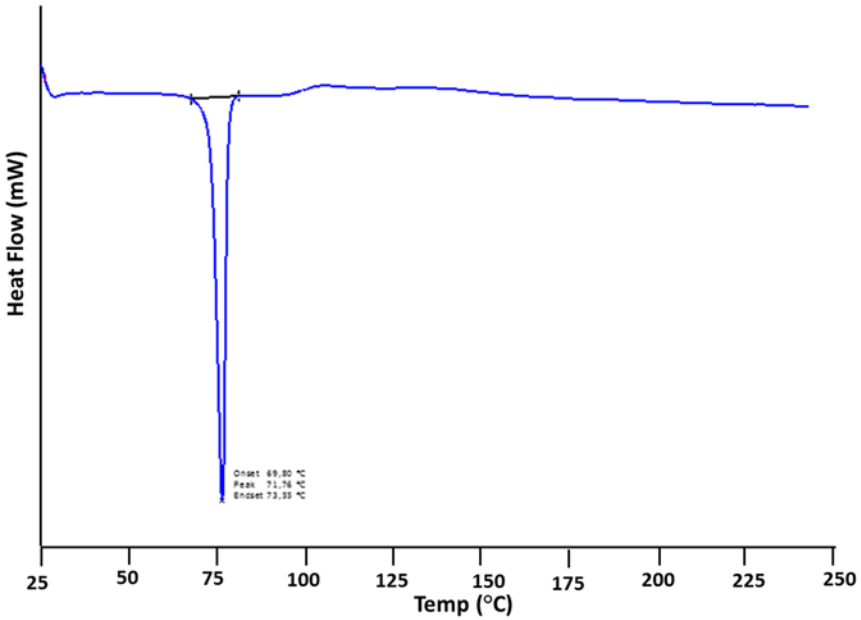

Figure 7.3.1.1. DSC scan of pure crypt-222 **1** on heating (10 °C/min).

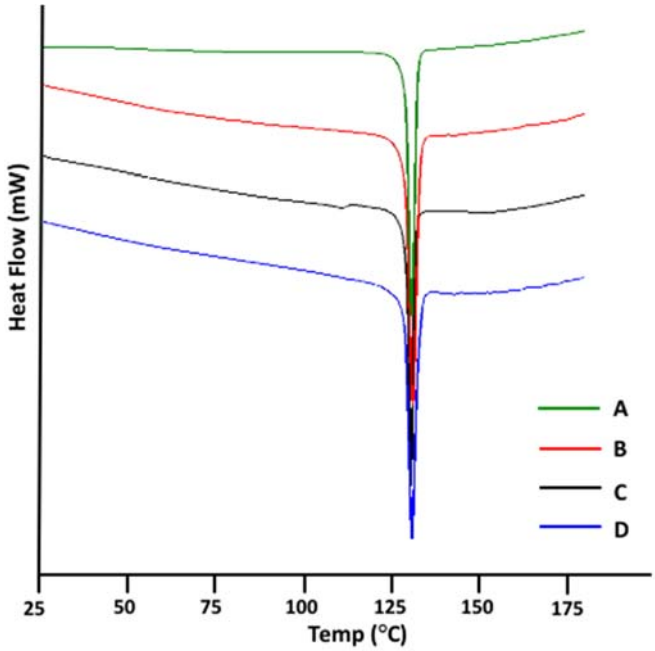

Figure 7.3.1.2. Comparison of DSC thermograms of **1**·**2c**·**3d** obtained from solutions wherein **1**, **2c** and **3d** were present in different stoichiometric ratios: **(A)** 1:1:1.5 ratio; **(B)** 1:1:2 ratio; **(C)** 1:1:1 ratio; **(D)** cocrystals formed from solutions obtained on dissolving the preformed cryptated cation **1**·**2c** and **3d** in 1:1.5 ratio.

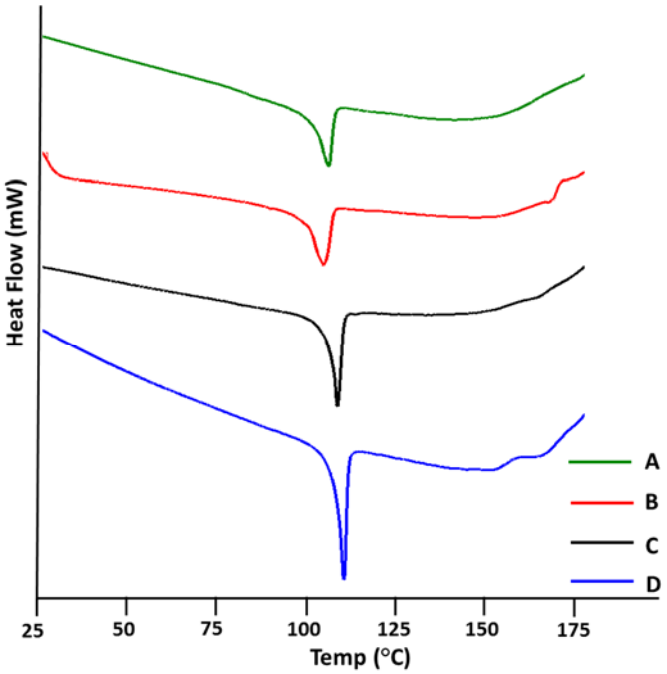

Figure 7.3.1.3. Comparison of DSC thermograms of **1**·**2h**·**3c** obtained from solutions wherein **1**, **2h**, and **3c** were present in different stoichiometric ratios**: (A)** 1:1:1.5; **(B)** 1:1:2; **(C)** 1:1:1; **(D)** cocrystals formed from solutions obtained on dissolving the preformed cryptated cation **1**·**2h** and **3c** in 1:1.5 ratio.

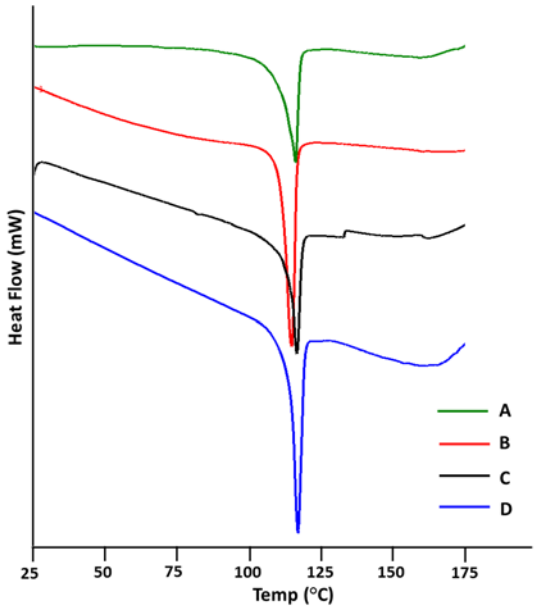

Figure 7.3.1.4. Comparison of DSC thermograms of **1**·**2j**·**3d** obtained from solutions wherein **1**, **2j** and **3d** were present in different stoichiometric ratios**: (A)** 1:1:1.5; **(B)** 1:1:2; **(C)** 1:1:1; **(D)** cocrystals formed from solutions obtained on dissolving the preformed cryptated cation **1**·**2j** and **3d** in 1:1.5 ratio.

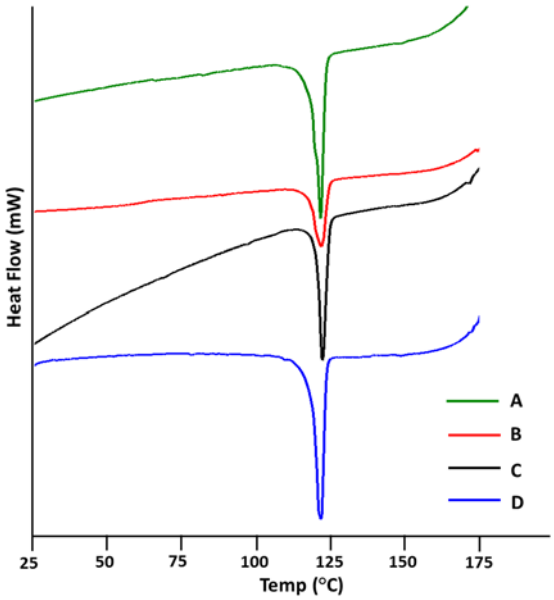

Figure 7.3.1.5. Comparison of DSC thermograms of **1**·**2l**·**3c** obtained from solutions wherein **1**, **2l** and **3c** were present in different stoichiometric ratios**: (A)** 1:1:1.5; **(B)** 1:1:2; **(C)** 1:1:1; **(D)** cocrystals formed from solutions obtained on dissolving the preformed cryptated cation **1**·**2l** and **3c** in 1:1.5 ratio.

7.3.1.5. Powder X-Ray diffraction (PXRD) analyses

Experiments aimed at establishing the most convenient conditions to synthesise the target library.

Assessment that the used solution stoichiometry and composition was not changing the formed cocrystal.

Crystalline powder material of cocrystals were packed on borosilicate glass slides and the data sets were collected on Bruker D8 instrument at 293 K. The measurements were made in Bragg–Brentano geometry using Johansson monochromator to produce pure CuKα_1 radiation (1.5406 Å; 45kV, 30mA) and step–scan technique in 2θ range of 3.5–40°. The data were acquired from a spinning sample by X´Celerator detector in continuous scanning mode with a step size of 0.0167° using sample dependently counting times of 40 to 440 s per step. The experimental PXRD patterns of cocrystals and simulated patterns from the single crystal are shown below. The comparison of simulated and experimental PXRD pattern confirms the structural uniformity of bulk cocrystal powders. Few additional peaks (much weaker than the intensity gain of the main phase) are occasionally present in simulated patterns with respect to experimental patterns; this is probably related to some structural disorder and differences in data collection temperatures.

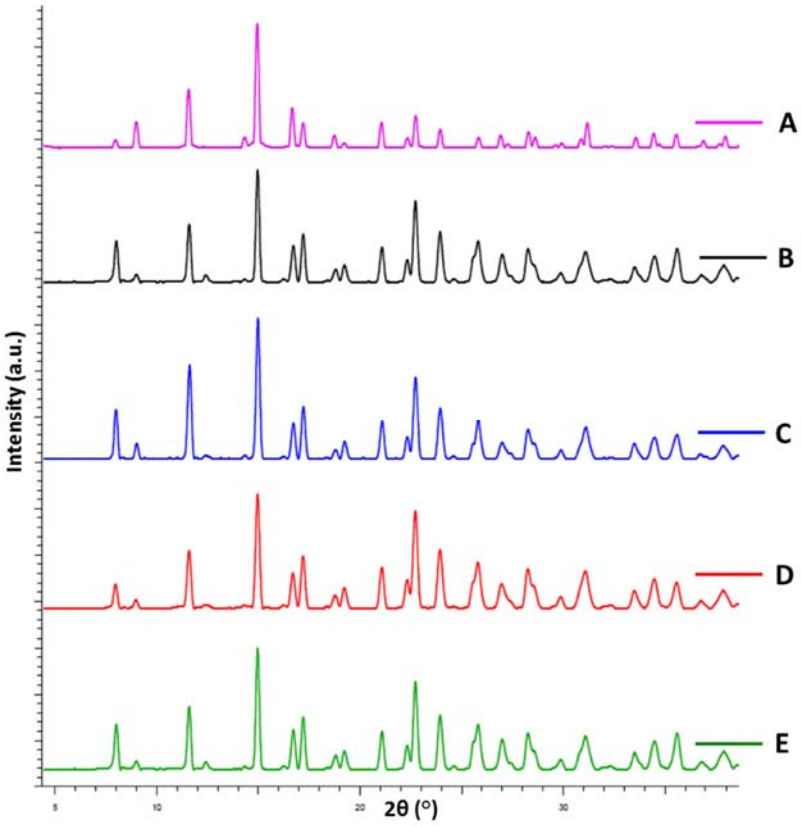

Figure 7.3.1.6. Comparison of simulated and experimental PXRD patterns of **1·2c·3d** obtained using different experimental conditions: **(A)** Simulated powder pattern from single crystal structure (90 K); **(B)** Experimental pattern of cocrystals formed from solutions wherein **1**, **2c** and **3d** were present in 1:1:1.5 ratio; **(C)** Experimental pattern of cocrystals formed from solutions wherein **1**, **2c** and **3d** were present in 1:1:2 ratio; **(D)** Experimental pattern of cocrystals formed from solutions wherein **1**, **2c** and **3d** were present in 1:1:1 ratio; **(E)** Cocrystals formed starting from solutions obtained on dissolving the preformed cryptated cation **1·2c** and **3d** in 1:1.5 ratio.

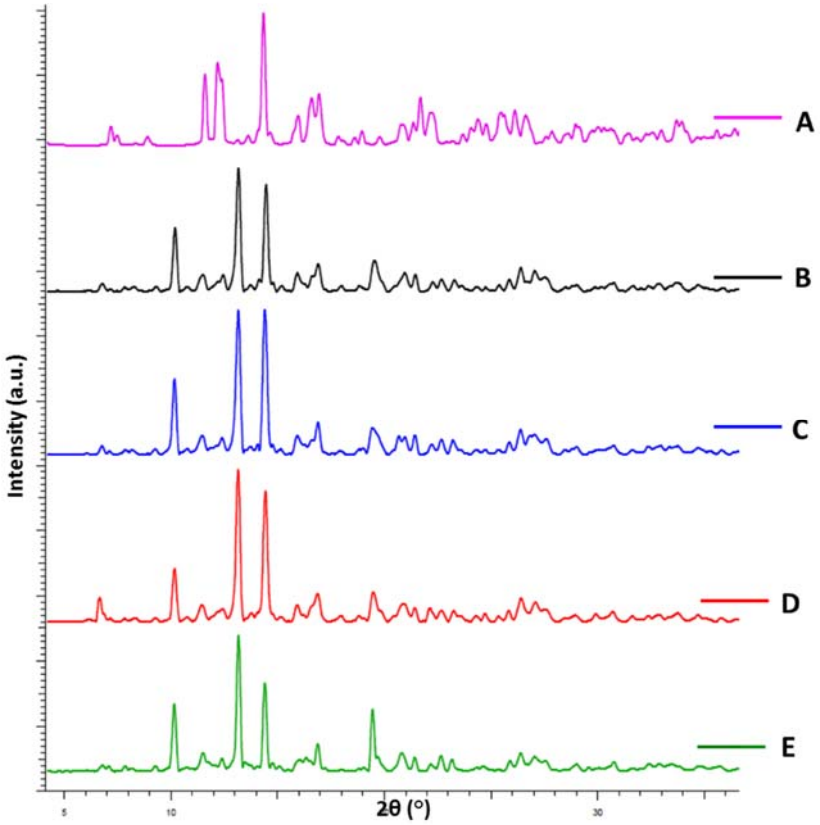

Figure 7.3.1.7. Comparison of simulated and experimental PXRD patterns of **1**·**2h**·**3c** obtained using different experimental conditions: **(A)** Simulated powder pattern from single crystal structure (90 K); **(B)** Experimental pattern of cocrystals formed from solutions wherein **1**, **2h** and **3c** were present in 1:1:1.5 ratio; **(C)** Experimental pattern of cocrystals formed from solutions wherein **1**, **2h** and **3c** were present in 1:1:2 ratio; **(D)** Experimental pattern of cocrystals formed from solutions wherein **1**, **2h** and **3c** were present in 1:1:1 ratio; **(E)** Cocrystals formed starting from solutions obtained on dissolving the preformed cryptated cation **1**·**2h** and **3c** in 1:1.5 ratio

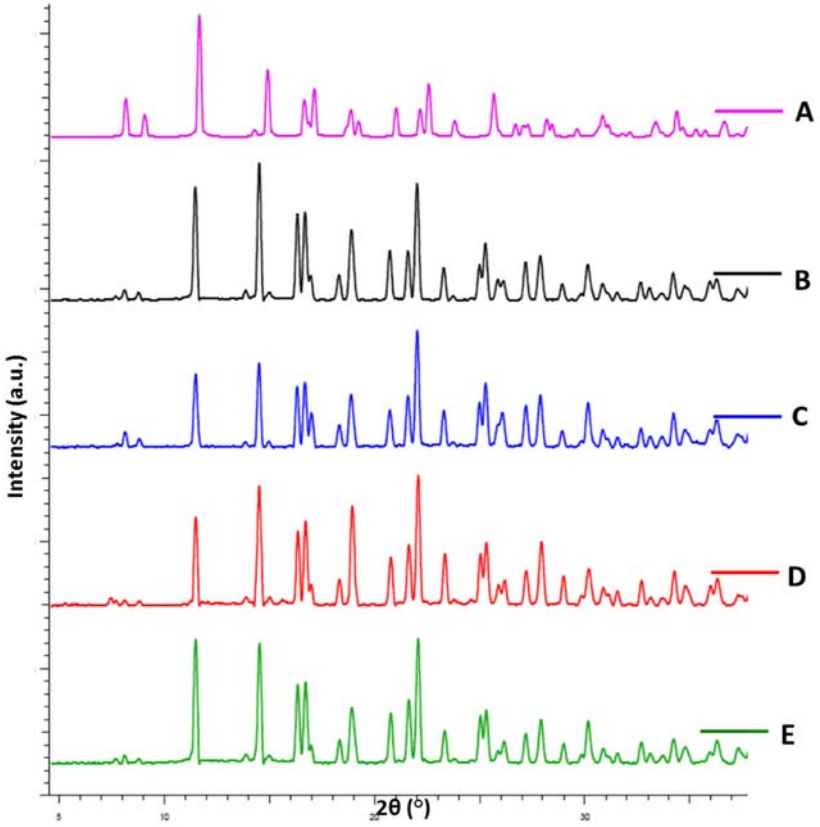

Figure 7.3.1.8. Comparison of simulated and experimental PXRD patterns of **1**·**2j**·**3d** obtained using different experimental conditions: **(A)** Simulated powder pattern from single crystal structure (90 K); **(B)** Experimental pattern of cocrystals formed from solutions wherein **1**, **2j** and **3d** were present in 1:1:1.5 ratio; **(C)** Experimental pattern of cocrystals formed from solutions wherein **1**, **2j** and **3d** were present in 1:1:2 ratio; **(D)** Experimental pattern of cocrystals formed from solutions wherein **1**, **2j** and **3d** were present in 1:1:1 ratio; **(E)** Cocrystals formed starting from solutions obtained on dissolving the preformed cryptated cation **1**·**2j** and **3d** in 1:1.5 ratio.

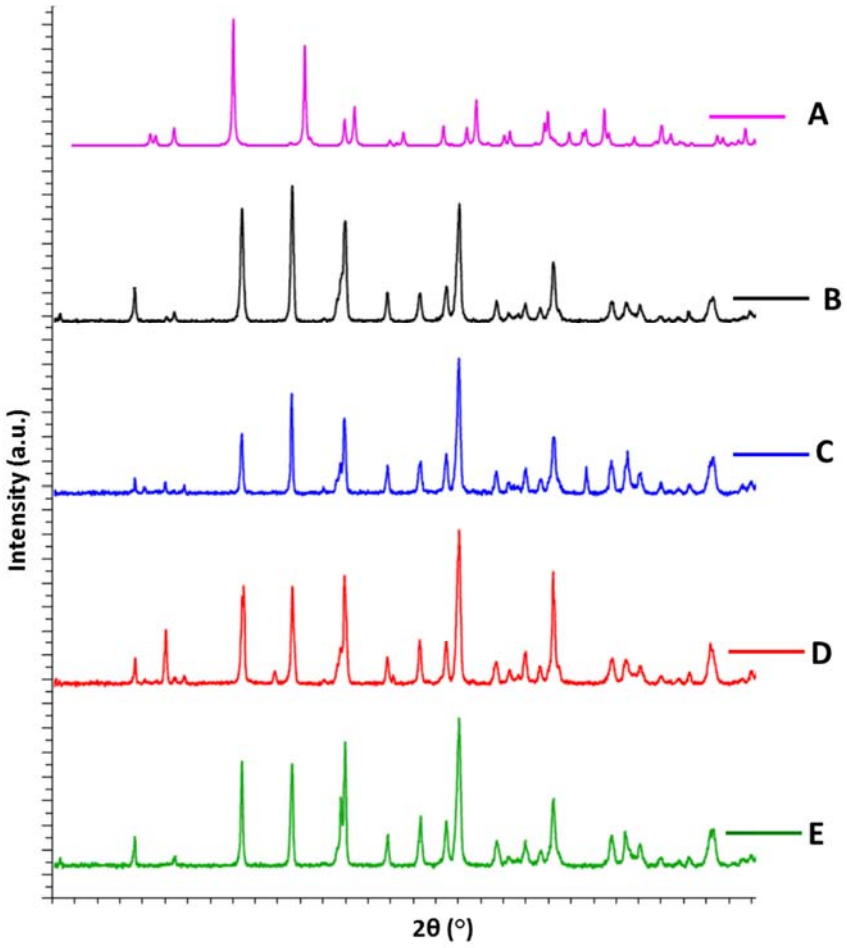

Figure 7.3.1.9. Comparison of simulated and experimental PXRD patterns of **1·2l·3c** obtained using different experimental conditions: **(A)** Simulated powder pattern from single crystal structure (90 K); **(B)** Experimental pattern of cocrystals formed from solutions wherein **1**, **2l** and **3c** were present in 1:1:1.5 ratio; **(C)** Experimental pattern of cocrystals formed from solutions wherein **1**, **2l** and **3c** were present in 1:1:2 ratio; **(D)** Experimental pattern of cocrystals formed from solutions wherein **1**, **2l** and **3c** were present in 1:1:1 ratio; **(E)** Cocrystals formed starting from solutions obtained on dissolving the preformed cryptated cation **1·2l** and **3c** in 1:1.5 ratio.

7.3.1.6. IR analysis

Experiments aimed at establishing that fifty two halogen bonded cocrystals are obtained on crystallization of solutions containing 1, 2a-l, and 3a-e.

IR spectra were obtained using a Nicolet IS50 FT-IR spectrometer. Selected FTIR absorptions are reported. The XB driven cocrystal formation was proven by observed shifts of absorptions in cocrystals with respect to pure starting compounds.

Table 7.3.1.6. Selected FTIR absorptions of starting tectons **1** and **3a-e** supramolecular cations **1·2a-l** and of cocrystals **1·2a-l·3a-e**. Shifts of observed absorptions in cocrystals with respect to pure starting compounds indicate the XB presence.

Compound	Frequency(cm^{-1})
1	2936, 2858, 2782, 1361, 1294
3a	1206, 1147, 1096
3b	1214, 1192, 1128
3c	1201, 1141, 1118
3d	1202, 1144, 1112
3e	1205, 1143, 1114

Compound	Frequency(cm^{-1})
1·2a	2967, 2879, 2820, 1360, 1304, 1263
1·2b	2966, 2874, 2816, 1360, 1304, 1263
1·2c	2956, 2857, 2806, 1355, 1300, 1260
1·2d	2960, 2884, 2814, 1355, 1295, 1259
1·2e	2958, 2884, 2812, 1354, 1295, 1259
1·2f	2963, 2858, 2815, 1357, 1290, 1262
1·2g	2957, 2882, 2812, 1352, 1296, 1258
1·2h	2957, 2881, 2810, 1351, 1295, 1258
1·2i	2956, 2873, 2819, 1349, 1294, 1258
1·2j	2960, 2882, 2811, 1359, 1296, 1258
1·2k	2964, 2878, 2809, 1358, 1301, 1260
1·2l	2968, 2877, 2812, 1359, 1296, 1259

Compound	Frequency(Cm^{-1})
1·2a·3a	2960, 2884, 2803, 1356, 1299, 1130, 1083
1·2a·3b	2973, 2865, 2814, 1353, 1299, 1185, 1115
1·2a·3c	2967, 2874, 2824, 1356, 1299, 1140, 1079
1·2a·3d	2973, 2884, 2824, 1356, 1302, 1130, 1075
1·2b·3a	2967, 2891, 2808, 1355, 1302, 1127, 1086

1·2b·3b	2972, 2889, 2816, 1358, 1301, 1186, 1120
1·2b·3c	2968, 2886, 2816, 1355, 1300, 1136, 1079
1·2b·3d	2971, 2889, 2824, 1355, 1300, 1140, 1105
1·2c·3a	2969, 2889, 2819, 1354, 1298, 1134, 1084
1·2c·3b	2969, 2892, 2820, 1358, 1301, 1187, 1120
1·2c·3c	2965, 2872, 2816, 1358, 1301, 1197, 1133
1·2c·3d	2968, 2892, 2819, 1358, 1301, 1140, 1112
1·2c·3e	2971, 2886, 2824, 1355, 1302, 1140, 1112
1·2d·3a	2960, 2884, 2813, 1355, 1298, 1139, 1097
1·2d·3b	2964, 2886, 2817, 1356, 1283, 1183, 1124
1·2d·3c	2966, 2883, 2813, 1353, 1298, 1136, 1079
1·2d·3d	2968, 2888, 2821, 1356, 1301, 1149, 1102
1·2d·3e	2967, 2887, 2819, 1354, 1301, 1152, 1102
1·2e·3a	2973, 2884, 2803, 1354, 1300, 1130, 1102
1·2e·3b	2974, 2886, 2814, 1355, 1301, 1187, 1121
1·2e·3c	2969, 2888, 2825, 1362, 1302, 1144, 1077
1·2e·3d	2969, 2885, 2822, 1363, 1301, 1150, 1103
1·2e·3e	2968, 2886, 2821, 1353, 1300, 1149, 1102
1·2f·3a	2971, 2864, 2801, 1362, 1300, 1133, 1085
1·2f·3b	2974, 2866, 2819, 1363, 1301, 1186, 1126
1·2f·3c	2966, 2888, 2823, 1363, 1303, 1143, 1077
1·2f·3d	2972, 2886, 2820, 1363, 1302, 1149, 1104
1·2f·3e	2965, 2890, 2812, 1362, 1303, 1140, 1112
1·2g·3a	2963, 2878, 2810, 1353, 1294, 1125, 1091
1·2g·3b	2965, 2880, 2813, 1353, 1298, 1179, 1128
1·2g·3c	2958, 2881, 2818, 1350, 1204, 1132, 1074
1·2g·3d	2959, 2880, 2808, 1351, 1295, 1135, 1108
1·2h·3a	2953, 2880, 2816, 1352, 1296, 1134, 1081
1·2h·3b	2962, 2882, 2812, 1353, 1280, 1177, 1097
1·2h·3c	2965, 2886, 2814, 1358, 1298, 1145, 1081
1·2h·3d	2961, 2885, 2811, 1353, 1296, 1138, 1104
1·2i·3a	2954, 2881, 2815, 1350, 1291, 1101, 1084
1·2i·3b	2964, 2886, 2809, 1354, 1296, 1181, 1110
1·2i·3c	2964, 2885, 2822, 1353, 1297, 1142, 1082
1·2i·3d	2959, 2879, 2807, 1350, 1298, 1148, 1101
1·2j·3a	2996, 2874, 2806, 1357, 1296, 1094
1·2j·3b	2961, 2883, 2817, 1357, 1297, 1183, 1100
1·2j·3c	2960, 2876, 2814, 1351, 1299, 1136, 1073
1·2j·3d	2969, 2885, 2818, 1360, 1304, 1150, 1100
1·2k·3a	2960, 2882, 2819, 1357, 1296, 1082
1·2k·3b	2964, 2885, 2815, 1359, 1300, 1186, 1117
1·2k·3c	2967, 2893, 2822, 1360, 1304, 1130, 1074
1·2k·3d	2966, 2887, 2817, 1362, 1298, 1150, 1073
1·2l·3a	2963, 2883, 2815, 1358, 1299, 1083
1·2l·3b	2962, 2883, 2814, 1359, 1300, 1187, 1127
1·2l·3c	2966, 2890, 2812, 1360, 1304, 1134, 1082
1·2l·3d	2963, 2879, 2809, 1358, 1296, 1147, 1102

7.3.1.7. Single crystal X-ray representations

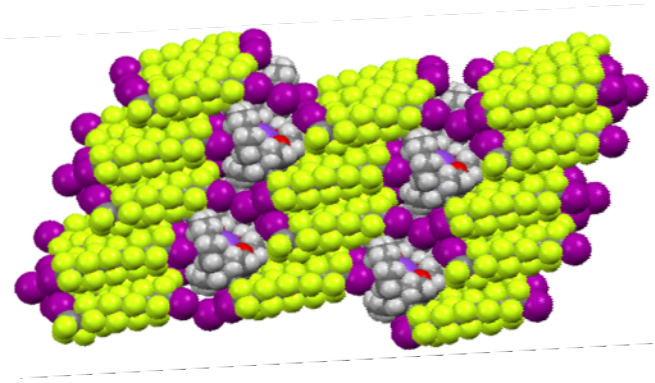

Figure 7.3.1.10. Space filling representation (Mercury 3.8) of the overall crystal packing of **1·2f·3e** along the *b* axis showing the segregation of supramolecular anions. Color code: Grey, carbon; green, fluorine; purple, iodine.

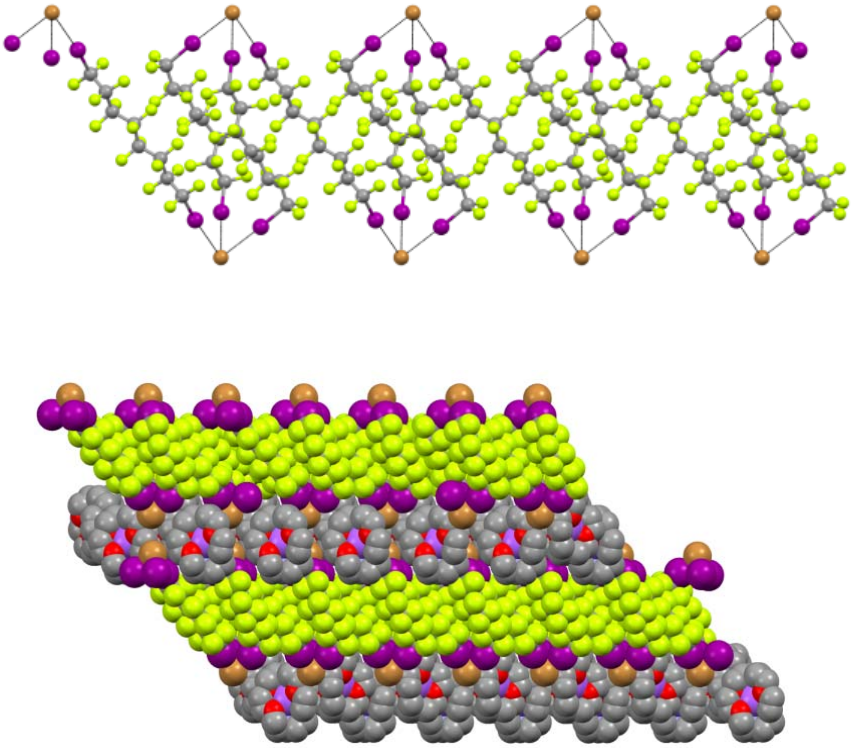

Figure 7.3.1.11. Representations (Mercury 3.8, along *a* axis) of cocrystal **1·2b·3d**. Top: fragment of a single necklace (in ball and stick) assembled via XB (dotted black lines). Bottom: alternating hydrocarbon and fluorous layers (in space filling) formed by supramolecular cations $Na^{+}\subset$crypt-222 and juxtaposed pearl-necklaces, respectively. Color codes: Grey, carbon; red, oxygen; violet, sodium; green, fluorine; purple, iodine; brown, bromine.

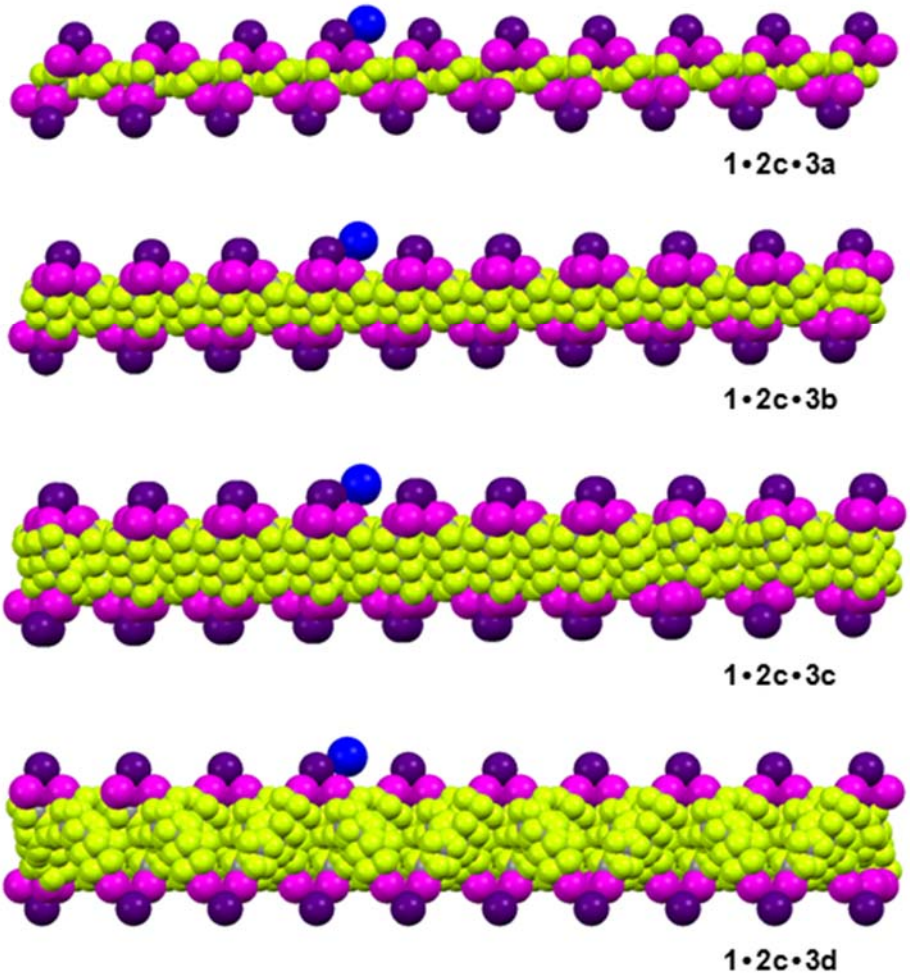

Figure 7.3.1.12. Space filling representation (Mercury 3.8, approximately along *a* axis) of the fluorous layers in cocrystals formed by **1**, sodium iodide (**2c**), and α, ω,-diodoperfluoroethane, -butane, -hexane, and -octane (**3a**, **3b**, **3c**, and **3d**, respectively). Only one Na^+ cation is represented, cryptand **1** has been omitted for sake of simplicity. Color codes: Green, fluorine; light purple, neutral iodine; dark purple, iodide anion; blue, sodium cation.

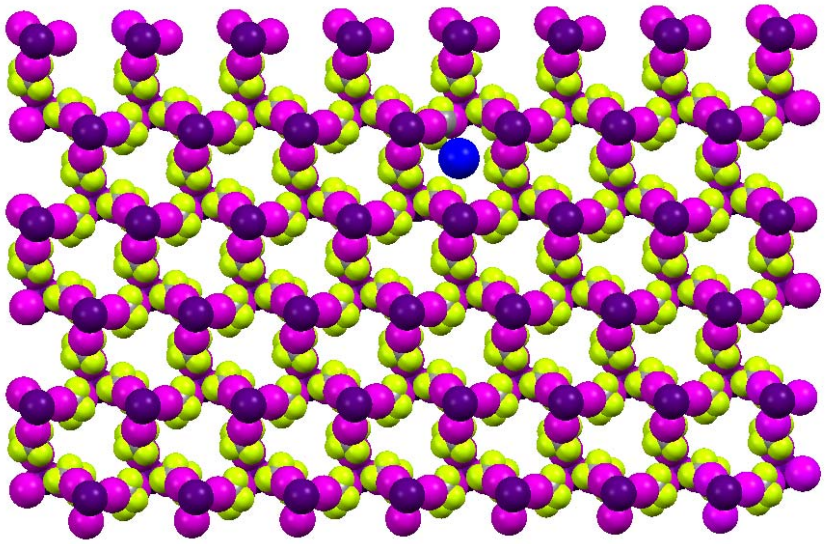

Figure 7.3.1.13. Space filling representation (Mercury 3.8) of one fluorinated layer of cocrystal **1·2c·3a** showing how it shapes up as a (6,3) net; one supramolecular cation (crypt-222 ⊂ Na^+) is depicted as the sodium species only. Colours are as follows: blue, sodium cation; violet, iodide anion; magenta, neutral iodine; green, fluorine; grey, carbon; violet, potassium.

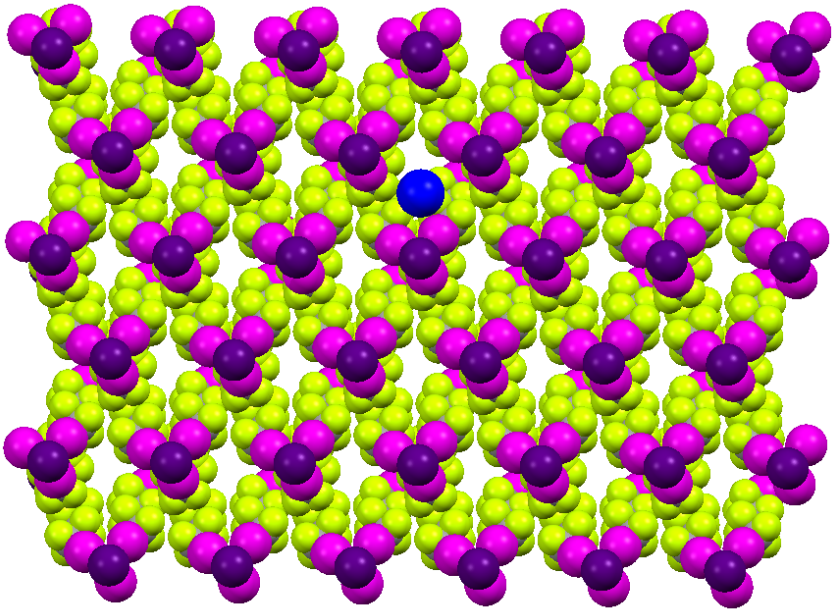

Figure 7.3.1.14. Space filling representation (Mercury 3.8) of one fluorinated layer of cocrystal **1·2c·3b** showing how it shapes up as a (6,3) net; one supramolecular cation (crypt-222 ⊂ Na^+) is depicted as the sodium species only. Colours as in Fig. 7.3.1.12.

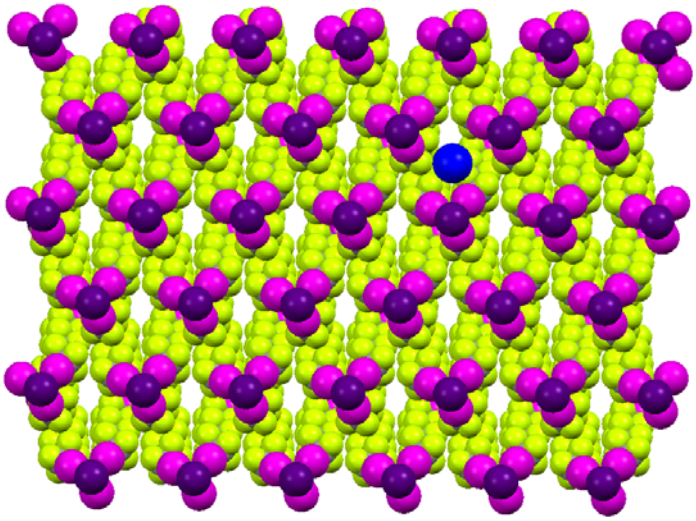

Figure 7.3.1.15. Space filling representation (Mercury 3.8) of one fluorinated layer of cocrystal **1·2c·3c** showing how it shapes up as a (6,3) net; one supramolecular cation (crypt-222 ⊂ Na^+) is depicted as the sodium species only. The pyramidal arrangement of diiodoperfluorohexane moiety around iodide anions results in an increased thickness of the fluorous layer compared to **1·2c·3a** and **1·2c·3b**, (Fig. 7.3.1.11), namely a greater separation between the two triangles defined by the alternating I^- (Fig. 4 of the paper). Colours as in Fig. 7.3.1.12.

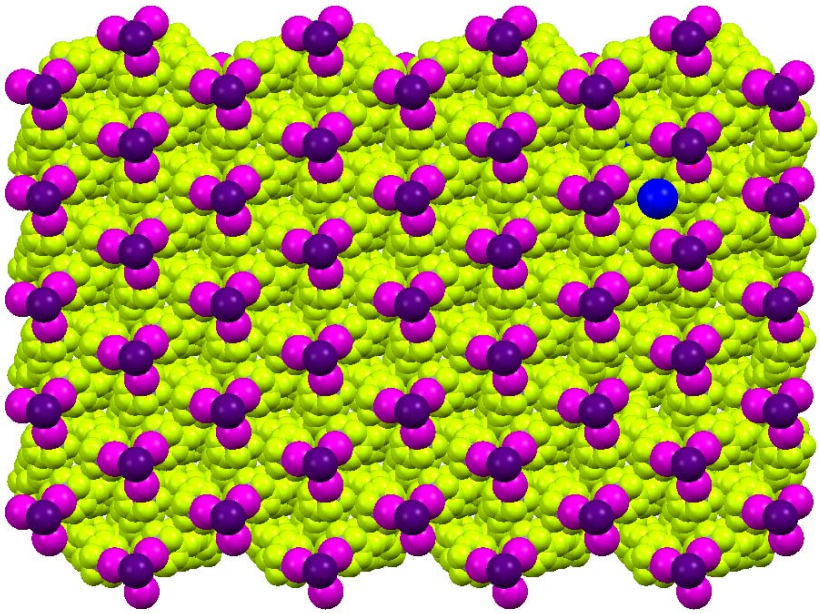

Figure 7.3.1.16. Space filling representation (Mercury 3.8) of one fluorinated layer of cocrystal **1·2c·3d** showing how it shapes up as a (6,3) net; one supramolecular cation (crypt-222 ⊂ Na^+) is depicted as the sodium species only. The pyramidal arrangement of diiodoperfluorooctane moiety around iodide anions results in a thickness of the fluorous layer greater than in **1·2c·3a**, **1·2c·3b**, and **1·2c·3c**, (Fig. 7.3.1.11), namely a greater separation between the two triangles defined by the alternating I^- (Fig. 4.1.4 of the paper). Colours as in Fig. 7.3.1.12

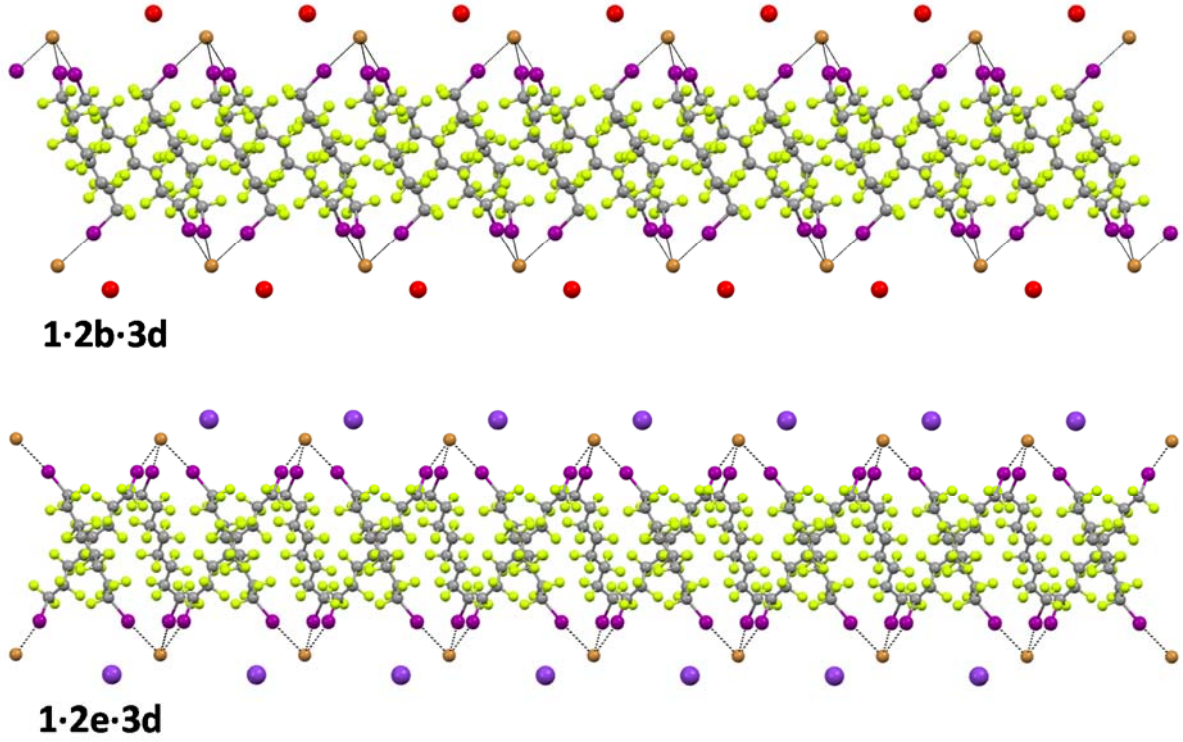

Figure 7.3.1.17. Representation (Mercury 3.8, along the *a* axis) of one fluorous layer and adjacent cations of the crystal packing of pearl necklace **1·2b·3d** (top) and Borromean **1·2e·3d** (bottom) evidencing the structural similarity in the two cocrystals. For sake of simplicity cations are represented as sodium and potassium ions only. Color code: Grey, carbon; green, fluorine; purple, iodine; brown, bromine; red, sodium; violet, potassium.

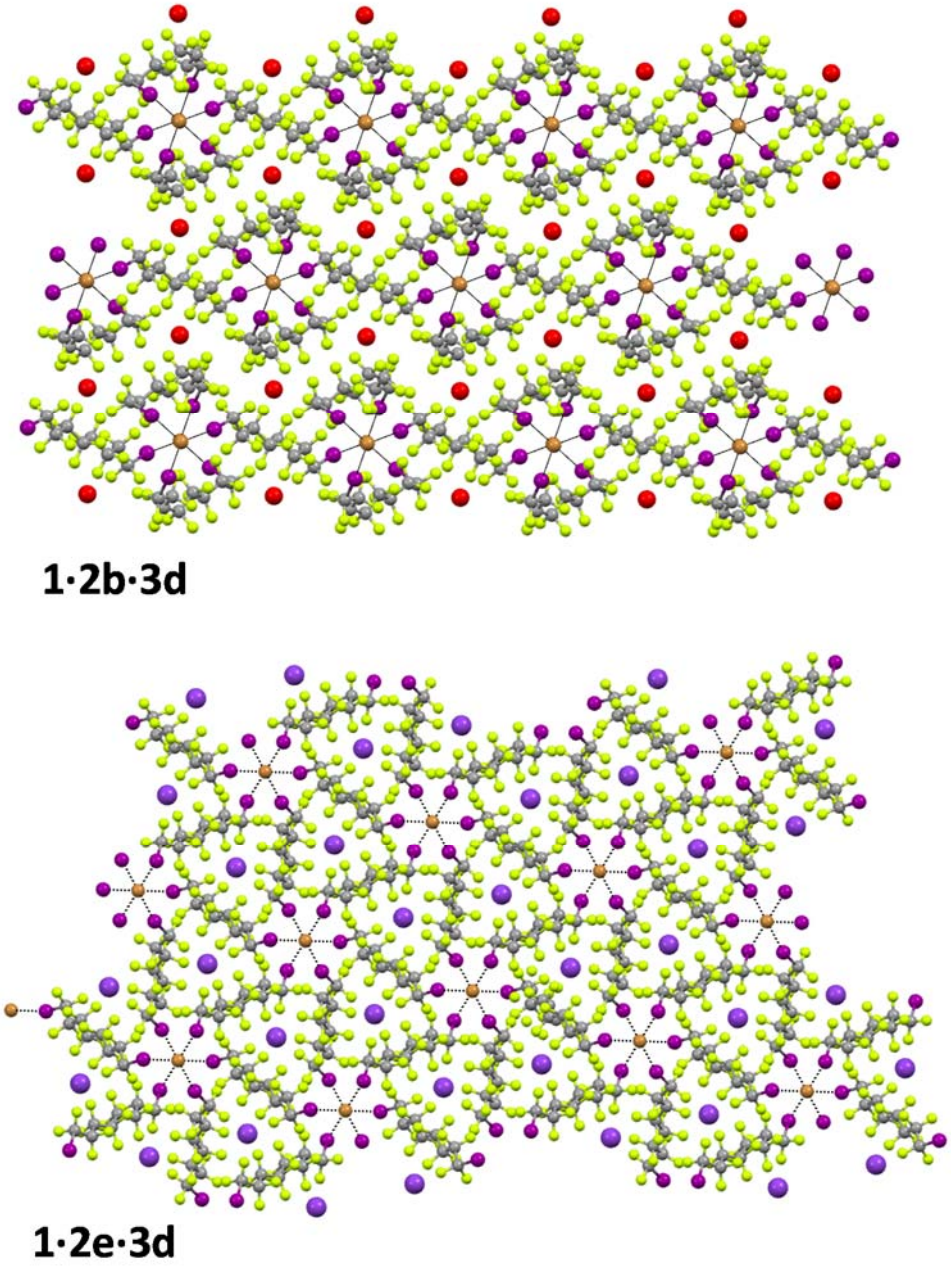

Figure 7.3.1.18. Representation (Mercury 3.8, along the *c* axis) of one fluorous layer and adjacent cations of the crystal packing of the pearl necklace **1·2b·3d** (top) and the Borromean system **1·2e·3d** (bottom) evidencing the structural similarity in the two cocrystals. For sake of simplicity cations are represented as sodium and potassium ions only. Color code: Grey, carbon; green, fluorine; purple, iodine; brown, bromine; red, sodium; violet, potassium.

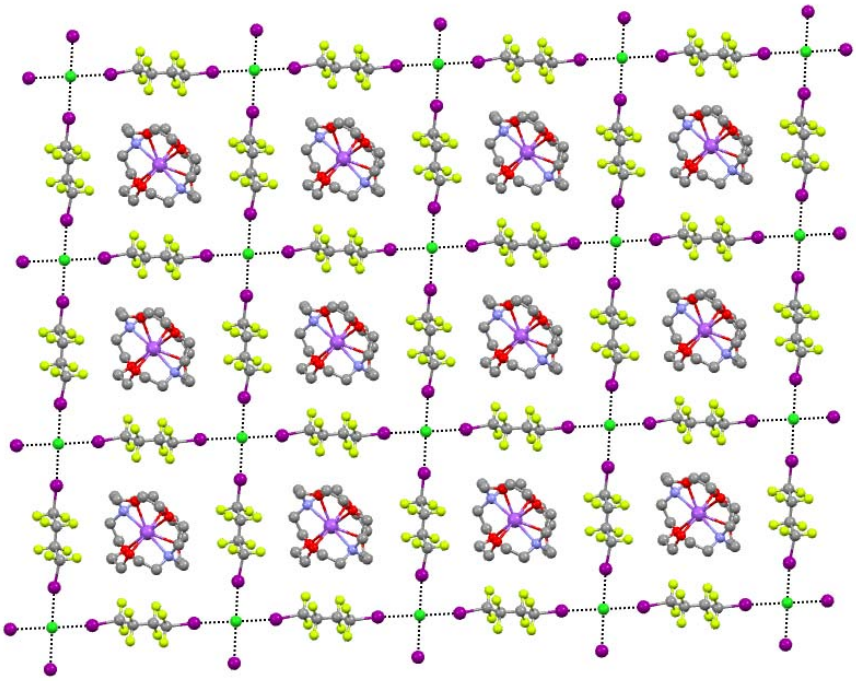

Figure 7.3.1.19. Ball-and-stick representations (Mercury 3.8) of the (4,4) network formed in **1·2a·3b** by chloride anions, working as planar and tetradentate XB acceptors, and 1,4-diiodoperfluorobutane **3b**, working as node spacers. Cryptated sodium cations sit in the squares. XB are black dotted lines. Color code: Grey, carbon; light green, fluorine; green, chlorine; purple, iodine; red, oxygen; blue, nitrogen; violet, sodium.

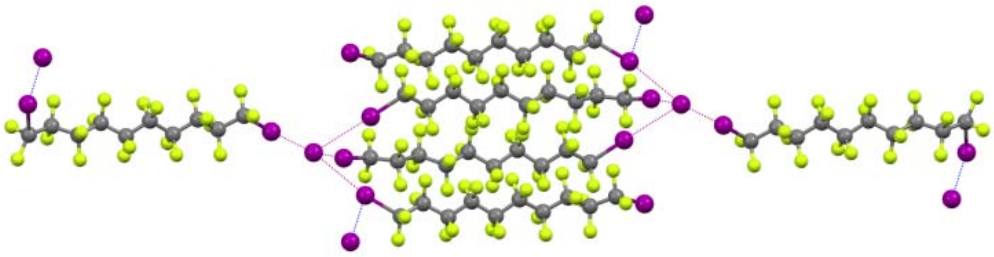

Figure 7.3.1.20. Ball-and-stick representations (Mercury 3.8) of the well-defined supramolecular anion formed in **1·2f·3e** *via* interaction of two iodide anions with two diiododecyl chains, which are bound to two iodide anions and bridge them, and with four other diiododecyl chains, which are bound to one iodide anion. These supramolecular anions are assembled *via* fairly short XBs (red dotted lines, 343.6 – 360.7 pm, which correspond to normalized contacts (*Nc*) spanning 0.83 – 0.87). Color code: Grey, carbon; green, fluorine; purple, iodine.

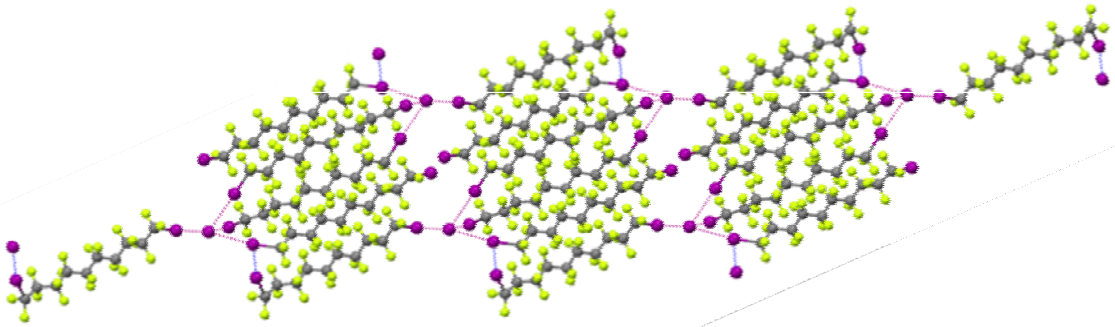

Figure 7.3.1.21. Ball-and-stick representations (Mercury 3.8) of a part of the infinite array formed, approximately along the *c* axis, by long XBs (blue dotted lines, 373.7 pm, *Nc* = 0.90) connecting the supramolecular anions described in Fig. 7.3.1.19. In these longer XBs the XB donors and acceptors sites are the positive cap and the negative belt of two iodine atoms of two diiododecyl chains of the supramolecular anion described in Fig. 7.3.1.19. Color code: Grey, carbon; green, fluorine; purple, iodine.

7.3.2. Assessing hydrogen bond in H^+⊂crypt-111 iodide via halogen bonded adducts formation

7.3.2.1. Materials and methods

Commercial AR grade Ethanol was used without any further purification for supramolecular synthesis and crystallization. Starting materials were purchased from Sigma–Aldrich, TCI (Europe and Japan) and Apollo Scientific. Melting points were determined with a Reichert instrument by observing the melting and crystallizing process through a polarizable optical microscope.

7.3.2.2. IR spectroscopy

IR spectra were obtained using a Nicolet IS50 FT-IR spectrometer equipped with UATR unit. All the spectra were corrected with the baseline correction tool of the OMNIC software. Selected FTIR absorptions are reported. The XB driven cocrystal formation was proven by observed shifts of absorptions in cocrystals with respect to pure starting compounds.

Table 7.3.2.1 Selected FTIR absorptions of H^+⊂Crypt-111 iodide **1,** α, ω-diiodoperfluorocarbons **2a-d** and of cocrystals **1·2a-d**. Shifts of observed absorptions in cocrystals with respect to pure starting compounds indicate the XB presence.

Compound	Frequency(cm^{-1})
1	2948, 2912, 2870, 2835, 1471
2a	1206, 1147, 1096
1·2a	2956, 2942, 2872, 1112, 1082
2b	1214, 1192, 1128
1·2b	2955, 2928,2883, 1178, 1116
2c	1201, 1141, 1118
1·2c	2955, 2918, 2877, 1142, 1082
2d	1202, 1144, 1112
1·2d	2952, 2926, 2882, 1140, 1106

7.3.2.3. Single crystal X-ray structure determination and data parameters

Single crystal X-ray data collection procedure and structural refinement details are described in section 7.1.4. Crystallographic data and structure refinement parameters for H^+⊂Crypt-111 iodide **1** and of cocrystals **1·2a-b** are reported below in Tables 7.3.2.2 and 7.3.2.3.

Table 7.3.2.2 Crystallographic data and structure refinement parameters for H^+⊂Crypt-111 iodide **1** and of cocrystals **1·2a,b**

Name	**1**	**1·2a**	**1·2b**
Chemical formula	C_{24} H_{50} N_4 O_6 I_2	C_{60} H_{100} N_8 O_{12} F_{24} I_{16}	C_{36} H_{50} N_4 O_6 F_{24} I_8
Formula weight	322.2	1806.0	2106.0
Crystal system, space group	Trigonal, P 6_3/m	Triclinic, P -1	Triclinic, P -1
Temperature (K)	100 K	100 K	100 K
a (Å)	7.4390(19)	11.1088(4)	10.8224(14)
b (Å)	7.4390(20)	11.5075(4)	11.0490(15)
c (Å)	16.1520(50)	20.5203(7)	13.5000(20)
α(°)	90	96.395(2)	81.664(12)
β (°)	90	91.947(2)	84.625(12)
γ(°)	120	93.145(2)	84.625(12)
V (Å^3)	774.08(4)	2600.83(7)	1499.37(62)
Z	2	2	1
μ (mm^{-1})	2.072	2.31	4.225
Crystal size (mm^3)	0.19, 0.16, 0.03	0.26, 0.08,0.05	0.21, 0.18, 0.04,
F(000)	376.0	1676.0	982
Data collection			
Diffractometer	Bruker APEX-II CCD area detector diffractometer		
Absorption correction	Based on multi-scan		
No. of measured, independent and observed reflections	16655, 100,3 737	56907, 18561, 12347	23169, 6838, 5150
θ_{min} (°)	2.52	1.78	1.62
θ_{max} (°)	33.41	33.14	27.67
$R_{\_all}$, $R_{\_obs}$	0.0446, 0.029	0.087, 0.048	0.055, 0.033
$wR2_{\_all}$, $wR2_{\_obs}$	0.052, 0.049	0.115, 0.101	0.060, 0.055
GOOF	1.161	1.012	0.975
No. of parameters	29	565	356
$\Delta\rho_{max}$, $\Delta\rho_{min}$ (e Å^{-3})	0.919, -1.359	4.826, -1.099	0.785, -0.851

Table 7.3.2.3 Crystallographic data and structure refinement parameters for cocrystals **1·2c,d**

Name	**1·2c**	**1·2d**
Chemical formula	C_{42} H_{50} N_4 O_6 F_{36} I_8	C_{48} H_{50} N_4 O_6 F_{48} I_8
Formula weight	2406.1	1270.0
Crystal system, space group	Trigonal, P 6_3/m	Triclinic, P -1
Temperature (K)	100 K	100 K
a (Å)	10.9112(42)	10.9507(7)
b (Å)	11.0336(12)	11.0332(6)
c (Å)	14.8836(14)	16.8392(12)
α(°)	85.546(12)	89.803(3)
β (°)	77.922(10)	82.830(4)
γ(°)	84.569(10)	84.757(3)
V (Å^3)	1741.22(42)	2010.11(12)
Z	1	1
μ (mm^{-1})	2.29	3.242
Crystal size (mm^3)	0.40, 0.37, 0.04	0.22, 0.06,0.04
F(000)	1126.0	1270.0
Data collection		
Diffractometer	Bruker APEX-II CCD area detector diffractometer	
Absorption correction	Based on multi-scan	
No. of measured, independent and observed reflections	53265, 16161, 13041	69425, 11852, 9226
θ_{min} (°)	1.86	1.85
θ_{max} (°)	36.27	30.55
R_{all}, R_{obs}	0.043, 0.030	0.051, 0.031
$wR2\_{all}$, $wR2\_{obs}$	0.075, 0.068	0.068, 0.063
GOOF	1.022	1.019
No. of parameters	437	518
$\Delta\rho_{max}$, $\Delta\rho_{min}$ (e Å^{-3})	1.586, -1.870	1.518, -0.677

7.3.2.4. Solid state NMR (SSNMR) spectroscopy

SSNMR measurements were carried out on a Bruker AVANCE II 400 instrument operating at 100.65 and 40.56 MHz for ^{13}C and ^{15}N, respectively. Powdered samples were packed in cylindrical 4 mm o.d. zirconia rotors, with sample volume of 80 μL. ^{15}N CPMAS (cross-polarization magic-angle spinning) spectra were recorded at room temperature at the spinning speed of 9 kHz. A ramp cross-polarization pulse sequence was used with contact time of 4 ms. All spectra were acquired with a resolution of 0.5 ppm, ^{15}N SSNMR spectra of cocrystal **1·2c** and **1·2d** are given below.

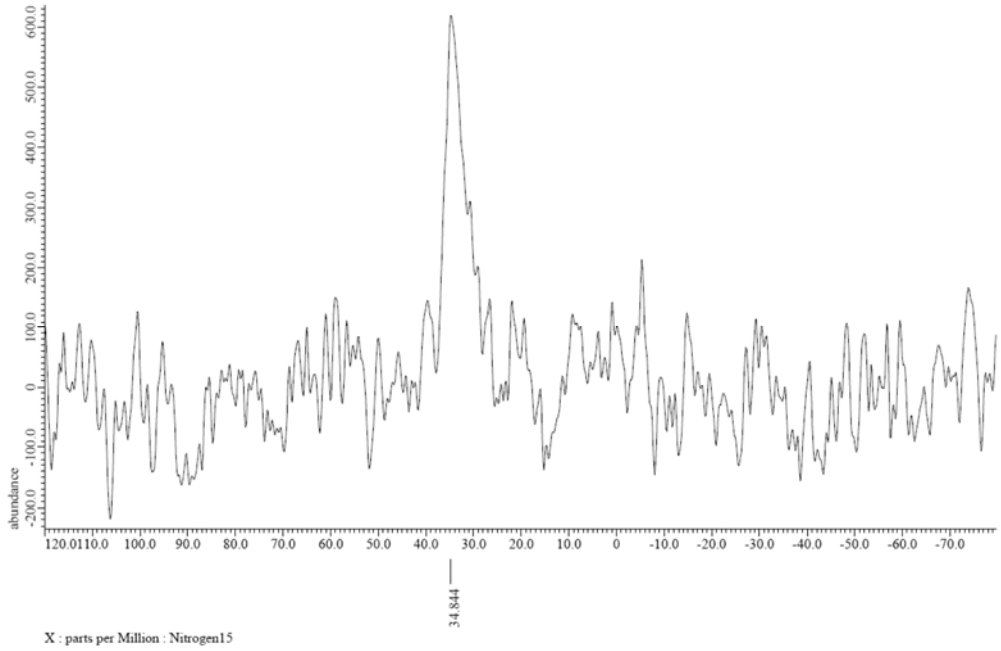

Figure 7.3.2.1 ^{15}N spectrum (r.t.) of cocrystal **1·2c.**

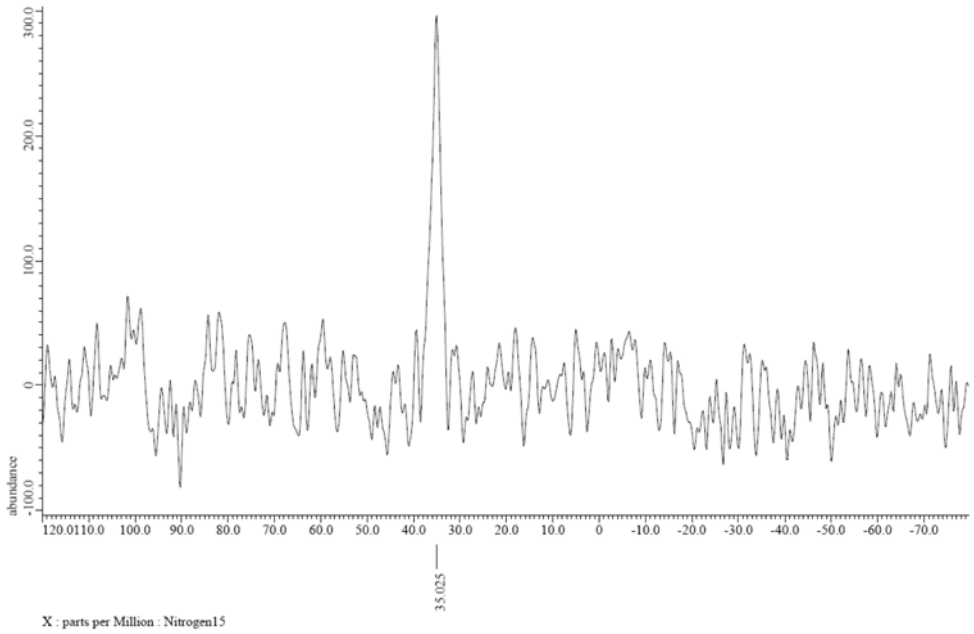

Figure 7.3.2.2 ^{15}N spectrum (r.t.) of cocrystal **1**·**2d**.

7.3.2.5. Quantum chemical calculations

All calculations were performed with Gaussian 09;[4] solvent effects were evaluated by the conductor-like polarizable continuum model (CPCM)[5] using water as solvent. Gibbs Free Energies were determined by thermal corrections for entropy and enthalpy at 298 K to the electronic energies. The natures of all stationary points were confirmed by normal-mode analysis. Three different density functional theory (DFT) methods were used: M06,[6] B97-D3[7] and B3LYP,[8] adopting the Dunning's correlation consistent basis set aug-cc-pVDZ.[9] The last two functionals employed the D3 version of Grimme's dispersion method with the Becke-Johnson damping scheme.[6] For B3LYP, the modified damping parameters, namely B3LYP-D3BJ(M), were used.[10] Wavefunction analysis have been performed with the help of Multiwfn.[11]

Figure 7.3.2.3 visualizes the weak interaction in $H^+\subset$crypt-111 and in its TS. The surfaces is the reduced density gradient *s*, on which it is mapped the values of sign $(\lambda_2)\cdot\rho$ (limited to ±0.180 to reduce the extension of the surface due to covalent bonds). Colors range from red (negative values of sign $(\lambda_2)\cdot\rho$, i.e. strong bonded interactions) to blue (positive values of sign $(\lambda_2)\cdot\rho$, i.e. non bonded interactions). In $H^+\subset$crypt-111 the strongest HB is between H and the three O atoms (yellow), but an extended green surface highlight the H-N interaction (several other Van der Waals interactions are also present). In the TS two red surfaces show the

very strong N-H-N HB, and three (equivalent) green surfaces assigned to O-H HBs. Also in this case other steric interactions appear.

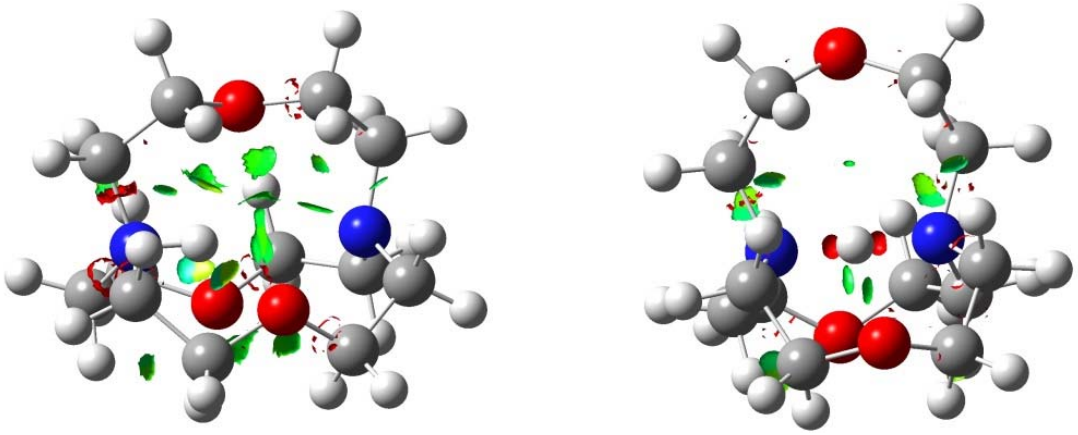

Figure 7.3.2.3 Plot of the sign $(\lambda_2)\cdot\rho$ (values outside ±0.180 have been omitted for clarity) mapped on the surface of the reduced density gradient *s*, (isovalue=0.3). Colors corresponds to negative (red) and positive (blue) values of sign $(\lambda_2)\cdot\rho$.

7.4. Structural Characterization of New Fluorinated Mesogens Obtained Through Halogen-Bond Driven Self-Assembly

7.4.1. Materials and methods

Commercial HPLC-grade solvents were used without further purification. Starting materials were purchased from Sigma-Aldrich, Acros Organics, and Apollo Scientific. IR spectra were obtained using a Nicolet Nexus FT-IR spectrometer equipped with UATR unit (4000–400 cm^{-1} range). Differential scanning calorimetry (DSC) analysis were performed on a Mettler Toledo DSC823e instrument using aluminum light 20 μL sample pans and the Mettler: STARe software for calculation of thermal behavior. The LC textures were studied with an Olympus BX51 polarized optical microscope equipped with a Linkam Scientific LTS 350 heating stage and a Sony CCD-IRIS/RGB video camera.

7.4.2. Synthesis of 6-(pyridin-4-yloxy)hexyl methacrylate (1)

The synthesis of the stilbazole methacrylate has been carried out according the literature. [12]
mp 78-80° C; ^{1}H NMR (400 MHz, $CDCl_3$) δ: 1.50 (m, 4H, CH_2), 1.72 (q, 2H, J=14.0 Hz, CH_2), 1.82 (q, 2H, J=13.8 Hz, CH_2), 1.95 (s, 3H, CH_3), 3.99 (t, 2H, J=6.5 Hz, $ArOCH_2$), 4.15 (t, 2H, J=6.5 Hz, OCH_2), 5.55 (m, 1H, C=H), 6.10 (m, 1H, C=H) 6.87 (d, 1H, J=15.4 Hz, CH) 6.90 (d, 2H, J=8.7 Hz, phenyl-H), 7.25 (d, 1H, J=16.3 Hz, CH), 7,33 (d, 2H, J=6.1 Hz, pyridyl-H), 7.47 (d, 2H, J=8.7 Hz, phenyl-H), 8.55 (d. 2H, J=6.1 Hz, pyridyl-H). ^{13}C NMR (400 MHz, $CDCl_3$) δ: 167.6, 159.7, 150.3, 150.1, 145.0, 136.6, 132.9, 128.8, 128.5, 128.3, 125.4, 125.2, 120.8, 120.5, 114.9, 114.8, 67.9, 64.7, 29.2, 28.6, 25.9, 25.8; FTIR (cm^{-1}): 3071, 3036, 2943, 2899, 2886, 1701, 1594, 1514, 1169, 1023, 873, 545; MS m/z. 366.13 (M^+H^+) (calculated for $C_{23}H_{27}NO_3$, 365.20)

7.4.3. Crystallization of cocrystals 3a-e.

Two equivalents of stilbazole methacrylate and one equivalent of 1,4-diiodoperfluorocarbons were dissolved in THF at room temperature in a clear borosilicate glass vial. The open vial was placed in a closed cylindrical wide-mouth bottle containing paraffin. The THF was allowed to diffuse at room temperature.

Cocrystal 3a. Yellowish needle shaped crystals; mp 95° C; FTIR (cm^{-1}): **1, 2-diiodotetrafluoroethane (2a):** 1206, 1146, 1096, 972, 833, 685, 574; **Complex 3a:** 3073, 3040, 2935, 2907, 1590, 1511, 1196, 1123, 1087, 1014, 962, 826, 700, 545

Co-crystal 3b. Yellowish needle shaped crystals; mp 106° C; FTIR (cm^{-1}): **1, 4-diiodooctafluorobutane (2b):** 1189, 1130, 1085, 1039, 977, 887, 834, 634, 555; **Complex 3b:** 3072, 3040, 3053, 2899, 2884, 1173, 1122, 1064, 1020, 954, 831, 760, 548

Cocrystal 3c. Yellowish needle shaped crystals; mp 98° C; IR (cm^{-1}): **1, 6-diiodododecafluorohexane (2c):** 1210, 1141, 1084, 925, 833, 789, 730, 634, 552; **Complex 3c:** 2955, 2878, 1174, 1113, 1061, 1016, 925, 833, 732, 549

Cocrystal 3d. Yellowish needle shaped crystals; mp 103° C; IR (cm^{-1}): **1, 8-diiodohexadecafluorooctane (2d):** 1207, 1146, 1055, 959, 838, 631, 561; **Complex 3d:** 3074, 3037, 2945, 2822, 1175, 1102, 1060, 1015, 955, 832, 545

Cocrystal 3e. Yellowish block shaped crystals; mp 113° C; IR (cm^{-1}): **1, 4-diiodotetrafluorobenzene (2e):** 1459, 1362, 1210, 969, 940, 757, 561; **Complex 3e:** 3096, 3044, 2906, 2894, 1707, 1511, 1456, 1196, 1123, 1087, 1014, 936, 540

7.4.4. Analysis by X-ray diffraction

SXRD data collection and structural refinement details were described in section 7.1.6. Diiodoperfluorooctane in complex **1d** was disordered in two opposite helical, nearly *all-trans* conformations, with great separation of fluorine atoms, so that the whole molecules could be split and refined with few restraints on the perfluorocarbon geometry.

Table 7.4.1. Crystallographic data and structure refinement parameters

Name	**3a**	**3b**	**3c**
Chemical formula	$C_{48}H_{54}N_2O_6F_4I_2$	$C_{50}H_{54}N_2O_6F_8I_2$	$C_{104}H_{108}N_4O_{12}F_{24}I_4$
Molecular weight	1084.8	1184.8	1284.8
Crystal system, space group	Triclinic, P -1	Triclinic, P -1	Triclinic, P -1
Temperature (K)	100K	100K	100K
a (Å)	7.6114(10)	6.1920(70)	7.5685(12)
b (Å)	10.9778(14)	7.6700(80)	17.9912(27)
c (Å)	14.6280(20)	27.7130(30)	20.4040(32)
α(°)	82.325(10)	91.690(38)	72.200(5)
β (°)	84.995(10)	91.550(30)	82.236(6)
γ(°)	74.288(8)	104.600(40)	89.356(6)
V (Å^3)	1164.38(31)	1272.30(14)	2619.76(51)
Z	1	1	2
μ (mm^{-1})	1.416	1.314	1.294
Crystal size (mm^3)	0.01, 0.07, 0.08	0.02, 0.08,0.14	0.06, 0.10, 0.27,
F(000)	546.0	594.0	1284.0
Data collection			
Diffractometer	Bruker APEX-II CCD area detector diffractometer		
Absorption correction	Based on multi-scan		
No. of measured, independent and observed reflections	35419, 5122, 3693	5343, 4541, 1794	74889, 11912, 8973
θ_{min} (°)	1.94	2.21	1.82
θ_{max} (°)	27.52	29.09	27.50
$R_{\_all}$, $R_{\_obs}$	0.085, 0.044	0.193, 0.064	0.099, 0.070
$wR2_{\_all}$, $wR2_{\_obs}$	0.078,0.069	0.177, 0.130	0.160, 0.148
GOOF	1.036	0.893	1.216
No. of parameters	280	316	669
$\Delta\rho_{max}$, $\Delta\rho_{min}$ (e Å^{-3})	0.712, -1.051	0.177, -0.130	2.252, -1.806

Table 7.4.1. Crystallographic data and structure refinement parameters (continuation)

Name	**3d**	**3e**
Chemical formula	$C_{108}\ H_{108}\ N_4\ O_{12}\ F_{32}\ I_4$	$C_{104}\ H_{108}\ N_4\ O_{12}\ F_8\ I_4$
Molecular weight	1384.8	1140.0
Crystal system, space group	Triclinic, P -1	Monoclinic, P21/n
Temperature (K)	100K	100K
a (Å)	7.5868(24)	17.350(30)
b (Å)	18.0066(59)	7.3842(14)
c (Å)	20.8838(71)	20.2780(40)
α(°)	76.406(18)	90
β (°)	88.022(19)	106.010(20)
γ(°)	89.463(17)	90
V (Å^3)	2771.41(13)	2497.17(15)
Z	2	2
μ (mm^{-1})	1.239	1.324
Crystal size (mm^3)	0.01, 0.07, 0.18	0.02, 0.09, 0.12
F(000)	1380.0	1140.0
Data collection		
Diffractometer	Bruker APEX-II CCD area detector diffractometer	
Absorption correction	Based on multi-scan	
No. of measured, independent and observed reflections	40034, 10408, 6356	22546, 3834, 2694
θ_{min} (°)	1.71	1.81
θ_{max} (°)	25.68	23.82
$R_{\_all}$, $R_{\_obs}$	0.109, 0.049	0.068, 0.036
$wR2_{\_all}$, $wR2_{\_obs}$	0.101, 0.084	0.070, 0.064
GOOF	0.984	0.961
No. of parameters	892	299
$\Delta\rho_{max}$, $\Delta\rho_{min}$ (e Å^{-3})	0.716, -0.828	0.462, -0.332

7.4.5. Single crystal X-ray representations

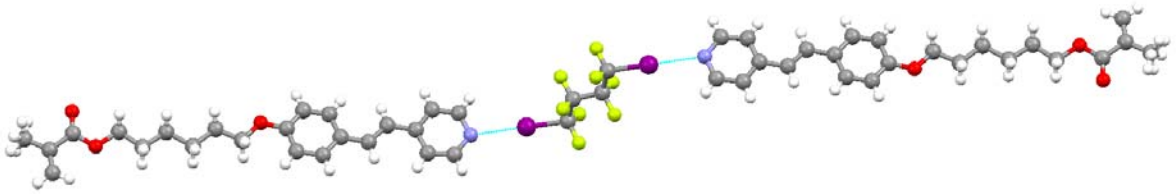

(B)

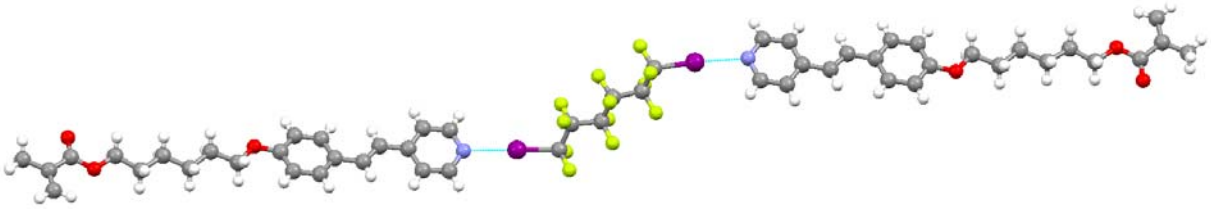

(C)

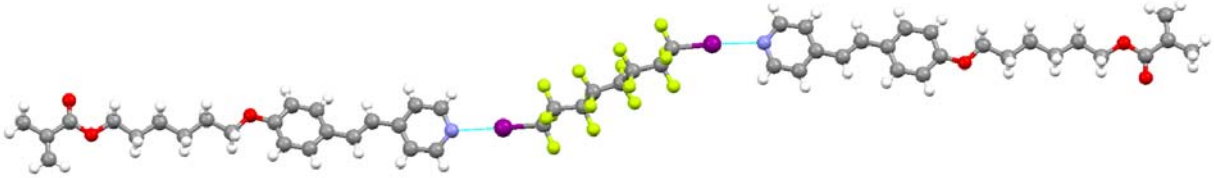

(D)

Figure 7.4.1: Ball-and-stick representation of the single crystal X-ray structure of complex **3b** (top), **3c** (middle)**,** and **3d** (bottom), showing the stepped organization between the XB donor and acceptor in the supramolecular trimer. Color codes: grey, carbon; blue, nitrogen; magenta, iodine; red, oxygen; yellow, fluorine and white, hydrogen. XB are light blue dotted lines.

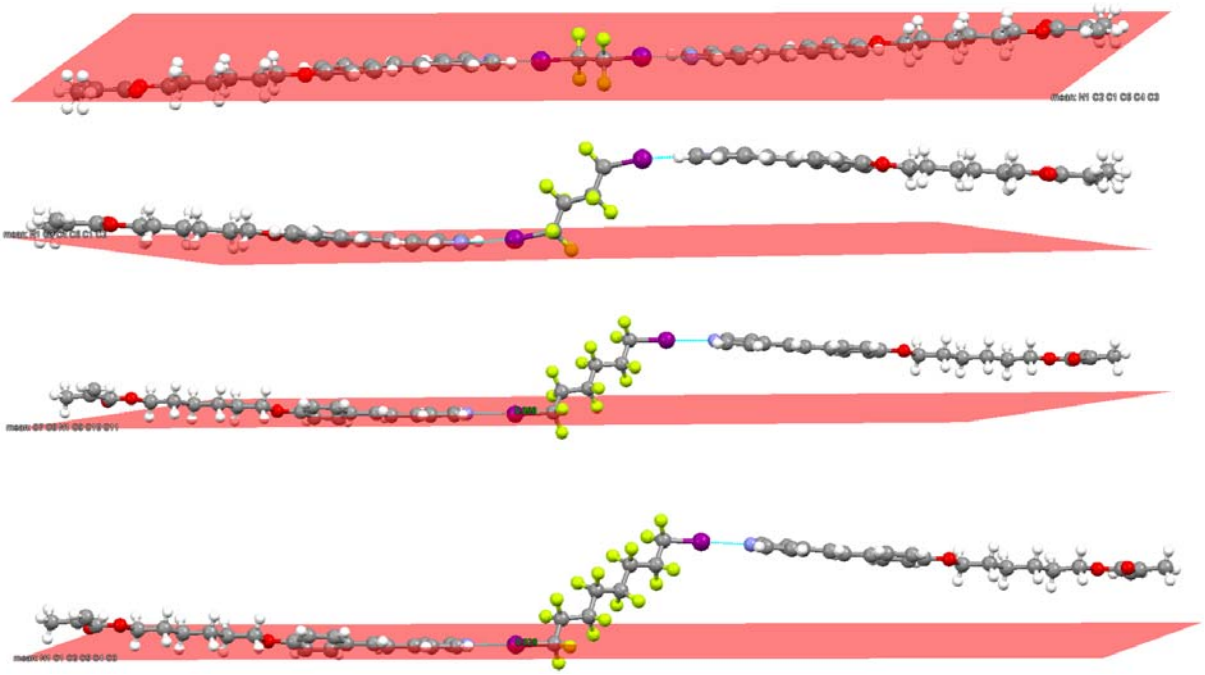

Figure 7.4.2. X-ray structure of complex **3a-3d** showing small differences in the arrangement of the donor/acceptor modules. In complex **3a** the CF_2 units lay on the same plane described by the pyridyl ring of the stilbazole **1**, while with longer perfluoroalkyl chains the α CF_2 units are perpendicular to the plane of the pyridyl rings. Color code as in Figure 7.4.1.

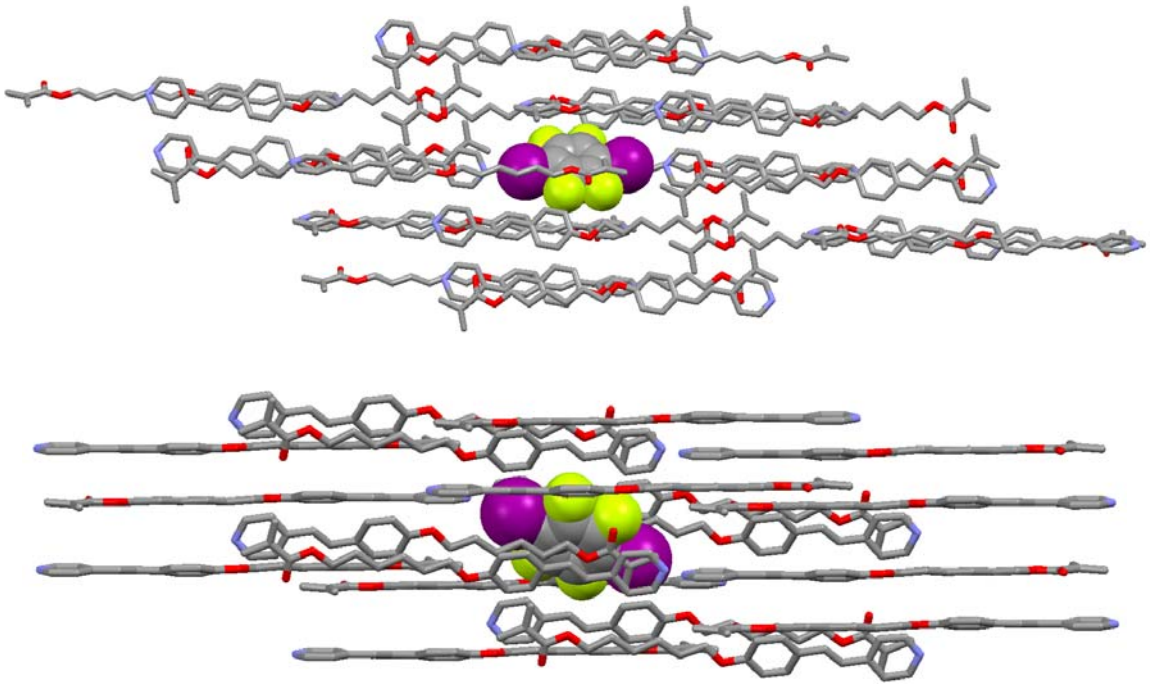

Figure 7.4.3. Crystal packing of complexes **3e** showing the lack of segregation between hydrocarbon and perfluorocarbon modules. Color code as in Figure 7.4.1.

7.4.6. Optical microscopy images

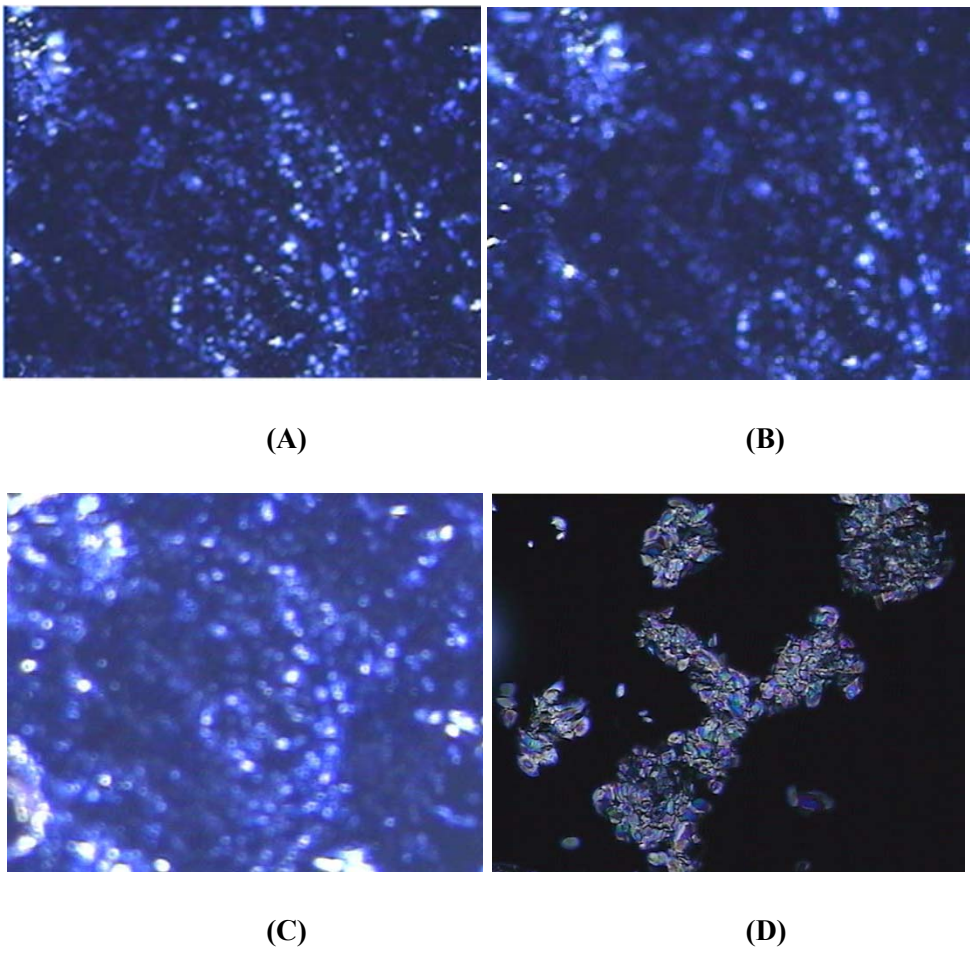

(A) **(B)**

(C) **(D)**

Figure 7.4.4. Optical textures of the smectic A phase observed on cooling from the isotropic state for the different complexes (**A)** Complex **3c** shows the I-Sm transition at 82 °C; **(D)** complex **3d** shows the I-Sm transition at 81 °C; **(C)** complex **3e** shows the I-Sm transition at 92 °C; **(D)** Sm A-Cr transition of complex **3e** at 78 °C.

7.5. References

1. G.M. Sheldrick, *Acta Crystallogr. Sect. A.*, 2008, **64**, 112.
2. C. F. Macrae, I. J. Bruno, J.A. Chisholm, P. R. Edgington, P.McCabe, E. Pidcock, L. Rodriguez-Monge, R. Taylor, J. van de Streek, P. A. Wood, *J. Appl. Cryst.*, 2008, **41**, 466.
3. A. L. Spek, *Acta Crystallogr. Sect. D*, 2009, **65**, 148.
4. *Gaussian 09,* Revision D.01; Gaussian, Inc.: Wallingford CT, 2009.

5. a) Barone,V.; Cossi, M. *J. Phys. Chem. A,* 1998, **102**, 1995-2001, b) Cossi, M.; Rega, N.; Scalmani, G.; Barone, V. *J. Comp. Chem.*, 2003, **24**, 669-681.
6. Zhao, V;Truhlar, D.G. *Theor. Chem. Acc.*, 2008, **120**, 215-241.
7. Grimme, S.; Ehrlich, S.; Goerigk, L. *J. Comp. Chem.*, 2011, **32***,* 1456-1465.
8. a) Becke, A. D. *J. Chem. Phys.*, 1993, **98**, 5648-5652; b) Lee, C.; Yang, W.; Parr, R. G. *Phys. Rev. B: Condens. Matter*, 1988, **37**, 785-789.
9. Dunning, T. H. *J. Chem. Phys.*, 1989, **90**, 1007-1023.
10. Smith, D. G. A.; Burns, L. A.; Patkowski, K.; Sherrill, C. D. *J. Phys. Chem. Lett.*, 2016, **7**, 2197-2203.
11. a) Lu, T.; Chen, F. *J. Comp. Chem*., 2012, **33**, 580-592. b) Lu, T.; Chen, F. *J. Mol. Graph. Model.,* 2012, **38**, 314-323.
12. H.C. Lin, J. Hendrianto, *Polymer,* 2005*,* **46**, 12146–12157.

List of publications at NFM lab

1. Halogen bonded Borromean networks by design: Topology invariance and metric tuning in a library of multi-component systems, **V. Kumar**. T. Pilati, G. Terraneo, F. Meyer, P. Metrangolo and G. Resnati, *Chem. Sci.,* 2016, DOI: 10.1039/c6sc04478f.

2. Structural characterization of new fluorinated mesogens obtained through halogen-bond driven self-assembly, **V. Kumar**, D. J. Mulder, G. Cavallo, T. Pilati, G. Terraneo, G. Resnati, A. P. H. J. Schenning and P. Metrangolo, submitted to *J. Fluor. Chem*., 2017, *(article in press)*

3. Assessing hydrogen bond in $H^+\subset$crypt-111 iodide via halogen bonded adducts formation, **V. Kumar**, T. Pilati, S. Quici, M. R. Chierotti, C. Nervi, R. Gobetto, P. Metrangolo and G. Resnati, to be submitted.

4. Supramolecular size-matching hosts for solubility enhancement and separation of dicarboxylic acid mixtures; **V. Kumar**, T. Pilati, G. Ciancaleoni, G. Terraneo, A. Macchioni, G. Resnati and P. Metrangolo, to be submitted.

5. Fluorination enables for chalcogen bond in crystalline solids; S. K. Nayak, **V. Kumar**, P. Metrangolo, J. Murray, P. Politzer, T. Pilati, G. Resnati and G. Terraneo, to be submitted.

6. Self-assembled $M_{12}L_{24}$ spherical cages to study the halogen bonding complexes in confined space, **V. Kumar**, D. Fujita, T. Pilati, G. Resnati, M. Fujita and P. Metrangolo, manuscript under preparation.

7. Carbon bonding: Structural confirmation in Barbituric acid derivatives; **V. Kumar**. T. Pilati, G. Terraneo, P. Metrangolo, and G. Resnati, manuscript under preparation